EFFECTS OF SURFACE REFLECTION ON RADIATION EMERGING FROM THE TOP OF A PLANETARY ATMOSPHERE

by

K. L. Coulson, G. M. B. Bouricius, and E. L. Gray

Final Report
of
Contract NAS 5-3925

Prepared by

Space Sciences Laboratory
General Electric Company
Philadelphia, Pennsylvania 19101

for

Goddard Space Flight Center
Greenbelt, Maryland

EFFECTS OF SURFACE REFLECTION ON RADIATION EMERGING FROM THE TOP OF A PLANETARY ATMOSPHERE

by

K. L. Coulson, G. M. B. Bouricius, and E. L. Gray

Final Report
of
Contract NAS 5-3925

Prepared by

Space Sciences Laboratory
General Electric Company
Philadelphia, Pennsylvania 19101

for

Goddard Space Flight Center
Greenbelt, Maryland

Abstract

The research reported here consists of two distinct, but related phases. First, measurements of the directional reflectance and degree of polarization have been made for a variety of natural surfaces for several wavelengths in the region $.36\ \mu < \lambda < 1.03\ \mu$. It is found that the reflectance of a given material generally increases with increasing wavelength, and that the degree of polarization generally decreases with increasing wavelength. The directional reflectance of the various materials considered exhibits a local maximum in the direction of the source. Both laboratory and sunlight measurements are presented, although differing angles of illumination preclude direct comparisons in most cases.

The second phase consists of introducing the measurements of both directional reflectance and the degree of polarization (considered linear) into the equation of radiative transfer. These are used as boundary conditions enabling one to compute the intensity and degree of polarization of radiation emerging from the top of a planetary atmosphere. The relevant assumptions and approximations are discussed in detail. In some instances, comparisons are made with the corresponding solution under the assumption that the "ground" is a Lambert surface.

TABLE OF CONTENTS

LIST OF FIGURES

LIST OF FIGURES

LIST OF FIGURES

LIST OF FIGURES

LIST OF FIGURES

LIST OF FIGURES

LIST OF FIGURES

LIST OF FIGURES

Introduction

The present investigation was started in recognition of the very important role which the reflection from a planetary surface plays in determining the characteristics of sunlight which is returned to space from the top of the planetary atmosphere. For the earth, such information finds obvious application in the interpretation of data from meteorological satellites and in problems of high altitude aerial photography. With respect to Mars, the principal interest in surface reflection data is in deducing the properties of the planetary surface material itself and in a better determination of the density of the Martian atmosphere. Additional problems in which surface reflection properties are important are a determination of the atmospheric energy budget on both small and large scales, investigations of the spectral distribution of skylight, and in bioclimatic and ecological studies.

The results reported here represent a continuation and elaboration of previous work in the area of surface reflection. Since reports of the earlier work are already available (Coulson, Bouricius, Gray - 1964, 1965), every effort is made here to avoid unnecessary duplication of the discussions. However a considerable number of new measurements have been made and several new aspects of the problems have been investigated since those reports were issued. It is mainly this new work which is detailed below. The report is divided into three main sections, each of which is devoted to one part of the problem. After a brief background survey of previous measurements, the instrument and the procedures by which our measurements were made are discussed in the first part of the report. The results of the measurements, including both directional reflectance and degree of polarization of the reflected radiation, constitute the second part. The third part is a discussion of the methods and results of introducing the reflection measurements into the radiative transfer equations and computing the characteristics of the radiation which would be directed outward from the top of two different models of the earth's atmosphere overlying different types of surface materials. Finally, the paper entitled "Effect of Surface Reflection on the Propagation of Optical Contrasts" which was presented at the Conference on Atmospheric Limitations to Optical Propagation, Boulder, Colorado on March 18, 1965 is included as an appendix.

Background

A relatively complete bibliography of the measurements by various authors of the reflection properties of natural surfaces was give by Coulson et al (1964, 1965). Before the present work was started, the most extensive measurements of the reflectance of natural terrestrial surfaces were those of Krinov (1947), in which the spectral reflectance, mainly in the nadir direction, was determined for various soils, rocks, sands, and different types of vegetation. The degree of linear polarization of visible light reflected from various mineral substances was determined in series of measurements by Lyot (1929) and Dollfus (1957, 1961) in an effort to explain the reflection properties of the moon and planets. Aside from these relatively extensive sets of measurements, data on both surface reflectance and state of polarization of the reflected light have been scattered and sparse.

Since the time the bibliography mentioned above was issued, a number of important publications on surface reflection characteristics have appeared. Gates (1965) has given detailed spectra of the radiation reflected from vegetation of various types. Kondratiev, et al (1965) have likewise shown spectra of reflected radiation for vegetation as well as for fallow ground, snow, and shallow water surfaces. Of particular interest in their results is the increase of reflectance at all wavelengths with increasing zenith angle of the sun. Hovis (1965) has measured the total spectral reflectance of a number of iron oxide minerals in the wavelength range from 0.5 to 6.0 microns and found a relatively strong dependence of reflectance on particle size, the dependence being most pronounced in the vicinity of 2 microns wavelength. Effects of water of hydration in the materials are shown by low reflectances at wavelengths of 0.9 microns and 3.0 microns. Similar measurements on quartz minerals also show pronounced effects of absorption by the water of hydration in the mineral, and confirm the fact that particle size significantly affects the total reflectance.

II. Instrumentation and Measurement Techniques

A. Theory of Measurement

The method of measuring directional reflectance has been given in detail in a previous report (Coulson, Bouricius, Gray - 1964) and that discussion will not be repeated here. Briefly, however, directional reflectance $\rho(\theta, \varphi)$ at any nadir angle θ and azimuth φ is given by the relation

$$\pi \rho(\theta, \varphi) = \frac{I(\theta, \varphi)}{I_s(\theta = 0)} . \qquad \text{(II-1)}$$

Here $I(\theta, \varphi)$ is the intensity of radiation reflected from the sample and $I_s(\theta = 0)$ is the intensity of radiation reflected from a standard surface under the same conditions of illumination. The factor π is a normalization constant arising from the requirement that the hemispheric integration of directional reflectance give the total monochromatic reflectance $R(\lambda)$ of the surface. If we let $\mu = \cos\theta$, the total monochromatic reflectance for the standard surface is

$$R_s(\lambda) = \int_0^1 \int_0^{2\pi} \rho_s(\lambda)\, \mu\, d\mu\, d\varphi = \rho_s(\lambda) \int_0^1 \int_0^{2\pi} \mu\, d\mu\, d\varphi = \pi \rho_s(\lambda) = 1, \qquad \text{(II-2)}$$

or ρ_s has the constant value π^{-1}.

The degree of linear polarization of the reflected radiation was measured by rotating an analyzer in the optical system and measuring, as a function of the angle ψ between the plane of transmission of the analyzer and an arbitrary direction, the relative intensity $I(\psi)$ of the transmitted radiation. For this case $I(\psi) = 1/2 \ I + Q \cos 2\psi + U \sin 2\psi$ (II-3) where I, Q, and U are the well-known Stokes parameters (cf. Chandrasekhar, 1950). The maximum I_{max} of the transmitted radiation would occur when the plane of transmission of the analyzer is parallel to the plane of polarization of the reflected radiation, and the minimum I_{min} would occur after a further rotation of the analyzer by $\pi/2$. In both of these cases $U \equiv 0$, and the degree of plane polarization is given by

$$P = \frac{I_{max} - I_{min}}{I_{max} + I_{min}} \tag{II-4}$$

For these measurements, the values of I_{max} and I_{min} were determined from a strip chart record of $I(\psi)$ taken during the continuous rotation of the analyzer.

B. Reflectometer Assembly Schematic

The instrument which was used for the measurements is shown schematically in Fig. 1. The material sample is contained in a 2 feet by 1 foot rectangular sample tray, S, which is illuminated by a light source, L, from a zenith angle, θ_o. The surface is viewed from a zenith angle, θ, and azimuth angle, φ, by the photo-electric reflectometer, R. The reflectometer

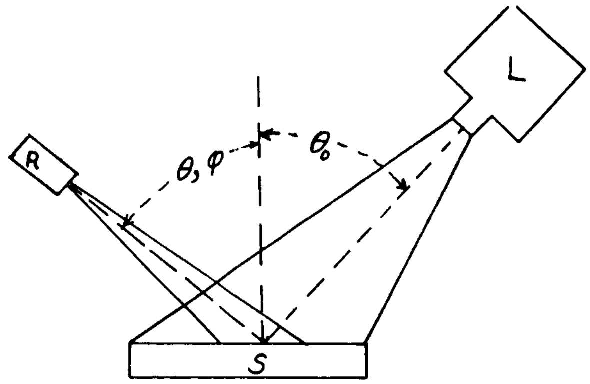

Fig. 1 - Schematic representation of apparatus used in reflection measurements

mount is shown in schematic form in Fig. 2. Basically it consists of a circular 1 1/4" plywood base 8 feet in diameter. A circular section 5 feet in dimater is cut from the center, thereby making an 8' plywood ring. A full 360° circular track on which the wheeled instrument carriage is mounted is attached to the plywood ring. This permits the carriage to be positioned at any desired azimuth angle φ with respect to the azimuth of the source and provides for easily changing azimuth as required.

An instrument carrier arm which moves in a vertical plane through a zenith angle θ of $\pm 80^{\circ}$ is attached to the movable carriage, thus providing two degrees of freedom for the orientation of the instrument. The reflectometer itself is mounted on the carrier arm in such an orientation that it always views the surface at the center of the 5 foot hole in the plywood base,

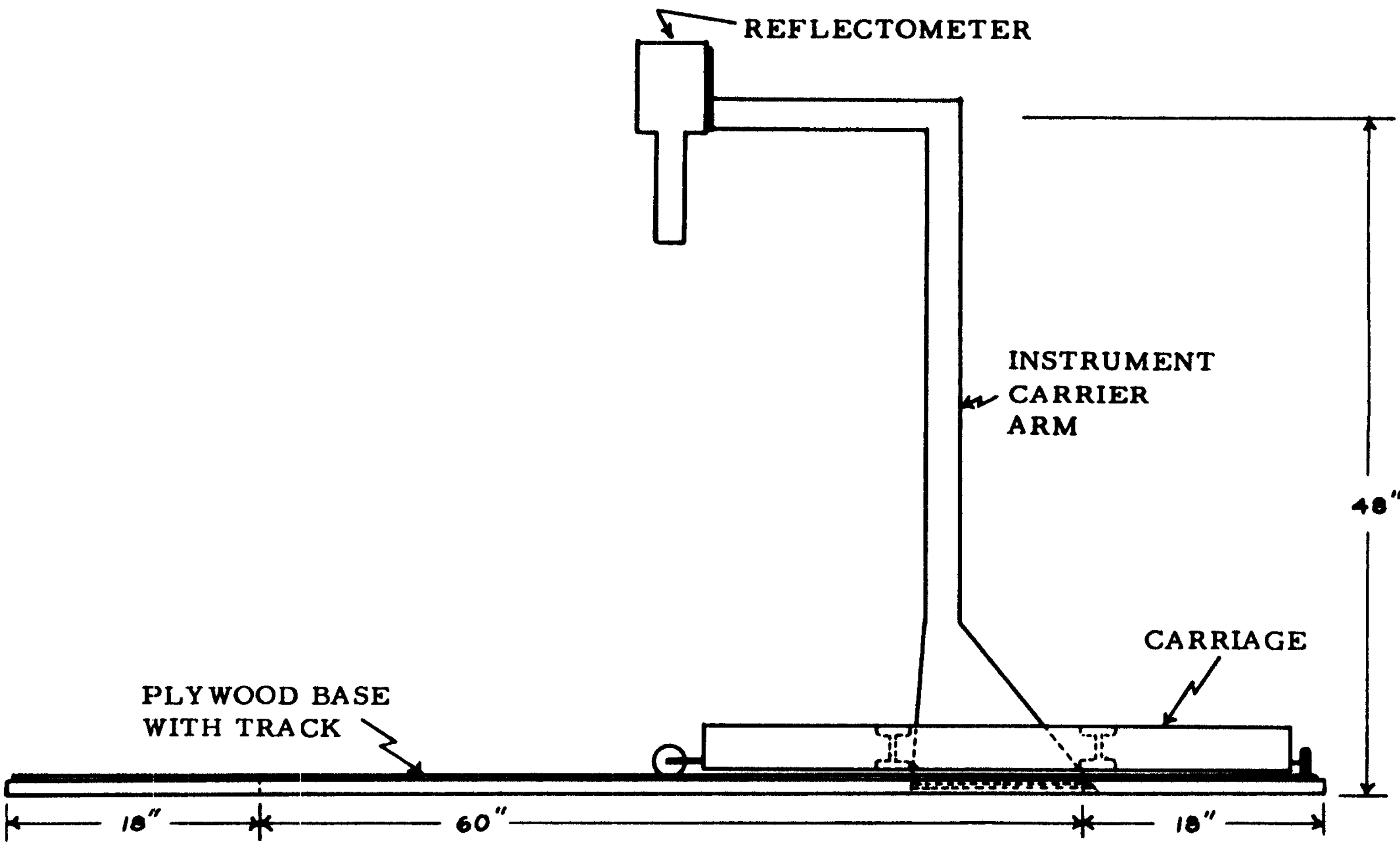

Fig. 2 Schematic diagram of movable reflectometer mount for reflection measurements.

Table I - Notation used in expressions of the five radiative components and not previously defined

D - subscript denoting direct transmission
d - subscript denoting diffuse transmission

$\underset{\sim}{N}$ - a three element column vector, the elements of which are given in terms of the measured degree of polarization $P(\mu, \varphi)$ of the reflected radiation and the angle x between the plane of polarization and the vertical plane through the viewed direction. The elements are
$1 + P(\mu, \varphi) \cos 2x$, $1 - P(\mu, \varphi) \cos 2x$, $2 P(\mu, \varphi) \sin 2x$

$\bar{R}$ - total reflectance of the surface

$\underset{\sim}{S}$ - atmospheric reflection matrix (cf. Chandrasekhar [1950])
s - subscript denoting "standard" case
$\underset{\sim}{T}$ - Atmospheric transmission matrix (cf. Chandrasekhar [1950])

$\bar{s}$ - a known function of τ only. Tabulations are available (cf. Sekera and collaborators [1952, 1953])

μ' - dummy variable of integration

φ' - dummy variable of integration

$\left.\begin{array}{l}\gamma_e(\mu)\\ \gamma_r(\mu)\\ \gamma_e(\mu_0)\\ \gamma_r(\mu_0)\end{array}\right\}$ Quantities which are functions of τ and θ or θ_0. Tabulations are available. (cf. Sekera and collaborators [1952, 1953]).

We now make the assumption that the diffuse radiation field is only negligibly affected by the existence of the target, which is tantamount to saying that the horizontal extent of the target is much smaller than the horizontal extent of the background material. This assumption is obviously valid in many practical problems, such as in the detection of so-called cultural targets from a position above the atmosphere. Then, following

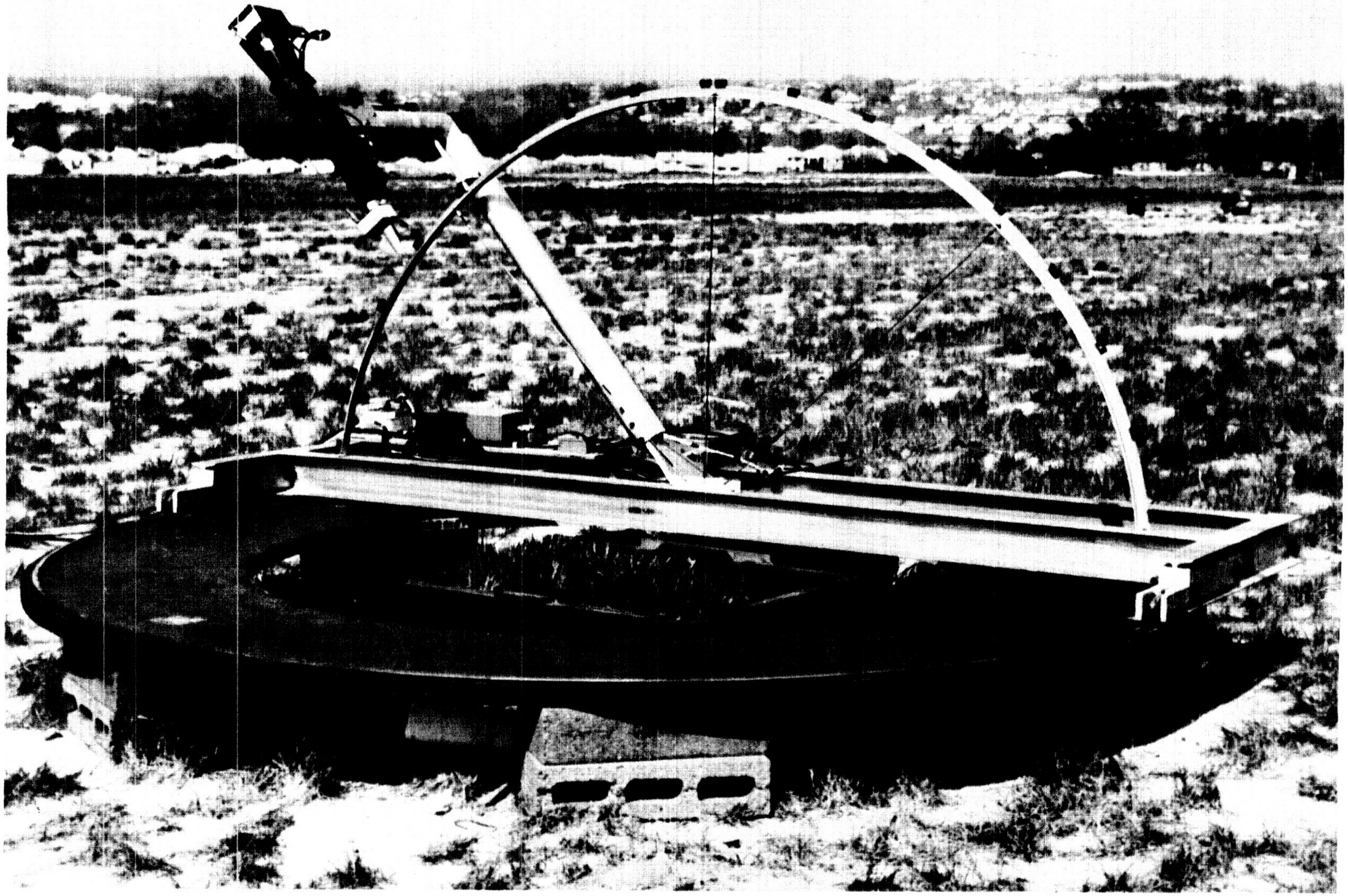

Fig. 3 Reflectometer in operation in sunlight. Data are being taken on a sample of clipped green grass. Construction details are shown.

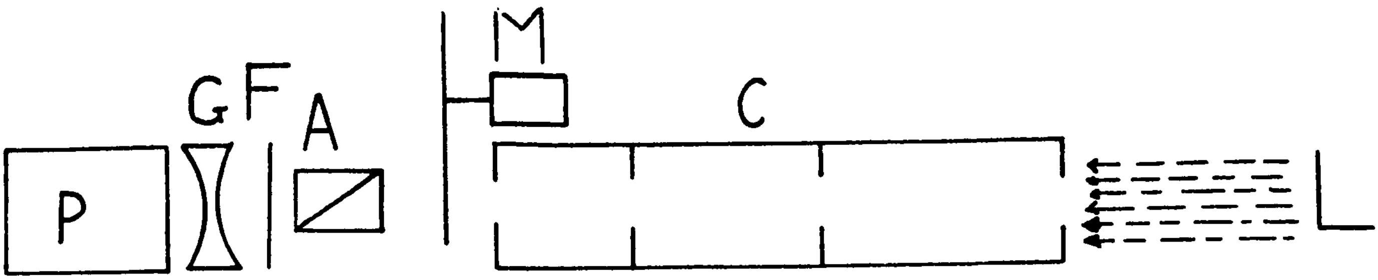

Fig. 4. Schematic of the Reflectometer Sensor Head

shining directly into the reflectometer showed that the polarization introduced by the instrument is less than 0.50 %; which is about the limit of the instrument.

Measurements were made at the following wavelengths:

3650Å
4050Å
4920Å
6430Å
7960Å
10250Å

The filter curves are shown in Fig. 5.

Measurements at 3650Å were made only outdoors in sunlight because of the difficulty of obtaining a source of sufficient strength at this wavelength in the laboratory. Measurements at 10250Å were made with a modified sensor head in which the photomultiplier tube was replaced with a solid state detector.

D. Electronics and Recording System

A block diagram of the recording system in shown in Fig. 6. The following figures show the details of the separate block items. Fig. 7 shows the photomultiplier tube voltage divider and AC amplifier. Since the photomultiplier cathode response does not extend to 10,250Å, a solid state detector was used with the 10,250Å filter. This solid state detector and associated AC amplifier is shown in Fig. 8. The AC signal from the AC amplifier is fed

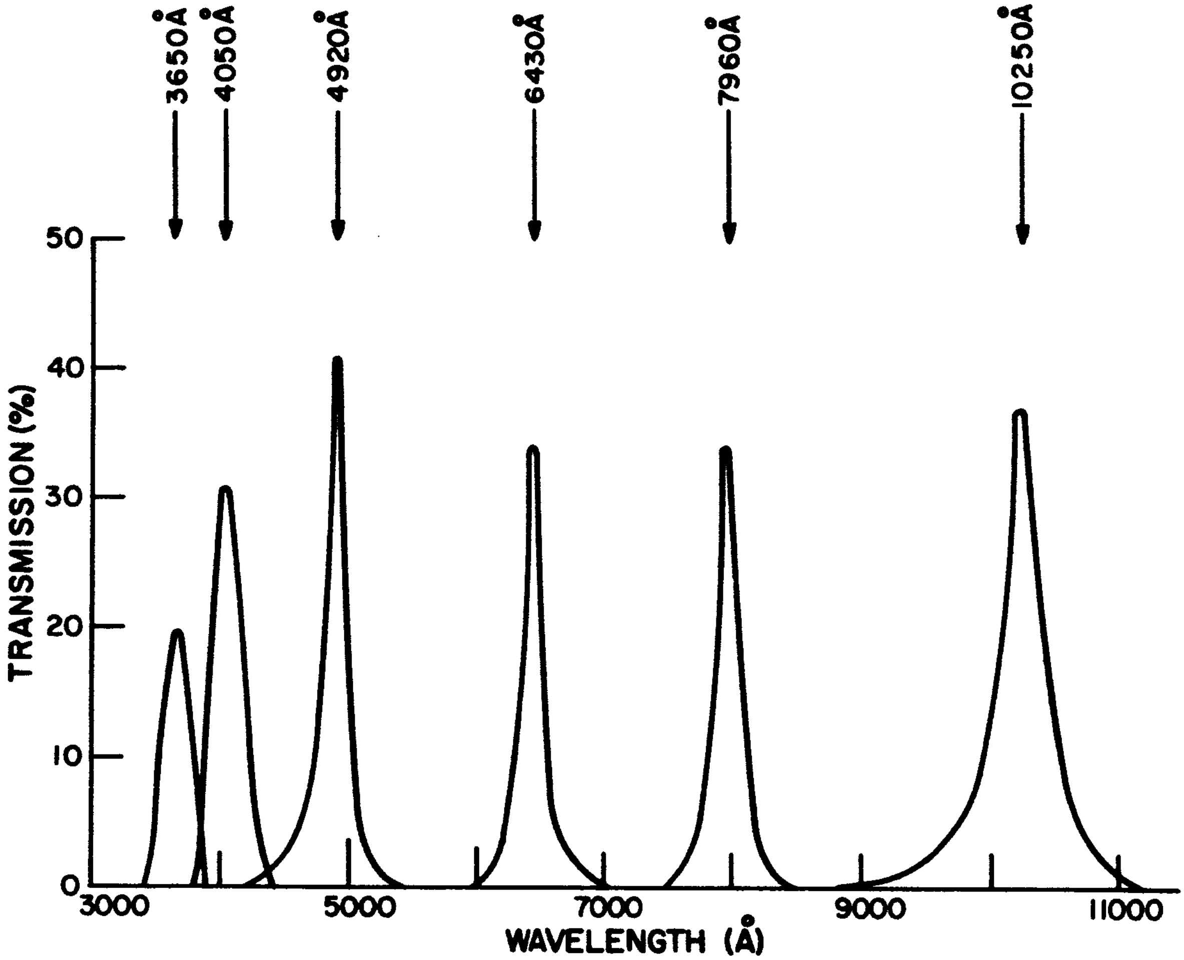

Fig. 5 Relative transmission, as a function of wavelength, of filters used in these reflection measurements

Fig. 6. A block diagram of the recording system is shown.

into the rectifier circuit, shown in Fig. 9, which produces a D. C. output proportional to the A. C. input. In order to have a reference on the chart recording of the orientation of the analyzer direction, the analyzer is turned by a synchronous motor from the same AC source as that which drives the strip chart recorder. Once each revolution of the analyzer, a circuit is made and broken. This circuit is a microswitch actuated mechanically from an eccentric cam fastened to the rotating analyzer mounting. The electrical circuit of the pulse marker is shown in Fig. 10. The pulse marker superposes an instantaneous pulse on the D. C. signal from the rectifier. Thus the pulse on the recording indicates the position angle of the analyzer at that time. By direct measurement on the chart recording, the intensity at any angle, ψ, may be obtained.

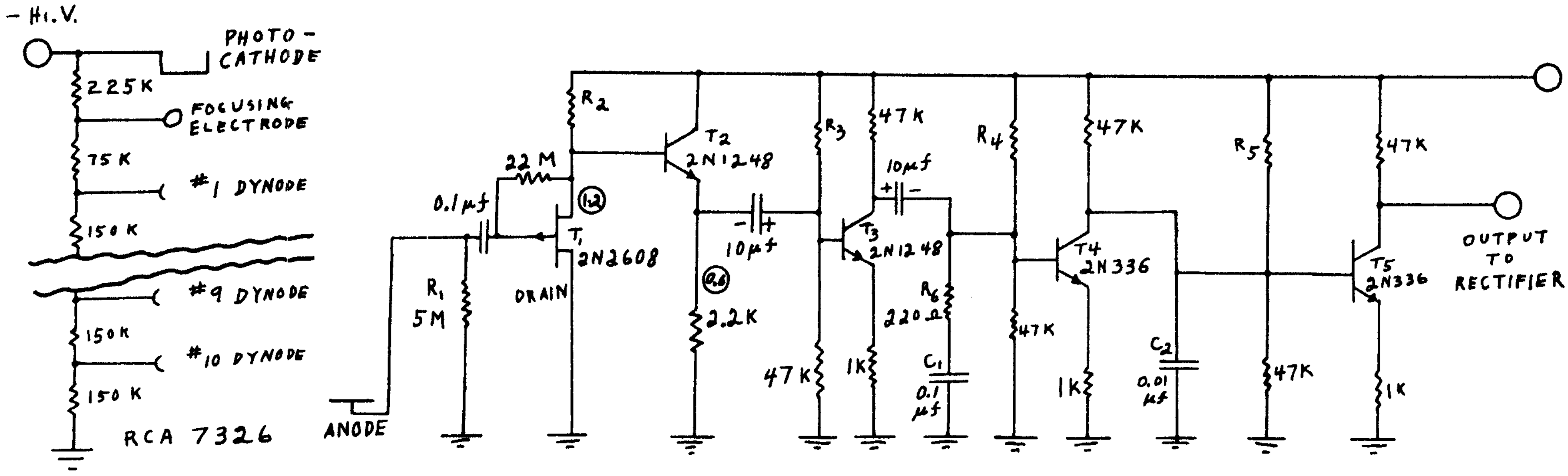

Fig. 7. Photomultiplier tube voltage divider and AC amplifier.

R_1 is the load on the anode of the photomultiplier. It is made up of 5 resistors; low noise, deposited metal film, 1 megohm each, in series.

T_1 is a field effect transistor for high input impedance as a source follower. R_2 is adjusted to produce the minimum noise. T_2 , is a low noise transistor as an emitter follower. Numbers in circles are voltages at these locations. Resistors R_3 , R_4 , R_5 are used to set the biases on T_3 , T_4 & T_5 to produce collector voltages of about 10 Volts. R_3, R_4 & R_5 are about 1 megohm each. R_6 , C_1 and C_2 limit the bandwidth. Maximum output of the amplifier is about 8 volts peak to peak before distortion. The AC amplifier circuit is shown connected to the photomultiplier tube.

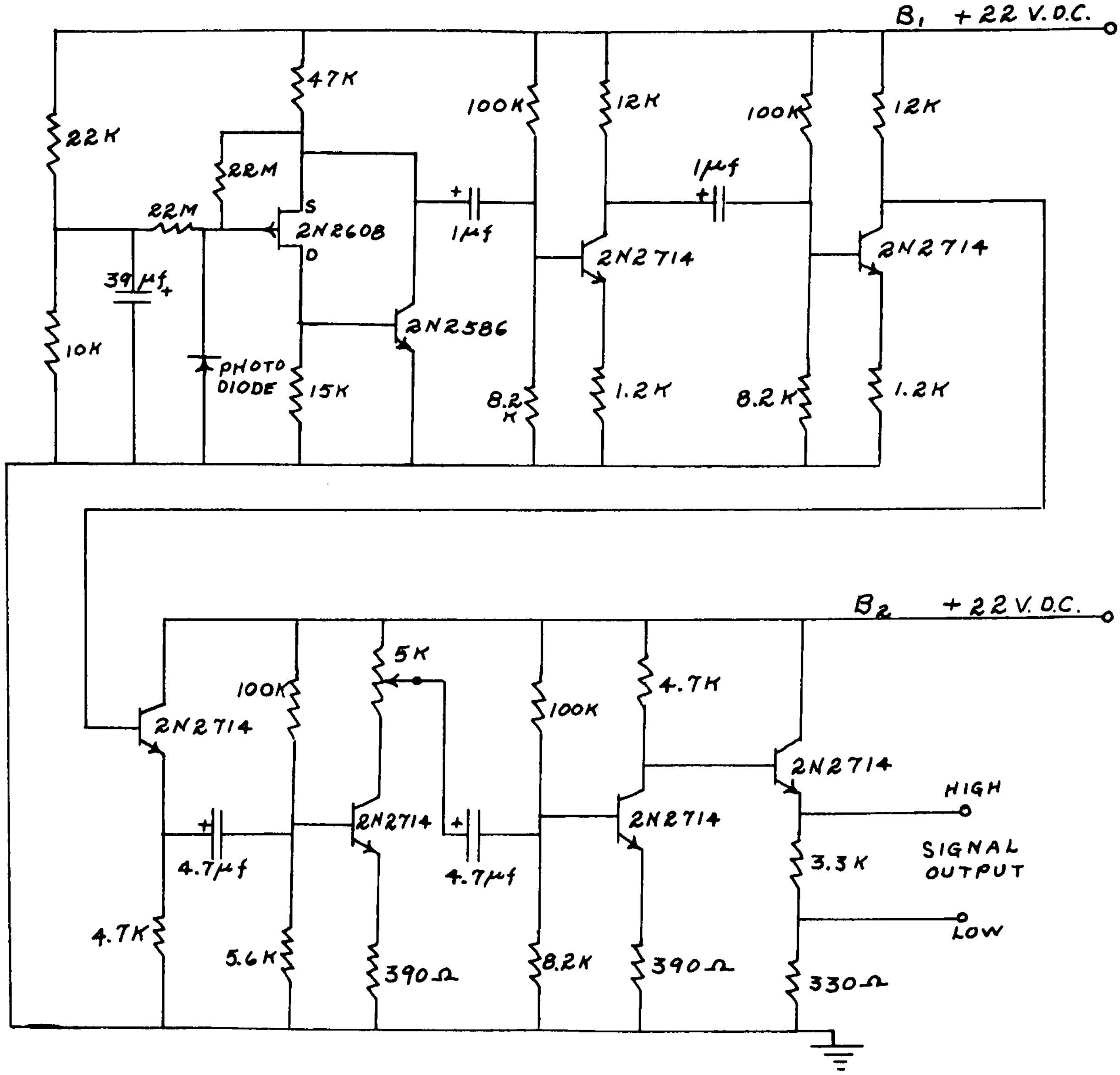

Fig. 8: Detector and A. C. Amplifier Circuit --- for Silicon Photodiode

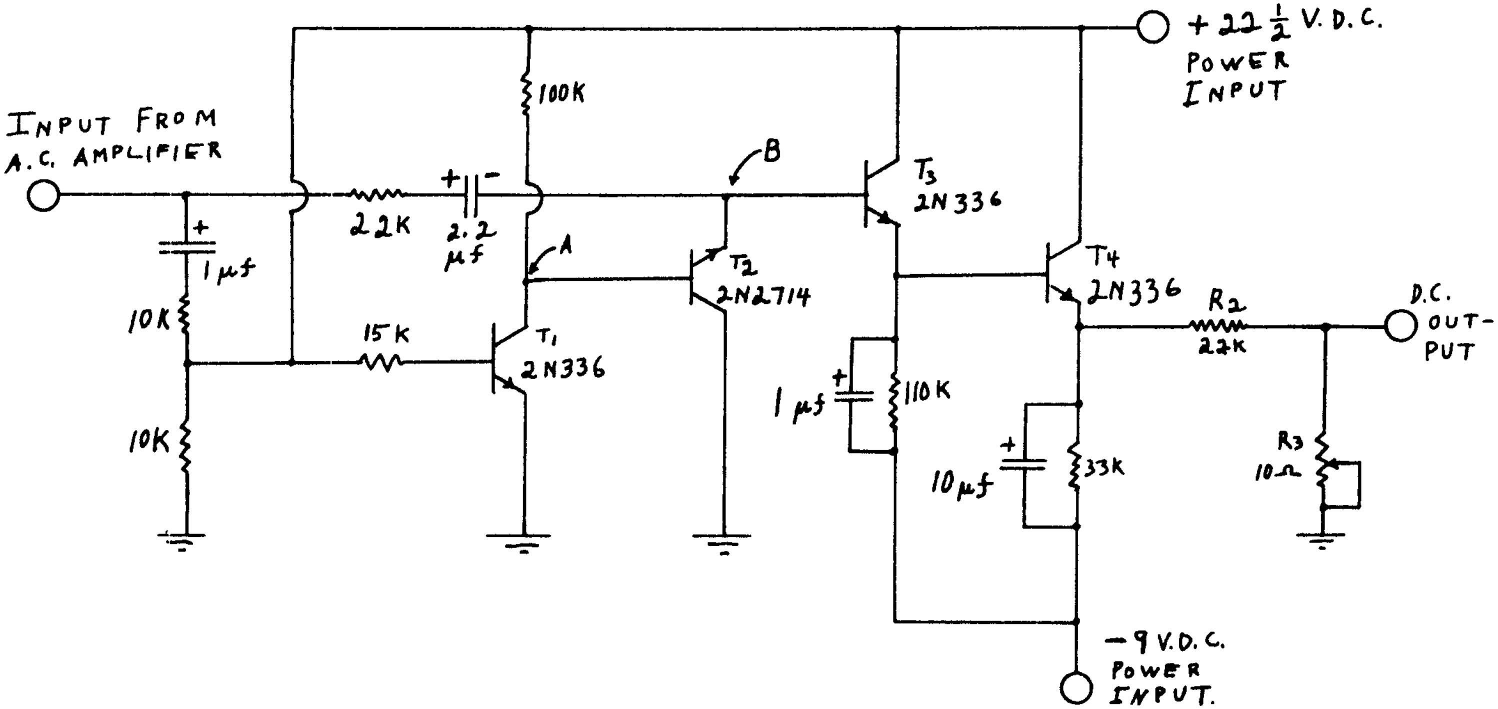

Fig. 9. Rectifier and D. C. Output Circuit

Amplifier T_1 drives the synchronous rectifier, T_2 . R_1 is adjusted so that the discontinuities in the scope trace looking at point A are about the same level. To prevent excessive non-linearity of the signal at B, the emitter followers T_3 & T_4 are used. Their emitters are returned to a negative supply to eliminate the base to emitter voltage problem in the output. Resistors R_2 & R_3 are a voltage divider. R_3 is adjusted to suit the recorder being used. AC signal input is monitored and when the input is 8V peak to peak, R_3 is adjusted for full output.

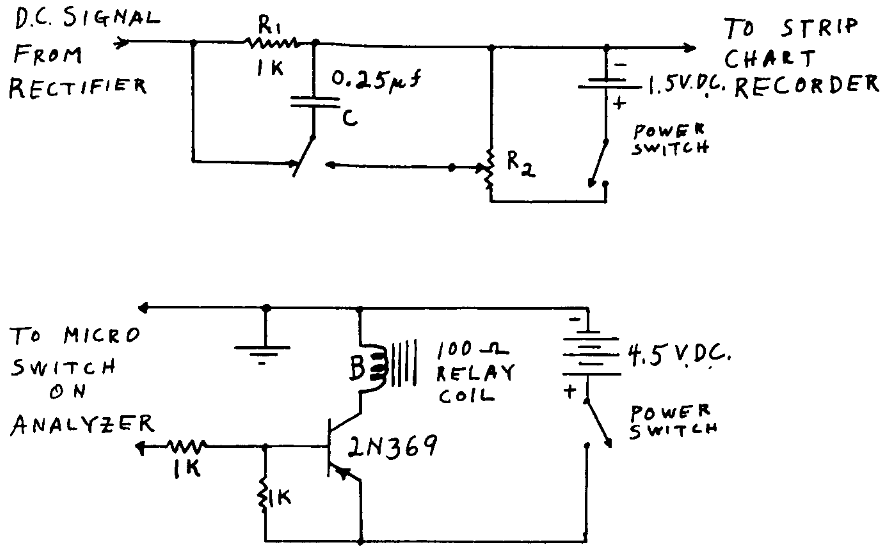

Fig. 10. Pulse Marker Circuit.

As the microswitch rides up on the cam on the analyzer and closes contacts, the relay, B, closes the normally open contact (N.O.) thus putting a charge on C. The amount of charge is determined by the value of C and the setting of R_2. When the microswitch opens, the relay de-energizes, thus discharging C through R_1. This causes a momentary pulse to appear on the trace on the recorder.

being equal, to use the I_i component and reject, by means of polarizing optics, the I_j component. This possibility has been discussed more fully by Fraser[1964b].

The total hemispheric distribution of Y_i is shown by Fig. 6. The patterns for Y and Y_j are similar to that of Y_i , but the maximums are reduced and broadened in accordance with the curves of Fig. 5.

The emergent intensity components for the case of desert soil, $\lambda = 6430\ \mathring{A}$, and $\theta_o = 53^{o}$ are plotted as a function of nadir angle in the principal plane in Fig. 7. The dominant roles played by I_{DD} and I_{dD} are evident throughout a wide angle around the nadir, as are the relatively minor contributions of the atmospheric scattered components $I_s^{(R)}$ and $I_s^{(A)}$. Introduction of this combination into Eq. (8) produces the very high contrast transmission curves of Fig. 8. Since the reflection of radiation at $\lambda = 6430\ \mathring{A}$ from desert sand produces only little polarization and the highly polarized components arising from atmospheric scattering are weak, there is relatively little difference between the contrast transmissions Y_i and Y_j . In such a case there would not be a great advantage in using polarizing optics for imaging devices viewing the surface from above the atmosphere.

An extreme case of large optical thickness being combined with low surface reflectance is represented by a clipped green grass surface at 4050 $\mathring{A}$. The emergent intensity components for this sytem are shown by the diagram of Fig. 9. As would be expected from the fact that the total reflectance of green grass at $\lambda = 4050\ \mathring{A}$ is only 0.026, all of the surface-reflected components are extremely weak. The two components due to skylight incident at the surface, I_{dD} and I_{dd} , are too small to even plot usefully on this scale. The components

(3) Series at azimuth $\varphi = 0^\circ$ as θ was varied in 10° steps from $\theta = 0^\circ$ to $\theta = 70^\circ$ and in 5° steps from $\theta = 70^\circ$ to $\theta = 80^\circ$.

(4) Secondary standard

(5) Repetition of (3) at $\varphi = 45^\circ$, 90°, 135°, 180°, with a return to the secondary standard after the series at each azimuth

(6) Short series of $\theta = 70^\circ$, 75°, 80° at $\varphi = 22.5^\circ$, 67.5°, 112.5°, and 157.5°, with a return to the secondary standard after the series at each azimuth

(7) Standard surface at $\theta = 0$.

This group of measurements, each of which gave directional reflectance and degree of linear polarization, furnished adequate data for construction of hemispheric maps of reflectance and state of polarization of the reflected radiation.

F. Standard Surface Preparation

The standard surface was made by depositing approximately two millimeters of magnesium oxide smoke on a flat aluminum plate which had already been painted with a white paint of the type used to cover the temperature elements of meteorological radiosondes. Thus a reflectance approaching 100% was assured. The standard surface was always viewed from the normal direction, thereby avoiding any effects of a non-isotropic reflection pattern of the magnesium oxide coating. This surface was used as a standard for all indoor measurements. An attempt was made to use this same type of standard surface outdoors, but the small gusts of wind would blow the magnesium oxide layer away. Therefore, a block of magnesium carbonate was used as a standard surface for outdoor measurements. These two standard surfaces were compared one with the other in laboratory measurements so that all experimental data on samples could be compared in a consistent manner.

The source of illumination for all indoor measurements was an incandescent lamp. The light from this lamp, when viewed directly by the reflectometer, was found to have less than 1% of linear polarization in the principal plane. Experiments were performed to determine the effect of this small amount of source polarization upon the reflection and polarization characteristics of the various samples. The results of these experiments showed that the effects were within experimental error, and so could be neglected.

G. Samples and Sample Preparation

The following samples were used; some more extensively than the others.

1. Crushed limestone (Philadelphia, Pa.)
2. Black loam (Mt. Ayr, Iowa)
3. Desert sand (Mojave, Calif.)
4. Clipped green grass (Philadelphia, Pa.)
5. Pulverized limonite (Tuscaloosa County, Ala.)
6. Weathered blacktop (Philadelphia, Pa.)
7. Quartz sand (Daytona Beach, Fla.)
8. Gypsum sand (White Sands National Monument, N. Mex.)
9. Yolo loam (Davis, Calif.)
10. Red clay (Philadelphia, Pa.)

Each sample was placed in a sample tray in such a manner that the surface to be viewed was level with the sides of the tray. For the granular samples, such as sands and soils, the surface was carefully levelled off by means of a straight edge. Every effort was made to avoid directional effects being introduced during the leveling process. The blacktop surface was readily adjusted for correct height in the sample tray. For the clipped green grass, the effective top of the grass blades, as judged by eye, was made to coincide with the level of the sides of the sample tray. Once the sample had been chosen and prepared in a sample tray, the tray was placed upon the stage of the reflectometer mount, where it was levelled and centered preparatory to viewing.

H. Data Reduction

The experimental data were taken on a strip-chart recorder. The equation giving the radiant intensity, I, as a function of analyzer angle of rotation, ψ, is in the form of a sine wave; see equation (II-3). In order to obtain the radiant intensity and degree of polarization, only the maximum and minimum values of $I(\psi)$ were required. The maximum and minimum values were read from the chart by eye and then punched onto computer cards. A computer program was written to obtain values for π times the reflectance and degree of polarization from these raw data. Built into the computer program was a third degree polynomial calibration equation to adjust for the slight non-linearity of the recording system. A least squares method was programed to obtain the numerical coefficients for the polynomial. The experimental data for the least squares program were the neutral density filter calibration data taken at the beginning of each day's operation. The tabulated data of the computer output were manually plotted for graphic presentation.

III Results of Measurements

In this section, we discuss the results of surface measurements of directional reflectance and degree of polarization. Several general characteristics of the measured surfaces, such as increase of reflectance with increasing wavelength, low reflectance corresponding to high polarization, and high reflectance to low polarization, will be emphasized in the following discussion. In addition to these characteristics, there is one other evident conclusion: namely, that the natural surfaces investigated here exhibit reflectance patterns which are not well approximated by either Lambert type or Fresnel type reflection.

A. Reflectance

1. The Backward Maximum

One of the most universal characteristics observed in the surfaces measured is the "backward" maximum, a relative maximum of the directional reflectance in the direction toward the source. The magnitude of this maximum is dependent on sample, wavelength, and source zenith angle. To illustrate this maximum, as well as its dependence on the above parameters, we have chosen samples of crushed limestone, black loam, and pulverized limonite. In the following curves, the ordinate scale is π times the directional reflectance.

Fig. 11 shows the directional reflectance in the principal plane of a crushed limestone sample, as a function of nadir angle, for several wavelengths and a source zenith angle of 53°. (The individual particles vary in size from 1/2" to 3/4", and are generally angular in shape as a result of the crushing

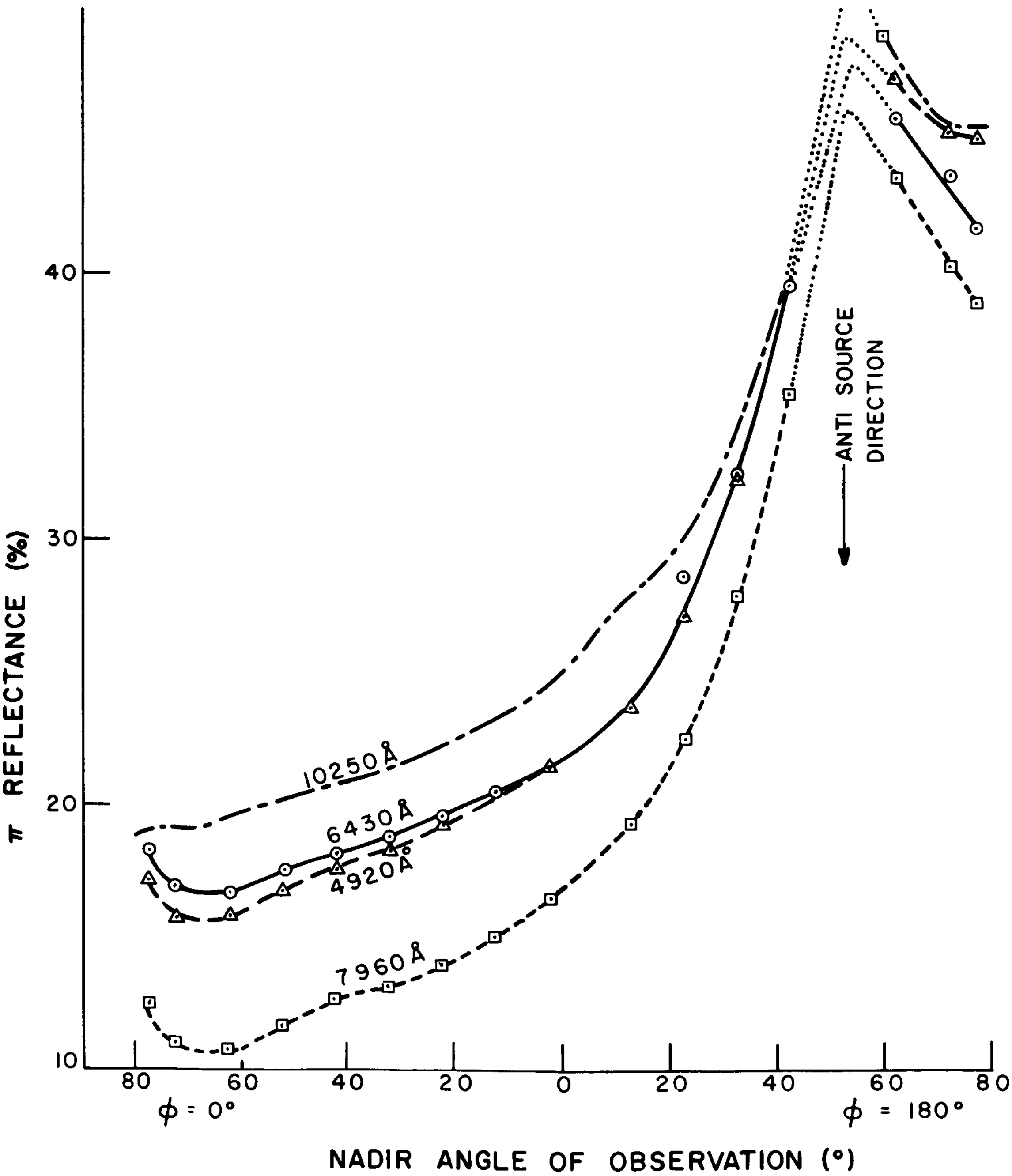

Fig. 11 Directional reflectance of crushed limestone (principal plane, $\theta_o = 53^o$)

process). The position of the backward maximum is clearly indicated, despite the fact that the dotted section of the various curves indicates an interpolation. The interpolation is necessary since for $\theta = \theta_o$, $\varphi = 180^o$, the observing instrument causes the sample tray to be in shadow. The magnitude of the maximum does not vary greatly with changes in the wavelength. In fact, in the backward direction, $.46 \leq \pi\rho \leq .50$ for all wavelengths at which measurements were made. This particular sample is interesting in another respect. Most surfaces exhibit a monotonic increase in reflectance as the wavelength is increased. The crushed limestone sample provides an exception to this, the measurements at $\lambda = 7960\text{Å}$ being considerably lower than at other wavelengths.

Fig. 12 shows the effect of a change in the source zenith angle θ_o on the magnitude of the backward maximum. These curves represent measurements of the same surface at the same wavelengths, but for $\theta_o = 78.5^o$. A good estimate of the actual values of directional reflectance in the backward direction is even more difficult here than previously, since it is difficult to obtain measurements for $\theta > 80^o$. The curves show a marked increase in the magnitude of the backward maximum for the larger value of θ_o. This is typical of most surfaces.

Fig. 13 shows the directional reflectance in the principal plane of black loam soil as a function of nadir angle, for several wavelengths and a source zenith angle of 53^o. (The sample was obtained in Southwestern Iowa near the town of Mt. Ayr). This set of curves is distinctly different from that of crushed limestone for the same source position. First, the magnitudes

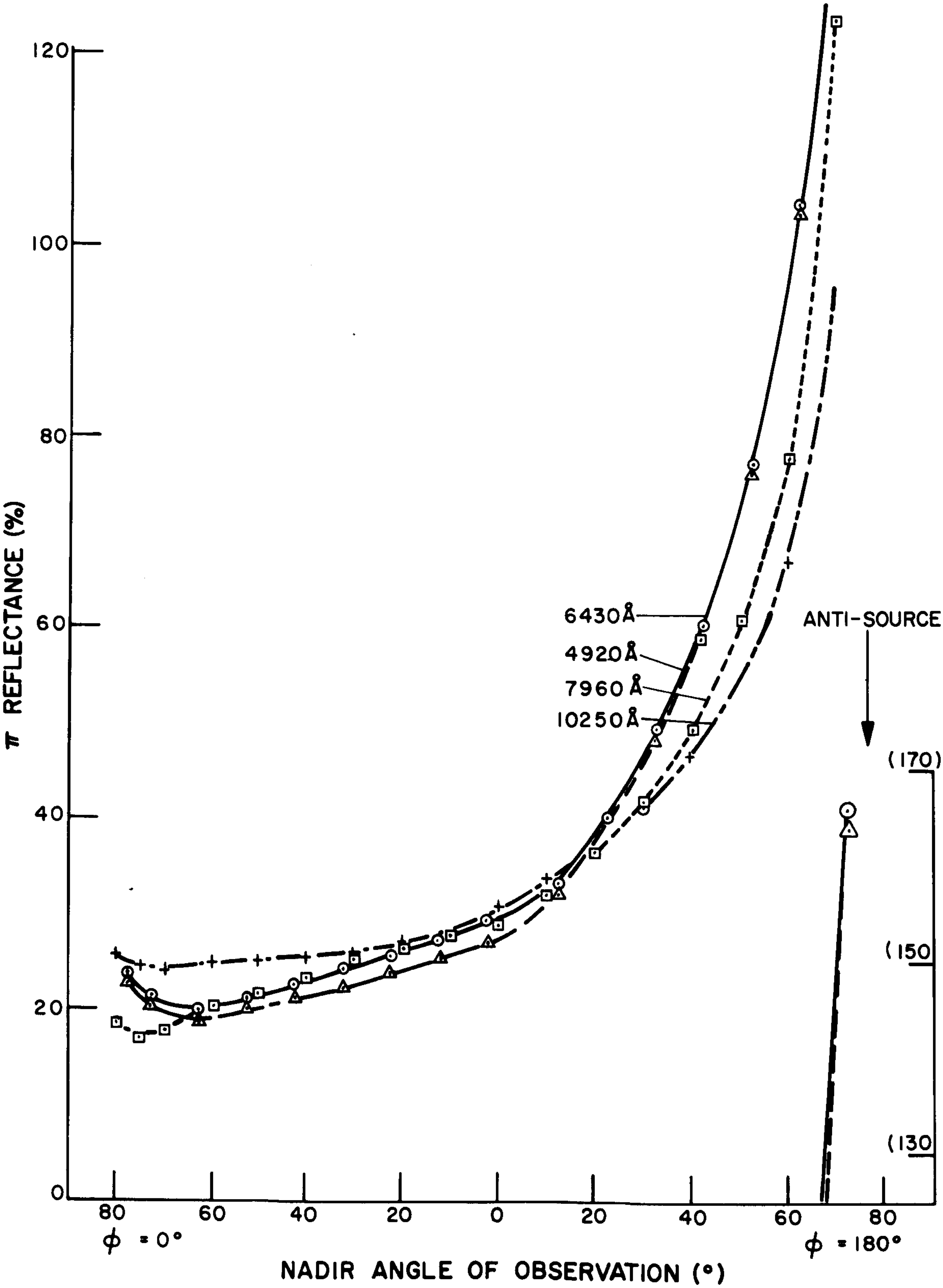

Fig. 12 Directional reflectance of crushed limestone (principal plane, θ_0 = 78.5°)

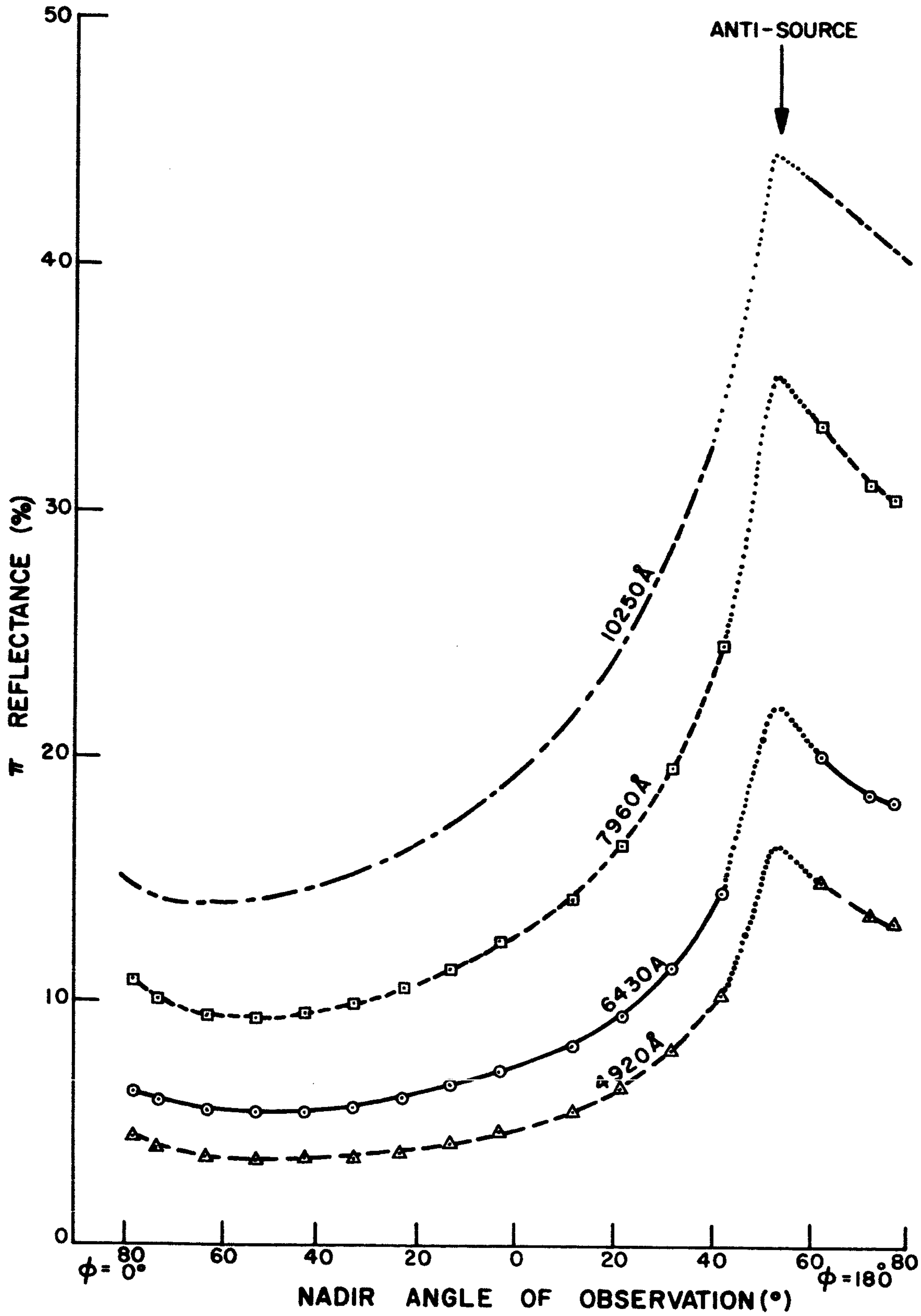

Fig. 13 Directional reflectance of black loam soil (principal plane, $\theta_o = 53^o$)

of the backward maxima are more dependent on wavelength, $\pi\rho$ varying from .165 to .445 as the wavelength varies from 4920Å to 10250Å. Secondly, the directional reflectance is seen to increase with increasing wavelength throughout the principal plane.

Fig. 14 shows curves for the same sample and same wavelengths, but for $\theta_o = 0°$. The curves are symmetrical with respect to the nadir direction, since the source is at the zenith. The magnitudes of the backward maxima are seen to be substantially reduced when compared with the previous figure. This is in accord with the observation of an increase in magnitude of the backward maximum with an increase in the source zenith angle. Again, the reflectance is seen to increase with increasing wavelength.

In Fig. 15 , the increase in the magnitude of the backward maximum with increasing θ_o is emphasized by choosing one wavelength for a given sample. The sample is pulverized limonite, having a mean particle size of 14 microns. The various curves represent the directional reflectance in the principal plane, as a function of nadir angle, for a wavelength of 4920Å, for the following values of θ_o: 0°, 23°, 37°, 53°, 67°, 78.5°, and 84°. The magnitude of the backward maximum increases rapidly with increasing θ_o.

In the sections to follow, various other characteristics of the measurements will be called to attention, and different samples will be used in illustrations. It should be realized that some of these characteristics are qualitatively independent of the sample. For example, in the following curves the presence of a backward maximum is a general characteristic, although the samples have been chosen to emphasize different features of

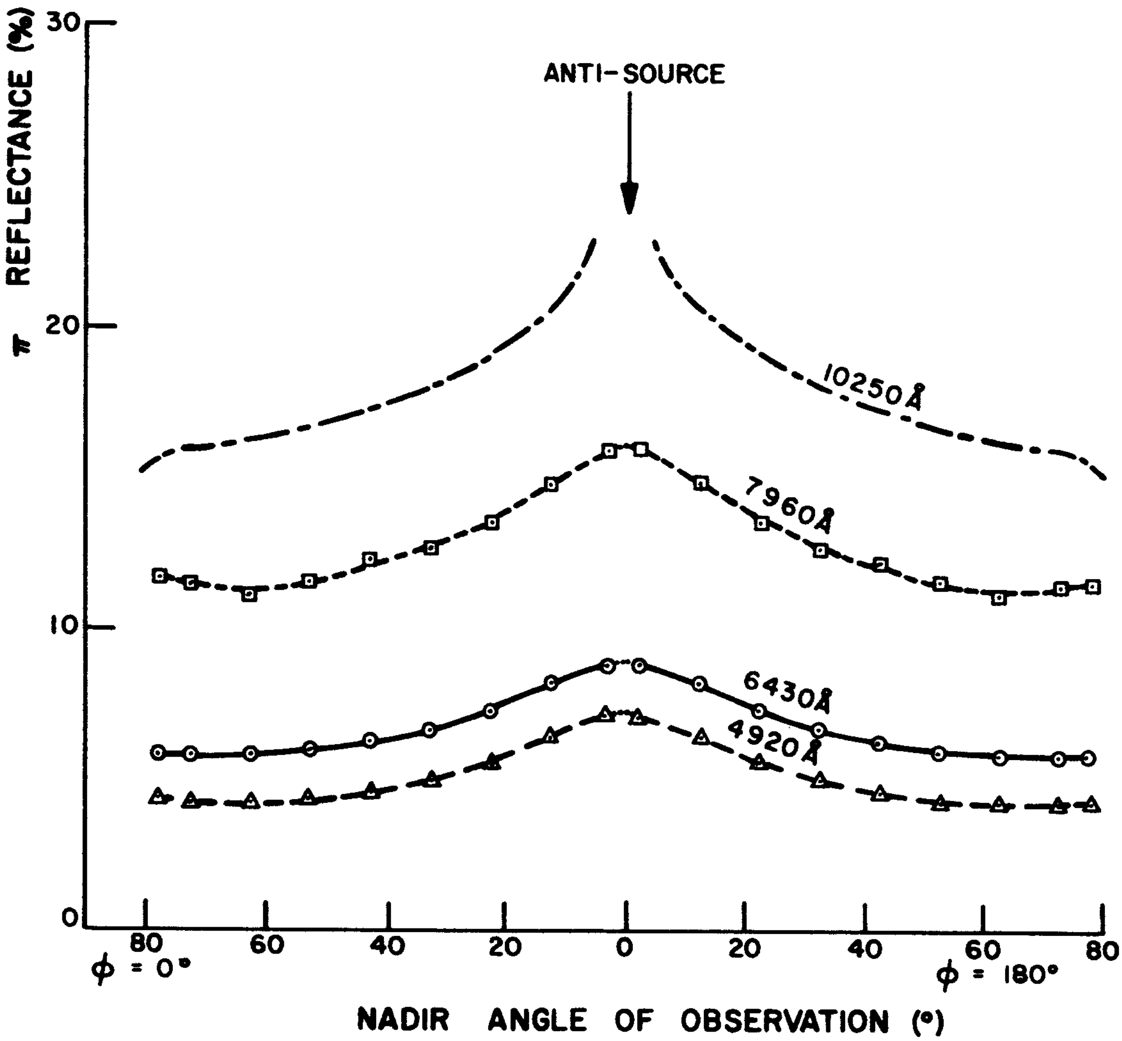

Fig. 14 Directional reflectance of black loam soil (results independent of azimuth, $\theta_0 = 0^{\circ}$)

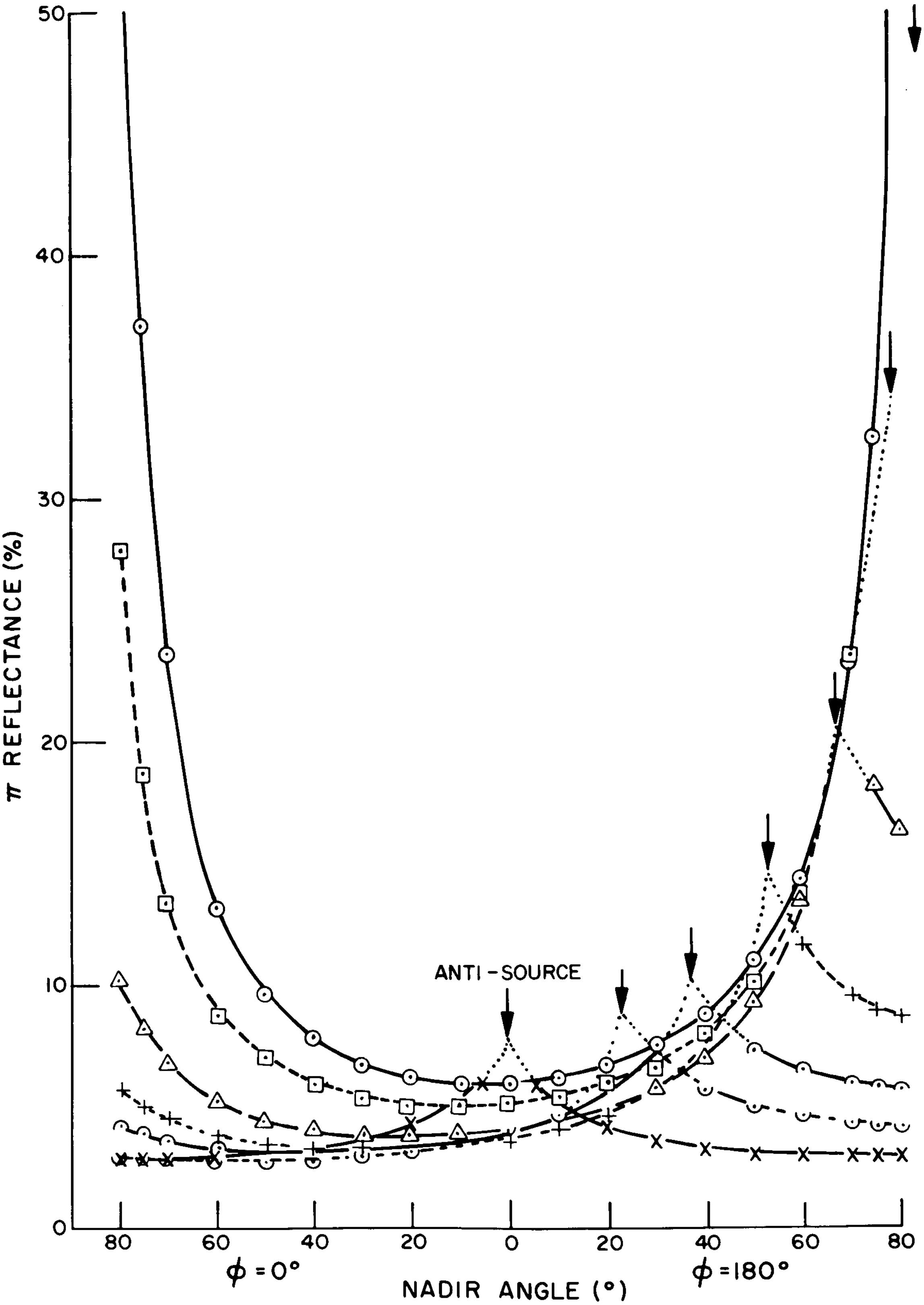

Fig. 15 The dependence of the directional reflectance upon source zenith angle is shown for pulverized red limonite at a wavelength of 4920Å

the reflection pattern.

2. Variation of Reflectance with Wavelength

We have indicated previously that the reflectance of a given sample generally increases for increasing wavelength, althrough crushed limestone is a notable exception. Figures 13 and 14 showed such an increase for black loam soil at $\theta_o = 53^\circ$ and $\theta_o = 0^\circ$, respectively, while Fig. 16 shows a similar characteristic for black loam at $\theta_o = 78.5^\circ$.

Fig. 17 shows the directional reflectance of a sample of desert sand obtained from the Mojave Desert about eleven miles northeast of Mojave. The measurements for $\lambda = 4050\text{Å}$, 4920Å, 6430Å, 7960Å, and 10250Å were made in the laboratory for $\theta_o = 53^\circ$, while the measurements at 3650Å were made outdoors at a sun zenith angle of approximately 40°. It should be pointed out that a part of the outside illumination is in the form of diffuse light from the sky, whereas in the laboratory the sample is illuminated from a single source. This difference may alter the relative shapes of the curves. Fig. 17 is a good example of the increase of reflectance with increasing wavelength, as is Fig. 18, which shows the reflectance of desert sand at $\theta_o = 78.5^\circ$. ($\theta_o = 54^\circ$ for $\lambda = 3650\text{Å}$). Fig. 19 shows the corresponding measurements of the desert sand sample for a source zenith angle of 0°.

The variation of reflectance with wavelength for desert sand can be appreciated from Fig. 20, in which $\pi\rho$ is shown as a function of λ for three observation angles ((1) $\varphi = 0^\circ$, $\theta = 45^\circ$; (2) $\varphi = 180^\circ$, $\theta = 45^\circ$; (3) $\theta = 0^\circ$) for source angle $\theta_o = 78.5^\circ$. The reflectance increases by a factor of three as the wavelength increases from 4050Å to 10250Å for all three viewing angles.

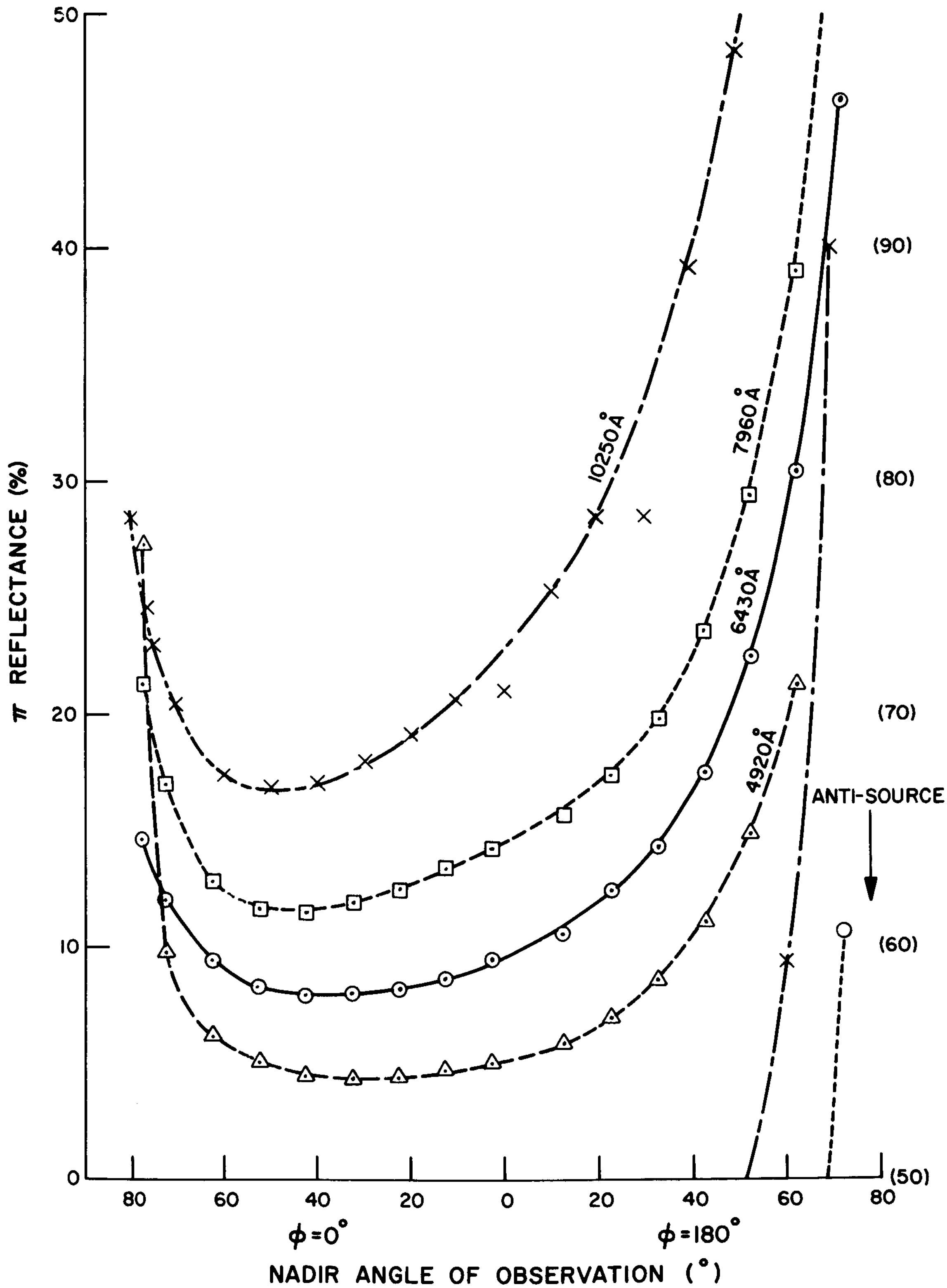

Fig. 16 Directional reflectance of black loam soil (principal plane, θ_o = 78.5°)

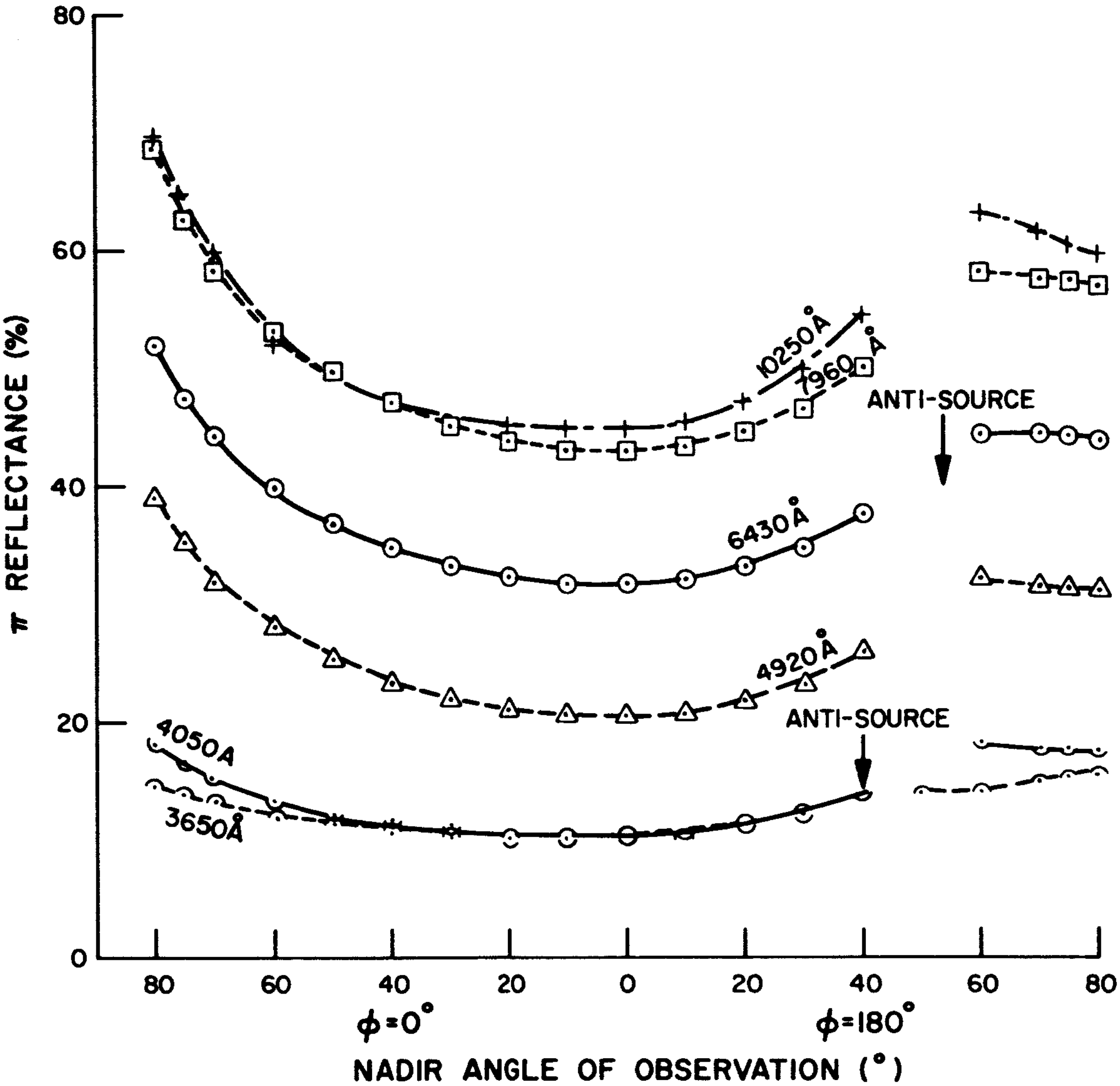

Fig. 17 Directional reflectance of desert sand (principal plane). For $\lambda = 3650\text{Å}$, $\theta_0 = 40^{\circ}$; for other λ's, $\theta_0 = 53^{\circ}$

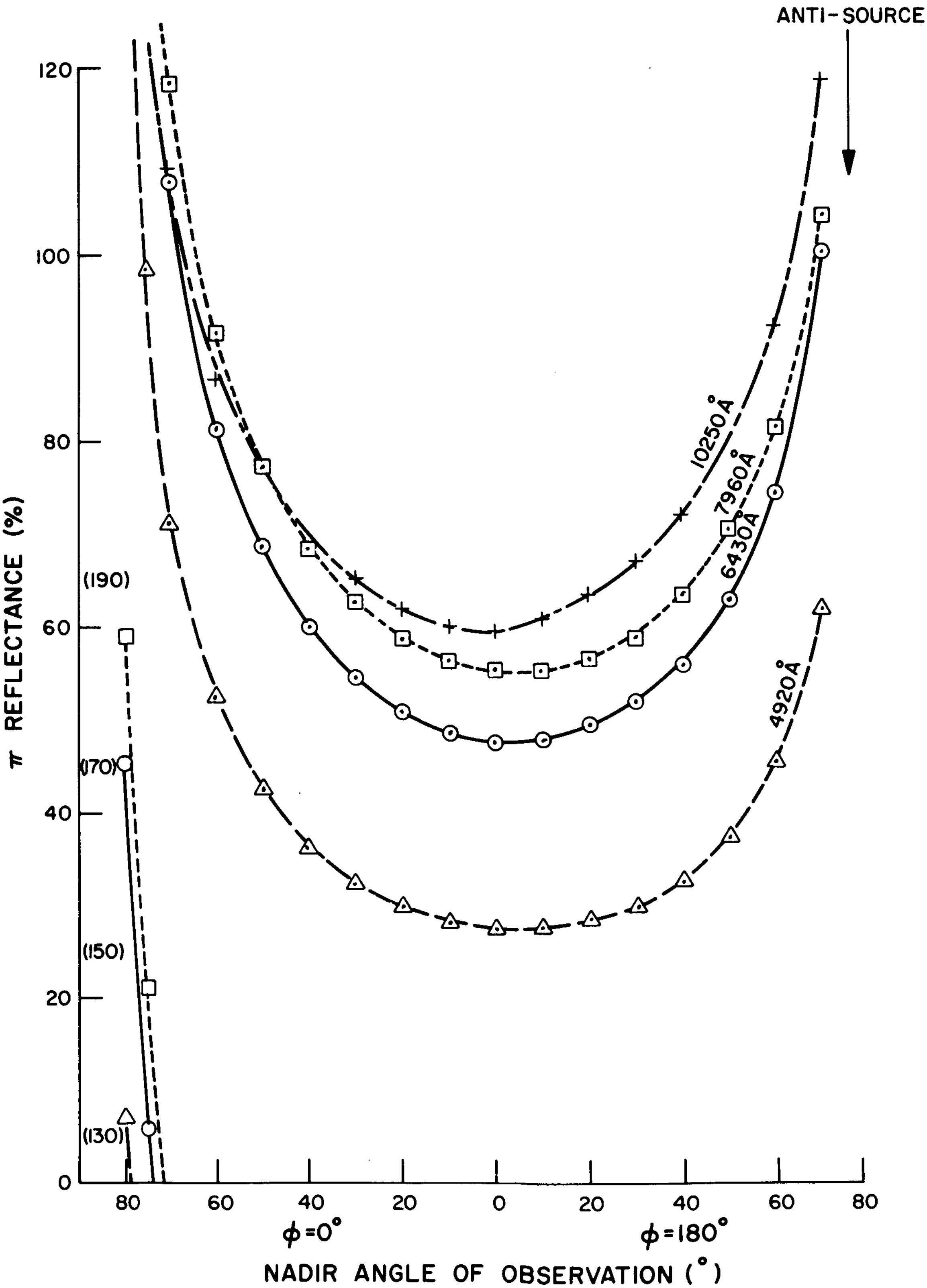

Fig. 18 Directional reflectance of desert sand (principal plane, $\theta_0 = 78.5^{\circ}$)

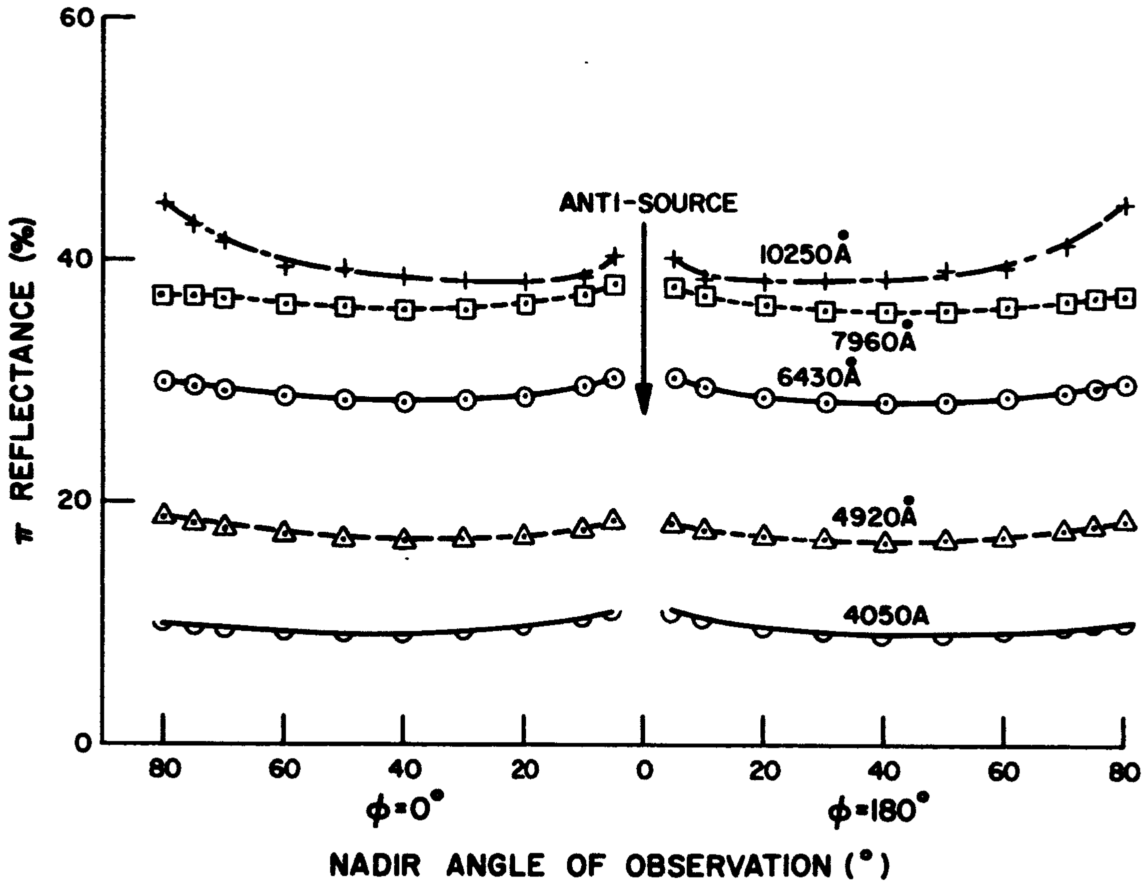

Fig. 19 Directional reflectance of desert sand (results independent of azimuth, $\theta_0 = 0^o$)

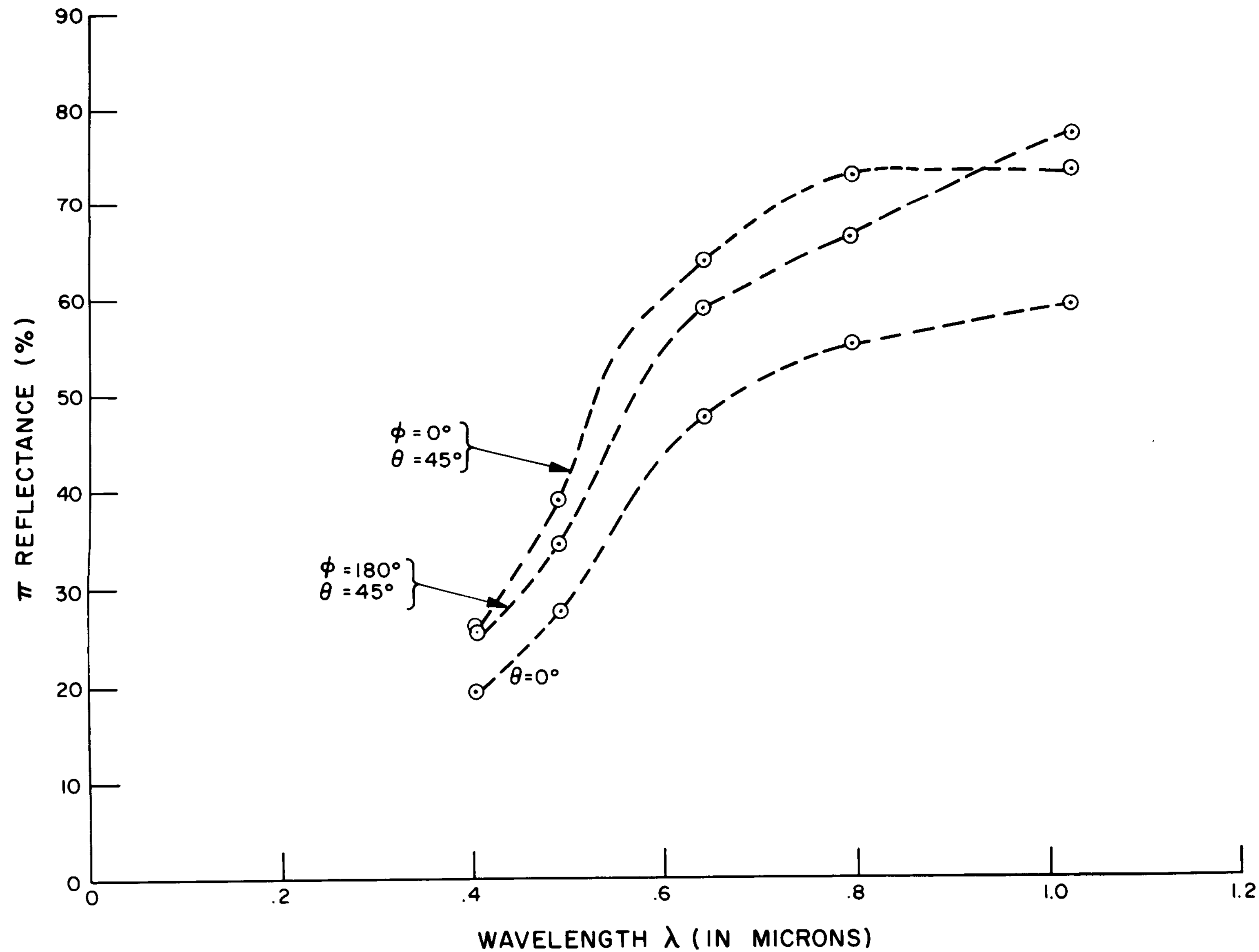

Fig. 20 Directional reflectance of desert sand is shown as a function of wavelength

Figures 17 and 18 illustrate another feature which is frequently shown by the measurements; that is, for source angles not near the zenith, the directional reflectance exhibits a broad minimum in the region of the nadir.

A sample of clipped green grass provides another example of increased reflectance for the longer wavelengths. Fig. 21 shows the directional reflectance in the principal plane as a function of nadir angle for the source at the zenith. The reflectance is seen to increase sharply as the wavelength is increased, the magnitude of $\pi\rho$ being .05 or less for $\lambda = 4920\text{Å}$ and 6430Å, and ranging from .20 to .45 at longer wavelengths. Fig. 22 is also for the clipped grass sample, but for different zenith angles of the source. In addition to the laboratory measurements at $\lambda = 7960\text{Å}$ and 10250Å at $\theta_o = 53°$, a sunlight measurement for $\lambda = 3650\text{Å}$ and $\theta_o = 40°$ is presented. The broad minimum surrounding the nadir direction and the maximum in the backward direction are especially apparent at the longer wavelengths. The reflectance at wavelength 7960Å is apparently greater than that for 10250Å at $\varphi = 0°$ and $\theta > 75°$. This reversal in magnitude is very pronounced in Fig. 23, which shows curves for the green grass sample for a source zenith angle of 78.5°. For $\lambda = 7960\text{Å}$ and 10250Å, the curves are extended beyond $\pi\rho = 125\%$ by use of an auxiliary scale.

3. Absence of Specular Reflection

Another characteristic of the measured reflectance patterns is the absence of specular reflection, as would be indicated by a maximum of reflected intensity at the direction $\varphi = 0°$, $\theta = \theta_o$. There are, however, surfaces which exhibit strong forward reflection. Fig. 24 provides such an example.

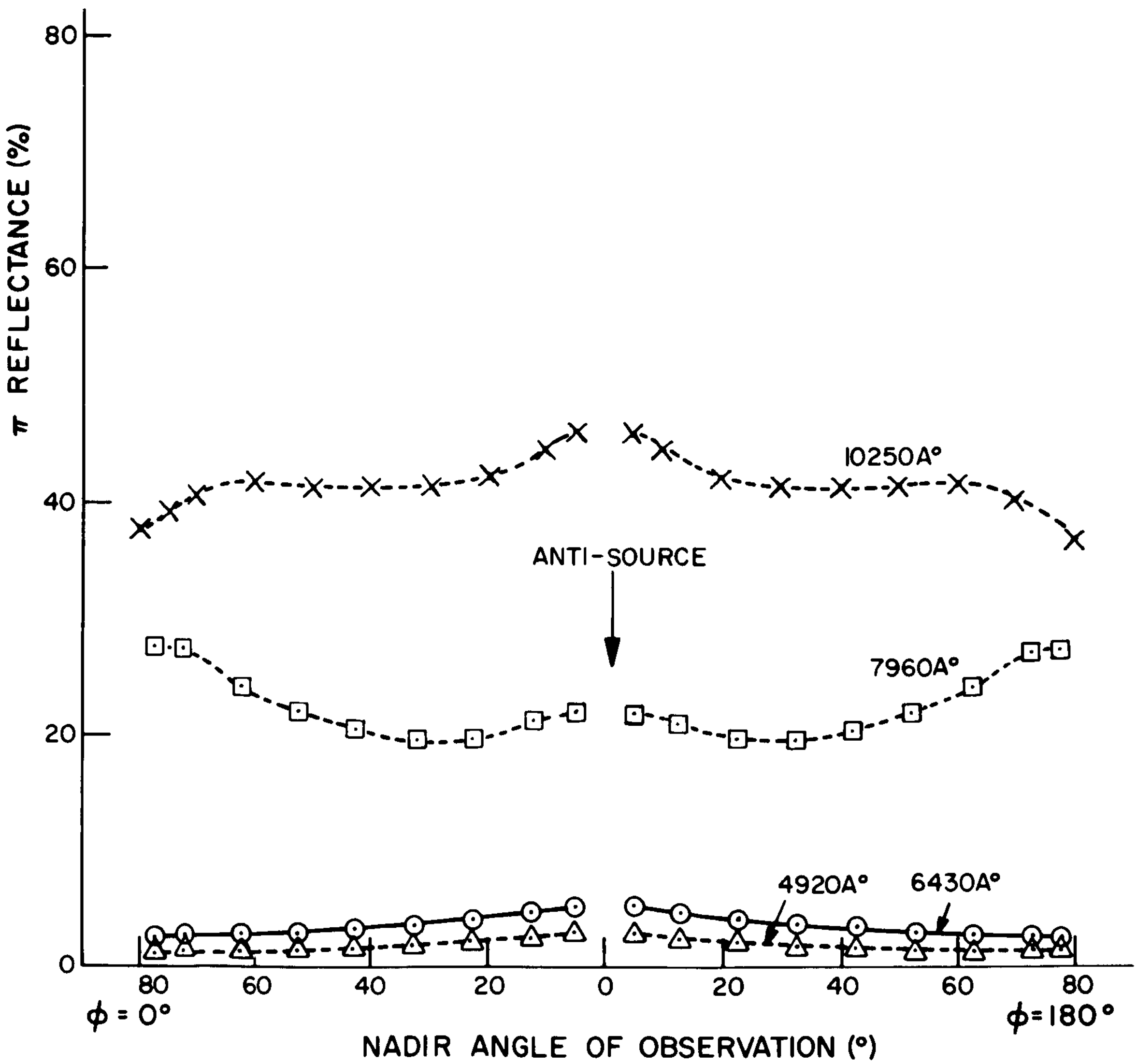

Fig. 21 Directional reflectance of clipped green grass (results independent of azimuth, $\theta_0 = 0^{\circ}$)

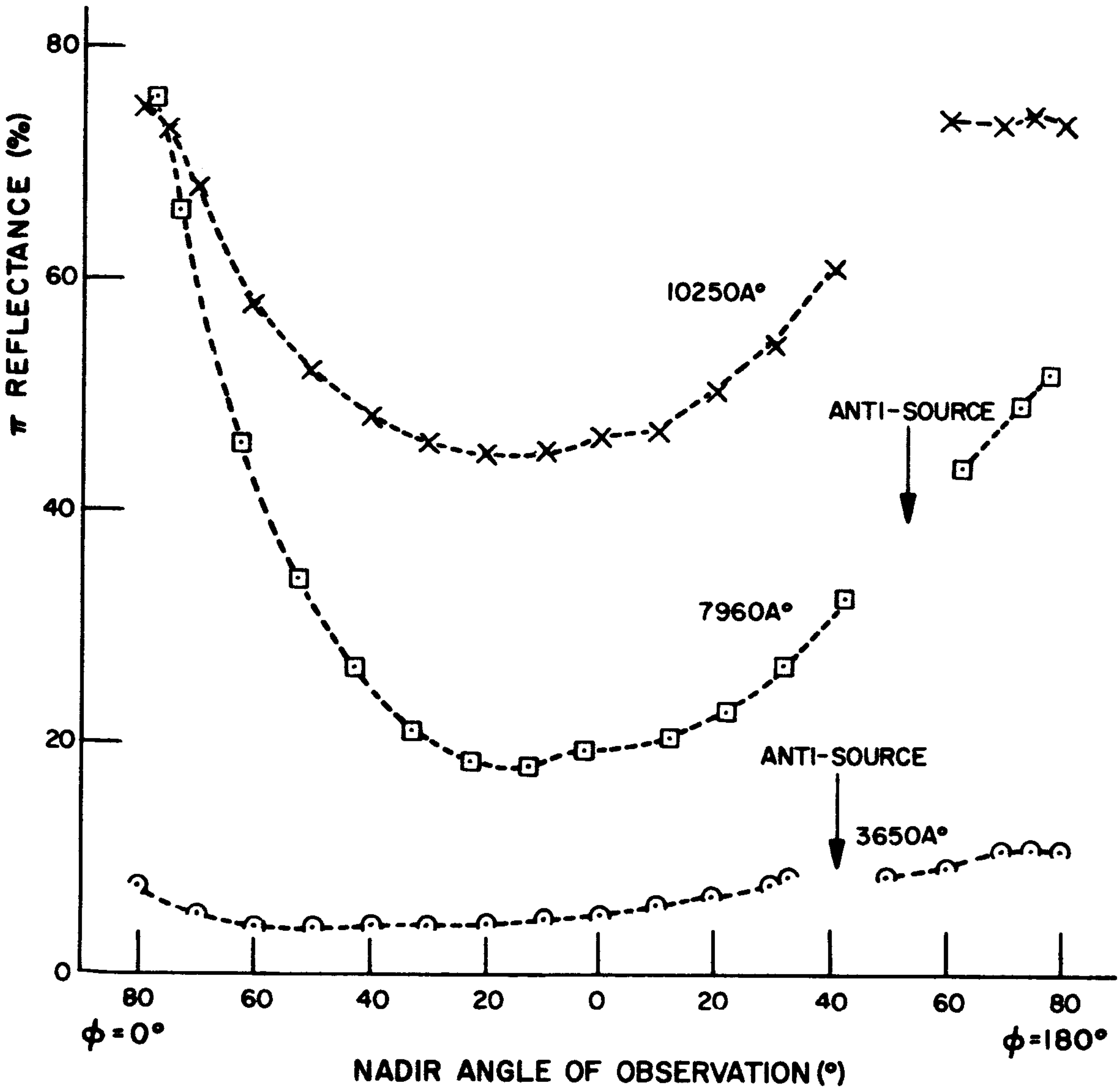

Fig. 22 Directional reflectance of clipped green grass (principal plane). For $\lambda = 3650\text{Å}$, $\theta_0 = 39.5^{\circ}$; for other λ's, $\theta_0 = 53^{\circ}$

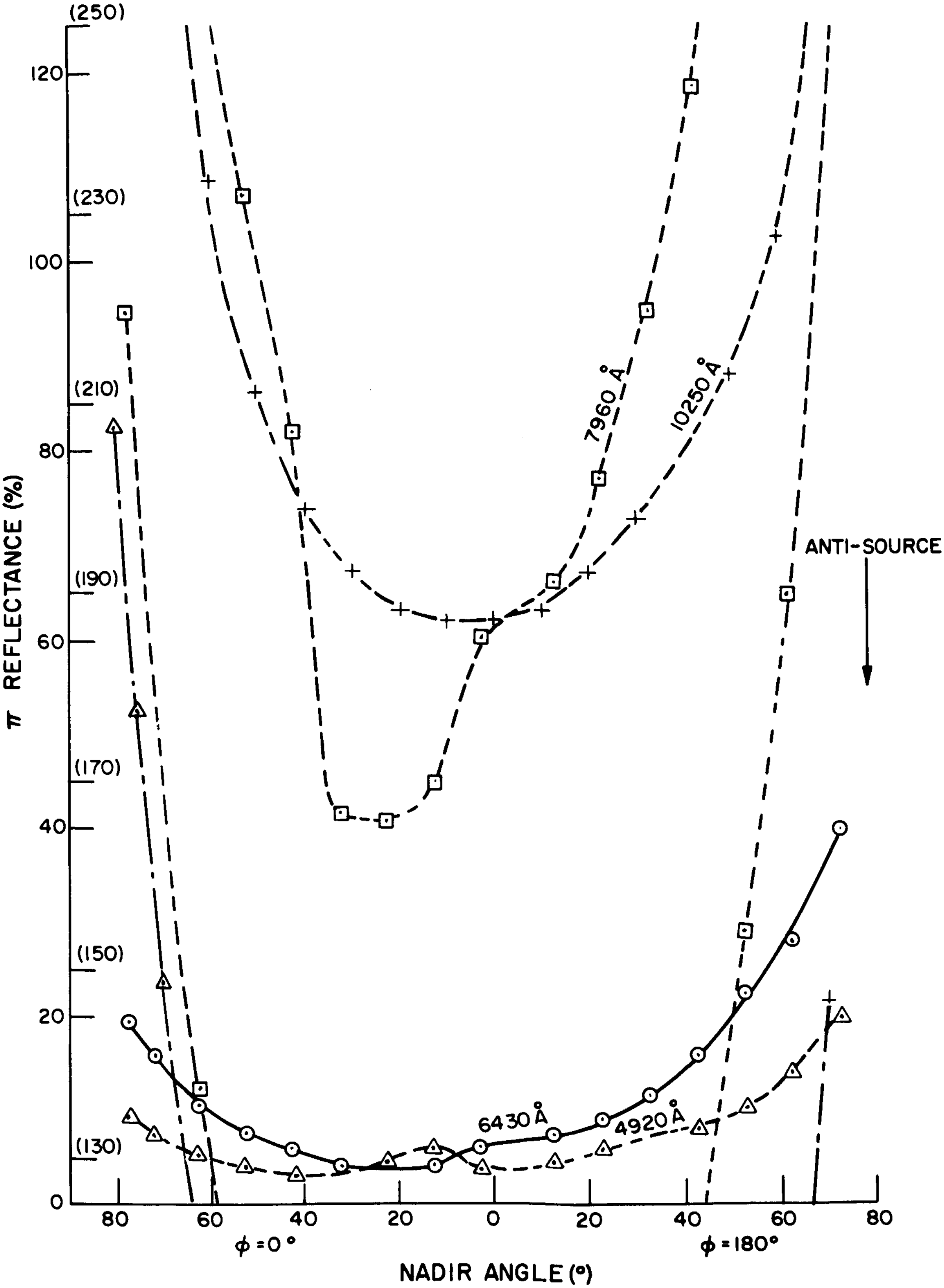

Fig. 23 Directional reflectance of clipped green grass (principal plane, θ_0 = 78.5°)

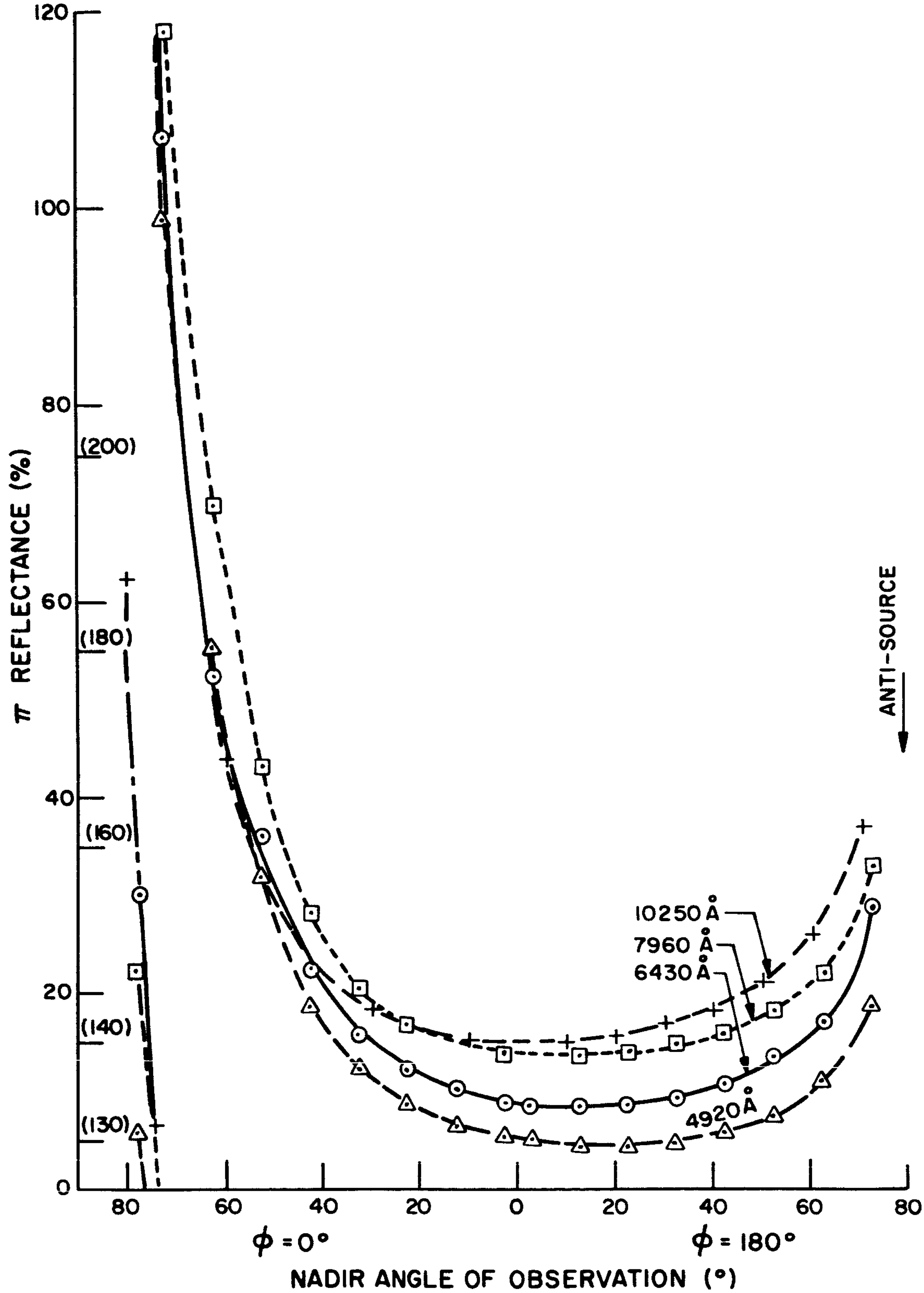

Fig. 24 Directional reflectance of weathered blacktop (principal plane, $\theta_o = 78.5^o$)

This sample of weathered blacktop (asphalt) was obtained from a road surface reconstruction project. The sample surface is not smooth, asphalt-covered pebbles protruding as much as one eighth to three sixteenths inches above the general level of the surface. Fig. 24 shows the directional reflectance in the principal plane as a function of nadir angle for several wavelengths, for a source zenith angle of 78.5°. The values of $\pi\ \rho$ are seen to exceed 125% for $\varphi = 0$, $\theta > 72$. The reflectance increases with wavelength throughout most of the range of nadir angles, the local backward maximum still persists, and the broad minimum around the nadir direction is apparent.

4. Additional Sunlight Measurements

In several of the preceding figures, some sunlight measurements have been included for comparison ($\lambda = 3650\mathring{A}$). In most instances, however, the zenith angle of the sun for the $3650\mathring{A}$ wavelength measurement did not correspond to the source zenith angle used for the longer wavelengths. Fig. 25 shows an interesting comparison between indoor and outdoor measurements and the same wavelength and similar zenith angles of the source. The upper two curves of Fig. 25 show the directional reflectance of desert sand in the principal plane, as a function of nadir angle, for a wavelength of $4920\mathring{A}$. The laboratory measurement was made for a source zenith angle $\theta_o = 53^{\circ}$, while the sunlight measurement was for a sun zenith angle of 57°. Except in the region surrounding the anti-solar direction, the two curves are quite similar. In this direction, the magntiude of the backward maximum for the sunlight measurement is about fifty percent higher than that for the laboratory measurement. There is no apparent reason for this higher value, and further

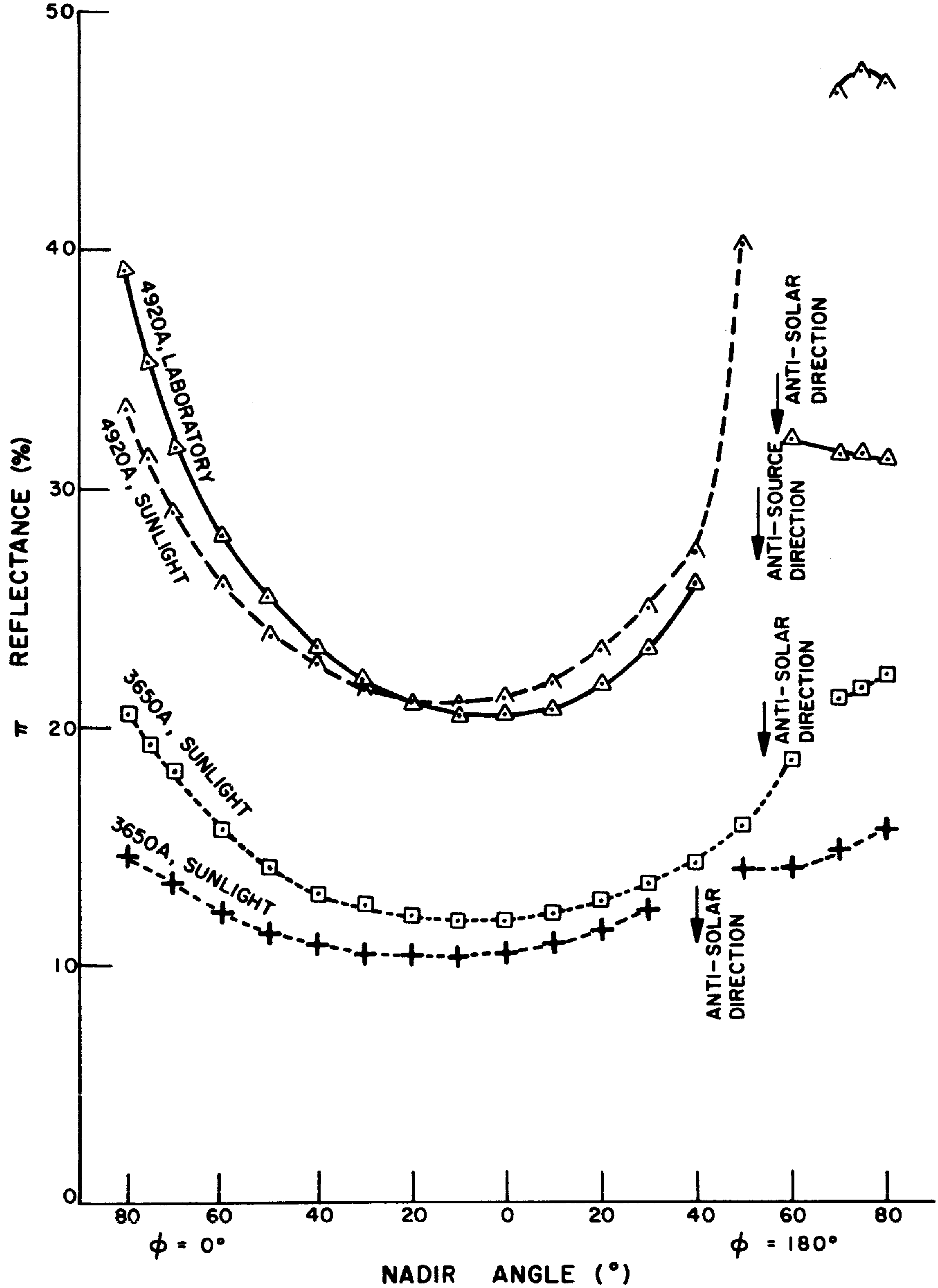

Fig. 25 Comparison of indoor laboratory source and outdoor sunlight source measurements of directional reflectances of desert sand

confirmation is desirable.

The lower two curves show sunlight measurements for the same surface at $\lambda = 3650\text{Å}$. The sun zenith angles are 54° for the upper curve and 40° for the lower curve. The reflectance at $\lambda = 4920\text{Å}$ is roughly twice that at $\lambda = 3650\text{Å}$.

Other examples of sunlight measurements are given by the curves of Fig. 26. The upper curve shows the directional reflectance of red clay in the principal plane as a function of nadir angle, for a wavelength $\lambda = 3650\text{Å}$ and a sun zenith angle of 35°. The lower curve is for clipped green grass at the same wavelength, but a sun zenith angle of 39°.

Fig. 27 shows the measurements of directional reflectance in the principal plane for red clay and desert soil at 4920Å. The sun zenith angle is 34° for the red clay measurement and 37° for the desert soil.

Sunlight measurements for surfaces with much lower reflectance are given by Fig. 28. They show the principal plane measurements for black loam and green grass at a wavelength of 4920Å. The sun zenith angle for the black loam measurement is 22°, and that for the green grass curve is 36°.

5. Comparison of Reflectance From Various Materials

The following figures show a comparison of directional reflectance of various surfaces for measurements made at the same wavelength. Fig. 29 shows measurements of directional reflectance in the principal plane at wavelength 6430Å for six different samples. They are, in order of increasing reflectance, green grass, black loam, pulverized limonite, desert sand, beach sand, and gypsum sand. The source zenith angle is

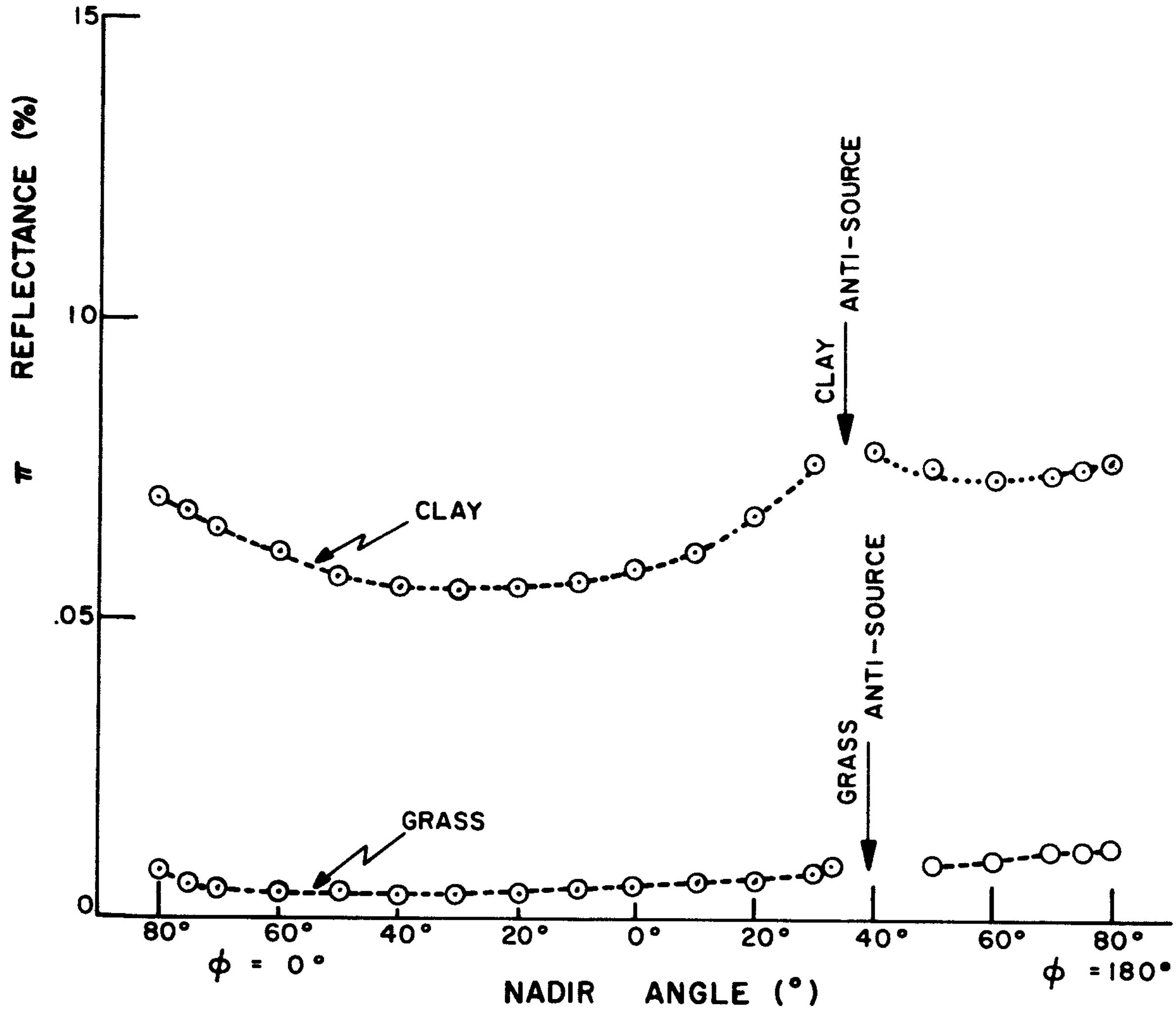

Fig. 26 Directional reflectance of sunlit surfaces of red clay and clipped green grass (λ = 3650Å, principal plane)

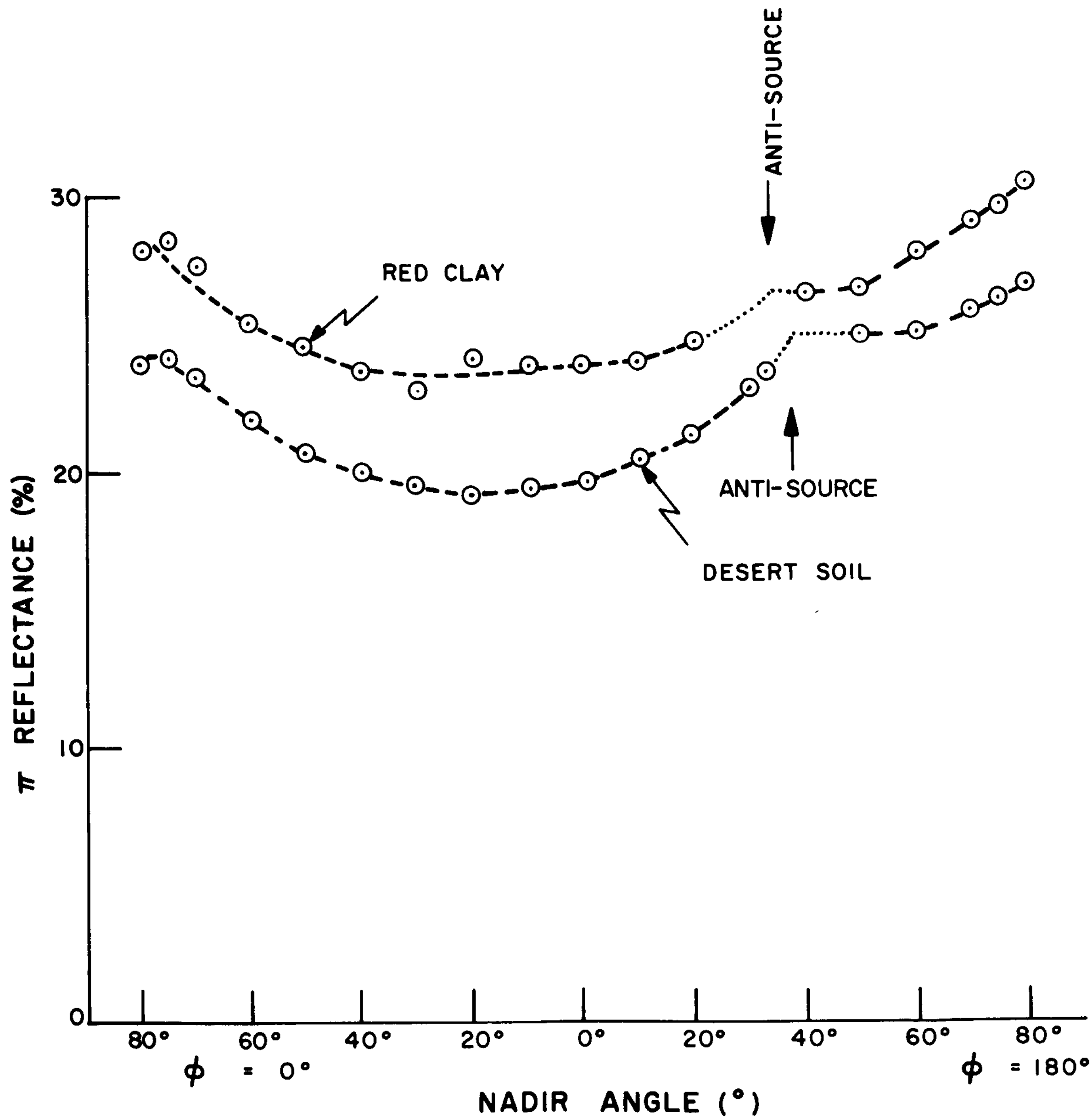

Fig. 27 Directional reflectance of sunlit surfaces of desert soil ($\lambda = 4920\mathring{A}$, principal plane)

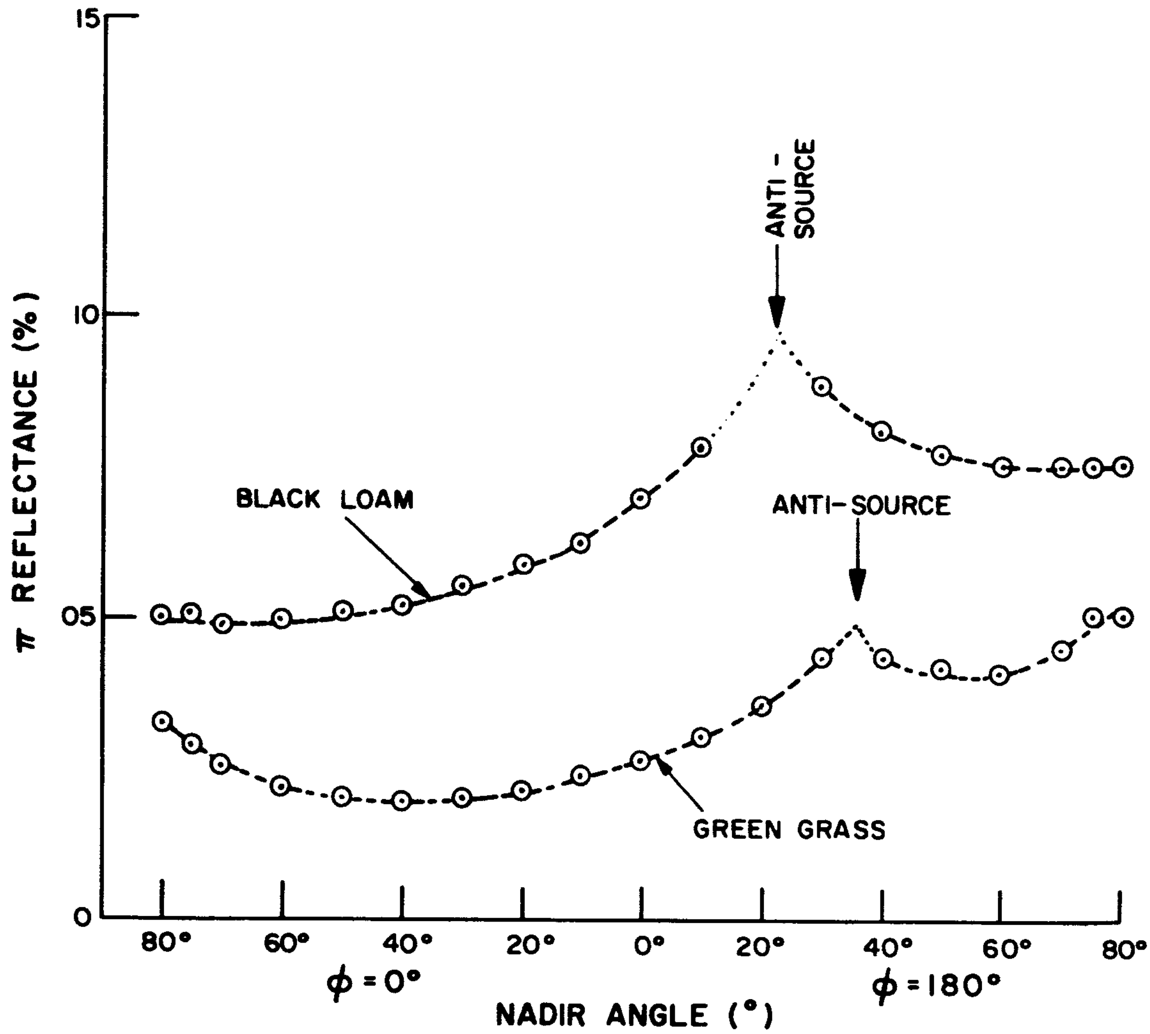

Fig. 28 Directional reflectance of sunlit surfaces of black loam and clipped green grass (λ = 4920Å, principal plane)

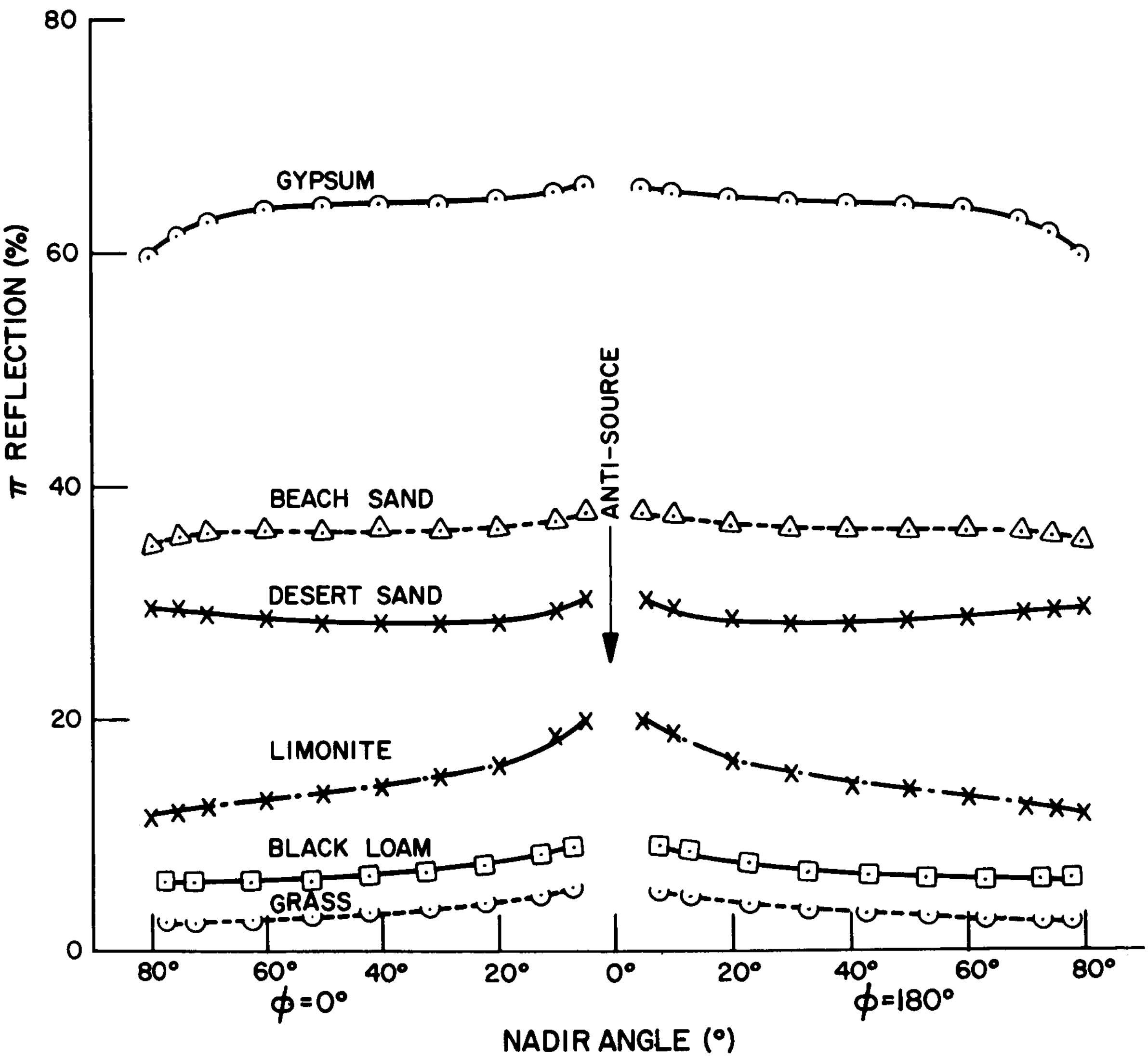

Fig. 29 Directional reflectance of various surfaces (λ = 6430Å, $\theta_o = 0^o$, principal plane)

$\theta_o = 0^o$. The curves show great differences in reflectance, low reflectance corresponding to absorbent materials represented by the black loam and limonite samples, and high reflectance corresponding to translucent materials such as gypsum sand. The backward maximum, at least for this source angle, is more pronounced for the limonite sample than for any of the others. Interestingly enough, the variation of reflectance with nadir angle of observation is small for all samples with the source at the zenith. Fig. 30 shows results for essentially the same samples, with the exception that Yolo loam is included and limonite deleted. The measurements are again for wavelength 6430Å, but the source zenith angle is $\theta_o = 53^o$. There is a marked increase in reflectance at this angle of incidence when compared to normal incidence for all samples except the green grass. An even greater increase in reflectance is seen by comparing the previous two figures with Fig. 31 , which shows data for the same surfaces at wavelength λ = 6430Å, but for a source zenith angle of 78.5^o. Both the white quartz sand and desert sand measurements show $\pi \rho > 125\%$ in the direction near the specular point, again an example of strong forward reflection. The magnitude of the backward maximum, as well as its ratio to the reflectance in the nadir direction, is seen to increase with increasing source zenith angle.

6. Effect of Particle Size

The measurements for the limonite sample provide some information about the effect of particle size on directional reflectance. This limonite was obtained from Wards Natural Science Establishment and is from Tuscaloosa County, Alabama. The bulk form was run through a hammer mill,

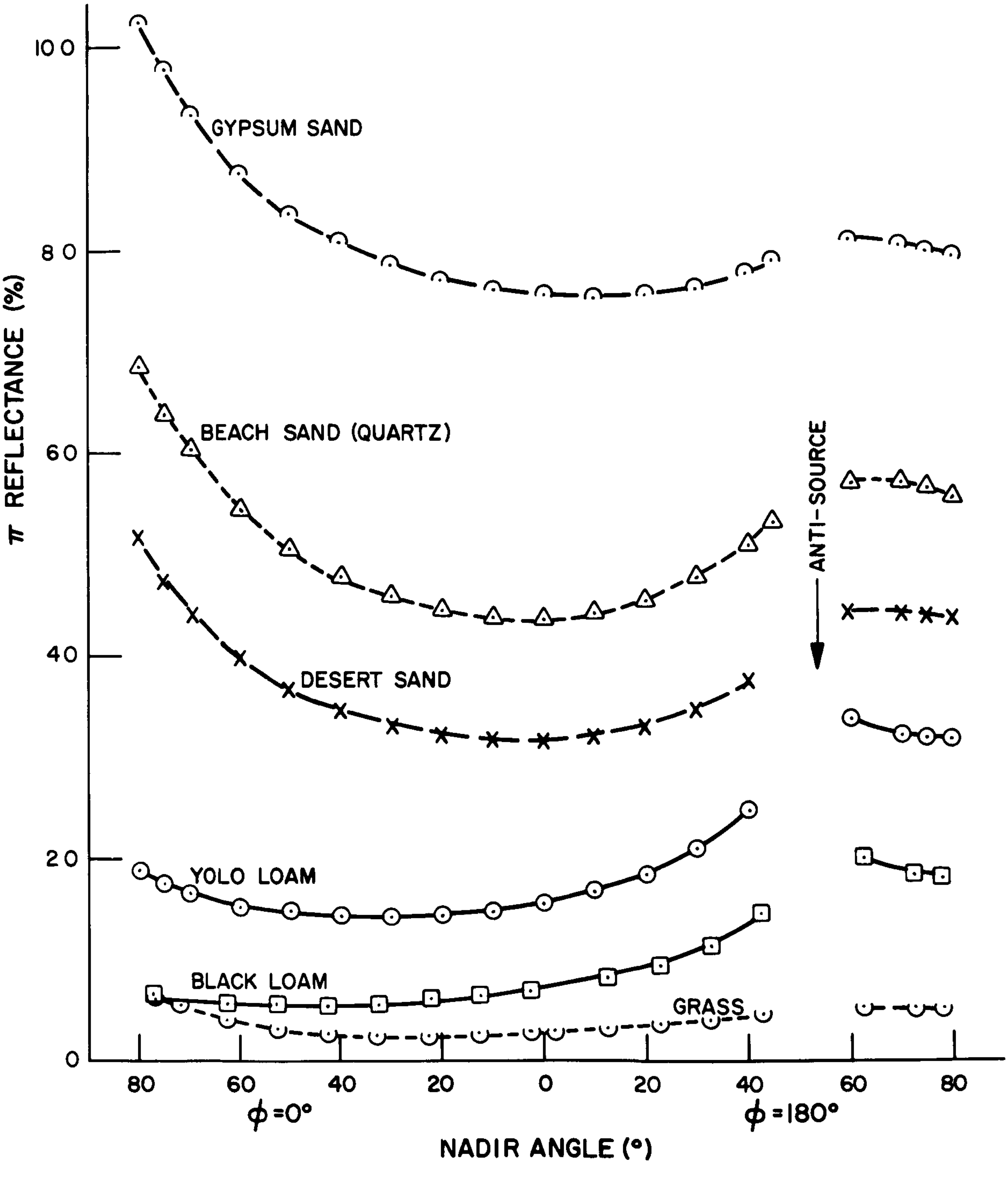

Fig. 30 Directional reflectance of various surfaces (λ = 6430Å, θ_0 = 53°, principal plane)

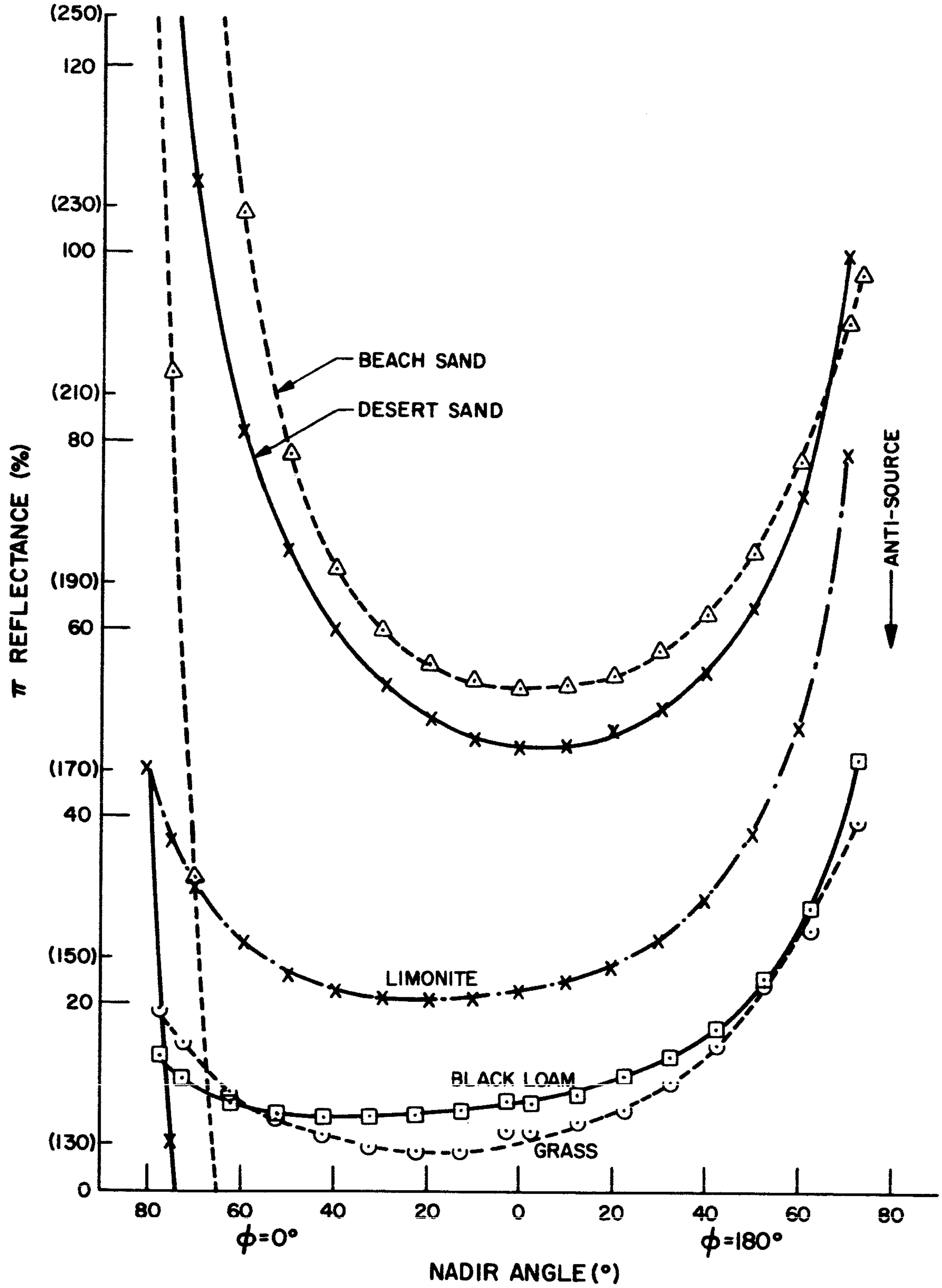

Fig. 31 Directional reflectance of various surfaces ($\lambda = 6430\mathring{A}$, $\theta_0 = 78.5^{\circ}$, principal plane)

producing a sample with an average particle size of about 400 microns. In the following curves, this is labeled as "coarse". A part of this sample was further pulverized to an average particle size of 14 microns. This latter sample is that described previously as "limonite", and is designated as "fine" in the following curves.

Fig. 32 shows the directional reflectance of these samples in the principal plane as a function of nadir angle, for wavelengths 4920Å and 6430Å, with the source at the zenith. The difference in reflectance between the two samples when measured at the longer wavelength is considerable when compared to the measurements at 4920Å. The "fine" sample is seen to produce higher reflectance at 6430Å, while at 4920Å, the situation is reversed. The backward maximum increases sharply as the anti-source direction is approached.

Fig. 33 represents measurements for the same samples, but for a source zenith angle of 53°. In addition, measurements at 7960Å are included. It is evident that, at least for this material, the effect of a change in average particle size becomes increasingly more important as the wavelength is increased. Fig. 34 shows the directional reflectance at λ = 4920Å and 6430Å for a source zenith angle of 78.5°. The difference in the "fine" and "coarse" curves, at least for the 6430Å measurement, seems to decrease with increasing source zenith angle. As in the two preceding curves, the reflectance of the "coarse" sample is slightly higher than the "fine" for the 4920Å measurement.

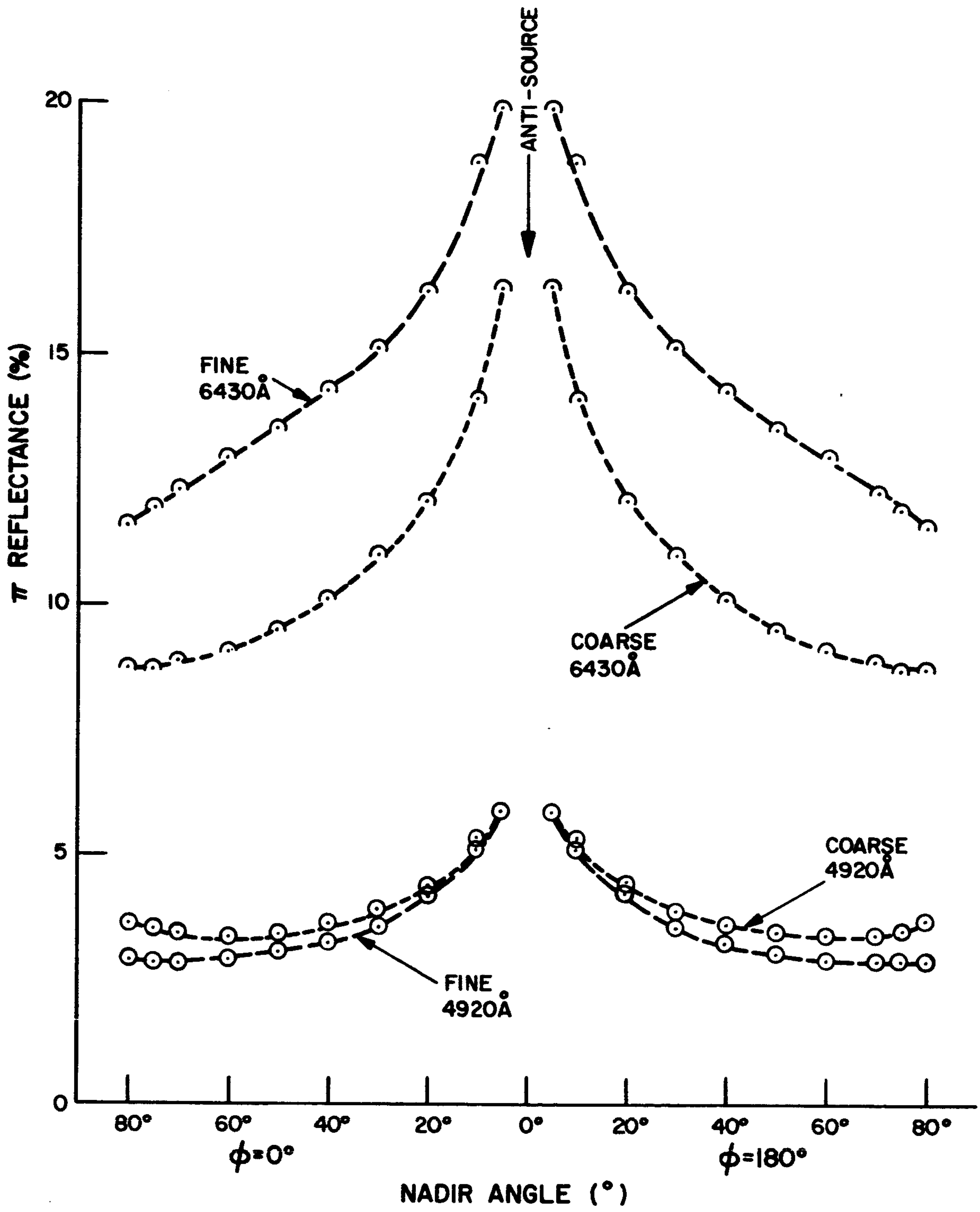

Fig. 32 Directional reflectance of fine and coarse limonite ($\theta_0 = 0^{\circ}$, principal plane)

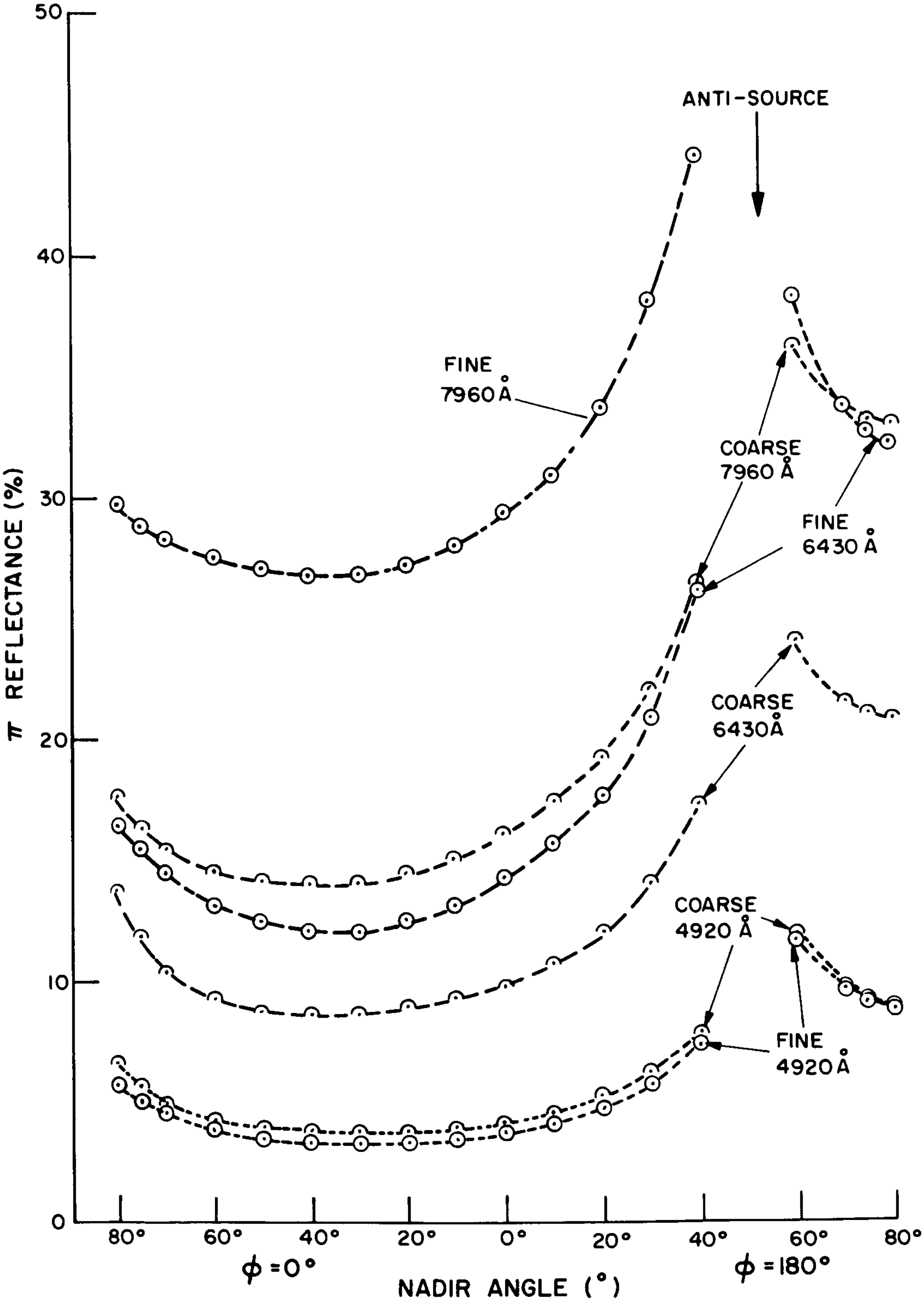

Fig. 33 Directional reflectance of fine and coarse limonite (θ_o = 53°, principal plane)

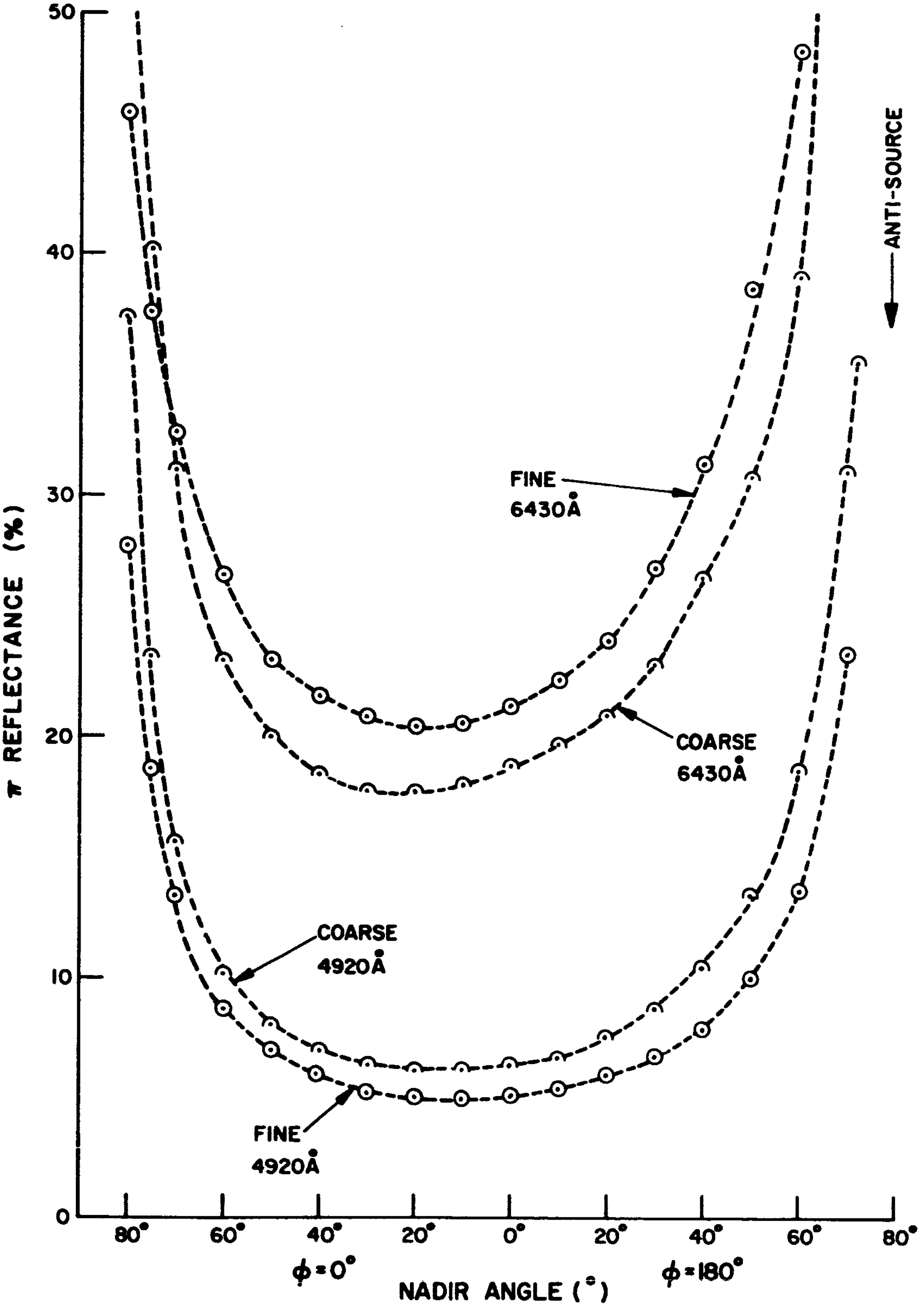

Fig. 34 Directional reflectance of fine and coarse limonite (θ_0 = 78.5°, principal plane)

7. Comparison of Reflectance From Different Limonite Samples

There is one other interesting comparison to make between the various limonite samples. Fig. 35 shows the effect of chemical composition or particle characteristics, or both, on directional reflectance. The measurements are made at 4920Å, 6430Å, and 7960Å for a source zenith angle of 53°. The samples being compared are the fine red limonite ($2Fe_2O_2 3H_2O$) shown in the preceding figures, and an industrially produced yellow ochre powder ($Fe_2O_3H_2O$). For each of the three wavelengths, the yellow limonite sample is seen to have the greater reflectance.

8. Azimuth Dependence of Directional Reflectance

It is interesting to see the variation of reflectance over the whole hemisphere, as is shown by hemispherical maps of reflectance. The following figures show isopleths of constant directional reflectance over the hemisphere (the actual quantity shown is $100 \times \pi\rho$). Only one half of the hemisphere is shown, since the measurements are symmetrical with respect to the principal plane. For each of the following surfaces, the albedo, $\overline{R}(\lambda, \theta_0) = \int_0^1 \int_0^{2\pi} \rho(\mu, \varphi)\, \mu \, d\mu \, d\varphi$ will be given. In the following figures the origin of coordinates represents the nadir direction; nadir angles are measured from the center (nadir direction) radially outward to 90° (horizon); azimuth is measured counter clock-wise from 0° to 180°. In all of these figures, a certain amount of smoothing is necessary in drawing the contour lines. Extrapolations are necessary to extend the data for $\theta > 80$.

Fig. 36 shows a hemispheric map of directional reflectance for the black loam sample; the source zenith angle is 53°, and the wavelength is

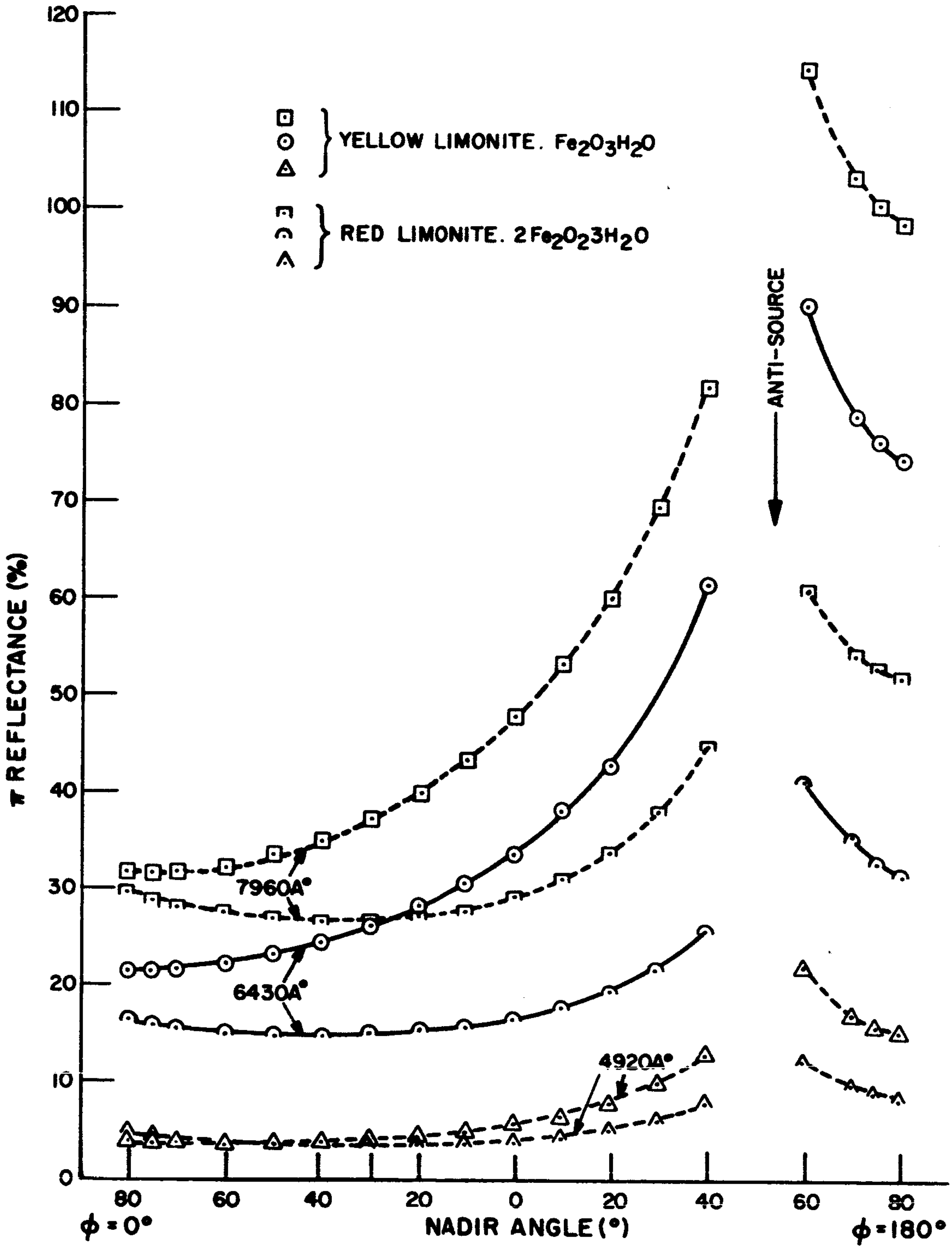

Fig. 35 Directional reflectance of red limonite ($2Fe_2O_23H_2O$) and yellow limonite ($Fe_2O_3H_2O$) ($\theta_o = 53°$, principal plane)

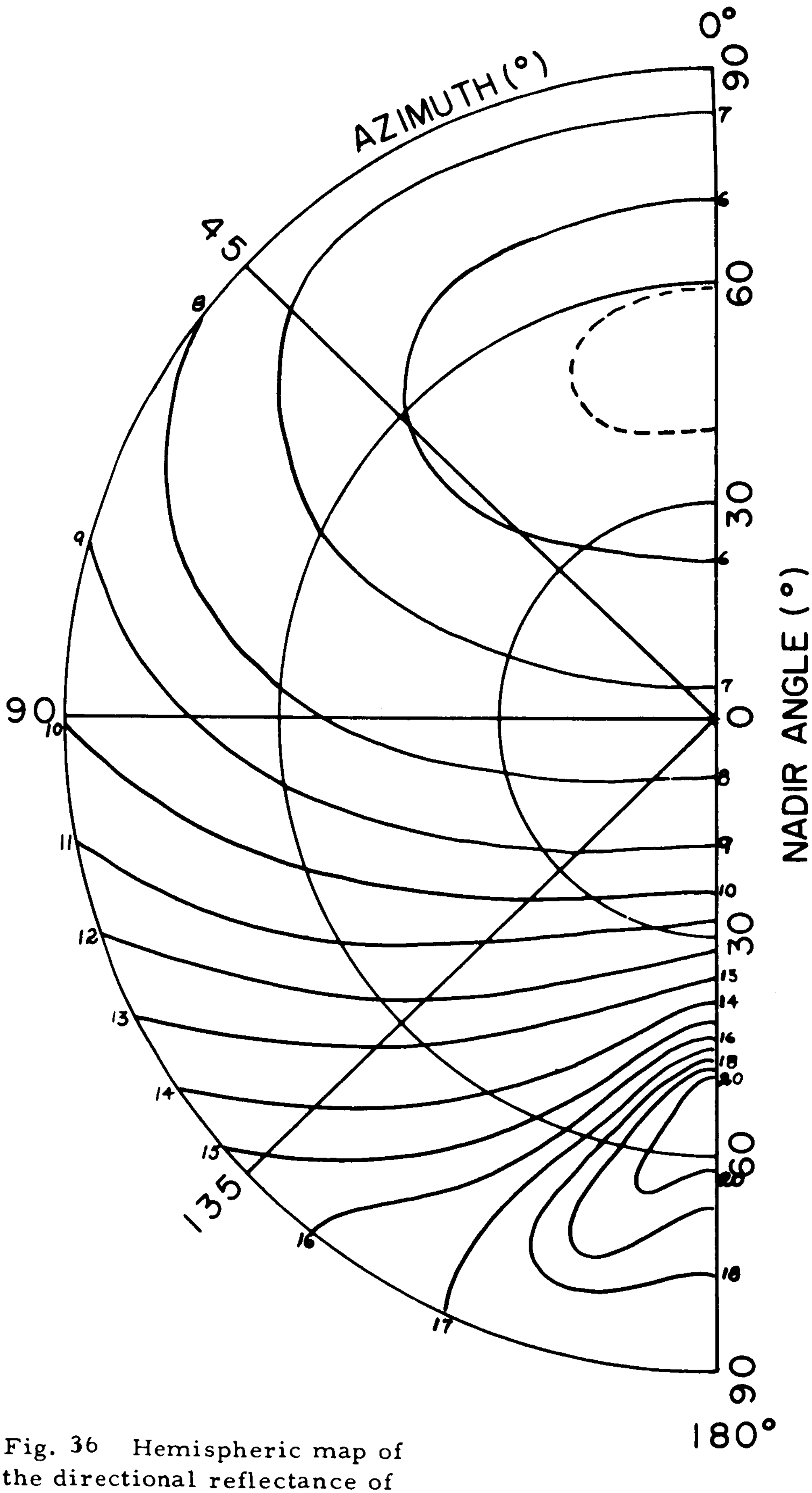

Fig. 36 Hemispheric map of the directional reflectance of black loam soil (θ_o = 53.1°, λ = 6430Å)

6430Å. For this sample, there is a general increase of reflectance with increasing azimuth, and a strong gradient is observed near the backward direction ($\theta = 53^{\circ}$, $\varphi = 180^{\circ}$). The calculated albedo, $\overline{R}$, from these data is .089.

Fig. 37 offers a notable contrast to the previous figure. It shows the directional reflectance of desert sand for a source zenith angle of 53° and wavelength of 6430Å. The reflectance is much higher, the albedo being .360. As was already shown in the plot of reflectance in the principal plane, the sample exhibits rather strong forward reflection, in addition to the local backward maximum. For this sample, there is considerable symmetry present in the reflectance pattern. The broad minimum surrounding the nadir direction is readily apparent.

Fig. 38 shows the reflectance pattern for a sample of clipped green grass for a source zenith angle of 53° and wavelength 6430Å. The reflectance is seen to be small over the whole hemisphere, the albedo being .037.

Fig. 39, which shows a hemispheric map of the reflectance from crushed limestone, exhibits a reflectance pattern similar to that of black loam, except that the limestone sample provides much higher reflectance, the albedo being .254, compared to .089 for the black loam. Again, the source zenith angle is 53° and the wavelength is 6430Å.

A quite different pattern is shown by the hemispheric map of directional reflectance of weathered blacktop of Fig. 40. The measurements were made at wavelength 6430Å for a source zenith angle of 53°. As pointed out previously, this sample exhibits rather strong forward reflection, which is

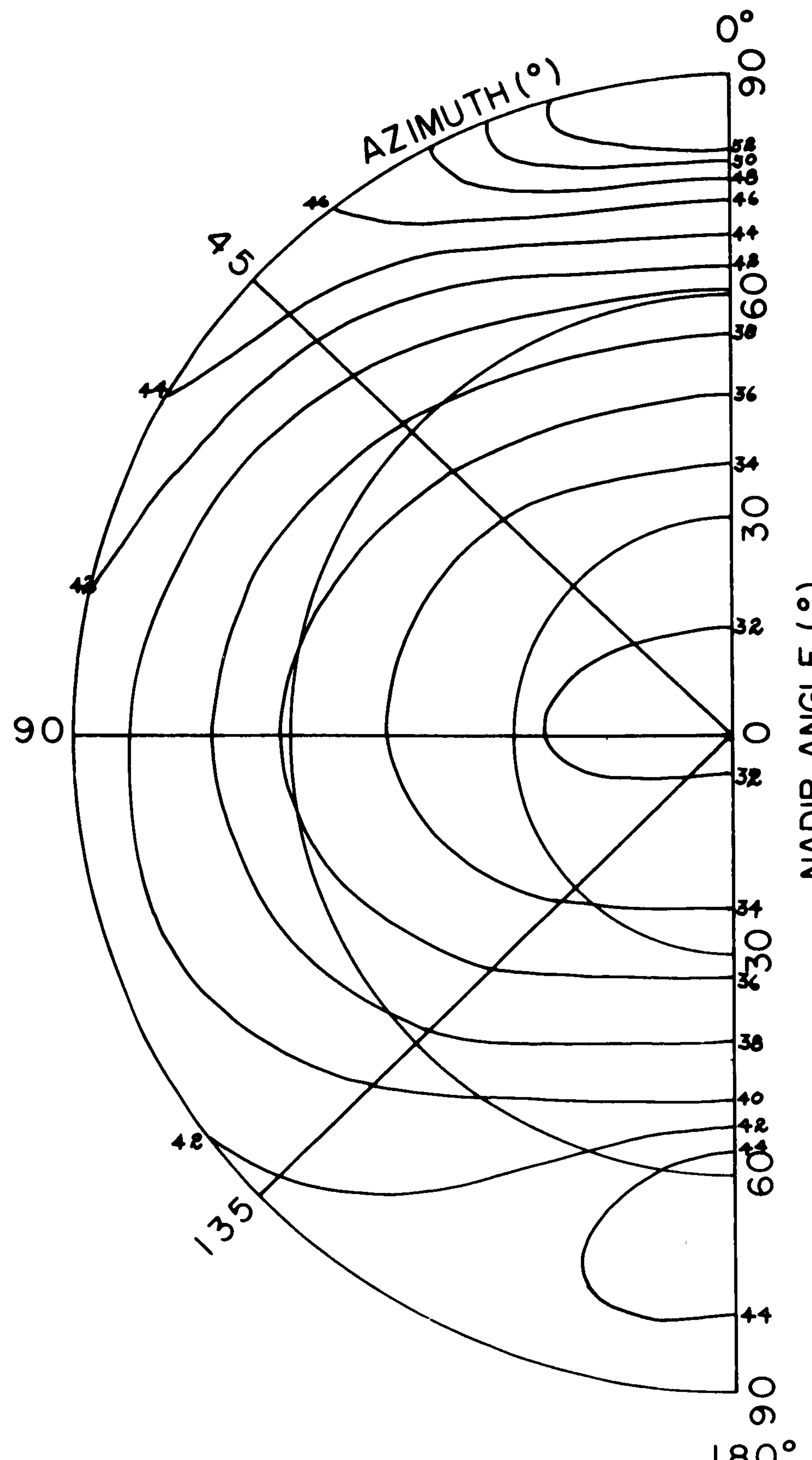

Fig. 37 Hemispheric map of the directional reflectance of desert sand (θ_o = 53.1°, λ = 6430Å)

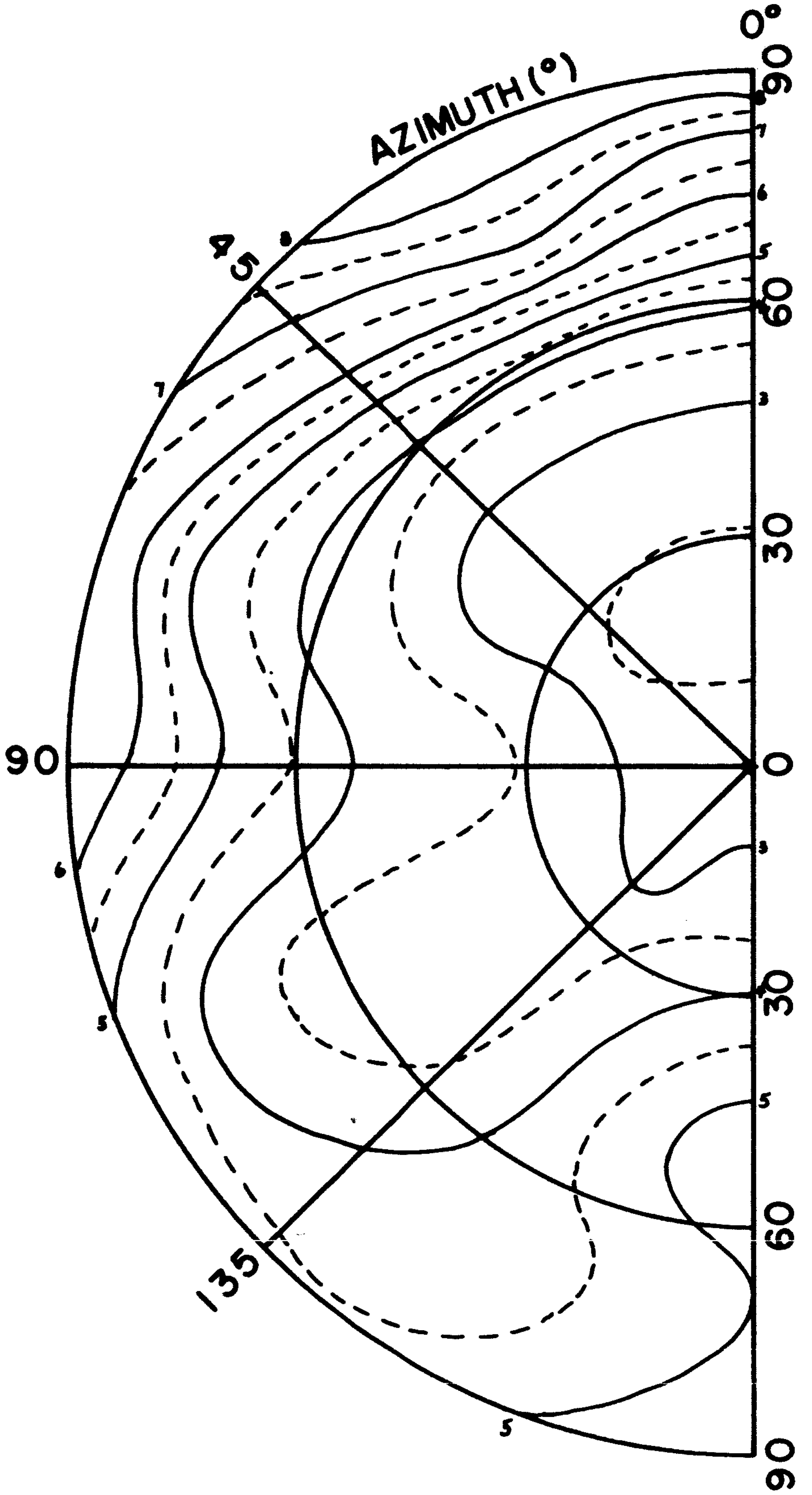

Fig. 38 Hemispheric map of the directional reflectance of clipped green grass ($\theta_o = 53.1^o$, $\lambda = 6430\text{\AA}$)

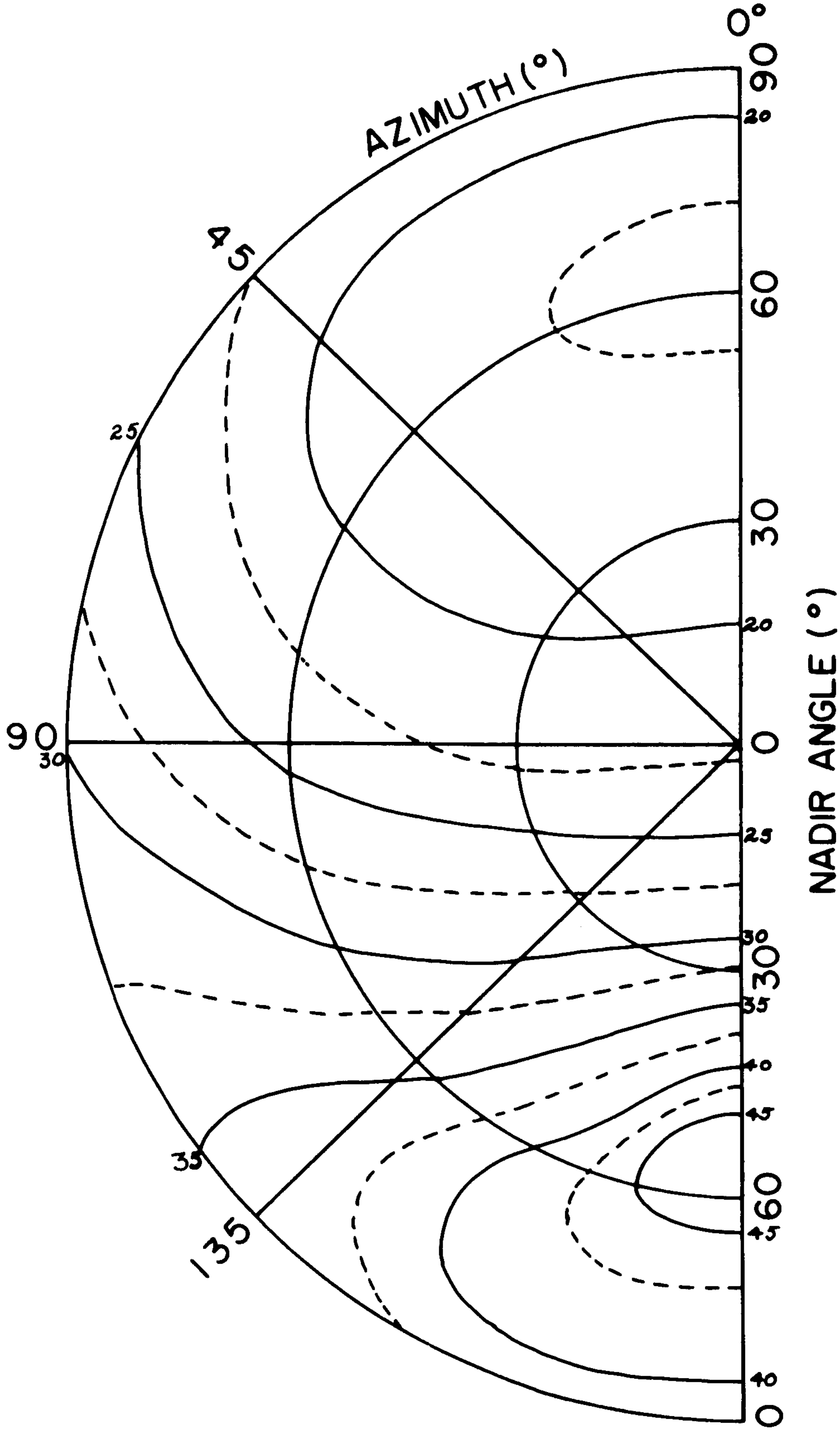

Fig. 39 Hemispheric map of the directional reflectance of crushed limestone gravel (θ_o = 53.1°, λ = 6430Å)

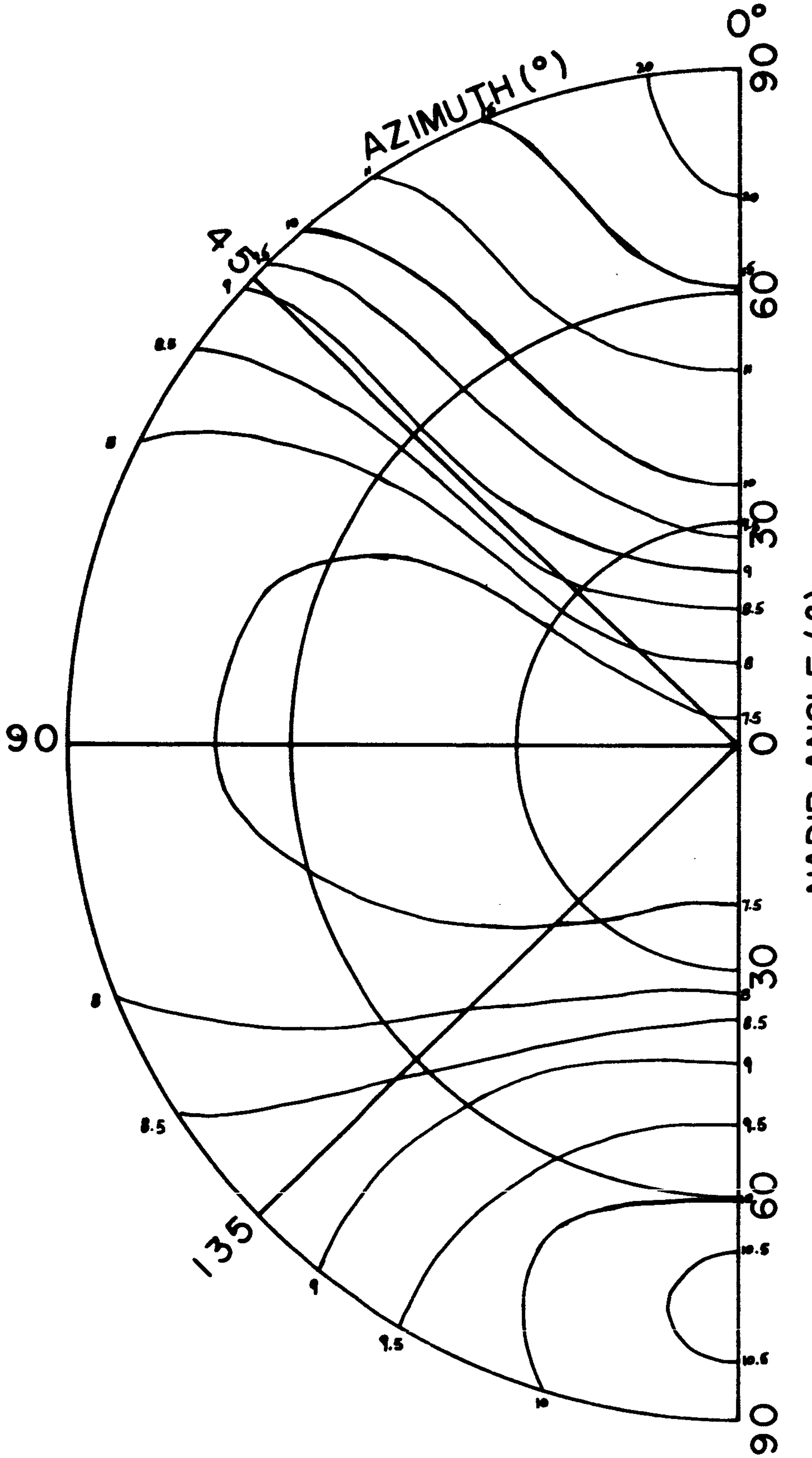

Fig. 40 Hemispheric map of the directional reflectance of weathered blacktop ($\theta_0 = 53.1^\circ$, $\lambda = 6430\text{Å}$)

seen to decrease rapidly with increasing azimuth. There is a very broad minimum in the region $60^\circ < \varphi < 120^\circ$, $0^\circ < \theta < 90^\circ$. The albedo for this surface is .085, about the same as that for the black loam sample.

B. Polarization

The measurements of the degree of polarization show several general characteristics. Perhaps the most obvious and universal one is the qualitative relationship between the degree of polarization and the reflectance. Stated briefly, it is found that surfaces exhibiting low reflectance are highly polarizing, and surfaces having high reflectance yield relatively small polarization. Since the reflectance of a surface generally increases with wavelength, it may be expected that a greater degree of polarization occurs for the shorter wavelengths. This is indeed found to be the case, although the decrease in polarization with increasing wavelength is not always monotonic.

Another feature which will be seen in the following curves is the existence of a region of negative polarization surrounding the anti-source direction. For sufficiently large values of θ_o, only one neutral point appears as seen from the measurements made at $\theta_o = 78.5^\circ$. Measurements at the shorter wavelengths generally exhibit a greater magnitude of negative polarization than those for the longer wavelengths. The position of the maximum degree of polarization in the principal plane varies from 90° to 135° from the direction of the anti-source. The angle depends on the sample, wavelength, and source zenith angle, and no consistent pattern is apparent.

In addition to the laboratory data, which comprise most of the measurements, some data were taken in the presence of sunlight, and this distinction will be pointed out in the following figures.

1. Variation of the Degree of Polarization with Wavelength

Fig. 41 shows the degree of polarization for black loam soil as a function of nadir angle in the principal plane for the source at the zenith, and for several wavelengths. The degree of polarization increases as θ increases, approaching 0.20 for $\lambda = 4920\text{Å}$ at $\theta = 80^\circ$. Over most of the range of nadir angles, the degree of polarization increases monotonically as the wavelength decreases. In the region surrounding the nadir direction, the analogous relationship exists with negative polarization, the shorter wavelengths being more highly negatively polarized.

Fig. 42 shows the polarization measurements for the same sample at the same wavelengths, but for a source zenith angle of 53°. Although the relationship of increasing polarization with decreasing wavelength is retained, there is little difference in the polarization profile between the measurements made at 6430Å and those made at 7960Å, the difference being everywhere 0.01 or less. The position of the maximum degree of polarization relative to the anti-source direction is rather insensitive to wavelength for $\lambda = 4920\text{Å}$, 6430Å, and 7960Å, the angular differences being 113°, 117°, and 116° respectively. The measurements for $\lambda = 10250\text{Å}$ show a steady increase in the degree of polarization with increasing θ. The measurements at $\theta_o = 53^\circ$ show an increase in the maximum degree of polarization over the case $\theta_o = 0^\circ$ for all wavelengths.

The polarization measurements for the black loam sample for the same wavelengths, but for a source zenith angle of 78.5° are shown in Fig. 43. There is a slight increase in the maximum degree of polarization at wavelengths 4920Å and 6430Å over the case $\theta_o = 53^\circ$. The maximum value remains

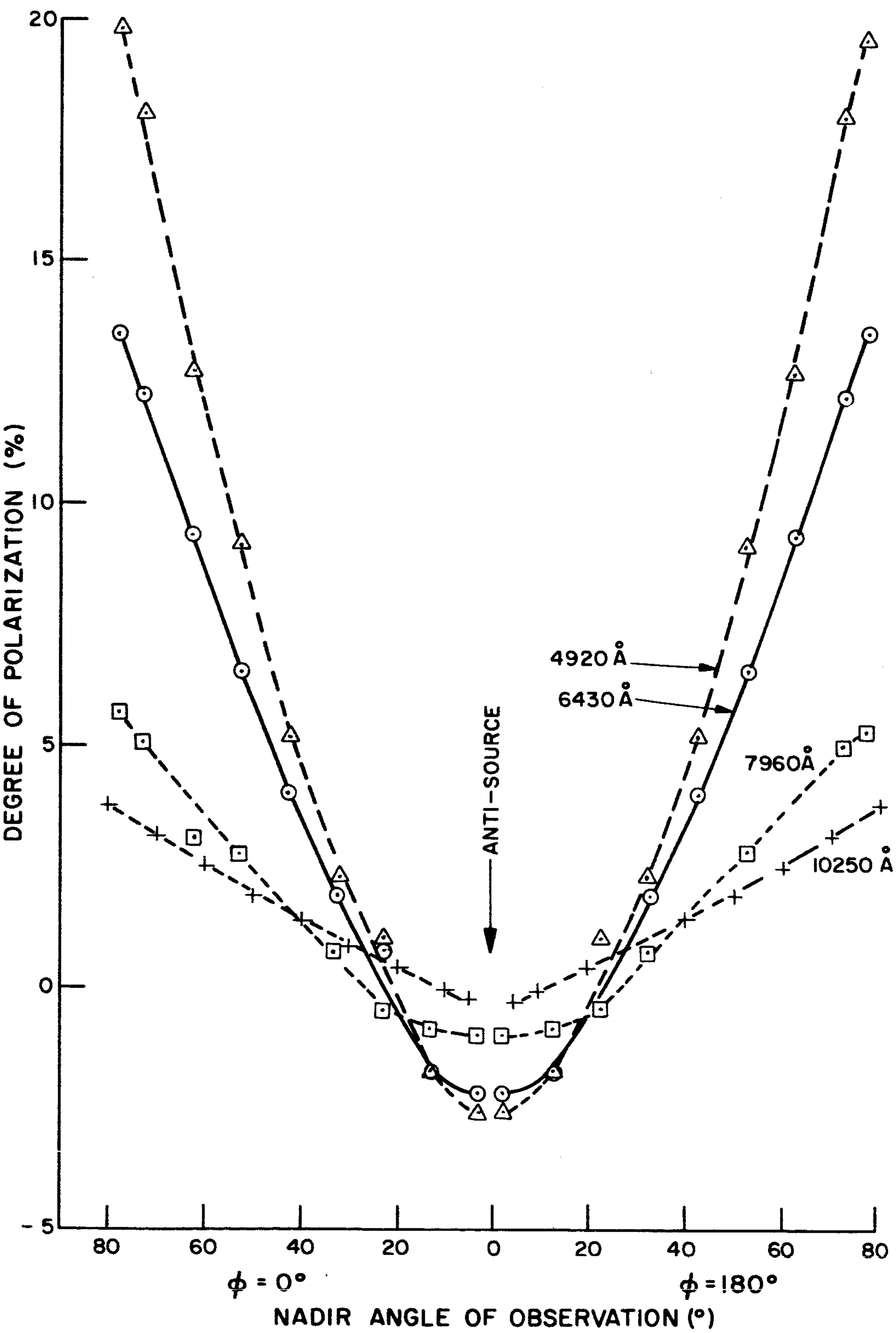

Fig. 41 Degree of polarization of radiation reflected from bl ack loam soil (results independent of azimuth, $\theta_0 = 0^\circ$)

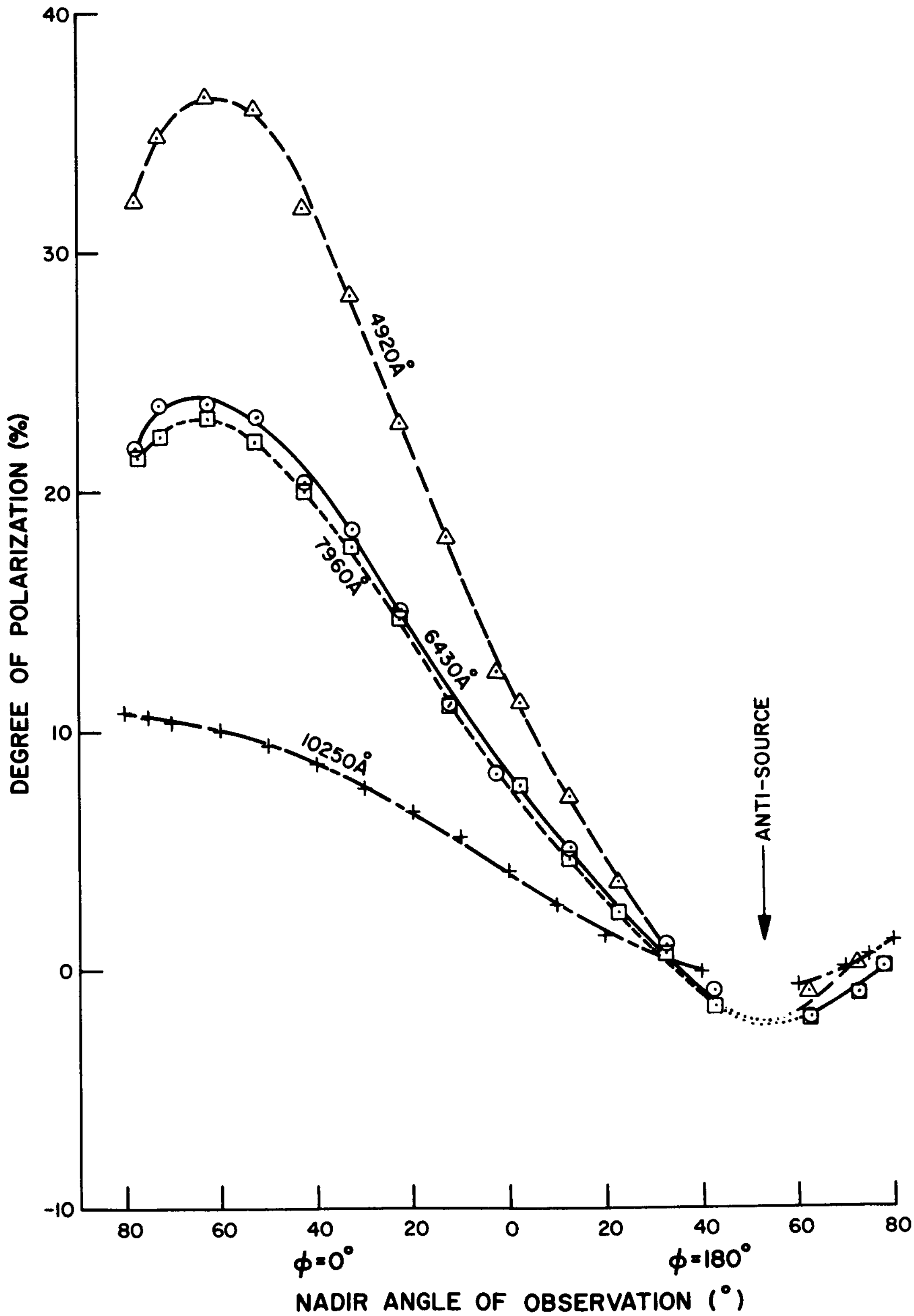

Fig. 42 Degree of polarization of radiation reflected from black loam soil (principal plane, $\theta_o = 53.1^o$)

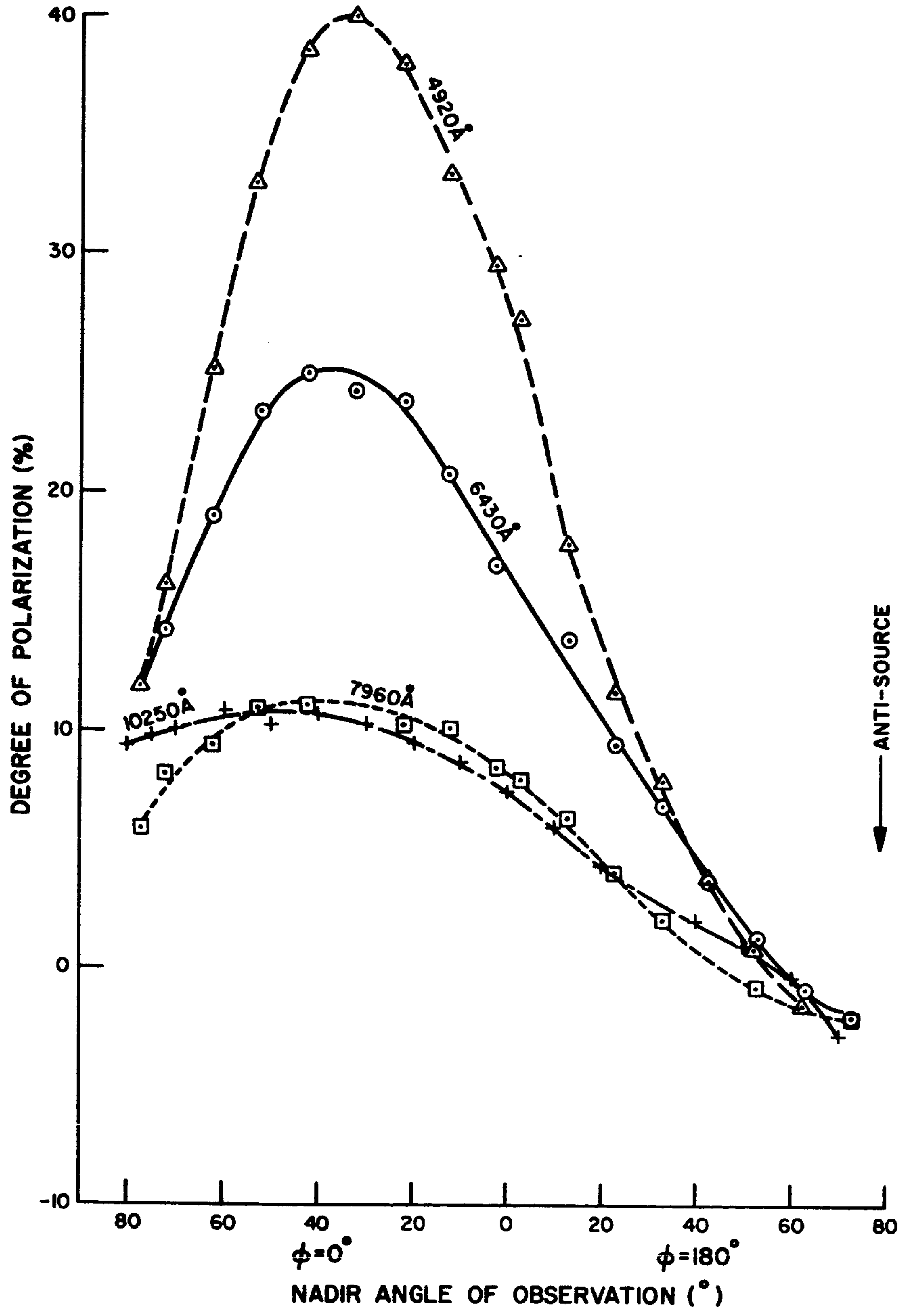

Fig. 43 Degreee of polarization of radiation reflected from black loam soil (principal plane, θ_o = 78.5°)

the same for $\lambda = 10250\AA$, and the degree of polarization is considerably lower at $\lambda = 7960\AA$ for $\theta_o = 78.5^\circ$. The curves for $\lambda = 7960\AA$ and $10250\AA$ are very similar, and the degree of polarization for $\lambda = 10250\AA$ is greater than that for $\lambda = 7960\AA$ over a considerable range of nadir angles. For this source angle, the measurements at $\lambda = 10250\AA$ show a maximum degree of polarization, which occurs about 128° from the direction of the anti-source. The maxima for the other wavelengths are again in approximately the same position, the angular measure from the anti-source being 111° for $\lambda = 4920\AA$, 115° for $\lambda = 6430\AA$, and 115° for $\lambda = 7960\AA$. As pointed out previously, only one neutral point appears for each wavelength at this source zenith angle. As in the preceding figures, there seems to be no consistent pattern for the position of the neutral points.

In discussing the sample of clipped green grass, it was observed that the directional reflectance measurements for wavelengths of $4920\AA$ and $6430\AA$ showed small values of reflectance when compared with the corresponding measurements made at $\lambda = 7960\AA$ and $10250\AA$. The following set of curves, showing the degree of polarization of the green grass sample, show a relatively high degree of polarization for the measurements at $\lambda = 4920\AA$ and $6430\AA$ when compared with the measurements at the longer wavelengths.

Fig. 44 shows the data for the source at the zenith. Over most of the range of nadir angles, the degree of polarization increases as the wavelength decreases. The degree of polarization for $\lambda = 7960\AA$ and $10250\AA$ is everywhere less than two percent in absolute value.

In Fig. 45, the degree of polarization is shown for the grass sample

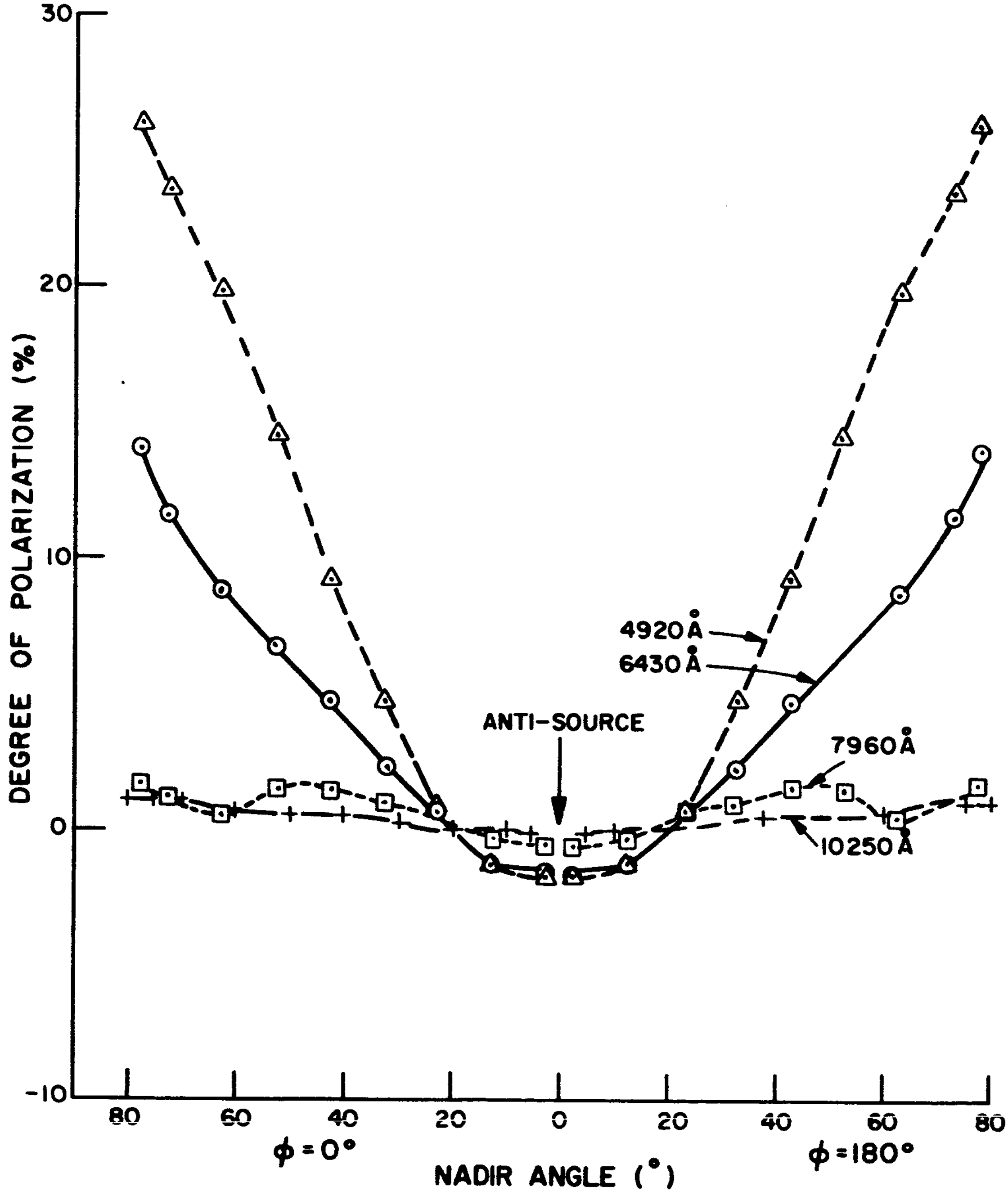

Fig. 44 Degree of polarization of radiation reflected from clipped green grass (results independent of azimuth, $\theta_o = 0^o$)

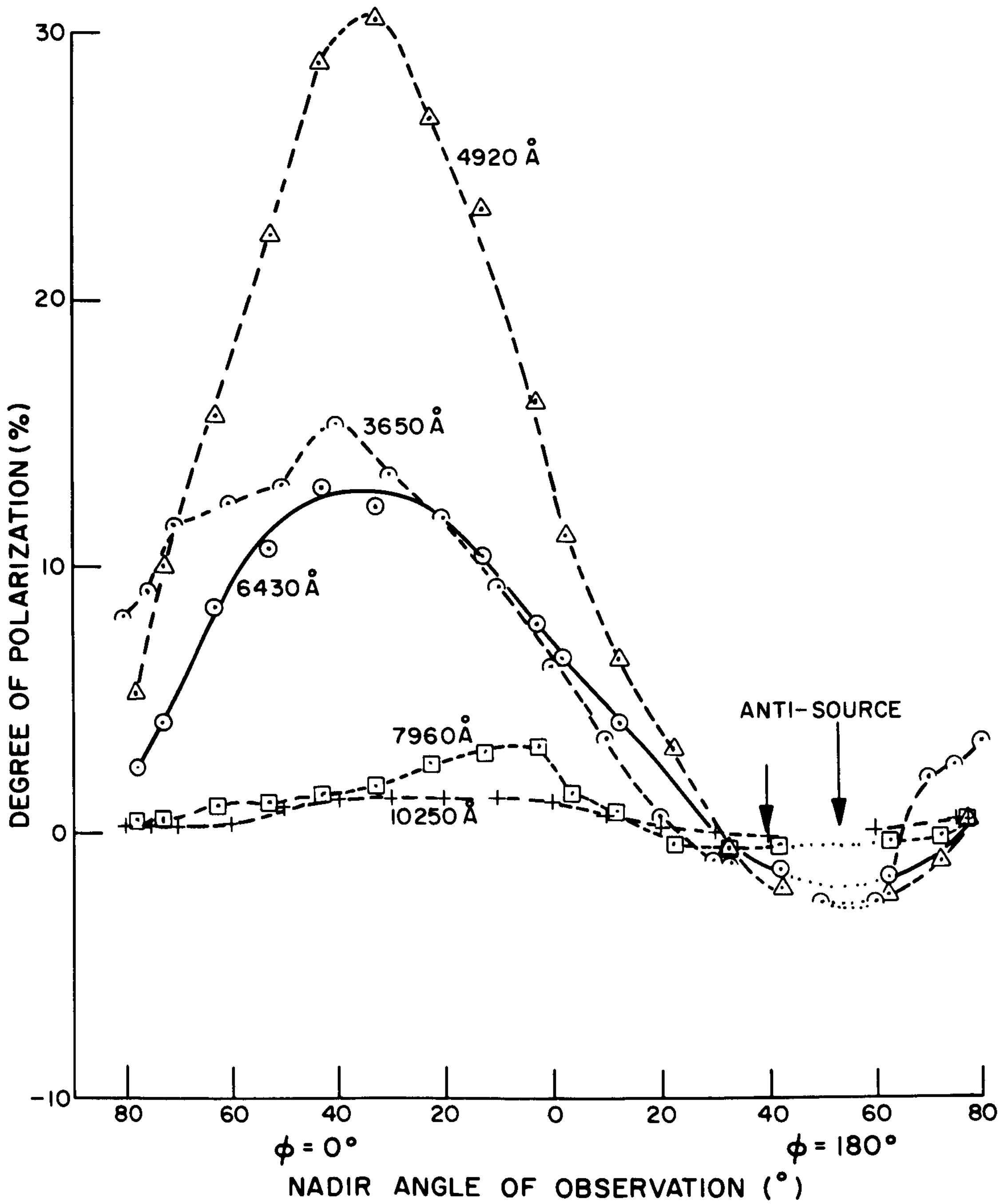

Fig. 45 Degree of polarization of radiation reflected from clipped green grass (principal plane, $\theta_o = 39.5^o$ for $\lambda = 3650\text{Å}$, for other curves $\theta_o = 53.1^o$)

for the same four wavelengths, but for a source zenith angle of 53°. In addition, a sunlight measurement is shown for $\lambda = 3650\text{Å}$ and a sun zenith angle of 39°. In the region of negative polarization surrounding the anti-source (sun) direction, the measurement at $\lambda = 3650\text{Å}$ exhibits a considerable degree of asymmetry with respect to the anti-source (sun) direction when compared to the laboratory measurements. The maximum degree of polarization for the 3650Å wavelength is considerably lower than what one would expect intuitively on the basis of this figure and the preceding one, if the premise of "short wavelength corresponds to high polarization" is reasonably accurate. The sun zenith angle of 39° is between the source zenith angles of 0° and 53°, and for both of these situations, the maximum degree of polarization for the measurements at $\lambda = 4920\text{Å}$ far exceeds that of $\lambda = 3650\text{Å}$, $\theta_o = 39^{\circ}$. In fact, the polarization curve for $\lambda = 3650\text{Å}$, $\theta_o = 39^{\circ}$ is similar to that for $\lambda = 6430\text{Å}$, $\theta_o = 53^{\circ}$ over a considerable range of nadir angles. One possible explanation for this apparent anomaly is that the grass samples used in the outdoor and indoor measurements were different, and the degree of polarization may depend strongly on such factors as blade density, differential growth pattern, preferred blade orientation, and average length.

Fig. 46 shows the degree of polarization of the green grass sample as a function of nadir angle in the principal plane for a source zenith angle of 78.5°. The maximum degree of polarization is seen to be considerably greater, at least for the measurements at $\lambda = 4920\text{Å}$ and 6430Å, when compared to the measurements at $\theta_o = 53^{\circ}$. The curves show a marked degree of irregularity, probably due to a combination of surface texture and large source zenith angle.

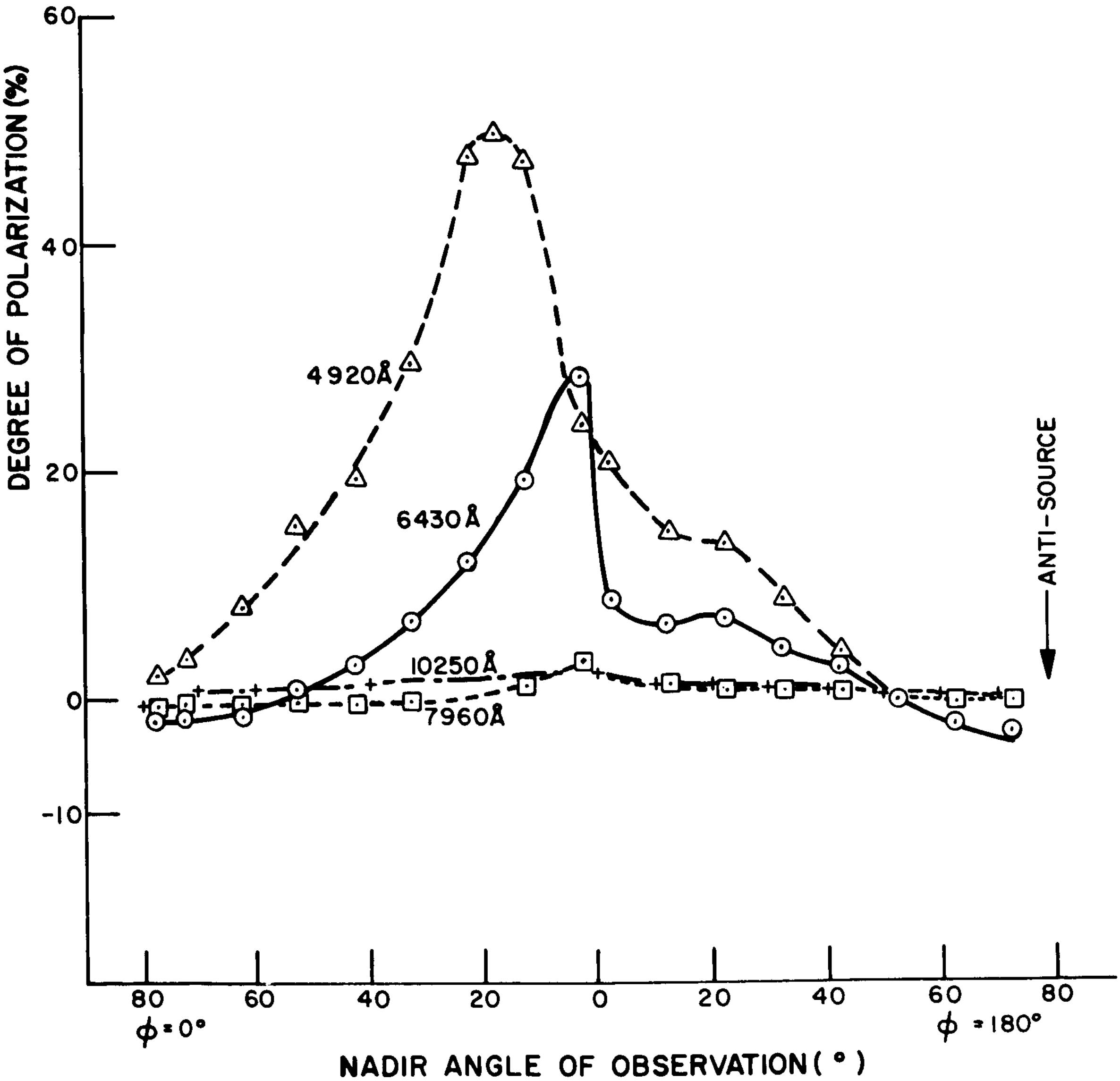

Fig. 46 Degree of polarization of radiation reflected from clipped green grass (principal plane, $\theta_o = 78.5^o$)

It is to be noted that the degree of polarization in the infra-red region is less than three percent for all source zenith angles, while considerable polarization is present at the shorter wavelengths. This should be compared with the curves of directional reflectance for the green grass sample, in which the inverse relationship is seen to exist.

The following curves show the degree of polarization of desert sand, a sample which has a much higher reflectance at the shorter wavelengths than did the preceding samples. A corresponding decrease in the maximum degree of polarization will be observed. Fig. 47 shows the degree of polarization of desert sand in the principal plane as a function of nadir angle for several wavelengths with the source at the zenith. There is generally an increase in the degree of polarization with decreasing wavelength, although the increase is not monotonic, since the measurements at $\lambda = 10250\text{Å}$ are greater than those for $\lambda = 7960\text{Å}$. In fact, over a limited region of nadir angles, the measurements at $\lambda = 10250\text{Å}$ exceed those of all other wavelengths. The degree of polarization for $\lambda = 4920\text{Å}$ is less than .09 at $\theta = 80^\circ$. This compares with .20 for black loam and .26 for green grass for the same source zenith angle.

Fig. 48 shows data for the same sample, but for a source zenith angle of 53°. In addition, a sunlight measurement at $\lambda = 3650\text{Å}$ for a sun zenith angle of 40° is included. This ultra-violet measurement is interesting because of the absence of a neutral point, an occurrence not found in the laboratory measurements. Apparently, the reason for the absence of a neutral point at $\lambda = 3650\text{Å}$ is the addition of positive polarization due to the sky-light.

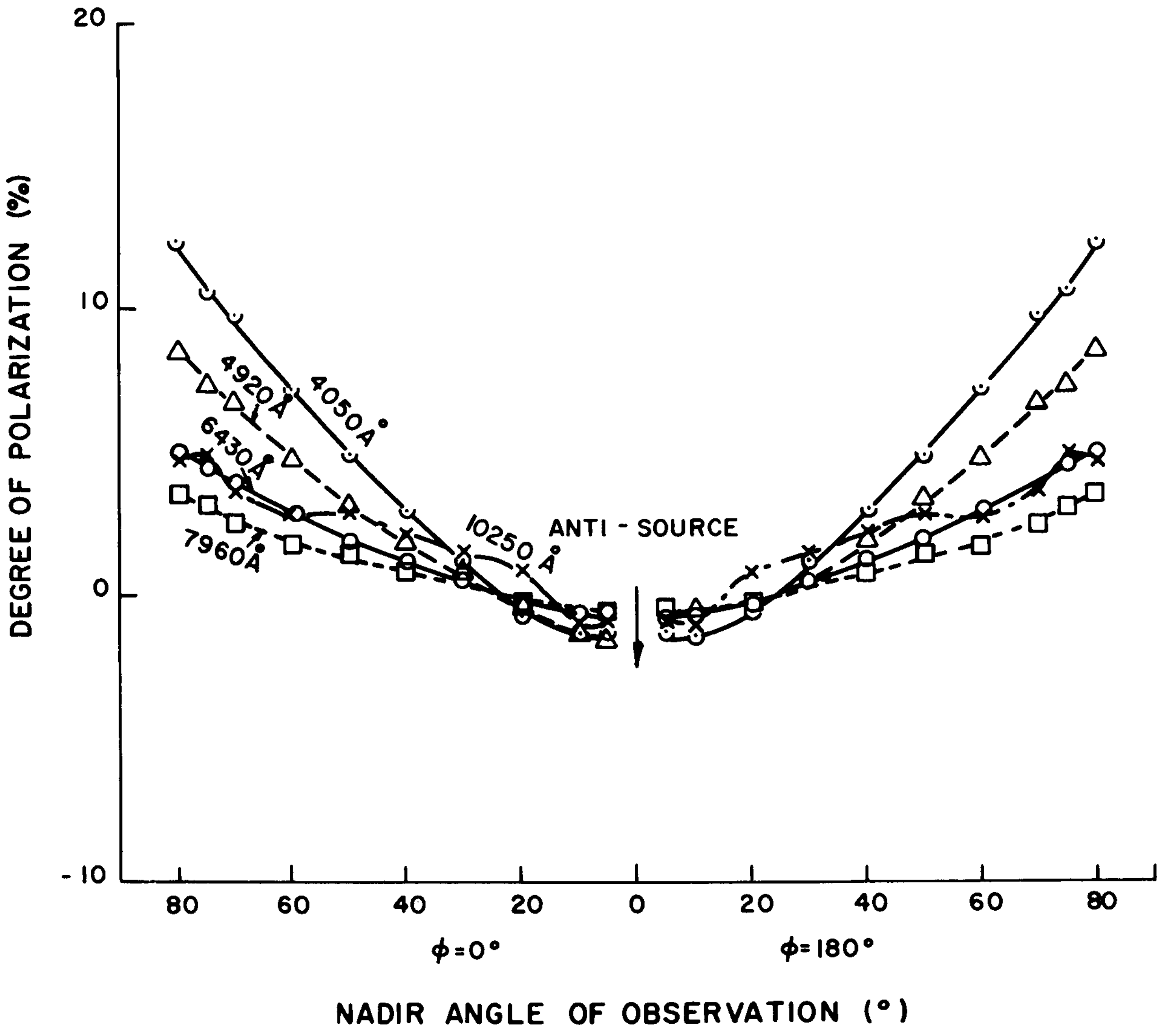

Fig. 47 Degree of polarization of radiation reflected from desert sand (results independent of azimuth, $\theta o = 0^{o}$)

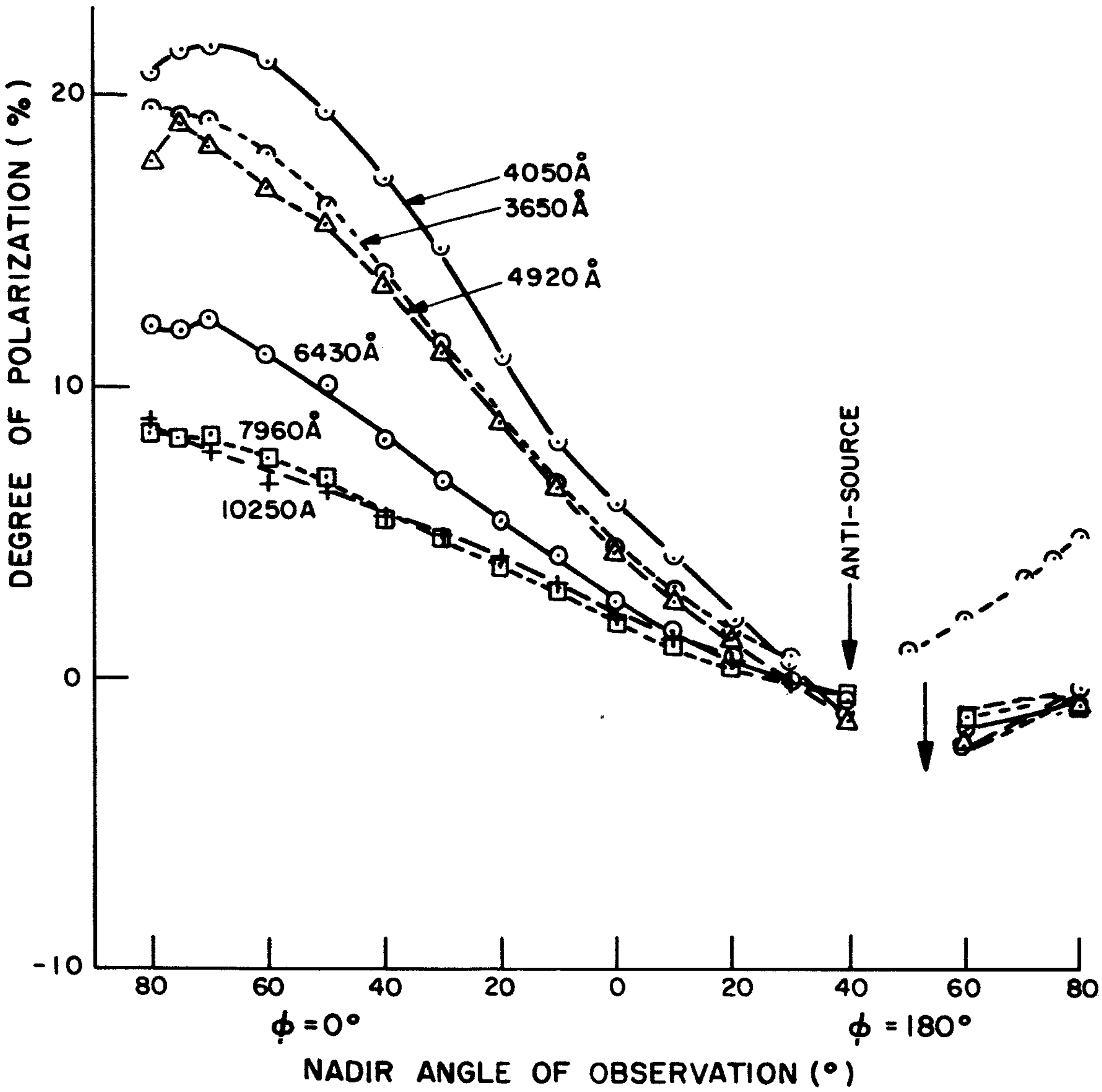

Fig. 48 Degree of polarization of radiation reflected from desert sand (principal plane, $\theta_o = 40^\circ$ for $\lambda = 3650A$; for other curves $\theta_o = 53.1^\circ$)

Fig. 49 shows the laboratory measurements of the same sample for $\theta_o = 78.5^o$, and a sunlight measurement at $\lambda = 3650\text{Å}$ for a sun zenith angle of 54^o. Again, there is no neutral point present for the measurement at $\lambda = 3650\text{Å}$. The degree of polarization is greater for the 10250Å data than for $\lambda = 7960\text{Å}$ over most of the range of nadir angles.

2. Additional Sunlight Measurements

An additional sunlight measurement of the degree of polarization of desert sand is given in Fig. 50. The 3650Å measurements and the laboratory measurement at 4920Å have been shown previously in the discussion of the desert sand measurements, and are included here for comparison. The fourth curve represents the degree of polarization for a sunlight measurement at wavelength 4920Å for a sun zenith angle $\theta_o = 57^o$. Since the laboratory measurement for $\lambda = 4920\text{Å}$ is for $\theta_o = 53^o$, a comparison can be made between the indoor measurement and sunlight measurement at approximately the same source zenith angle. The curves are similar, the laboratory measurement exhibiting a greater degree of polarization. It is interesting to note that neutral points occur for the 4920Å sunlight measurement.

Fig. 51 shows the degree of polarization of red clay and green grass in the presence of sunlight. The sun zenith angle for the clay sample is 35^o, and $\theta_o = 39^o$ for the green grass sample. The measurements are for wavelength 3650Å for both samples. The curve for green grass was shown in Fig. 45 and is repeated here for comparison. It is seen that the polarization data for red clay exhibit no neutral points, while the measurement for green grass shows rather strong negative polarization. Since these measurements

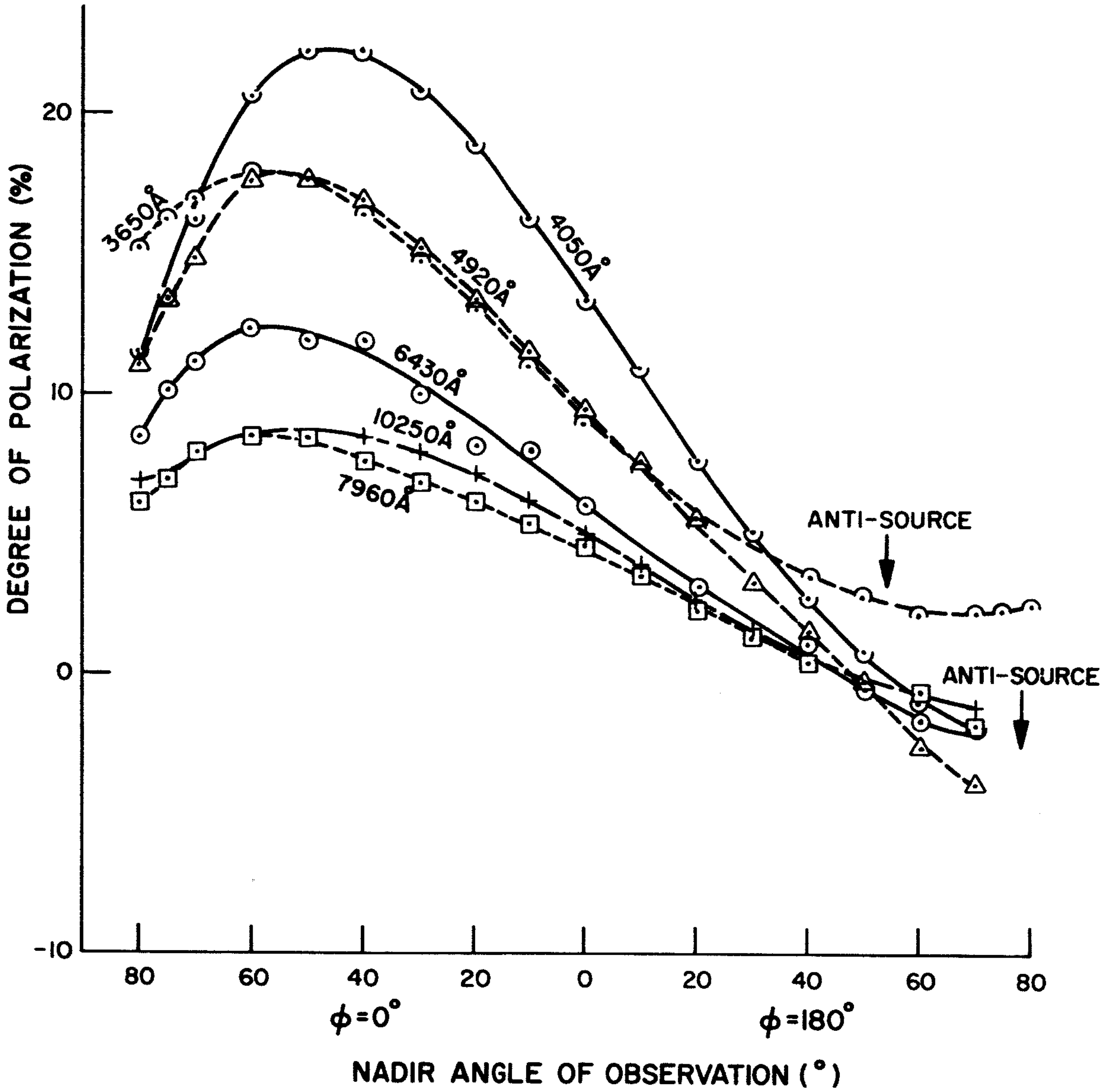

Fig. 49 Degree of polarization of radiation reflected from desert sand (principal plane, $\theta_0 = 54°$ for $\lambda = 3650 \text{Å}$; for other curves $\theta_0 = 78.5°$)

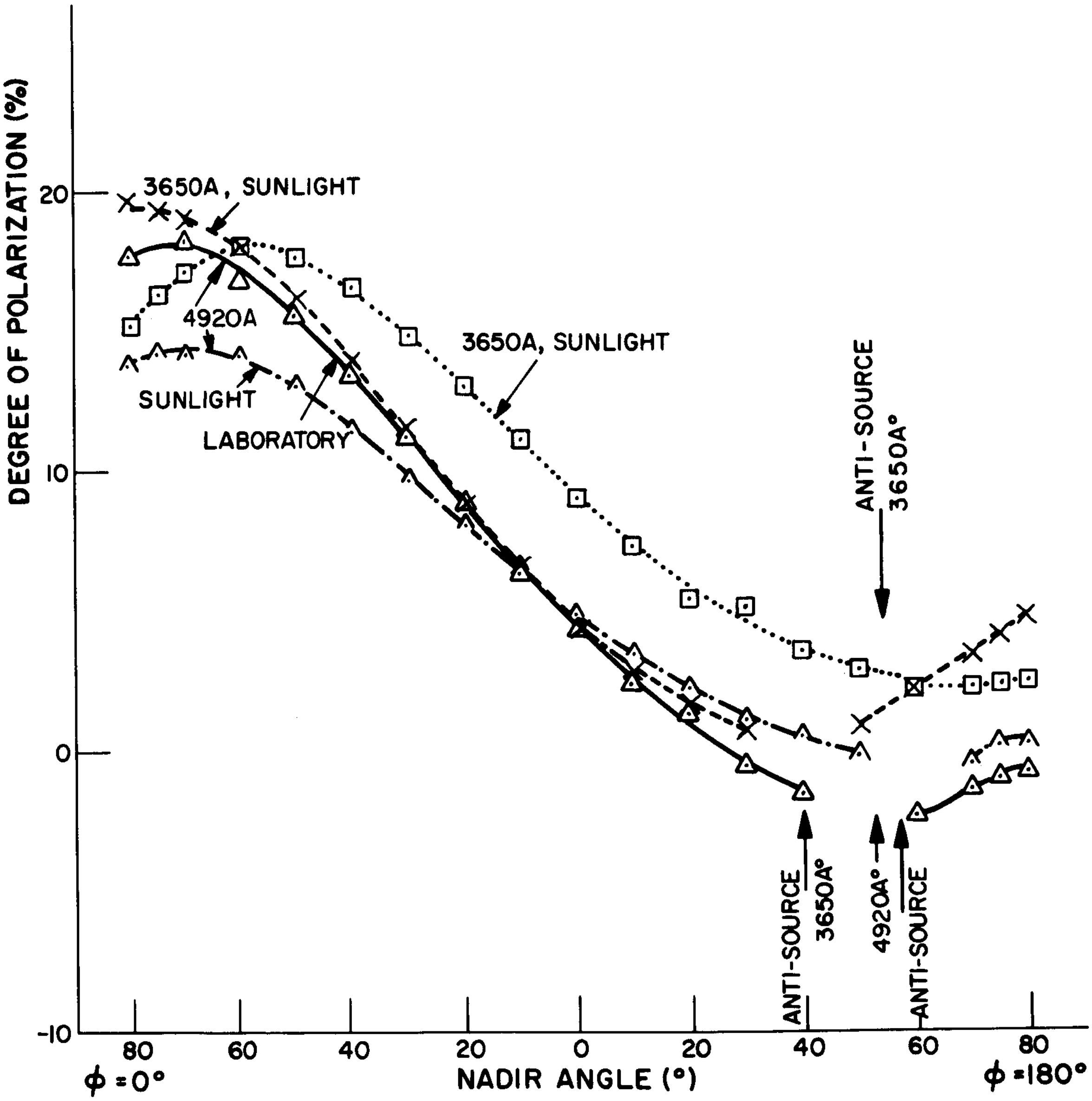

Fig. 50 Degree of polarization of radiation reflected from desert sand (principal plane, $\theta_o = 40^o, 54^o$ for $\lambda = 3650Å$; $\theta_o = 57^o, 53^o$ for $\lambda = 4920Å$)

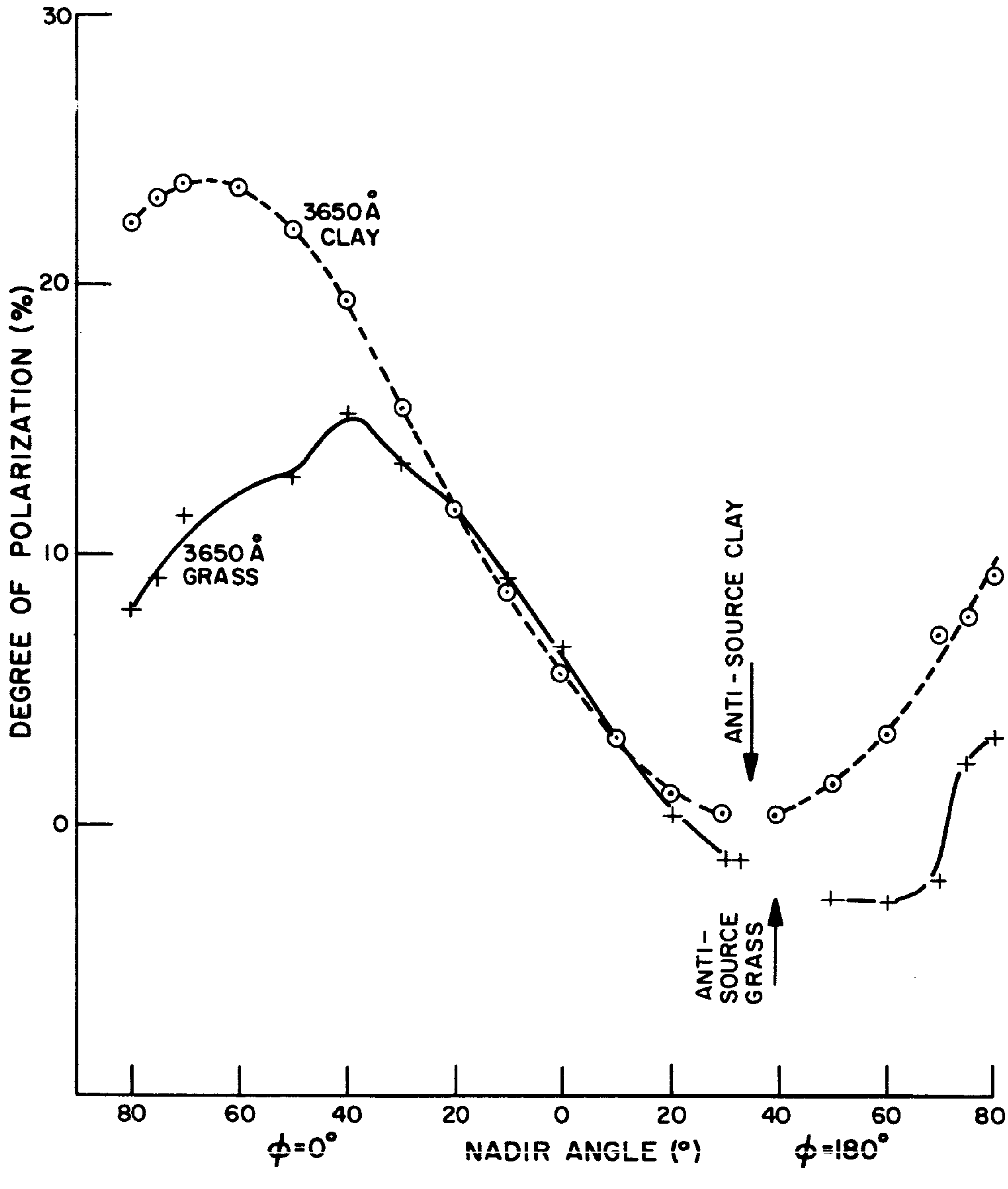

Fig. 51 Degree of polarization of sunlight reflected from samples of clay and grass (principal plane, λ = 3650Å)

were made on different days, there may be some effect due to changes in the "clear" atmosphere. Other contributing causes for this difference may be due to different sky-light effects for different surface textures, and a critical dependence on the sun zenith angle.

Fig. 52 shows the degree of polarization as a function of nadir angle in the principal plane for desert sand and red clay. The sun zenith angle for the red clay measurement is 34°; for the measurements of desert soil, $\theta_o = 37^{\circ}$. For both samples, $\lambda = 4920\text{Å}$. The polarization profiles are very similar, the desert soil exhibiting a greater degree of polarization. Neutral points exist for both samples.

The degree of polarization of radiation reflected from green grass is compared with that from black loam in Fig. 53. The sun zenith angle for the black loam measurement is 22°; for the green grass measurement, $\theta_o = 37^{\circ}$. For both samples, $\lambda = 4920\text{Å}$. The maximum degree of polarization for the black loam is double that for green grass, although the difference in sun zenith angle prevents a direct comparison. Neutral points exist for both sets of measurements.

3. Comparison of the Degree of Polarization from Various Materials

The following figures show a comparison of the degree of polarization for various surfaces for measurements made at the same wavelength. Fig. 54 shows measurements of the degree of polarization in the principal plane at wavelength 4920Å for six different samples. They are, in order of increasing maximum polarization, gypsum sand, beach sand, desert sand, pulverized limonite, black loam, and green grass. The source zenith angle

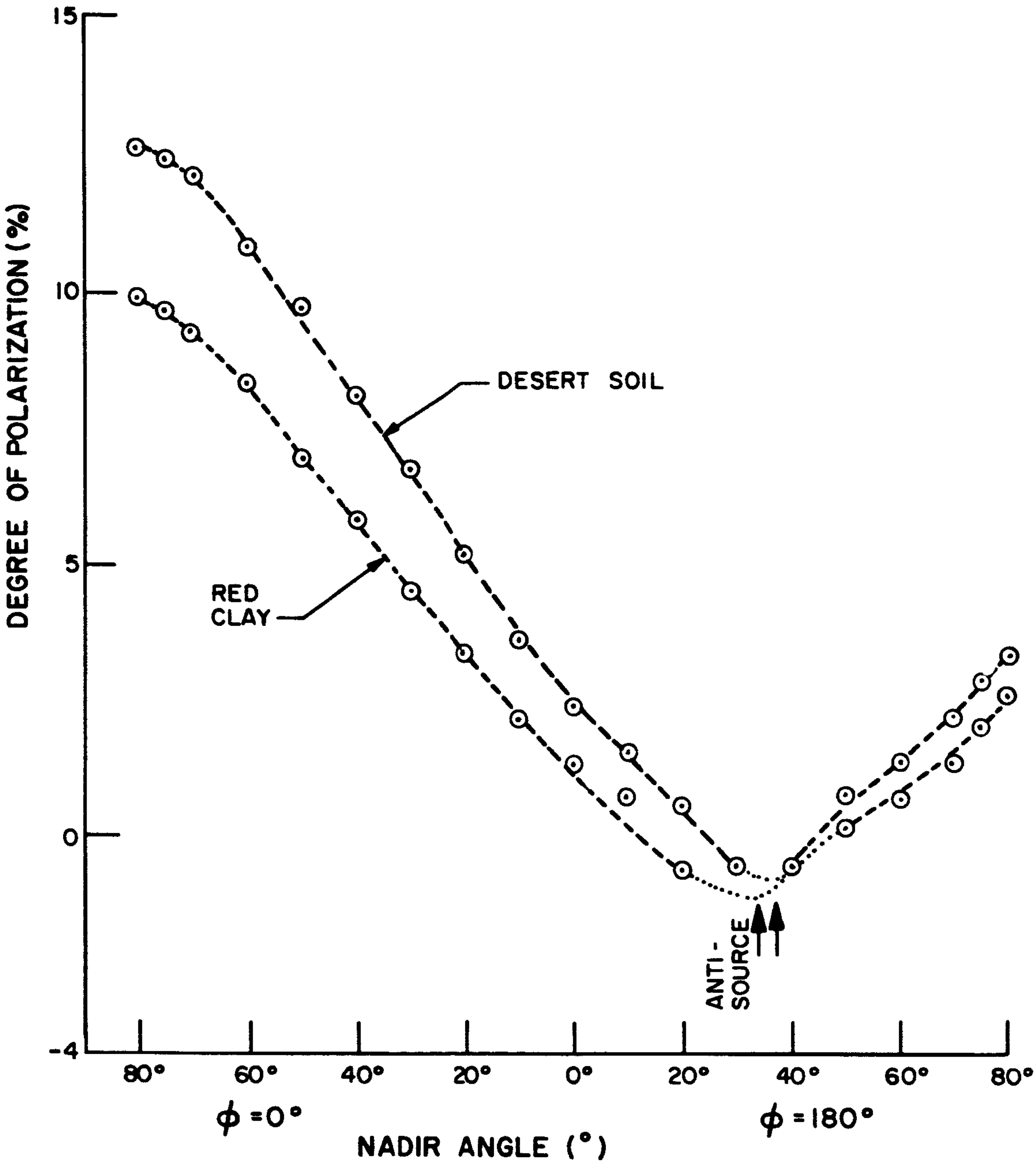

Fig. 52 Degree of polarization of sunlight reflected from samples of desert soil and red clay (principal plane, $\lambda = 4920\text{Å}$; $\theta_o = 34^{\circ}$ for red clay; $\theta_o = 37^{\circ}$ for desert soil)

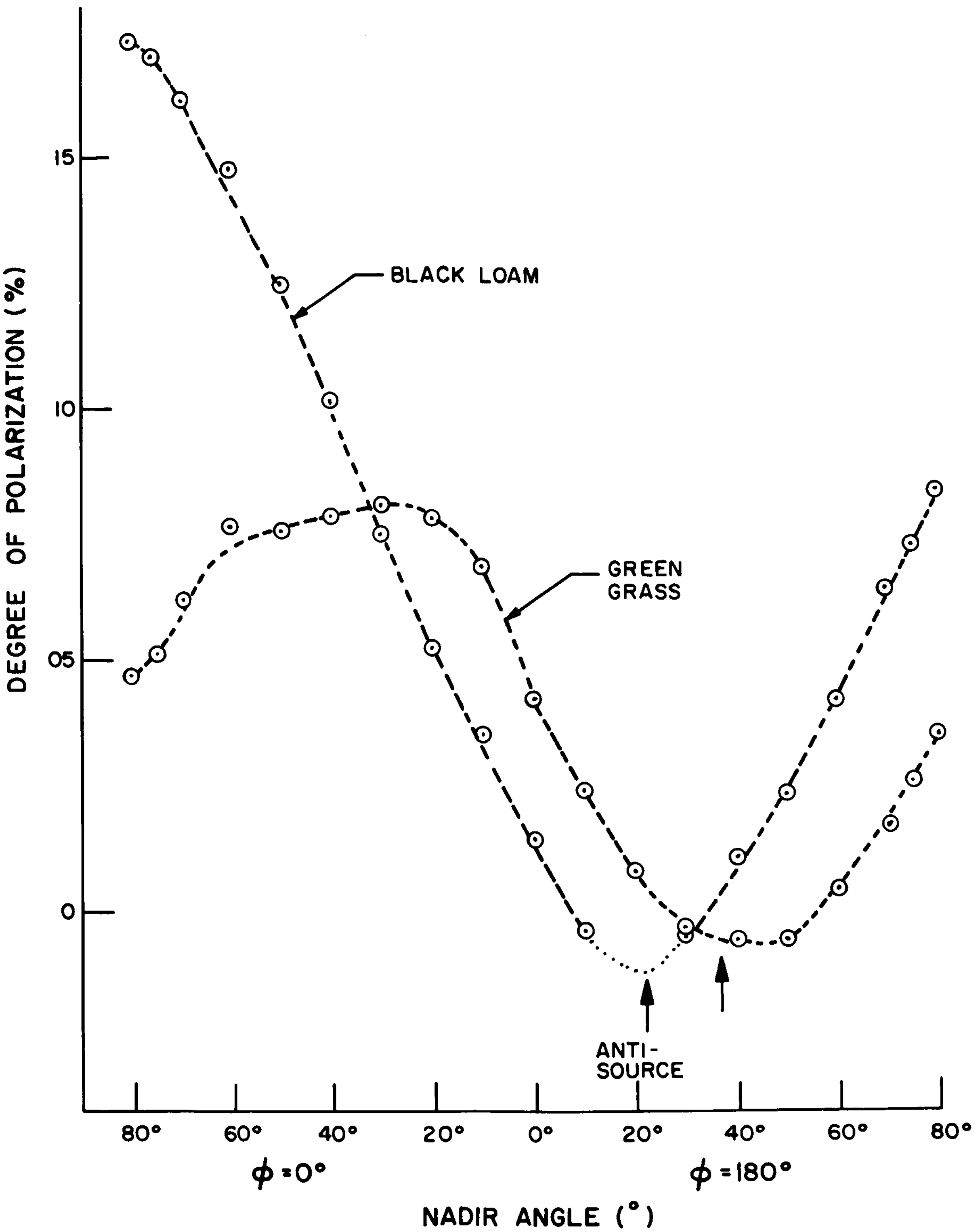

Fig. 53 Degree of polarization of sunlight reflected from samples of black loam and green grass (principal plane, $\lambda = 4920\text{\AA}$; $\theta_o = 22^o$ for black loam; $\theta_o = 37^o$ for green grass)

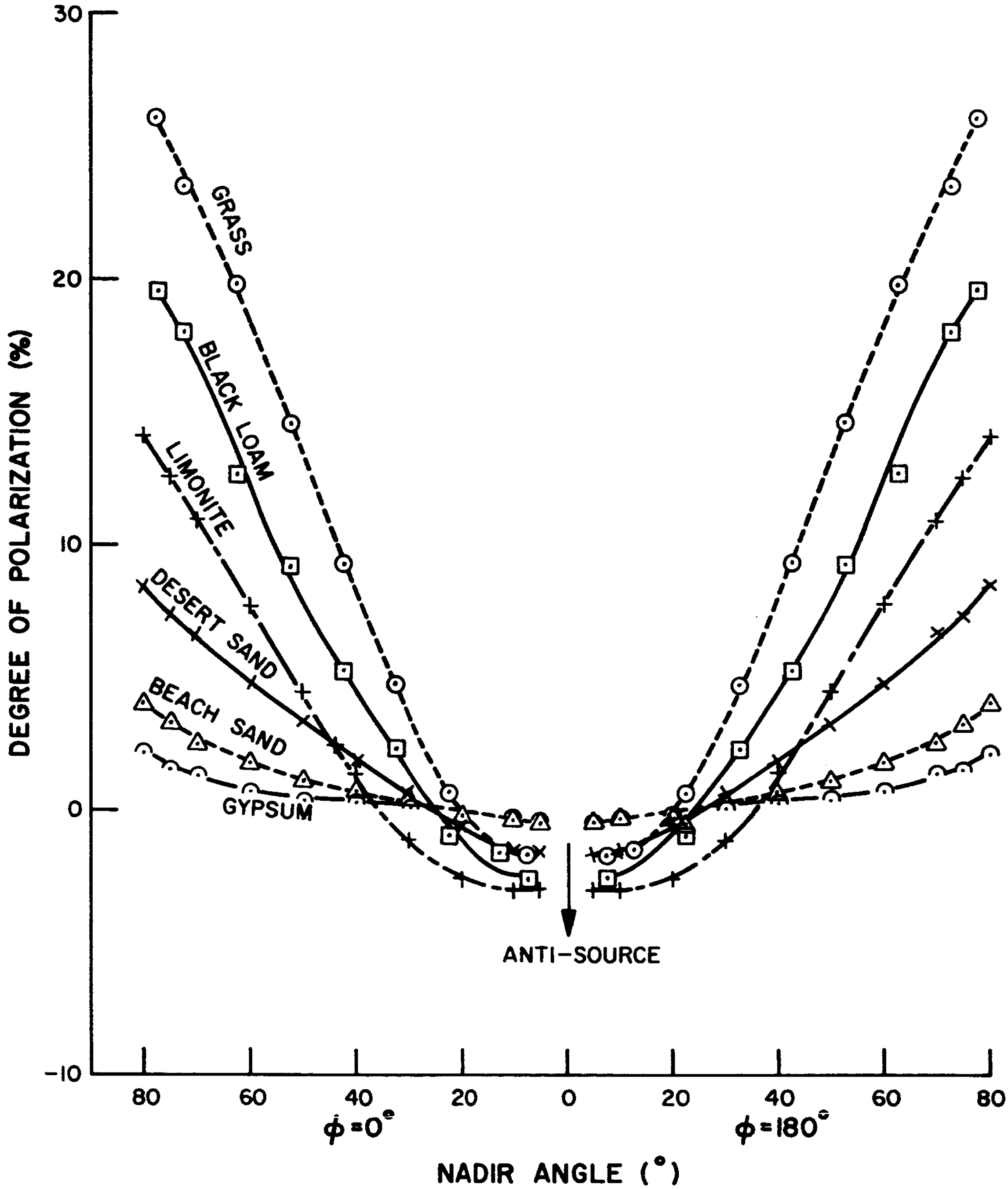

Fig. 54 Degree of polarization of radiation reflected from various sample surfaces (principal plane, $\lambda = 4920\text{Å}$, $\theta_o = 0^o$).

is $\theta_o = 0^o$. It should be noted that these are the same materials for which data were presented in Fig. 29. In that figure, the reflectance of the various materials, measured at $\lambda = 6430\text{Å}$, was seen to increase in exactly the same order as the maximum degree of polarization decreases; i.e., from green grass through gypsum sand. The indication is that translucent materials are generally less polarizing than absorbent materials.

Fig. 55 shows results for essentially the same samples, with the exception that Yolo loam is included and limonite deleted. The measurements are for wavelength 4920Å, and a source zenith angle $\theta_o = 53^o$. The maximum degree of polarization is seen to be higher here than in the previous Figure for each sample, excluding limonite, and the black loam now exhibits a greater degree of polarization than does the green grass sample. A further increase in the degree of polarization is seen in Fig. 56, which shows the polarization data for these materials for $\theta_o = 78.5^o$ and wavelength 4920Å.

4. Effect of Particle Size

The following set of curves show the polarization results for pulverized limonite. This sample was described in the discussion of reflectance properties, and the use of the words "fine" and "coarse", introduced previously, are retained. Fig. 57 shows the degree of polarization of limonite in the principal plane as a function of nadir angle, for wavelengths 4920Å and 6430Å, with the source at the zenith. For both wavelengths, the "coarse" sample exhibits a greater degree of polarization. The corresponding measurements for a source zenith angle of 53^o are given by Fig. 58. In addition, measurements for wavelength 7960Å are included. The difference in the

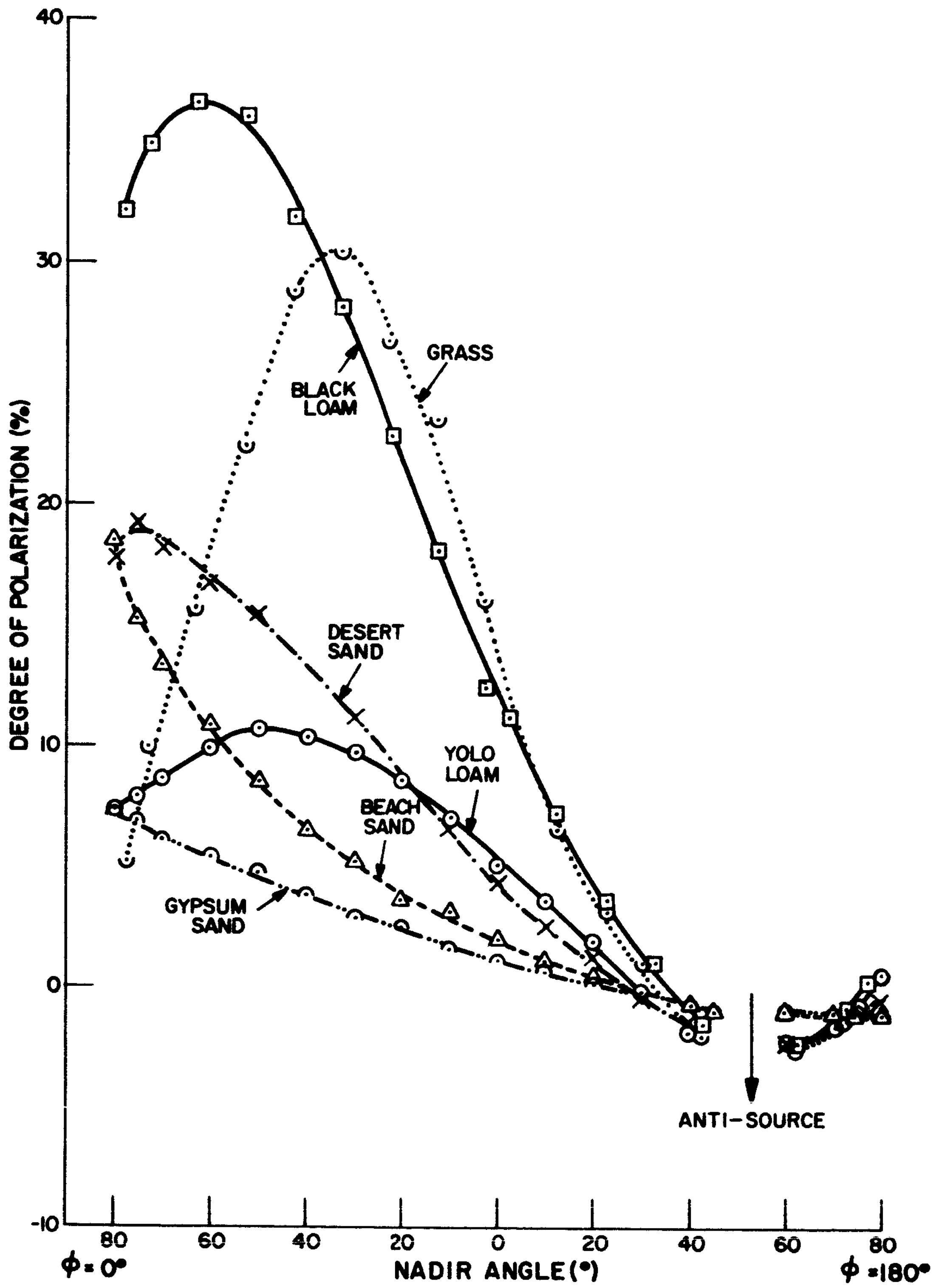

Fig. 55 Degree of polarization of radiati on reflected from various sample surfaces (principal plane, $\lambda = 4920\mathring{A}$, $\theta_o = 53°$)

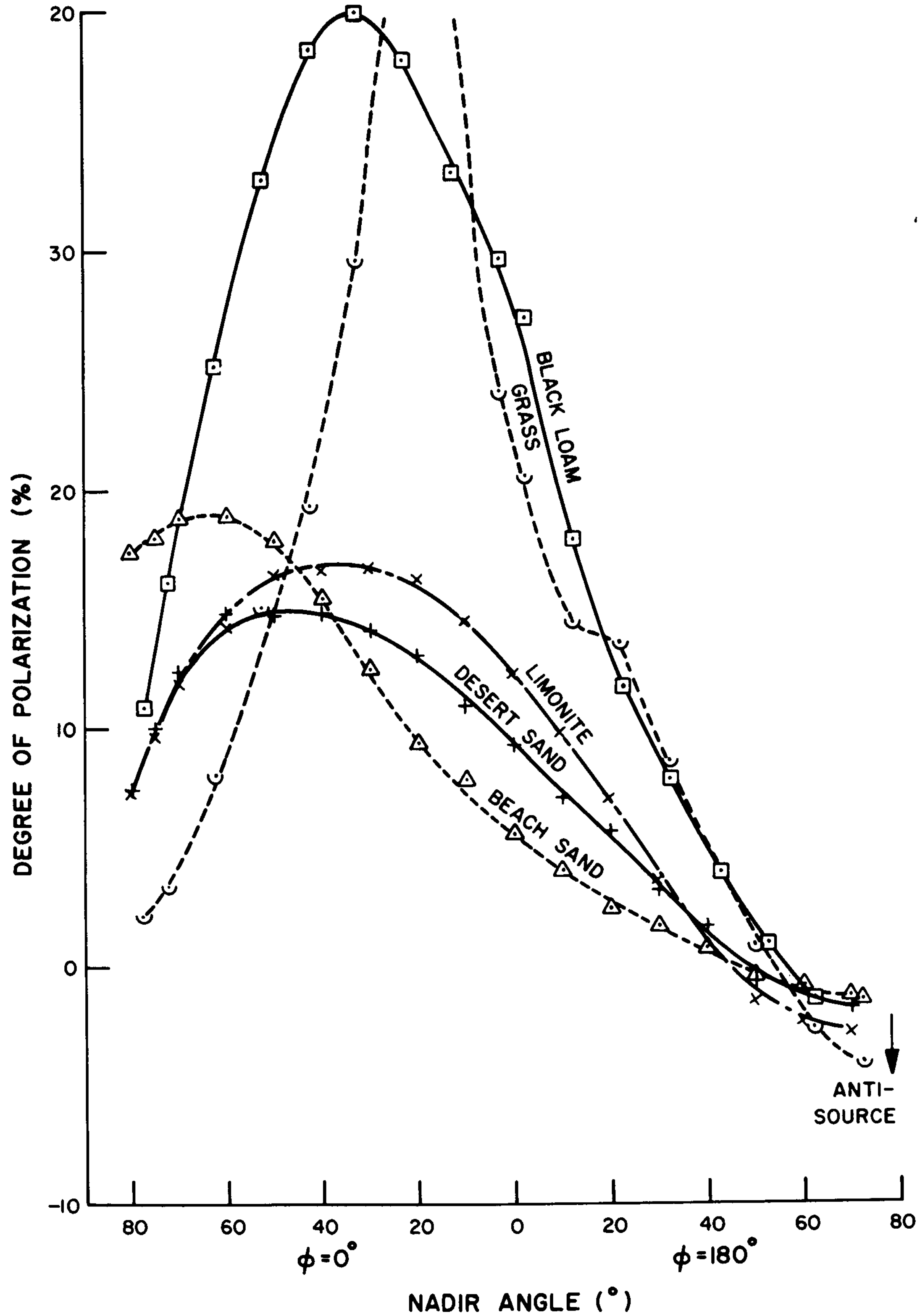

Fig. 56 Degree of polarization of radiation reflected from various sample surfaces (principal plane, λ = 4920Å, θ_o = 78.5°)

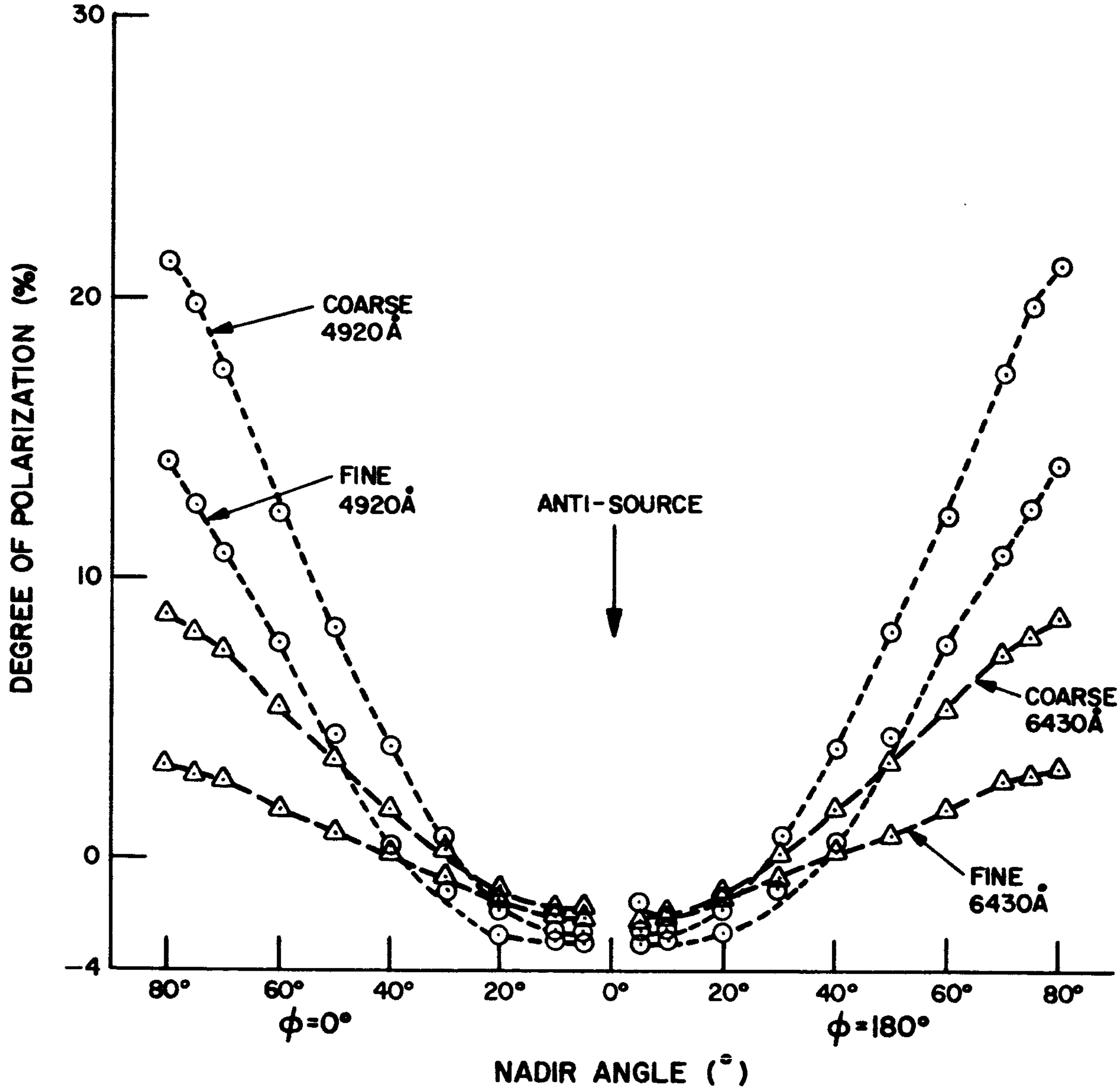

Fig. 57 Degree of polarization of radiation reflected from coarse and fine limonite (principal plane, λ = 4920Å and 6430Å; $\theta_o = 0^o$)

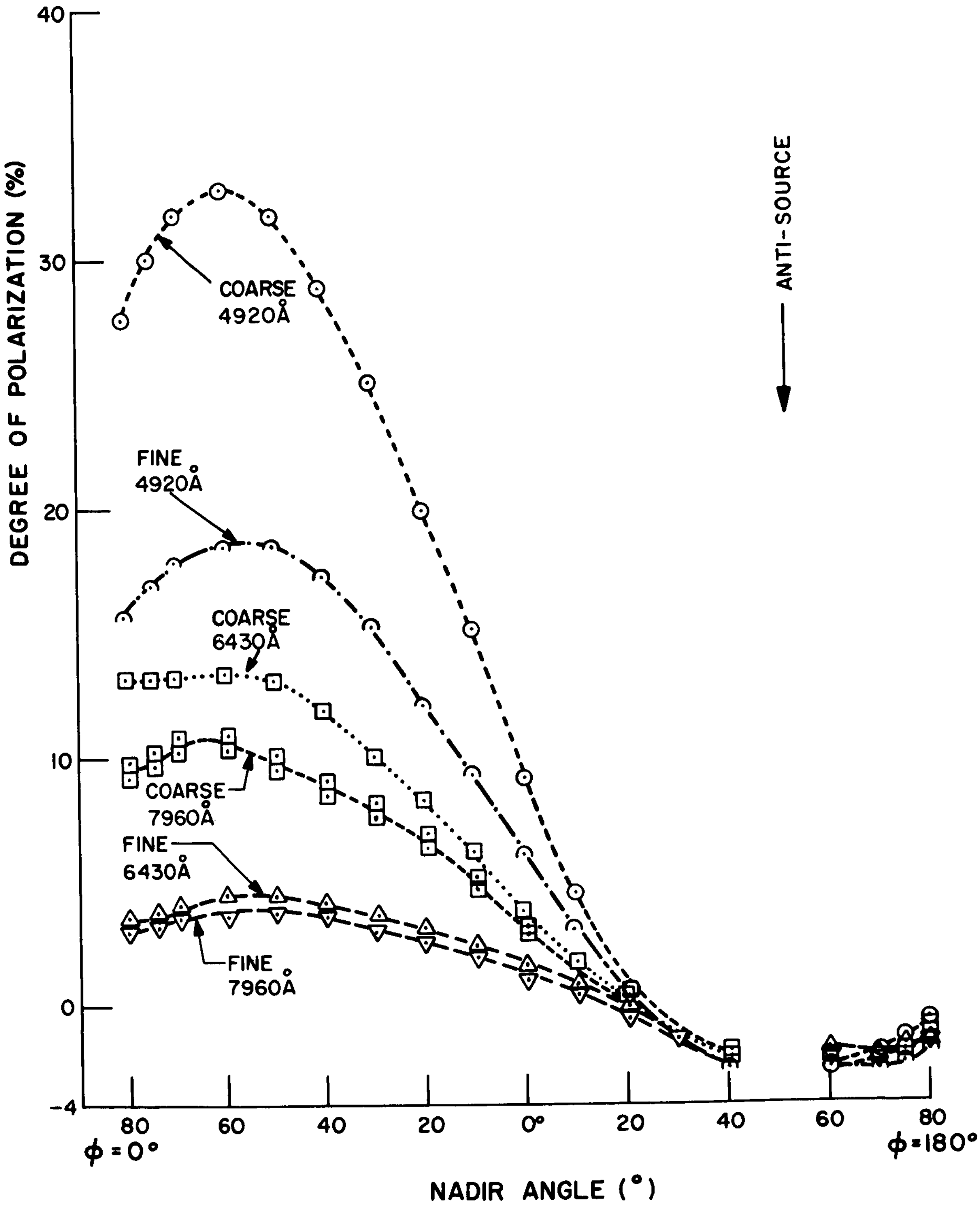

Fig. 58 Degree of polarization of radiation reflected from coarse and fine limonite (principal plane, $\lambda = 4920$Å, 6430Å, and 7960Å; $\theta_o = 53°$)

degree of polarization between the "fine" and "coarse" samples for a given wavelength is more pronounced when compared to the case of normal incident light. The maximum degree of polarization is seen to increase for each sample and wavelength when compared to the case $\theta_o = 0^o$. Measurements for a source zenith angle of 78.5^o are shown in Fig. 59. The difference in the degree of polarization between the "fine" and "coarse" samples is about the same as that for the case $\theta_o = 53^o$. In fact, the maximum degree of polarization for a given sample and wavelength is approximately the same as for $\theta_o = 53^o$. In all cases, it is observed that the "coarse" sample is more highly polarizing than the "fine" sample.

5. Comparison of the Degree of Polarization from Different Limonite Samples

Fig. 60 shows the effect of chemical composition or particle characteristics, or both, on the degree of polarization. The measurements are made at 4920Å, 6430Å, and 7960Å for a source zenith angle of 53^o. The samples being compared are described in section 7 of the discussion of Reflectance. It was noted there that for each of the three wavelengths, the yellow limonite gave rise to a greater reflectance. The present figure shows a reciprocal relation to exist for the degree of polarization; namely, that for each of the three wavelengths, the sample of red limonite is more highly polarizing.

6. Azimuth Dependence of the Degree of Polarization

The variation of the degree of polarization over the hemisphere is shown by the following polar maps. A description of the coordinate system was given in section 8 of the discussion of Reflectance.

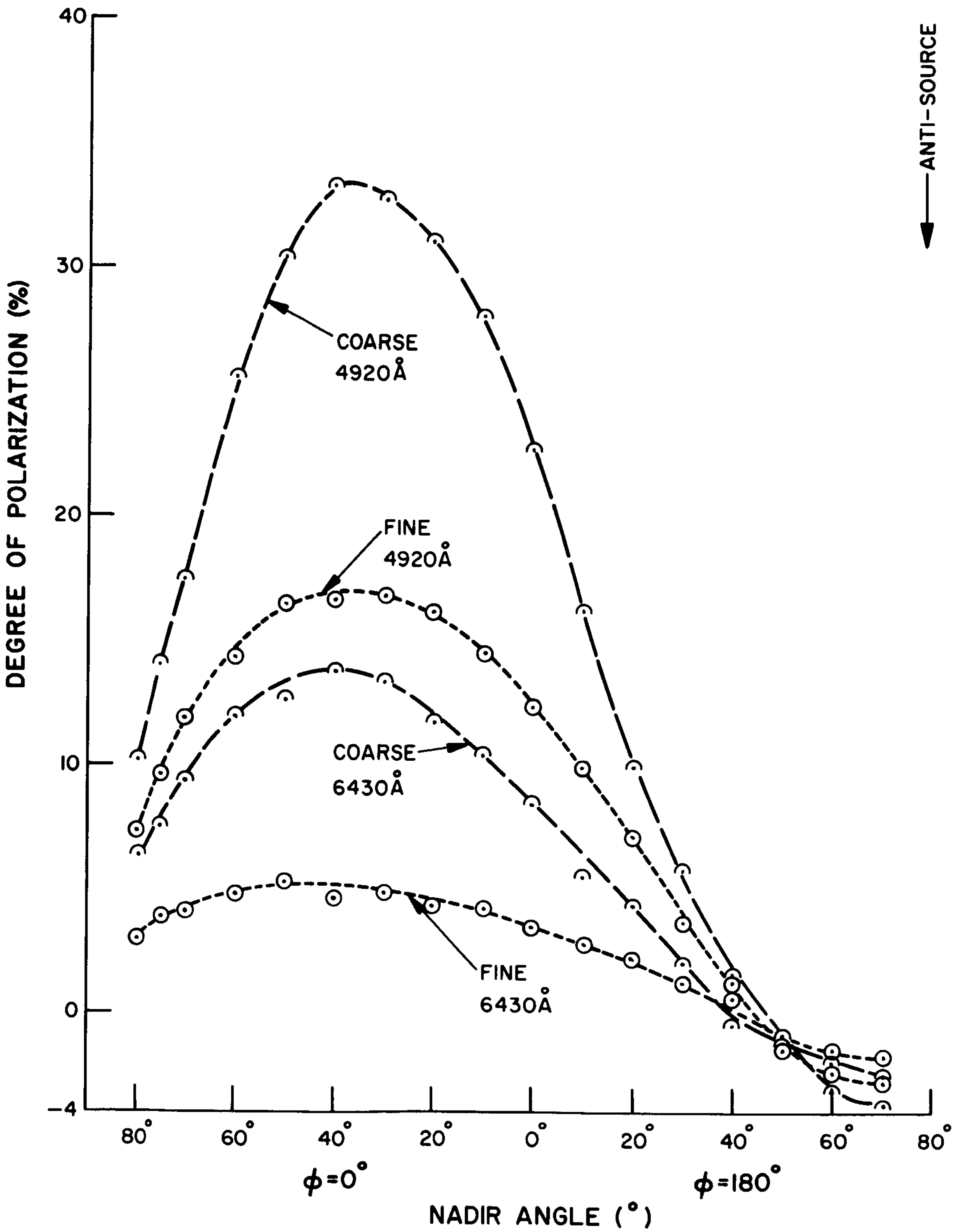

Fig. 59 Degree of polarization of radiation reflected from coarse and fine limonite (principal plane, $\lambda = 4920\text{Å}$ and 6430Å ; $\theta_o = 78.5^{\circ}$)

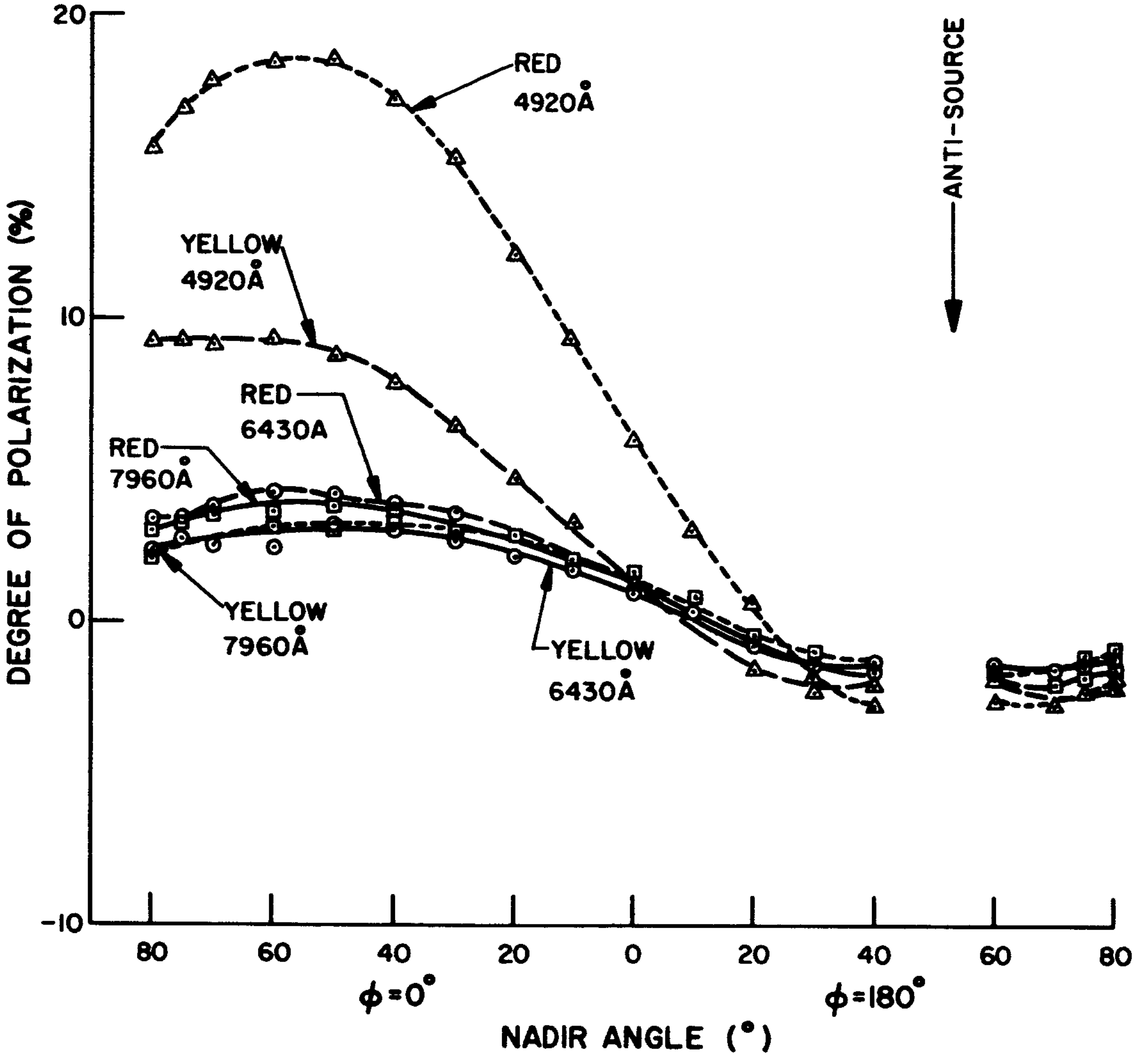

Fig. 60 Degree of polarization of radiation reflected from samples of red limonite and yellow limonite (principal plane, λ = 4920Å, 6430Å, and 7960Å ; θ_o = 53°)

Fig. 61 shows a hemispheric map of the degree of polarization for the black loam sample; the source zenith angle is 53°, and the wavelength is 6430Å. The various contours are lines of constant degree of polarization, shown at 2 1/2% increments. There is a broad maximum in the region near $\theta = 60^{\circ}$ and extending in azimuth from $\varphi = 0^{\circ}$ to $\varphi = 60^{\circ}$.

Fig. 62 shows a decrease in the degree of polarization over the whole hemisphere when compared to the previous figure. Fig. 62 shows the degree of polarization of desert sand for a source zenith angle of 53° and wavelength of 6430Å. The maximum degree of polarization is seen to be about one half that of the maximum for black loam. It will be recalled that the total reflectances for these surfaces at 6430Å and $\theta_o = 53^{\circ}$ are .089 for black loam and .360 for desert sand. Thus figures 61 and 62, showing the degree of polarization over the whole hemisphere, provide a good example of the correspondence of high reflectance to low polarization, and low reflectance to high polarization.

Fig. 63 shows the degree of polarization of clipped green grass for a source zenith angle of 53° and wavelength of 6430Å. The principal difference in this polarization pattern from those of the preceding two figures is the existence of a region of low polarization at $\varphi = 0^{\circ}$ and large nadir angles of observation. The pattern is relatively symmetrical about the 90° azimuth, the direction of the maximum degree of polarization.

Fig. 64 shows the degree of polarization for the sample of crushed limestone. The source zenith angle is 53° and wavelength 6430Å. This sample is characterized by a relatively small degree of polarization, P being everywhere less than 0.06.

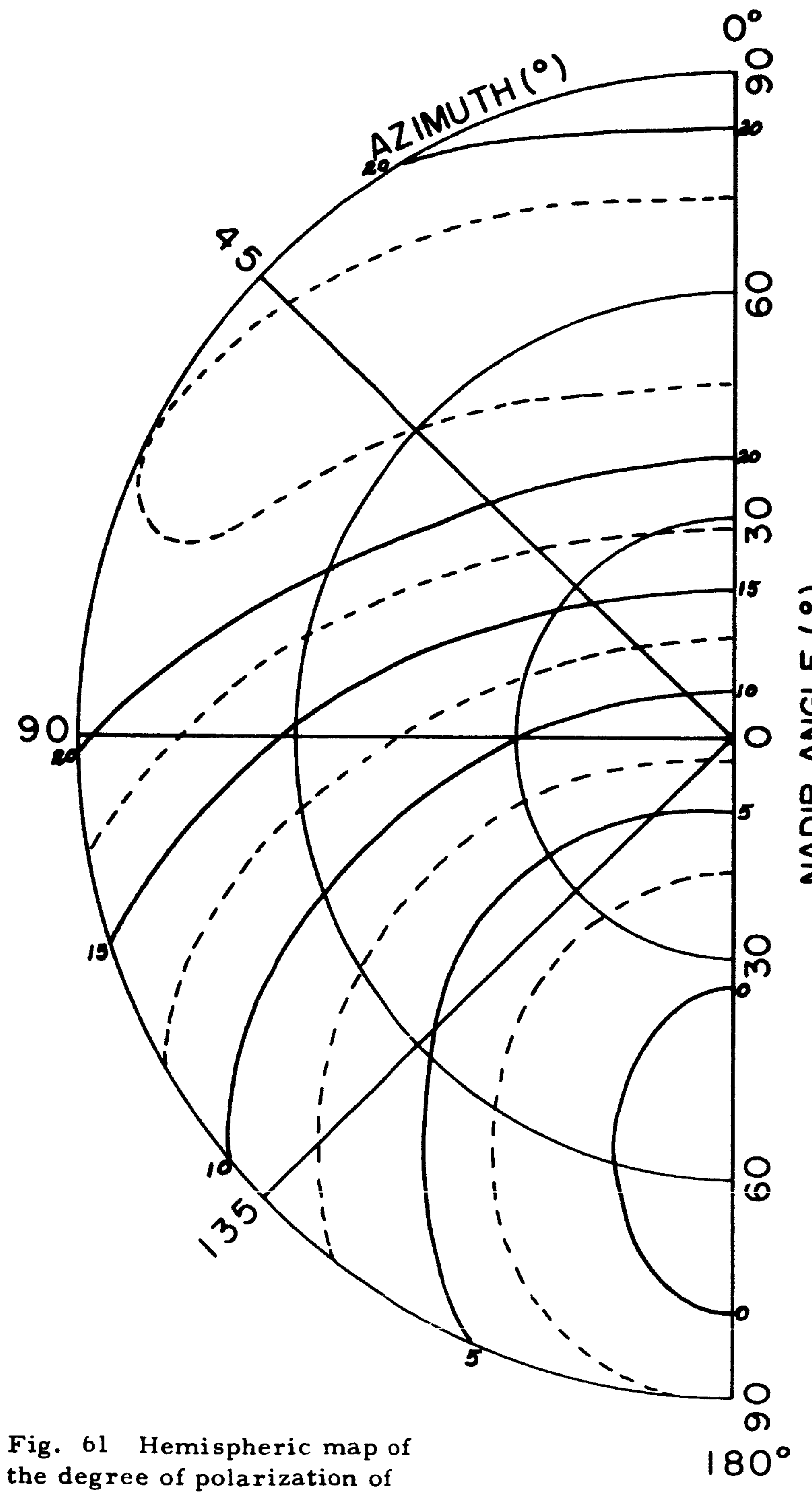

Fig. 61 Hemispheric map of the degree of polarization of radiation reflected from black loam soil ($\theta_o = 53.1^o$, $\lambda = 6430Å$)

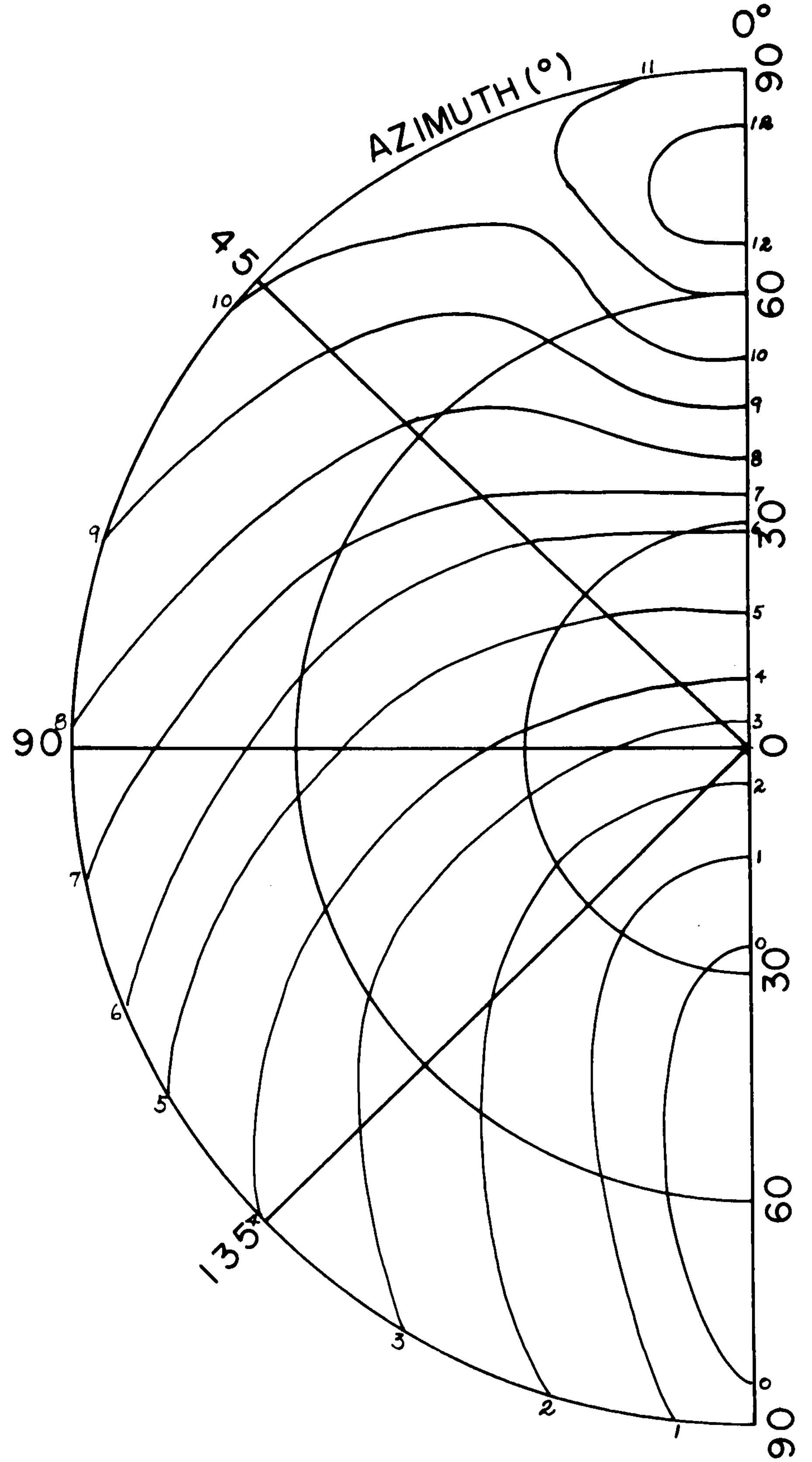

Fig. 62 Hemispheric map of the degree of polarization of radiation reflected from desert sand ($\theta_0 = 53.1^{\circ}$, $\lambda = 6430\text{Å}$)

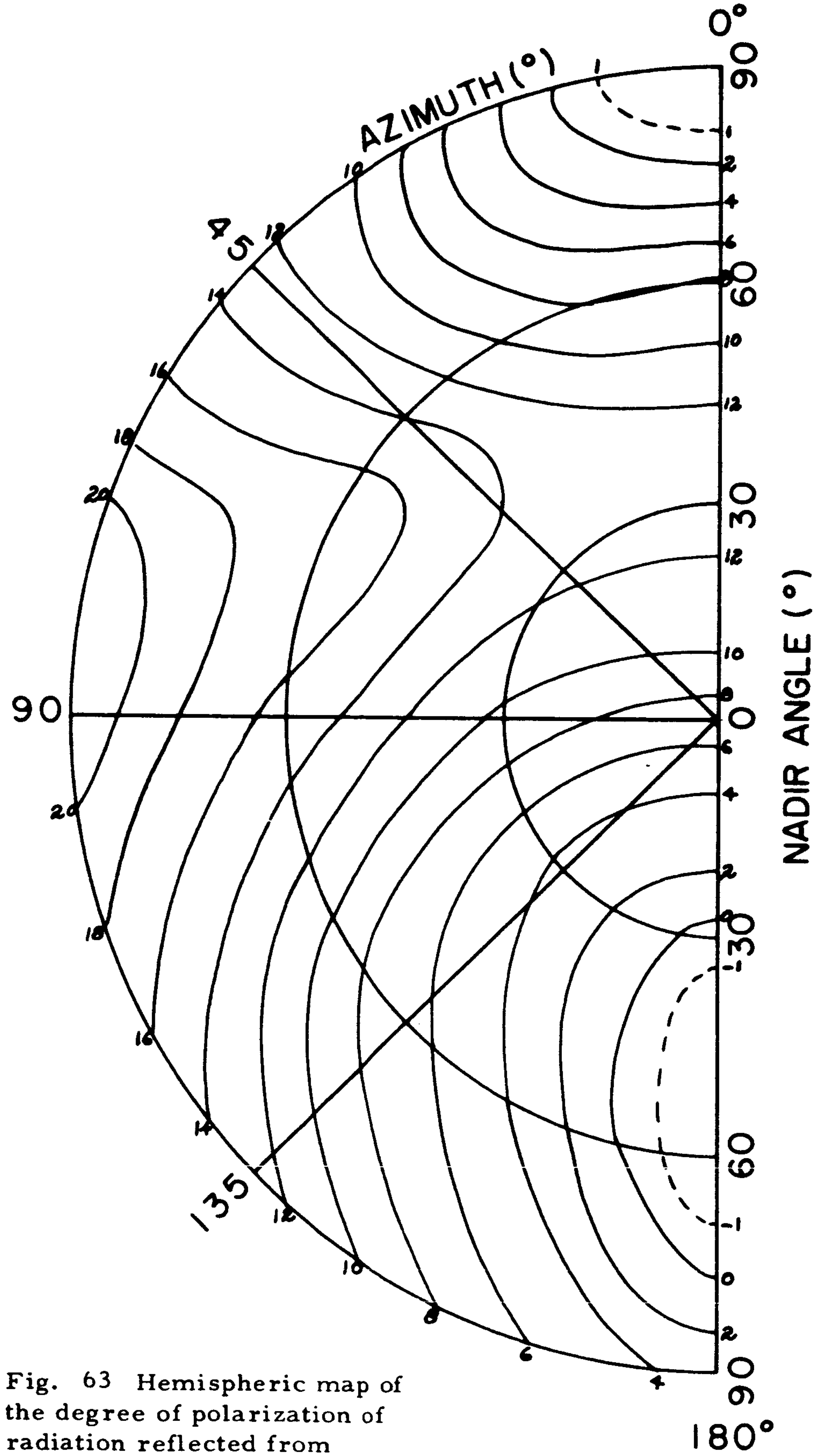

Fig. 63 Hemispheric map of the degree of polarization of radiation reflected from clipped green grass (θ_o = 53.1° λ = 6430Å)

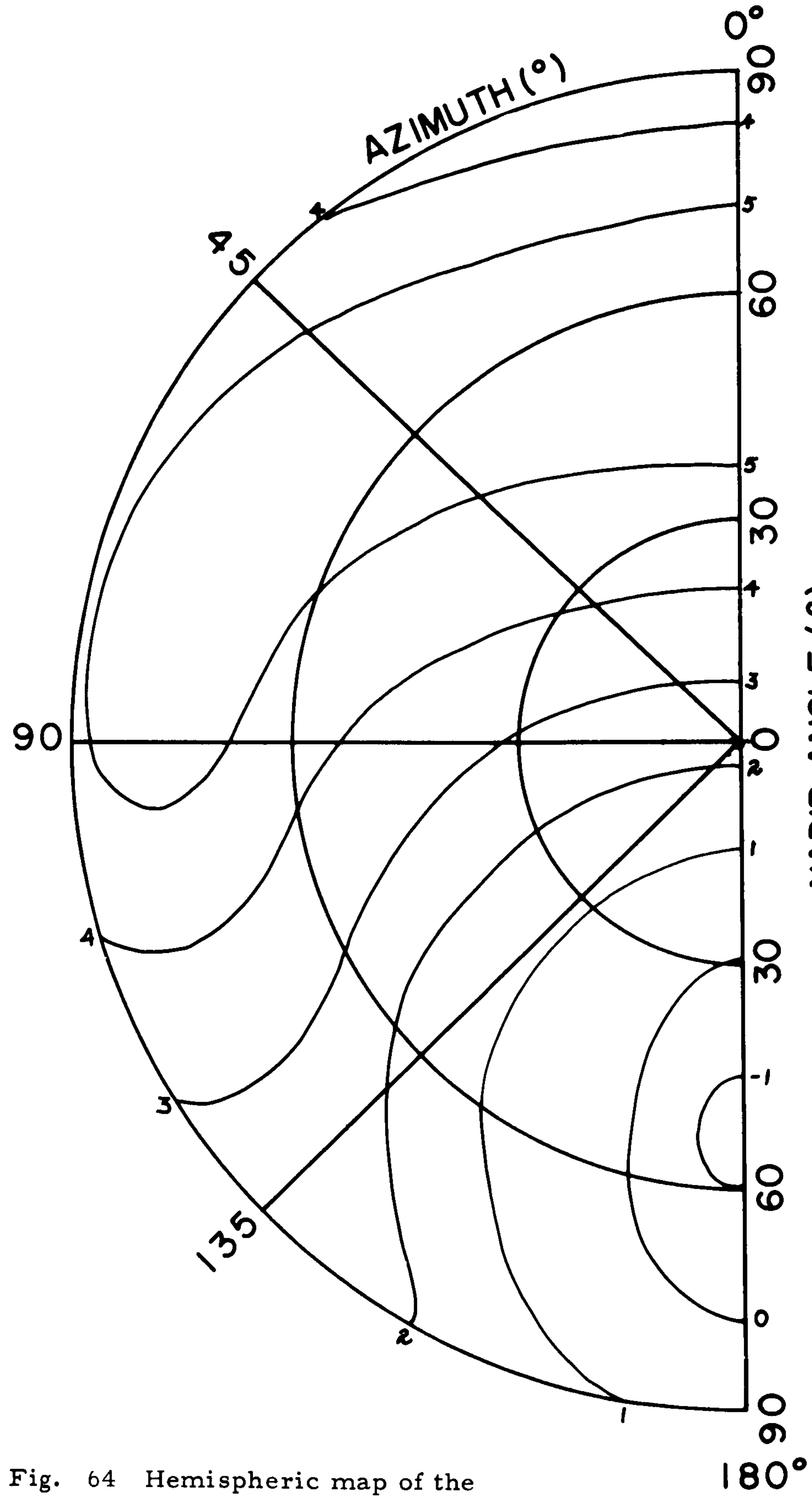

Fig. 64 Hemispheric map of the degree of polarization of radiation reflected from crushed limestone gravel (θ_o = 53.1°, λ = 6430Å)

The weathered blacktop sample provides a much greater degree of polarization than any of the preceding samples, as can be seen from Fig. 65. Again, the source zenith angle is 53° and the wavelength is 6430Å. A maximum of 0.75 occurs in the region surrounding $\varphi = 0^{\circ}$, $\theta = 60^{\circ}$.

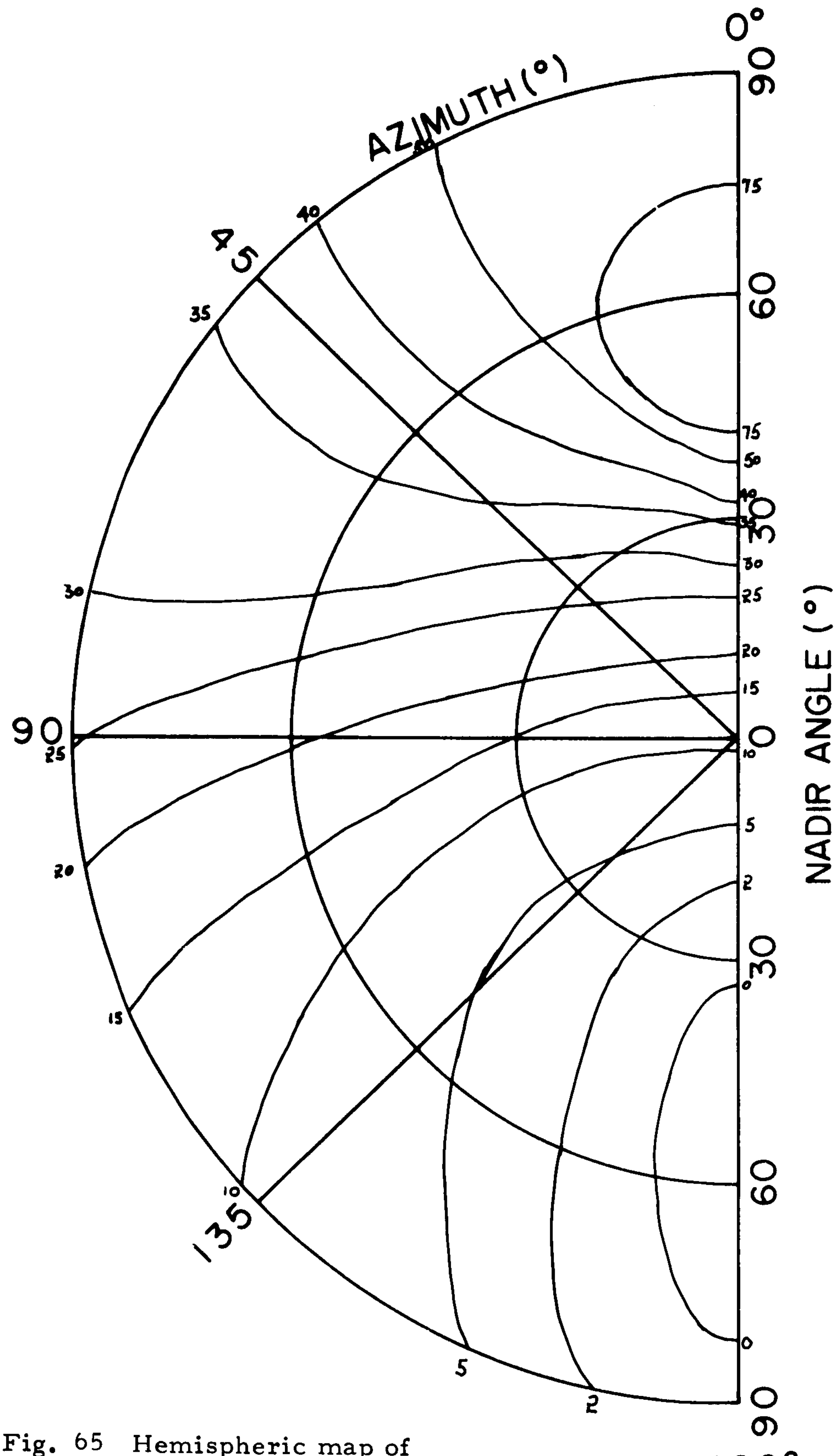

Fig. 65 Hemispheric map of the degree of polarization of radiation reflected from weathered blacktop (θ_o = 53.1°, λ = 6430Å)

IV. Computations of Radiation Emerging from Top of Atmosphere

A. Theoretical Derivations

We shall for the most part be concerned with a plane parallel Rayleigh atmosphere, and utilize the solution obtained by Chandrasekhar (1950) for this problem. His solution with the assumption that there is a perfectly absorbing ground at the lower boundary of the atmosphere is referred to as the "standard case" solution. The radiation emerging from the top of the atmosphere under the above constraint will be denoted by $\vec{I}_s\ (0;\ \mu,\ \varphi)$. The variables appearing in $\vec{I}_s$ are:

$\tau(\lambda)$, the normal optical thickness of the atmosphere.

τ = 0 at the top of the atmosphere.

μ = cos θ, where θ is the viewing angle of the observer relative to the nadir.

φ = azimuth of the vertical plane passing through the position of the observer.

The vector notation emphasizes the fact that the Stokes parameter representation for a beam of light is being used. The explicit form of $\vec{I}_s(0;\ \mu, \varphi)$ is

$$\begin{bmatrix} (I_l)_s & (0;\mu,\varphi) \\ (I_r)_s & (0;\mu,\varphi) \\ (U)_s & (0;\mu,\varphi) \end{bmatrix}$$

In general, these components have the following significance: The total intensity, I, in a beam of light is given by the sum of any two orthogonal components. It is convenient, for theoretical considerations, to chose I_l, the component parallel to the vertical plane through the azimuth of the observer, and I_r, the component perpendicular to the vertical plane. The U component, which indicates the orientation of the plane of polarization, is defined by:

$U \doteq (I_l - I_r)\tan 2X$, where X is the angular measure between the plane of polarization and the vertical plane. The fourth Stokes parameter, V, characterizing the degree of ellipticity of the polarization, is assumed to be zero in this report, and polarization is considered to be only linear polarization. To summarize the above definitions, we list the following relationships:

$$I = I_l + I_r \tag{1}$$

$$U = (I_l - I_r)\tan 2X \tag{2}$$

It is sometimes useful to use an alternate parameter, Q, defined by:

$$Q = I_l - I_r \quad . \tag{3}$$

In terms of the above parameters, the degree of linear polarization, P, is given by:

$$P = \frac{\left(Q^2 + U^2\right)^{1/2}}{I} \tag{4}$$

In Chandrasekhar's solution to the problem of diffuse reflection and transmission, use is made of a scattering matrix $\underset{\sim}{S}(\tau_1 \; ; \mu, \varphi; \mu_o, \varphi_o)$, and a transmission matrix $\underset{\sim}{T}(\tau_1 \; ; \mu, \varphi; \mu_o, \varphi_o)$, such that the reflected and the transmitted intensities are given by

$$\vec{I}_s(0; +\mu, \varphi) = \frac{1}{4\mu} \underset{\sim}{S}(\tau_1; \mu, \varphi; \mu_o, \varphi_o) \; \vec{F}_o \tag{5}$$

and $$\vec{I}_s(\tau_1; -\mu, \varphi) = \frac{1}{4\mu} \underset{\sim}{T}(\tau_1; \mu, \varphi; \mu_o, \varphi_o) \; \vec{F}_o \tag{6}$$

The sign preceding μ is to distinguish the upward radiation field from the downward. $(+ \equiv \uparrow)$

$\mu_o \equiv \cos\theta_o$, θ_o = the zenith angle of the sun.

$\varphi_o \equiv$ the azimuth of the sun. It is convenient to let $\varphi_o = 0$.

For convenience, it is customary to assume that parallel radiation of flux πF_o per unit area normal to the beam is incident on the top of the atmosphere. For simplicity, F_o is taken to be unity. Using the Stokes parameter representation $\vec{F}_o$ assumes the form

$$\begin{bmatrix} 1/2 \\ 1/2 \\ 0 \end{bmatrix} .$$

The presence of a ground with known reflecting properties will augment the standard case solution by an increase in the emergent intensity due to the presence of ground reflected light. More specifically, if $\vec{I}^*(0;\mu,\varphi)$ represents the emergent intensity in the presence of a ground, then

$$\vec{I}^*(0;\mu,\varphi)=\vec{I}_s(0;\mu,\varphi)+\vec{I}_g(\tau_1;\mu,\varphi)\, e^{-\tau_1/\mu} + \frac{1}{4\pi\mu}\int_0^1\int_0^{2\pi} \underset{\sim}{T}(\tau_1;\mu,\varphi;\mu',\varphi')\vec{I}_g(\mu',\varphi')\, d\mu'\, d\varphi' \quad (7)$$

Here $\vec{I}_g(\tau_1;\mu,\varphi)$ denotes the surface reflected radiation at the ground in the direction given by (μ,φ). The second term on the right hand side of equation (7) represents the direct transmission through the atmosphere of the surface reflected radiation. The third term represents the contribution to the emergent intensity arising from the diffuse transmission of the surface reflected light. Since $\vec{I}_s(0;\mu,\varphi)$ has been tabulated for various values of $\tau_1(\lambda)$ by Coulson, Dave, and Sekera(1960),the problem is reduced essentially to determining $\vec{I}_g(\tau_1;\mu,\varphi)$. The integration appearing in the third term is awkward, but straightforward. We concern ourselves then, with a determination of $\vec{I}_g(\tau_1;\mu,\varphi)$.

The surface reflected intensity, $\vec{I}_g(\tau_1;\mu,\varphi)$ must be related to the normal incident flux per unit area of surface. If $\vec{F}^{(inc)} = \begin{bmatrix} F_l^{(inc)} \\ F_r^{(inc)} \\ F_U^{(inc)} \end{bmatrix}$

represents this incident flux, then ideally one would wish to determine a global reflection matrix $\underset{\sim}{R}(\tau_1;\mu_o,\varphi;\mu,\varphi)$ such that:

$$\vec{I}_g(\tau_1;\mu,\varphi) = \underset{\sim}{R}(\tau_1;\mu_o,\varphi_o;\mu,\varphi)\ \vec{F}^{(inc)}\ . \tag{8}$$

The word global is used to signify that the components of $\underset{\sim}{R}$, say r_{ij}, i, j = 1, 2, 3, are functions of μ_o, μ, and φ such that if any desired values of these direction parameters are inserted in the expressions for r_{ij}, the appropriate values for $\vec{I}_g(\tau_1;\mu,\varphi)$ are obtained. In opposition to this reflection matrix formulation, our measurements procedure could be termed a local one. More specifically, for a fixed μ_o, μ, and φ, one determines a directional reflectance ρ, degree of polarization, P, and the angle χ, the orientation of the plane of polarization with respect to the vertical. The significance of ρ is that it is the scalar ratio of the intensity reflected into the μ,φ direction to the total flux incident on the surface. For a given surface, wavelength, and sun zenith angle, ρ may depend not only on the direction parameters μ and φ, but on the state of polarization of the incident flux as well. However, for brevity, we shall write $\rho(\mu,\varphi)$, and mean that the value of ρ so written is to have relevance for the incident flux at which the measurement was made. We have in mind here a distinction between measurements made in sunlight as opposed to laboratory measurements. More will be said about this later when discussing the approximation scheme that was used in connection with incorporating the laboratory measurements into the computations. We assume, for the present discussion, that ρ, P, and χ are determined in the presence of an atmosphere so that sky-light effects are included in the incident flux.

Before proceeding, we show how $\vec{I}_g(\tau_1;\mu,\varphi)$ may be determined from $\rho(\mu,\varphi)$, $P(\mu,\varphi)$, and $\chi(\mu,\varphi)$. Let $\vec{I}_g(\tau_1;\mu,\varphi) = \begin{bmatrix} I_{lg}(\tau_1;\mu,\varphi) \\ I_{rg}(\tau_1;\mu,\varphi) \\ U_g(\tau_1;\mu,\varphi) \end{bmatrix}$;

further, let $I_g(\tau_1;\mu,\varphi) = I_{lg}(\tau_1;\mu,\varphi) + I_{rg}(\tau_1;\mu,\varphi)$, $Q_g(\tau_1;\mu,\varphi) = I_{lg}(\tau_1;\mu,\varphi) - I_{rg}(\tau_1;\mu,\varphi)$, and $F^{(inc)} = F_l^{(inc)} + F_r^{(inc)}$.

Then: $$I_g(\tau_1;\mu,\varphi) = \rho(\mu,\varphi)\, F^{(inc)} \tag{9}$$

and $$P(\mu,\varphi) = \frac{\left\{Q_g^2(\mu,\varphi) + U_g^2(\mu,\varphi)\right\}^{1/2}}{I_g(\mu,\varphi)} \tag{10}$$

(We have dropped the τ_1 dependence in (10))

Since $U_g(\mu,\varphi) = Q_g(\mu,\varphi)\tan 2\chi(\mu,\varphi)$,

$$\left\{Q_g^2(\mu,\varphi) + U_g^2(\mu,\varphi)\right\}^{1/2} = Q_g(\mu,\varphi)\sec 2\chi(\mu,\varphi) = \left\{I_{lg}(\mu,\varphi) - I_{rg}(\mu,\varphi)\right\}\sec 2\chi(\mu,\varphi),$$

and $$P(\mu,\varphi)\, I_g(\mu,\varphi) = \left\{I_{lg}(\mu,\varphi) - I_{rg}(\mu,\varphi)\right\}\sec 2\chi(\mu,\varphi)$$

or $$P(\mu,\varphi)\, I_g(\mu,\varphi)\cos 2\chi(\mu,\varphi) = I_g(\mu,\varphi) - 2\, I_{rg}(\mu,\varphi).$$

Solving for $I_{rg}(\mu,\varphi)$, and substituting $I_g(\mu,\varphi) = \rho(\mu,\varphi)\, F^{(inc)}$,

we have

$$I_{rg}(\mu,\varphi) = \tfrac{1}{2}\rho(\mu,\varphi)\, F^{(inc)}\left\{1 - P(\mu,\varphi)\cos 2\chi(\mu,\varphi)\right\} \tag{11}$$

$$I_{lg}(\mu,\varphi) = \tfrac{1}{2}\rho(\mu,\varphi)\, F^{(inc)}\left\{1 + P(\mu,\varphi)\cos 2\chi(\mu,\varphi)\right\} \tag{12}$$

$$U_g(\mu,\varphi) = \left\{I_{lg}(\mu,\varphi) - I_{rg}(\mu,\varphi)\right\}\tan 2\chi(\mu,\varphi) \tag{13}$$

The problem is now reduced to that of determining $F^{(inc)}$. We shall actually find expressions for $\vec{F}^{(inc)}$.

$\vec{F}^{(inc)}$ is composed of three parts:

(1) the directly transmitted solar flux. The expression for this term is

$$\mu_0 \pi \vec{F}_0 \, e^{-\tau_1/\mu_0} = \mu_0 \pi \, e^{-\tau_1/\mu_0} \begin{bmatrix} 1/2 \\ 1/2 \\ 0 \end{bmatrix} \tag{14}$$

(2) the flux due to the diffusely transmitted intensity, $\vec{I}(\tau_1; -\mu, \varphi)$. The expression for this term is

$$\int_0^1 \int_0^{2\pi} \vec{I}(\tau_1; -\mu, \varphi) \, \mu \, d\mu \, d\varphi = \frac{1}{4} \int_0^1 \int_0^{2\pi} \vec{F}_0 \, \underset{\sim}{T}(\tau_1; \mu, \varphi; \mu_0, \varphi_0) \, d\mu \, d\varphi \tag{15}$$

(3) the flux due to the scattering by the atmosphere of the surface reflected light. The expression for this term is $\int_0^1 \int_0^{2\pi} \vec{I}_g^{(ref)}(-\mu, \varphi) \, \mu \, d\mu \, d\varphi$ (16)

where $\vec{I}_g^{(ref)}(-\mu, \varphi)$ is the intensity in the $(-\mu, \varphi)$ direction which has arisen as a consequence of the scattering by the atmosphere of ground reflected light. The expression for $\vec{I}_g^{(ref)}(-\mu, \varphi)$ is given by

$$\frac{1}{4\pi\mu} \int_0^1 \int_0^{2\pi} \underset{\sim}{S}(\tau_1; \mu, \varphi; \mu', \varphi') \, \vec{I}_g(\mu', \varphi') \, d\mu' \, d\varphi' \tag{17}$$

Substituting (17) into (16), the third term may be written as

$$\frac{1}{4\pi} \int_0^1 \int_0^{2\pi} \left\{ \int_0^1 \int_0^{2\pi} \underset{\sim}{S}(\tau_1; \mu, \varphi; \mu', \varphi') \, \vec{I}_g(\mu', \varphi') \, d\mu' \, d\varphi' \right\} d\mu \, d\varphi \tag{18}$$

Collecting the above, we have:

$$\vec{F}^{(inc)} = \begin{bmatrix} F_l^{(inc)} \\ F_r^{(inc)} \\ F_U^{(inc)} \end{bmatrix} = \mu_0 \pi \, e^{-\tau_1/\mu_0} \begin{bmatrix} \frac{1}{2} \\ \frac{1}{2} \\ 0 \end{bmatrix} +$$

$$+ \frac{1}{4} \int_0^1 \int_0^{2\pi} \underset{\sim}{T}(\tau_1; \mu, \varphi; \mu_0, \varphi_0) \begin{bmatrix} \frac{1}{2} \\ \frac{1}{2} \\ 0 \end{bmatrix} d\mu \, d\varphi \quad +$$

$$+\frac{1}{4\pi}\int_0^1\int_0^{2\pi}\int_0^1\int_0^{2\pi} \underset{\sim}{S}(\tau_1;\mu,\varphi;\mu',\varphi')\begin{bmatrix} I_{lg}(\mu',\varphi') \\ I_{rg}(\mu',\varphi') \\ U_g(\mu',\varphi')\end{bmatrix} d\mu'\, d\varphi'\, d\mu\, d\varphi \tag{19}$$

The first and second terms on the right hand side do not depend on the characteristics of the surface, and their evaluation is immediate in terms of the γ functions introduced by Chandrasekhar (1950) equations(226) and (227), Chap. X. The γ functions have been tabulated by Sekera and collaborators (1952, 53) for several values of τ_1 (λ). In terms of them, we have:

$$\mu_0 \pi e^{-\tau_1/\mu_0}\begin{bmatrix}\frac{1}{2}\\ \frac{1}{2}\\ 0\end{bmatrix} + \frac{1}{4}\int_0^1\int_0^{2\pi} \underset{\sim}{T}(\tau_1;\mu,\varphi;\mu_0,\varphi_0)\begin{bmatrix}\frac{1}{2}\\ \frac{1}{2}\\ 0\end{bmatrix} d\mu\, d\varphi = \frac{\pi\mu_0}{2}\begin{bmatrix}\gamma_l(\mu_0)\\ \gamma_r(\mu_0)\\ 0\end{bmatrix} \tag{20}$$

In considering the third term, it is worthwhile to look at the matrix $S(\tau_1;\mu,\varphi;\mu',\varphi')$ in some detail. We use the notation of Chandrasekhar:

$$\underset{\sim}{S}(\mu,\varphi;\mu',\varphi') = \underset{\sim}{Q}\left[\frac{3}{4}\underset{\sim}{S}^{(0)}(\mu,\mu') + (1-\mu^2)^{1/2}(1-\mu'^2)^{1/2}\,\underset{\sim}{S}^{(1)}(\mu,\varphi;\mu',\varphi') + \underset{\sim}{S}^{(2)}(\mu,\varphi;\mu',\varphi')\right] \tag{21}$$

where $\underset{\sim}{Q} = \begin{bmatrix} 1 & 0 & 0\\ 0 & 1 & 0\\ 0 & 0 & 2\end{bmatrix}$,

$\underset{\sim}{S}^{(0)}(\mu,\mu')$ is given in terms of the so-called scattering functions: $\psi, \phi, \chi, \zeta, \xi, \eta, \sigma$, and θ. These functions can be expressed in terms of the X and Y functions, which play an important role in the theory. The functions X and Y depend on τ_1 and μ. The particular form for $\underset{\sim}{S}^{(0)}(\mu,\mu')$ is given by:

$$\left(\frac{1}{\mu'}+\frac{1}{\mu}\right)\underset{\sim}{S}^{(0)}(\mu,\mu') = \begin{bmatrix}\psi(\mu) & \sqrt{2}\,\phi(\mu) & 0\\ \chi(\mu) & \sqrt{2}\,\zeta(\mu) & 0\\ 0 & 0 & 0\end{bmatrix}\begin{bmatrix}\psi(\mu') & \chi(\mu') & 0\\ \sqrt{2}\,\phi(\mu') & \sqrt{2}\,\zeta(\mu') & 0\\ 0 & 0 & 0\end{bmatrix} - \begin{bmatrix}\xi(\mu) & \sqrt{2}\,\eta(\mu) & 0\\ \sigma(\mu) & \sqrt{2}\,\theta(\mu) & 0\\ 0 & 0 & 0\end{bmatrix}\begin{bmatrix}\xi(\mu') & \sigma(\mu') & 0\\ \sqrt{2}\,\eta(\mu') & \sqrt{2}\,\theta(\mu') & 0\\ 0 & 0 & 0\end{bmatrix} \tag{22}$$

We shall write:

$$\underset{\sim}{S}^{(0)}(\mu,\mu') = \begin{bmatrix} S_{11}^{(0)}(\mu,\mu') & S_{1r}^{(0)}(\mu,\mu') & 0 \\ S_{rl}^{(0)}(\mu,\mu') & S_{rr}^{(0)}(\mu,\mu') & 0 \\ 0 & 0 & 0 \end{bmatrix} \tag{23}$$

$\underset{\sim}{S}^{(1)}(\mu,\varphi;\mu',\varphi')$ and $\underset{\sim}{S}^{(2)}(\mu,\varphi;\mu',\varphi')$ are given by:

$$\left(\frac{1}{\mu'}+\frac{1}{\mu}\right)\underset{\sim}{S}^{(i)}(\mu,\varphi;\mu',\varphi') = \left[X^{(i)}(\mu)\,X^{(i)}(\mu') - Y^{(i)}(\mu)\,Y^{(i)}(\mu')\right]\underset{\sim}{P}^{(i)}(\mu,\varphi;-\mu',\varphi')$$

$$i = 1, 2 \tag{24}$$

where

$$P^{(1)}(\mu,\varphi;-\mu',\varphi') = \frac{3}{4}\begin{bmatrix} -4\mu\mu'\cos(\varphi'-\varphi) & 0 & 2\mu\sin(\varphi'-\varphi) \\ 0 & 0 & 0 \\ 2\mu'\sin(\varphi'-\varphi) & 0 & \cos(\varphi'-\varphi) \end{bmatrix} \tag{25}$$

$$P^{(2)}(\mu,\varphi;-\mu',\varphi') = \frac{3}{4}\begin{bmatrix} \mu^2\mu'^2\cos 2(\varphi'-\varphi) & -\mu^2\cos 2(\varphi'-\varphi) & -\mu^2\mu'\sin 2(\varphi'-\varphi) \\ -\mu'^2\cos 2(\varphi'-\varphi) & \cos 2(\varphi'-\varphi) & \mu'\sin 2(\varphi'-\varphi) \\ -\mu\mu'^2\sin 2(\varphi'-\varphi) & \mu\sin 2(\varphi'-\varphi) & -\mu\mu'\cos 2(\varphi'-\varphi) \end{bmatrix} \tag{26}$$

We shall write:

$$(1-\mu^2)^{1/2}(1-\mu'^2)^{1/2}\underset{\sim}{S}^{(1)}(\mu,\varphi;\mu',\varphi') = \begin{bmatrix} S_{11}^{(1)}(\mu,\mu')\cos(\varphi'-\varphi) & 0 & S_{13}^{(1)}(\mu,\mu')\sin(\varphi'-\varphi) \\ 0 & 0 & 0 \\ S_{31}^{(1)}(\mu,\mu')\sin(\varphi'-\varphi) & 0 & S_{33}^{(1)}(\mu,\mu')\cos(\varphi'-\varphi) \end{bmatrix} \tag{27}$$

$$\underset{\sim}{S}^{(2)}(\mu,\varphi;\mu',\varphi') = \begin{bmatrix} S_{11}^{(2)}(\mu,\mu')\cos 2(\varphi'-\varphi) & S_{12}^{(2)}(\mu,\mu')\cos 2(\varphi'-\varphi) & S_{13}^{(2)}(\mu,\mu')\sin 2(\varphi'-\varphi) \\ S_{21}^{(2)}(\mu,\mu')\cos 2(\varphi'-\varphi) & S_{22}^{(2)}(\mu,\mu')\cos 2(\varphi'-\varphi) & S_{23}^{(2)}(\mu,\mu')\sin 2(\varphi'-\varphi) \\ S_{31}^{(2)}(\mu,\mu')\sin 2(\varphi'-\varphi) & S_{32}^{(2)}(\mu,\mu')\sin 2(\varphi'-\varphi) & S_{33}^{(2)}(\mu,\mu')\cos 2(\varphi'-\varphi) \end{bmatrix} \tag{28}$$

For convenience, we collect the above terms and write:

$$\underset{\sim}{S}(\tau_1;\mu,\varphi;\mu',\varphi') = \begin{bmatrix} s_{11} & s_{12} & s_{13} \\ s_{21} & s_{22} & s_{23} \\ s_{31} & s_{32} & s_{33} \end{bmatrix} , \tag{29}$$

where the explicit formulae for s_{ij}, i, j = 1, 2, 3 are:

$$s_{11} = 3/4\, S_{11}^{(0)}(\mu,\mu') + S_{11}^{(1)}(\mu,\mu') \cos(\varphi'-\varphi) + S_{11}^{(2)}(\mu,\mu') \cos 2(\varphi'-\varphi)$$
$$s_{12} = 3/4\, S_{1r}^{(0)}(\mu,\mu') + S_{12}^{(2)}(\mu,\mu') \cos 2(\varphi'-\varphi)$$
$$s_{13} = S_{13}^{(1)}(\mu,\mu') \sin(\varphi'-\varphi) + S_{13}^{(2)}(\mu,\mu') \sin 2(\varphi'-\varphi)$$
$$s_{21} = 3/4\, S_{r1}^{(0)}(\mu,\mu') + S_{21}^{(2)}(\mu,\mu') \cos 2(\varphi'-\varphi)$$
$$s_{22} = 3/4\, S_{rr}^{(0)}(\mu,\mu') + S_{22}^{(2)}(\mu,\mu') \cos 2(\varphi'-\varphi)$$
$$s_{23} = S_{23}^{(2)}(\mu,\mu') \sin 2(\varphi'-\varphi)$$
$$s_{31} = 2\, S_{31}^{(1)}(\mu,\mu') \sin(\varphi'-\varphi) + 2\, S_{31}^{(2)}(\mu,\mu') \sin 2(\varphi'-\varphi)$$
$$s_{32} = 2\, S_{32}^{(2)}(\mu,\mu') \sin 2(\varphi'-\varphi)$$
$$s_{33} = 2\, S_{33}^{(1)}(\mu,\mu') \cos(\varphi'-\varphi) + 2\, S_{33}^{(2)}(\mu,\mu') \cos 2(\varphi'-\varphi)$$

The integral in equation (19) may then be written:

$$\frac{1}{4\pi}\int_0^1\int_0^{2\pi}\int_0^1\int_0^{2\pi}\left\{s_{11}\, I_{lg}(\mu',\varphi') + s_{12}\, I_{rg}(\mu',\varphi') + s_{13}\, U_g(\mu',\varphi')\right\} d\mu'\, d\varphi'\, d\mu\, d\varphi \tag{30}$$

$$\frac{1}{4\pi}\int_0^1\int_0^{2\pi}\int_0^1\int_0^{2\pi}\left\{s_{21}\, I_{lg}(\mu',\varphi') + s_{22}\, I_{rg}(\mu',\varphi') + s_{23}\, U_g(\mu',\varphi')\right\} d\mu'\, d\varphi'\, d\mu\, d\varphi \tag{31}$$

$$\frac{1}{4\pi}\int_0^1\int_0^{2\pi}\int_0^1\int_0^{2\pi}\left\{s_{31}\, I_{lg}(\mu',\varphi') + s_{32}\, I_{rg}(\mu',\varphi') + s_{33}\, U_g(\mu',\varphi')\right\} d\mu'\, d\varphi'\, d\mu\, d\varphi \tag{32}$$

These terms represent contributions to $F_l^{(inc)}$, $F_r^{(inc)}$, and $F_U^{(inc)}$, respectively. It appears that these expressions may be considerably simplified by performing the integration over φ first. The components I_{lg}, I_{rg}, and U_g

have no φ dependence, and the s_{ij} functions have a simple cos, sin relationship. Only the components s_{ij}, i, j = 1, 2 will have a non-zero contribution. In particular, the contribution to $F_U^{(inc)}$ is zero.

Performing the integrations over φ, we have:

$$\frac{3}{8}\int_0^1\int_0^{2\pi}\int_0^1 \left\{ S_{\ell\ell}^{(o)}(\mu,\mu') I_{\ell g}(\mu',\varphi') + S_{\ell r}^{(o)}(\mu,\mu') I_{rg}(\mu',\varphi') \right\} d\mu' d\varphi' d\mu \tag{30}$$

$$\frac{3}{8}\int_0^1\int_0^{2\pi}\int_0^1 \left\{ S_{r\ell}^{(o)}(\mu,\mu') I_{\ell g}(\mu',\varphi') + S_{rr}^{(o)}(\mu,\mu') I_{rg}(\mu',\varphi') \right\} d\mu' d\varphi' d\mu \tag{31}$$

Combining this result with equation (20), we have:

$$F_\ell^{(inc)} = \frac{\pi\mu_0}{2}\gamma_\ell(\mu_0) + \frac{3}{8}\int_0^1\int_0^{2\pi}\int_0^1 \left\{ S_{\ell\ell}^{(o)}(\mu,\mu') I_{\ell g}(\mu',\varphi') + S_{\ell r}^{(o)}(\mu,\mu') I_{rg}(\mu',\varphi') \right\} d\mu' d\varphi' d\mu \tag{33}$$

$$F_r^{(inc)} = \frac{\pi\mu_0}{2}\gamma_r(\mu_0) + \frac{3}{8}\int_0^1\int_0^{2\pi}\int_0^1 \left\{ S_{r\ell}^{(o)}(\mu,\mu') I_{\ell g}(\mu',\varphi') + S_{rr}^{(o)}(\mu,\mu') I_{rg}(\mu',\varphi') \right\} d\mu' d\varphi' d\mu \tag{34}$$

$$F_U^{(inc)} = 0 \tag{35}$$

Returning to equations (11) and (12), and remembering that $F^{(inc)} = F_l^{(inc)} + F_r^{(inc)}$, we then have an integral equation for I_{lg} and I_{rg}. If one wished, the triple integral in equations (33) and (34) could be reduced to a double integral by defining:

$s_{11}(\mu') = 3/8 \int_0^1 S_{11}^{(0)}(\mu,\mu') \, d\mu$, $\quad s_{1r}(\mu') = 3/8 \int_0^1 S_{1r}^{(0)}(\mu,\mu') \, d\mu$

$s_{rl}(\mu') = 3/8 \int_0^1 S_{rl}^{(0)}(\mu,\mu') \, d\mu$, and $s_{rr}(\mu') = 3/8 \int_0^1 S_{rr}^{(0)}(\mu,\mu') \, d\mu$.

Equations (11), (12), (33), and (34) represent the solution for the inclusion of a "real" ground.

B. Approximations Used

At this juncture we take cognizance of the fact that the measurements of ρ, P, and χ were performed in the laboratory. Because of the preceding remarks that these measurements may depend on the sky light effects, etc. it was decided to apply the measurements to the directly incident flux, $\pi\mu_o\vec{F}_o\ e^{-\tau_1/\mu_o}$. One could then use the distinction between direct and diffuse transmission, and the following streams of radiation emerge as a natural consequence:

(1) I_{DD} $\equiv$ that contribution to the emergent radiation which consists of light which was transmitted directly downward through the atmosphere, reflected, and transmitted directly outward through the atmosphere.

(2) I_{Dd} $\equiv$ that contribution to the emergent radiation which consists of light which was transmitted directly downward through the atmosphere, reflected, and transmitted diffusely outward through the atmosphere.

(3) I_{dD} $\equiv$ that contribution to the emergent radiation which consists of light which was transmitted diffusely downward through the atmosphere, reflected, and transmitted directly outward through the atmosphere.

(4) I_{dd} $\equiv$ that contribution to the emergent radiation which consists of light which was transmitted diffusely downward through the atmosphere, reflected, and transmitted diffusely outward through the atmosphere.

Clearly the laboratory measurements could be applied to the first and second components, since they originate from directly incident flux. The question arises as to what approximations to make for the computations of components (3) and (4). It was decided that for these components, the ground would be considered a Lambert Surface reflecting with an albedo $\bar{R}$, given by $\int_0^1 \int_0^{2\pi} \rho(\mu, \varphi)\, \mu\, d\mu\, d\varphi$. This is probably not a bad assumption.

These two components tend to be rather small, and the hemispheric integration tends to smooth out the directional dependence. The diffusely incident flux then, needed for components (3) and (4), is the total incident flux in the presence of a Lambert surface less the directly incident flux. This total incident flux can be derived from equations (33) and (34). The flux expression is given by Chandrasekhar, equation (231), Chap. X). In (33) and (34), let $I_{lg}(\mu', \varphi') = I_{rg}(\mu', \varphi') = 1/2\, I_g$, and independent of direction. Integrating over φ', we have:

$$F_l^{(inc)} = \frac{\pi\mu_0}{2} \gamma_l(\mu_0) + \frac{3\pi I_g}{8} \int_0^1\int_0^1 \left\{ S_{ll}^{(0)}(\mu,\mu') + S_{lr}^{(0)}(\mu,\mu') \right\} d\mu'\, d\mu \tag{36}$$

$$F_r^{(inc)} = \frac{\pi\mu_0}{2} \gamma_r(\mu_0) + \frac{3\pi I_g}{8} \int_0^1\int_0^1 \left\{ S_{rl}^{(0)}(\mu,\mu') + S_{rr}^{(0)}(\mu,\mu') \right\} d\mu'\, d\mu \tag{37}$$

define

$$S_l(\mu) = \frac{3}{8}\int_0^1 \left\{ S_{ll}^{(0)}(\mu,\mu') + S_{lr}^{(0)}(\mu,\mu') \right\} d\mu' \tag{38}$$

$$S_r(\mu) = \frac{3}{8}\int_0^1 \left\{ S_{rl}^{(0)}(\mu,\mu') + S_{rr}^{(0)}(\mu,\mu') \right\} d\mu' \tag{39}$$

Then

$$F_l^{(inc)} = \frac{\pi\mu_0}{2} \gamma_l(\mu_0) + \pi I_g \int_0^1 S_l(\mu)\, d\mu \tag{40}$$

$$F_r^{(inc)} = \frac{\pi\mu_0}{2} \gamma_r(\mu_0) + \pi I_g \int_0^1 S_r(\mu)\, d\mu \tag{41}$$

Finally, letting ,

$$\bar{S} = \int_0^1 \left\{ S_l(\mu) + S_r(\mu) \right\} d\mu$$

$$(I_{DD})_r(0;\mu,\varphi) = \frac{1}{2}\rho(\mu,\varphi)\pi\mu_0 e^{-\tau_1/\mu_0} e^{-\tau_1/\mu}\{1 - P(\mu,\varphi)\cos 2\chi\} \tag{47}$$

$$(I_{DD})_U(0;\mu,\varphi) = \{(I_{DD})_\ell - (I_{DD})_r\}\tan 2\chi \tag{48}$$

In the actual calculations, the angle χ was not measured with great accuracy. Gross measurements seemed to indicate that the plane of polarization was roughly oriented perpendicular to the scattering plane. This was adopted as a convention, thus enabling one to compute χ from the geometry.

(2) $\vec{I}_{Dd}(0;\mu,\varphi)$.

This component was computed as in equation (7).

i.e. $$\vec{I}_{Dd}(0;\mu,\varphi) = \frac{1}{4\pi\mu}\int_0^1\int_0^{2\pi} \underset{\sim}{T}(\tau_1;\mu,\varphi;\mu',\varphi')\,\vec{I}_g(\mu',\varphi')\,d\mu'\,d\varphi'$$

The components $I_{lg}(\mu',\varphi')$, $I_{rg}(\mu',\varphi')$ and $U_g(\mu',\varphi')$ were computed from (11), (12), and (13). The integration was performed using a Gaussian quadrature with 6 values of μ' and 16 values of φ'.

(3) $I_{dD}(0;\mu)$

In the third and fourth components, only the scalar value of intensity was computed. The amount of polarization, characterized by the difference in the γ functions is very small and was neglected. The relevant incident flux is given by equation (45). The reflected intensity per unit solid angle is given by $\frac{\bar{R}}{\pi}$ times this quantity. This reflected intensity is further attenuated an amount $e^{-\tau_1/\mu}$ in its direct outward traverse. The final expression is:

$$I_{dD}(0;\mu) \quad \bar{R}\mu_0\left[\frac{\gamma_\ell(\mu_0)+\gamma_r(\mu_0)}{2(1-\bar{R}\bar{s})} - e^{-\tau_1/\mu_0}\right]e^{-\tau_1/\mu} \tag{49}$$

we have,

$$F^{(inc)} = F_{\ell}^{(inc)} + F_{r}^{(inc)} = \pi\left[\frac{\mu_0\gamma_\ell(\mu_0)}{2} + \frac{\mu_0\gamma_r(\mu_0)}{2} + I_g\bar{s}\right] \tag{42}$$

This is equation (231) of Chandrasekhar. The function $\bar{s}$ (τ_1) has been tabulated by Sekera et al.(1952, 53). An expression for I_g can now be derived for the Lambert surface by an appeal to the definition of the albedo; $\bar{R} = \dfrac{F^{(out)}}{F^{(inc)}}$.

But $$F^{(out)} = \int_0^1\int_0^{2\pi} I_g\,\mu\,d\mu\,d\varphi = \pi I_g$$

Therefore $$\pi I_g = \bar{R}\pi\left[\frac{\mu_0}{2}\left\{\gamma_\ell(\mu_0) + \gamma_r(\mu_0)\right\} + \bar{s}\,I_g\right] ,$$

and $$I_g = \frac{\bar{R}\mu_0}{2(1-\bar{R}\bar{s})}\left\{\gamma_\ell(\mu_0) + \gamma_r(\mu_0)\right\} \tag{43}$$

Substituting (43) into (42), we have

$$F^{(inc)} = \frac{\pi\mu_0}{2(1-\bar{R}\bar{s})}\left\{\gamma_\ell(\mu_0) + \gamma_r(\mu_0)\right\} \tag{44}$$

The scalar diffusely incident flux is then

$$\frac{\pi\mu_0}{2(1-\bar{R}\bar{s})}\left\{\gamma_\ell(\mu_0) + \gamma_r(\mu_0)\right\} - \pi\mu_0 e^{-\tau_1/\mu_0}$$

$$= \pi\mu_0\left[\frac{\gamma_\ell(\mu_0) + \gamma_r(\mu_0)}{2(1-\bar{R}\bar{s})} - e^{-\tau_1/\mu_0}\right] \tag{45}$$

We can now list explicitly the expressions used for each of these various components.

(1) $\vec{I}_{DD}(0;\mu,\varphi)$.

The expressions needed have essentially been obtained in equations (11), (12), (13). We need only regard $F^{(inc)}$ to be $\pi\mu_0 e^{-\tau_1/\mu_0}$. Since the reflected intensity is attenuated an amount $e^{-\tau_1/\mu}$ in its outward traverse, we have

$$\left(I_{DD}\right)_\ell(0;\mu,\varphi) = \tfrac{1}{2}\rho(\mu,\varphi)\pi\mu_0 e^{-\tau_1/\mu_0} e^{-\tau_1/\mu}\left\{1 + P(\mu,\varphi)\cos 2\chi\right\} \tag{46}$$

(4) $I_{dd}(0;\mu)$

For this component, the reflected intensity per unit solid angle is also:

$$\bar{R}\mu_0 \left[\frac{\gamma_l(\mu_0) + \gamma_r(\mu_0)}{2(1-\bar{R}\bar{s})} - e^{-\tau_1/\mu_0} \right] \tag{50}$$

Let us denote the quantity given by (50) as I_{gd}. We need the diffuse transmission of this quantity through the outward hemisphere. Although we are considering only the scalar intensity, it is convenient to employ the matrix notation, since the final expression may be written in terms of the γ_l, γ_r functions which are tabulated. We have

$$\vec{I}_{dd}(0;\mu,\varphi) = \begin{bmatrix} (I_{dd})_l\,(0;\mu) \\ (I_{dd})_r\,(0;\mu) \\ 0 \end{bmatrix} = \frac{1}{4\pi\mu}\int_0^1\int_0^{2\pi} \underset{\sim}{T}(\tau_1;\mu,\varphi;\mu',\varphi') \begin{bmatrix} \frac{1}{2}I_{gd} \\ \frac{1}{2}I_{gd} \\ 0 \end{bmatrix} d\mu'\,d\varphi' \tag{51}$$

Then

$$(I_{dd})_l\,(0;\mu) = \frac{I_{gd}}{2\mu}\,\frac{3}{8}\int_0^1 \left\{ T_{ll}^{(0)}(\mu,\mu') + T_{lr}^{(0)}(\mu,\mu') \right\} d\mu' \tag{52}$$

$$(I_{dd})_r\,(0;\mu) = \frac{I_{gd}}{2\mu}\,\frac{3}{8}\int_0^1 \left\{ T_{rl}^{(0)}(\mu,\mu') + T_{rr}^{(0)}(\mu,\mu') \right\} d\mu' \tag{53}$$

The integrals in (52) and (53) are denoted by Chandrasekhar as follows:

$$t_l(\mu) = \frac{3}{8}\int_0^1 \left\{ T_{ll}^{(0)}(\mu,\mu') + T_{lr}^{(0)}(\mu,\mu') \right\} d\mu' \tag{54}$$

$$t_r(\mu) = \frac{3}{8}\int_0^1 \left\{ T_{rl}^{(0)}(\mu,\mu') + T_{rr}^{(0)}(\mu,\mu') \right\} d\mu' \tag{55}$$

The advantage, as far as we are concerned, is the relationship of the t functions to the tabulated γ functions. The relationship is given by equation (219), Chandrasekhar, Chap. X, as follows:

$$\gamma_l(\mu) = \frac{t_l(\mu)}{\mu} + e^{-\tau_1/\mu} \quad , \quad \gamma_r(\mu) = \frac{t_r(\mu)}{\mu} + e^{-\tau_1/\mu} \tag{56}$$

$$\Rightarrow \quad t_l(\mu) = \mu\left\{ \gamma_l(\mu) - e^{-\tau_1/\mu} \right\} \quad , \quad t_r(\mu) = \mu\left\{ \gamma_r(\mu) - e^{-\tau_1/\mu} \right\} \tag{57}$$

Substitution in (52) and (53), employing (54) and (55) yields:

$$(I_{dd})_\ell(0;\mu) = \frac{I_{gd}}{2}\left\{\gamma_\ell(\mu) - e^{-\tau_1/\mu}\right\} \tag{58}$$

$$(I_{dd})_r(0;\mu) = \frac{I_{gd}}{2}\left\{\gamma_r(\mu) - e^{-\tau_1/\mu}\right\} \tag{59}$$

The scalar intensity $I_{dd}(0;\mu)$ is then given by:

$$\frac{I_{gd}}{2}\left\{\gamma_\ell(\mu) + \gamma_r(\mu) - 2e^{-\tau_1/\mu}\right\} \tag{60}$$

Using (50), the final expression becomes:

$$I_{dd}(0;\mu) = \frac{\bar{R}\mu_0}{2}\left[\frac{\gamma_\ell(\mu_0)+\gamma_r(\mu_0)}{2(1-\bar{R}\bar{s})} - e^{-\tau_1/\mu_0}\right]\left[\gamma_\ell(\mu) + \gamma_r(\mu) - 2e^{-\tau_1/\mu}\right] \tag{61}$$

This concludes a derivation of the expressions used for the various components. The result is seen to be a mixture of experimentally measured values and pre-tabulated functions.

C. Calculations of Emergent Radiation for Selected Surfaces

1. Intensity

The following discussion will have two segments. The first section will deal with the intensity calculations for a Rayleigh atmosphere including the effects of surface reflection for a red clay surface and a white quartz sand surface. These results have been discussed previously in General Electric Technical Information Series R64SD74(1964). However, for the convenience of the reader, and for the sake of completeness, the discussion is essentially repeated here. In the figures now presented, slight deviations from the original figures appearing in the reference are apparent. They reflect the inclusion of component I_{dd}, which was not programmed at the time of the original draft, and the correction of a small error in the data handling process.

The second part will deal with intensity calculations with the surfaces being desert soil and green grass. These calculations were made in conjunction with the problem of contrast degradation by atmospheric transmission. For this purpose, the effects of a model aerosol were crudely approximated. Specific information about the model and the approximations made for its inclusion will be given. A copy of the paper, discussing the results of the contrast work, is included as an appendix.

a. Outward Radiation for Red Clay and White Quartz Sand

For purposes of these computations, an infinite plane surface of the selected material has been assumed to underlie a plane parallel Rayleigh model of the Earth's atmosphere.

(1) Results for Red Clay Surface

The relative intensities of the individual components, and of their sum, for the case of a red clay surface are shown, as a function of nadir angle in the principal plane, by the curves of Fig 66. The zenith angle of the source here is 53°, and the wavelength is 4920 Å, which corresponds to a normal optical thickness of $\tau_1 = 0.15$ for the Earth's atmosphere.

The well-known limb brightening which occurs for the I_s component dominates the picture at large nadir angles, but it rapidly decreases with decreasing angle and becomes equal to the I_{DD} component at $\theta = 62^{\circ}$ at both azimuths. At angles of $\theta < 62^{\circ}$, I_{DD} is greater than I_s, but never by a factor of more than two for this case. For the components I_{Dd} and I_{dd}, the

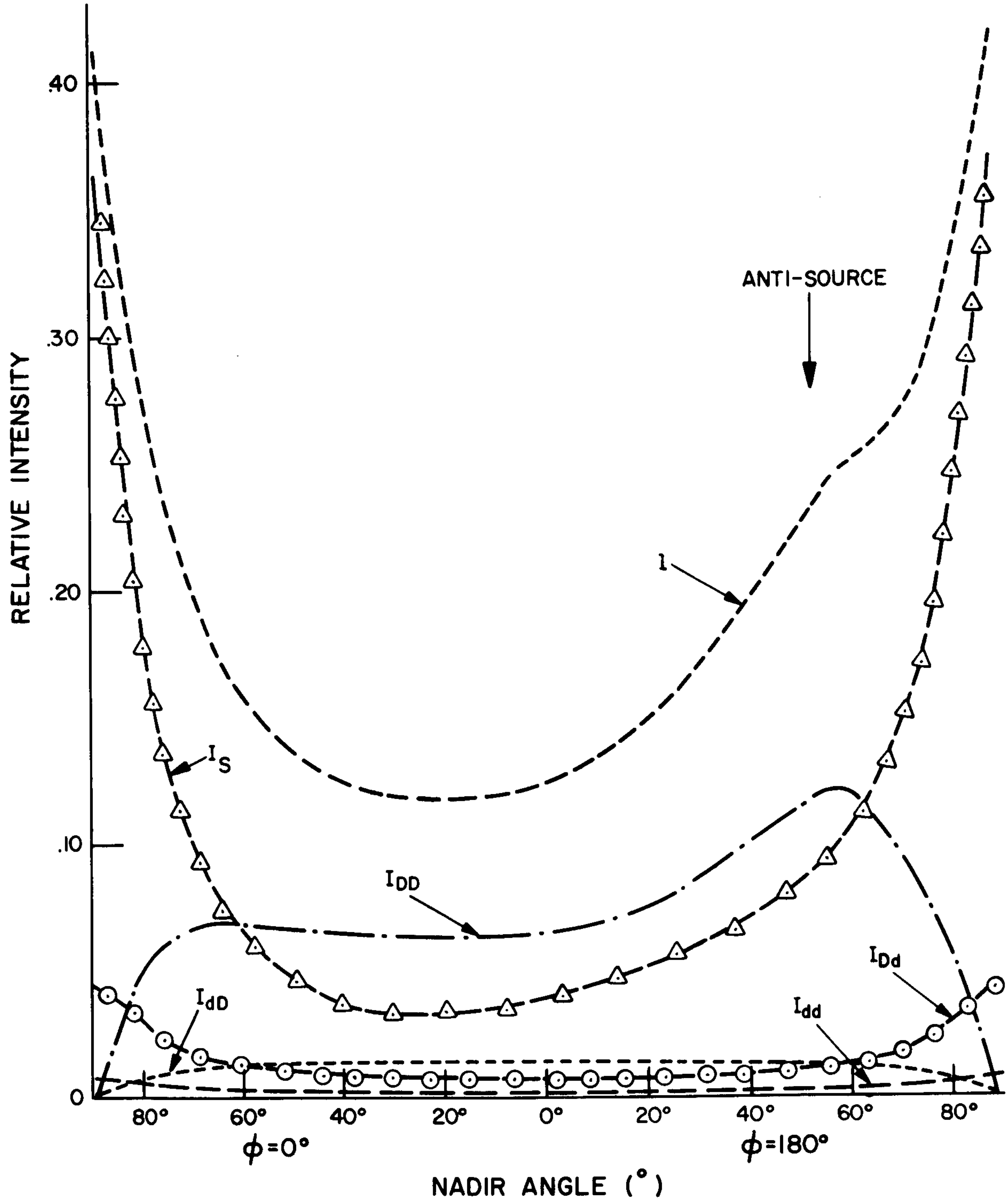

Fig. 66 Relative intensity of outward total radiation and of the individual components, as a function of nadir angle in the principal plane, for a red clay surface ($\theta_o = 53^o$, $\lambda = 4920 \AA$)

intensity values increase as θ increases. This is to be expected since they are diffusely transmitted outward through increasingly longer path lengths. Conversely I_{dD} decreases as θ increases, since the direct transmission is attenuated more for larger values of θ. It is seen that throughout a wide angular region surrounding the nadir direction, the sum of the four components in which surface reflection is involved dominates the outward radiant intensity in that region of the hemisphere.

A change of wavelength has a strong effect on both the total outward radiant intensity and the relative contributions of the various components. Fig. 67 shows the same surface, again for a sun zenith angle of 53°, but for a wavelength $\lambda = 6430$ Å, corresponding to a normal optical thickness of $\tau_1 = .05$. The total intensity is everywhere increased by a factor of at least 2, corresponding to an increase of component I_{DD}, which dominates the region $\theta < 80^{\circ}$.

(2) Results for a White Quartz Sand Surface

The relative intensities of the individual components and of their sum for the case of a white quartz sand surface are shown, as a function of nadir angle in the principal plane, for $\theta_o = 53^{\circ}$ and $\lambda = 4920$ Å, by the curves of Fig. 68 . The high reflectance of quartz sand at $\lambda = 4920$ Å makes the reflected components considerably greater here than in the case of red clay. For instance, the relative intensity of component I_{DD} in the nadir direction for white sand has a value of 0.187, while for clay it is only 0.066. While the regions at large nadir angles are still dominated by the limb-brightened I_s, the surface-reflected components, and particularly I_{DD}, dominate

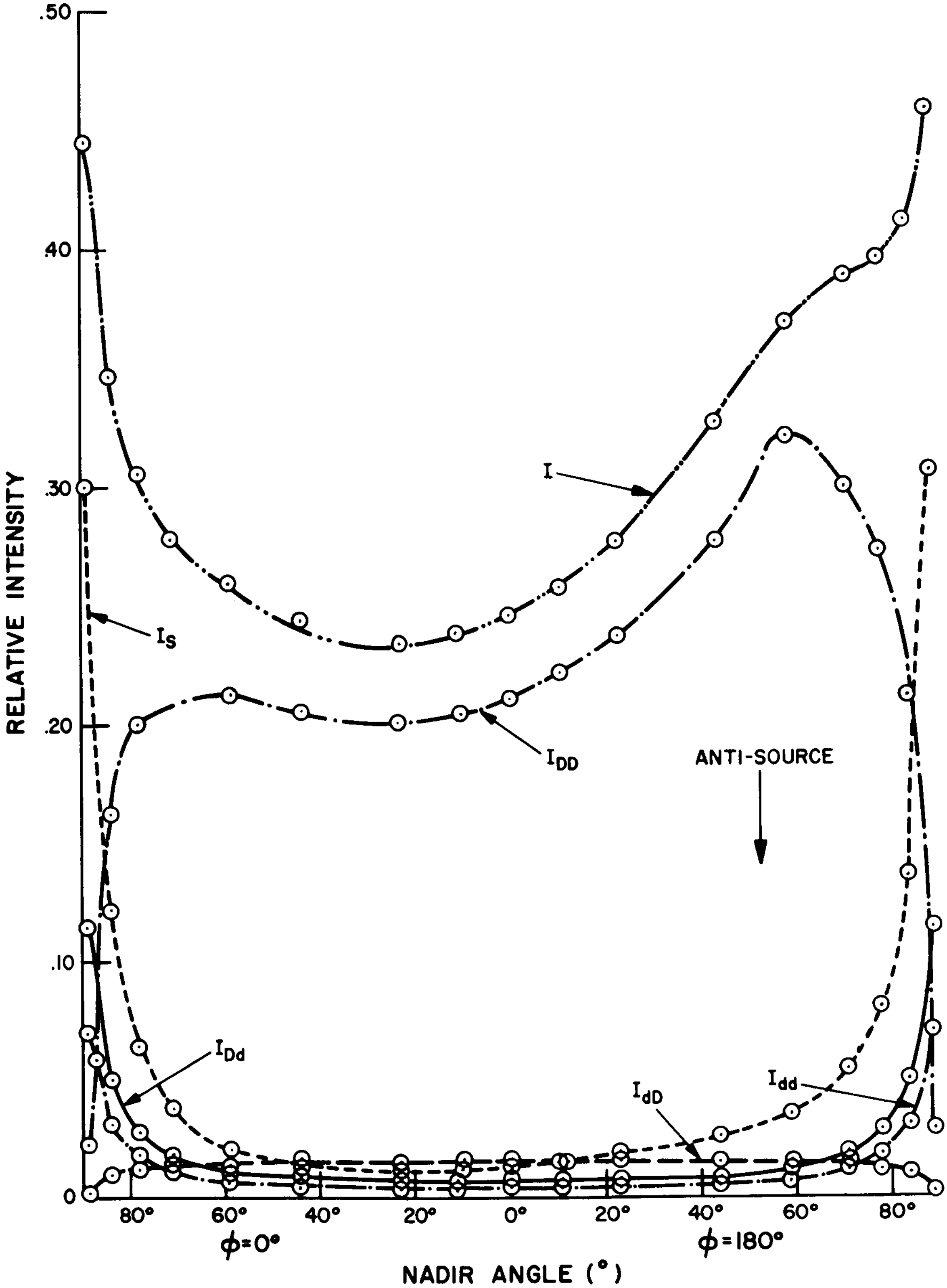

Fig. 67 Relative intensity of outward total radiation and of the individual components, as a function of nadir angle in the principal plane, for red clay surface ($\theta_o = 53^o$, $\lambda = 6430\text{Å}$)

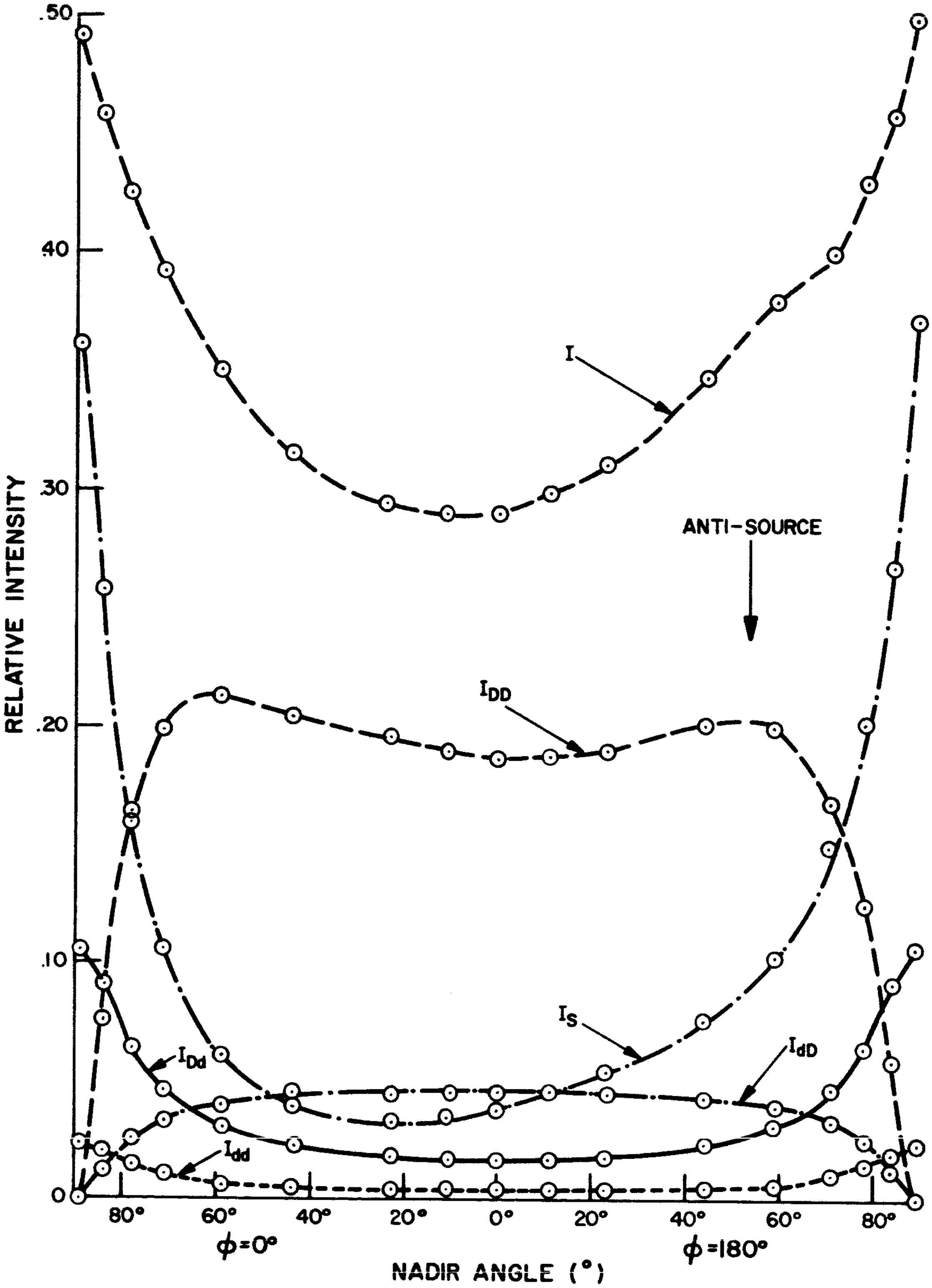

Fig. 68 Relative intensity of outward total radiation and of the individual components, as a function of nadir angle in the principal plane, for a white quartz sand surface ($\theta_o = 53^\circ$, $\lambda = 4920\text{Å}$)

the entire region of $\theta < 70^{\circ}$. The intensity pattern is more symmetrical around $\theta = 80^{\circ}$ here than for clay, a feature which is the result of a very symmetric reflection pattern for white sand.

Fig. 69 shows the relative intensities in the principal plane for white quartz sand at $\lambda = 6430$ Å and $\theta_o = 53^{\circ}$. The minor role played by atmospheric scattering at this longer wavelength is evident in the generally low values of all components except I_{DD} at $\theta < 80$. The high reflectance of quartz sand makes a high total intensity, which is contributed mostly by the I_{DD} component.

The case for white quartz sand at $\theta_o = 0^{\circ}$ and $\lambda = 6430$ Å is shown by Fig. 70. Since the reflectance is independent of azimuth for $\theta_o = 0^{\circ}$, the pattern over the whole hemisphere can be visualized by a rotation of these curves around the nadir. A pronounced brightness would exist in the vicinity of the nadir, with a gradual decrease of intensity out to $\theta = 60^{\circ}$. Beyond $\theta = 60^{\circ}$ the strong decrease of reflectance evident in I_{DD} more than compensates for the limb brightening of I_s, the resultant showing a very prounounced darkening at large nadir angles. The dominance of the component I_{DD} is obvious.

b. Outward Radiation for Desert Soil and Green Grass

In connection with calculations of contrast degradation by atmospheric transmission, the intensity of the emergent radiation was computed assuming the surface to be desert soil and green grass. More specifically, the following cases were considered:

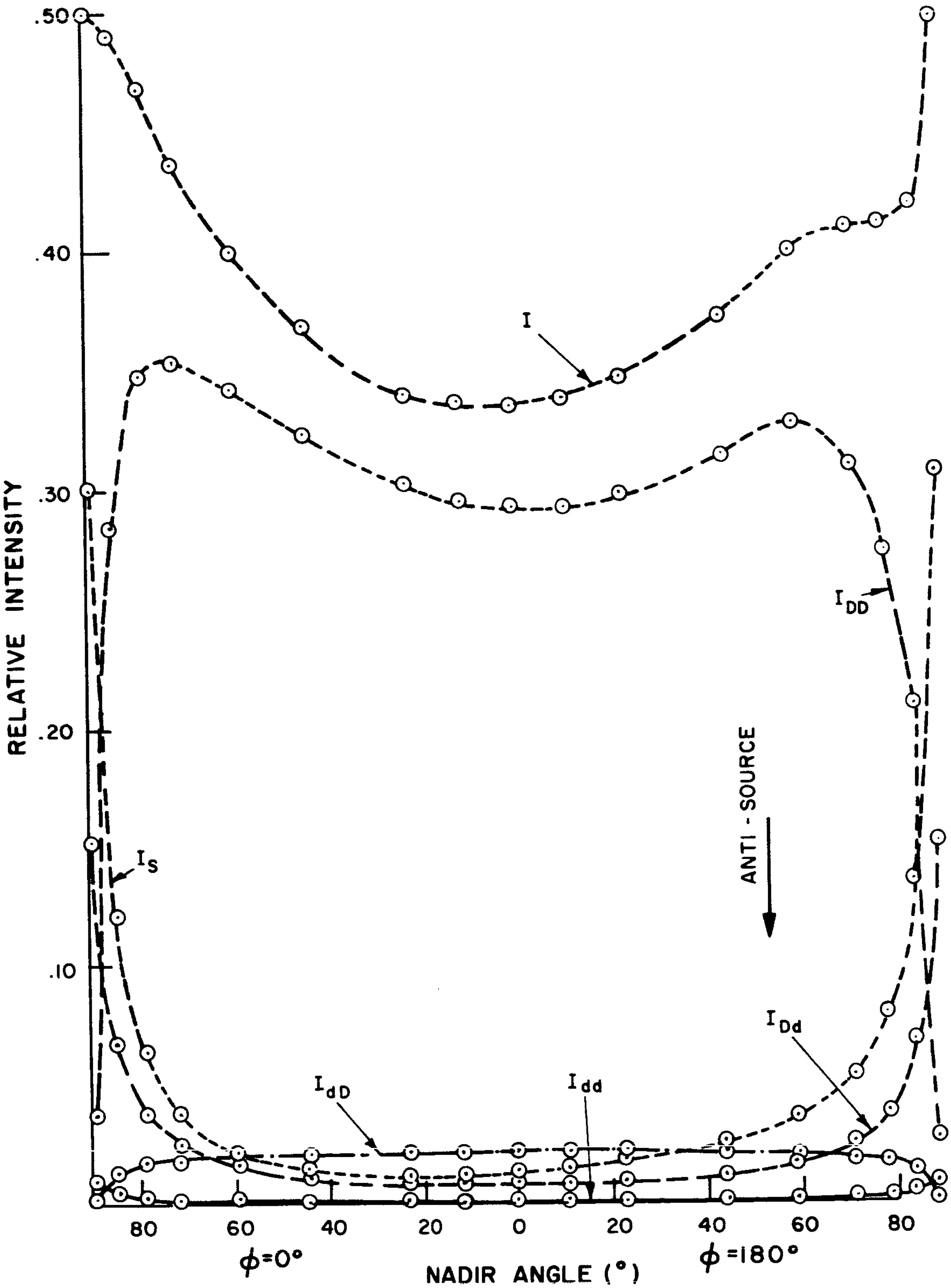

Fig. 69 Relative intensity of outward total radiation and of the individual components, as a function of nadir angle in the principal plane, for a white quartz sand surface (θ_o = 53°, λ = 6430Å)

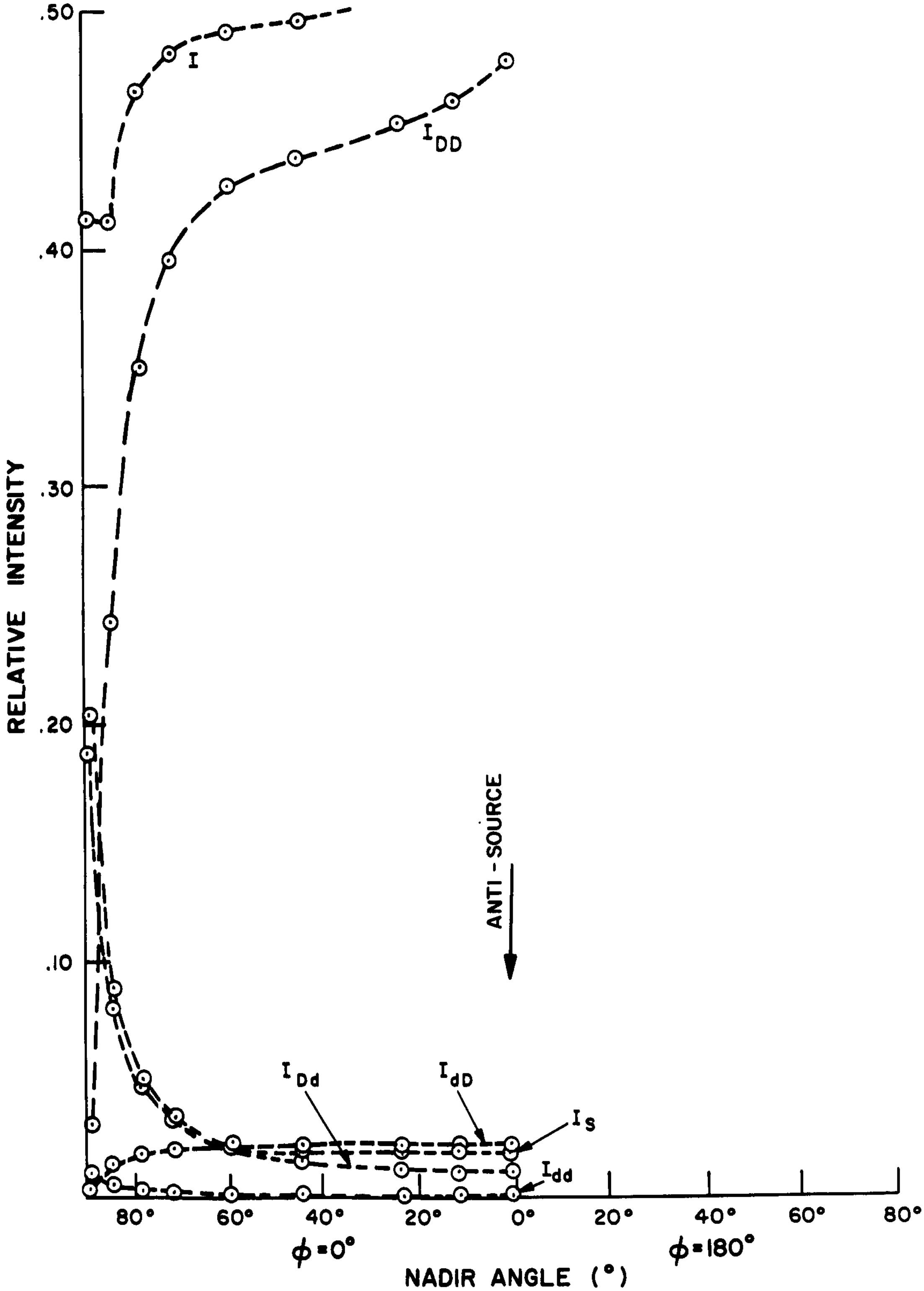

Fig. 70 Relative intensity of outward total radiation and of the individual components, as a function of nadir angle in the principal plane, for a white quartz sand surface ($\theta_0 = 0^{\circ}$, $\lambda = 6430 \mathrm{\mathring{A}}$)

(1) Desert sand, $\lambda = 4920$ Å, $\theta_o = 78.5^\circ$, $\mu_o = .20$

(2) Desert sand, $\lambda = 6430$ Å, $\theta_o = 53.1^\circ$, $\mu_o = .60$

(3) Green grass, $\lambda = 4050$ Å, $\theta_o = 53.1^\circ$, $\mu_o = .60$

For these computations, the effect of an atmospheric aerosol model was approximated. The particular model chosen was one considered by Fraser (1959), and is referred to as a "continental" model aerosol. It is characterized by the following size distribution:

Interval of radius, a (micron) Lower	Upper	Number of particles per cm^3 of air per micron of radius	Number of particles per cm^3
.03	0.1	2.251×10^4	1575.7
0.1	20.0	$2.251 \times a^{-4}$	753.3
			2329.0

The vertical density is assumed to decrease exponentially with a scale-height H = .98km, as suggested by Penndorf (1954). Fraser has computed both the volume scattering coefficients, and the normalized matrix elements of the phase matrix required by the transfer equation for wavelengths $\lambda = 3650$ Å, 4600 Å, and 6250 Å. We have interpolated these values in order to approximate these functions for the wavelengths used in our measurements and computations. In particular, we have the following values for the volume scattering coefficient, $\beta(z, \lambda)$:

$\beta(0, 4050\ \text{Å}) = 1.58 \times 10^{-6}\ cm^{-1}$

$\beta(0, 4920\ \text{Å}) = 1.32 \times 10^{-6}\ cm^{-1}$

$\beta(0, 6430\ \text{Å}) = 1.03 \times 10^{-6}\ cm^{-1}$

We can then calculate $\tau_1^A(\lambda)$, the normal optical thickness of the aerosol content.

$$\tau_1^A(\lambda) \equiv \int_0^\infty \beta^A(z,\lambda)\; dz = \int_0^\infty \beta^A(0,\lambda)\; e^{-z/H}\; dz = \beta^A(0,\lambda)\; H$$

Therefore:

$\tau_1^A(4050\mathring{A}) = .155$

$\tau_1^A(4920\mathring{A}) = .129$

$\tau_1^A(6430\mathring{A}) = .101$

In the computations, the following approximations were made:

(1) In computing the "standard" case solution, the aerosol scattering was assumed to be independent of Rayleigh scattering, so that the solution is just the sum of the two independent solutions.

(2) Only primary scattering was considered in approximating the "standard" case solution for the aerosol content.

(3) In considering the components involving ground reflection, the presence of the aerosols was assumed only to increase the optical depth.

Denoting the Rayleigh optical thickness by τ_1^R, the total normal optical thickness is $\tau_1 = \tau_1^A + \tau_1^R$. Therefore, component I_{DD} was computed accurately, but some error was introduced into the other three components by assuming the aerosol phase function to be the same as that of the molecules.

The values of $\tau_1(\lambda)$ are:

λ	τ_1^A	τ_1^R	τ_1
4050 Å	.155	.342	.497
4920 Å	.129	.150	.279
6430 Å	.101	.050	.151

For components I_{Dd}, I_{dD}, and I_{dd} which require tabulated functions for their determination, the values of τ_1 that were used are .50, .25, and .15 respectively. The Rayleigh "standard" case solution for τ_1^R = .342 was interpolated. We proceed to a discussion of the primary scattering solution for the aerosol "standard" case.

The requisite transfer equation for primary scattering may be written:

$$\mu \frac{d\vec{I}}{d\tau} = \vec{I} - 1/4 \; e^{-\tau/\mu_o} \underset{\sim}{P}^A \vec{F} \tag{61}$$

where

$$\vec{I} = \begin{bmatrix} I \\ Q \end{bmatrix} = \begin{bmatrix} I_i + I_j \\ I_i - I_j \end{bmatrix} \tag{62}$$

$$\underset{\sim}{P}^A = \begin{bmatrix} \hat{L}_{11}(\gamma) & \hat{L}_{12}(\gamma) \\ \hat{L}_{12}(\gamma) & \hat{L}_{11}(\gamma) \end{bmatrix} \tag{63}$$

$$\vec{F} = \begin{bmatrix} 1 \\ 0 \end{bmatrix} \tag{64}$$

The scattering matrix $\underset{\sim}{P}^A$ describes the aerosol scattering of incident light, and enables one to compute the intensity components I_i and I_j parallel and perpendicular to the scattering plane, which is taken normal to the plane of polarization. The elements $\hat{L}_{11}$ and $\hat{L}_{12}$ are functions of γ, the scattering angle. The angle γ may be readily determined from the parameters μ_o, μ, and φ. As mentioned previously, the values of $\hat{L}_{11}$ and $\hat{L}_{12}$ were interpolated from a tabulation by Fraser. An important fact, pointed out by Deirmendjian (1957), is that the assumption of exponential density decrease of aerosol content ensures that $\frac{\partial \hat{L}_{ij}(\gamma)}{\partial \tau} = 0$. This means that in solving the transfer equation above, these elements can be brought out from under an integral with respect to τ. In fact, since

$$\underset{\sim}{P}\overset{A\rightarrow}{F} = \begin{bmatrix} \hat{L}_{11}(\gamma) & \hat{L}_{12}(\gamma) \\ \hat{L}_{12}(\gamma) & \hat{L}_{11}(\gamma) \end{bmatrix} \begin{bmatrix} 1 \\ 0 \end{bmatrix} = \begin{bmatrix} \hat{L}_{11}(\gamma) \\ \hat{L}_{12}(\gamma) \end{bmatrix} \tag{65}$$

the transfer equation assumes the form:

$$\mu \frac{d\begin{bmatrix} I \\ Q \end{bmatrix}}{d\tau} = \begin{bmatrix} I \\ Q \end{bmatrix} - \frac{1}{4} e^{-\tau/\mu_0} \begin{bmatrix} \hat{L}_{11}(\gamma) \\ \hat{L}_{12}(\gamma) \end{bmatrix} \tag{66}$$

or:

$$\mu \frac{dI}{d\tau} = I - \frac{1}{4} \hat{L}_{11}(\gamma) e^{-\tau/\mu_0} \qquad \text{66a)}$$

$$\mu \frac{dQ}{d\tau} = Q - \frac{1}{4} \hat{L}_{12}(\gamma) e^{-\tau/\mu_0} \tag{66b}$$

The solutions to these linear differential equations may be written, remembering that the boundary conditions are such that there is no radiation reflected from the "ground", as:

$$I = I_i + I_j = \frac{1}{4\mu} \hat{L}_{11}(\gamma) \frac{\mu \mu_0}{\mu + \mu_0} \left\{ 1 - e^{-\tau_1^A \left\{ \frac{1}{\mu} + \frac{1}{\mu_0} \right\}} \right\} \tag{67a}$$

$$Q = I_i - I_j = \frac{1}{4\mu} \hat{L}_{12}(\gamma) \frac{\mu \mu_0}{\mu + \mu_0} \left\{ 1 - e^{-\tau_1^A \left\{ \frac{1}{\mu} + \frac{1}{\mu_0} \right\}} \right\} \qquad (67$$

The corresponding intensity components I_l and I_r may be computed employing a linear transformation corresponding to a rotation of the axes through an angle $90^{\circ} - \chi$.

(1) <u>Results for Desert Sand Surface</u>

The relative intensities of the individual components, and of their sum, for the case of a desert sand surface are shown, as a function of nadir angle in the principal plane, by the curves of Fig 71. The zenith angle of the source is 78.5°, and the wavelength is 4920Å. The rather large normal optical thickness, in combination with a low sun angle, tend to minimize the importance of the surface reflected light. Except in the direction of the nadir, the "standard" case solutions dominate the scene. The difference between Rayleigh scattering and aerosol scattering characteristics is clearly seen by comparing the curves $I_s^{(A)}$ and $I_s^{(R)}$. The strong asymmetry shown by $I_s^{(A)}$ is, of course, a result of the strong forward scattering of aerosol particles.

Changes in wavelength and sun zenith angle combine to increase the importance of surface reflected radiation. Fig.72 shows the relative intensities of the various components for a wavelength $\lambda = 6430$Å, and a sun zenith angle $\theta_o = 53.1^{\circ}$. The components I_{DD} and I_{dD} account for most of the intensity of emergent radiation for $\theta < 60^{\circ}$ on either side of the nadir.

(2) Results for a Green Grass Surface

Fig. 73 shows the relative intensities of the individual components, and of their sum, as a function of nadir angle in the principal plane, for a surface of clipped green grass. The calculations are for a sun zenith angle of 53.1° and a wavelength $\lambda = 4050$Å. The short wavelength, with its corresponding large optical depth, combines with a low surface reflectivity, ($\bar{R} = .026$) to produce a negligible contribution from the ground reflected radiation to the emergent intensity. The component $I_s^{(R)}$ is seen to dominate the picture over most of the range of nadir angles.

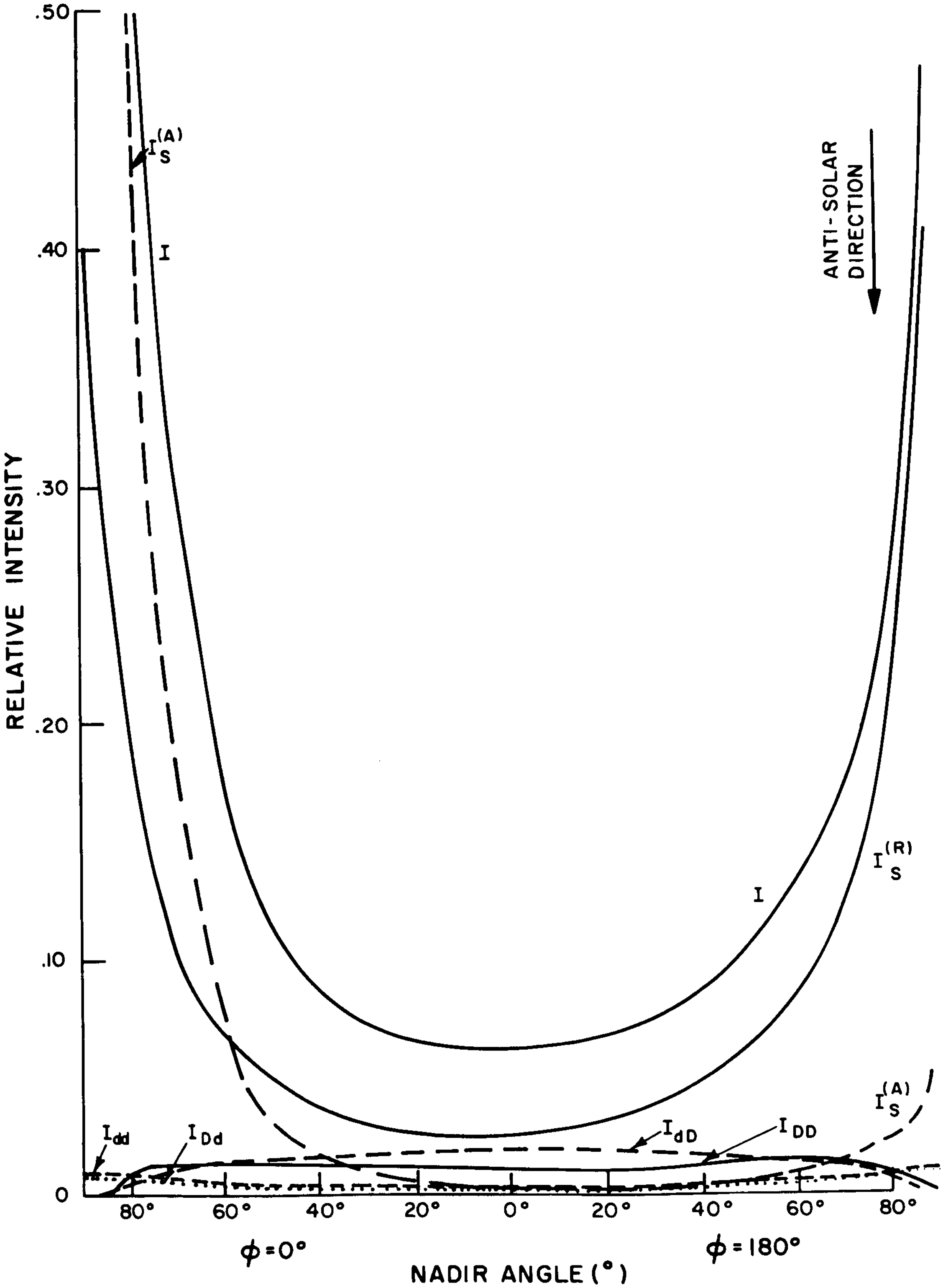

Fig. 71 Total intensity and intensity of individual components of radiation emerging from top of slightly turbid atmosphere overlying a surface of desert sand ($\lambda = 4920 \text{Å}$, $\theta_0 = 78.5°$, principal plane)

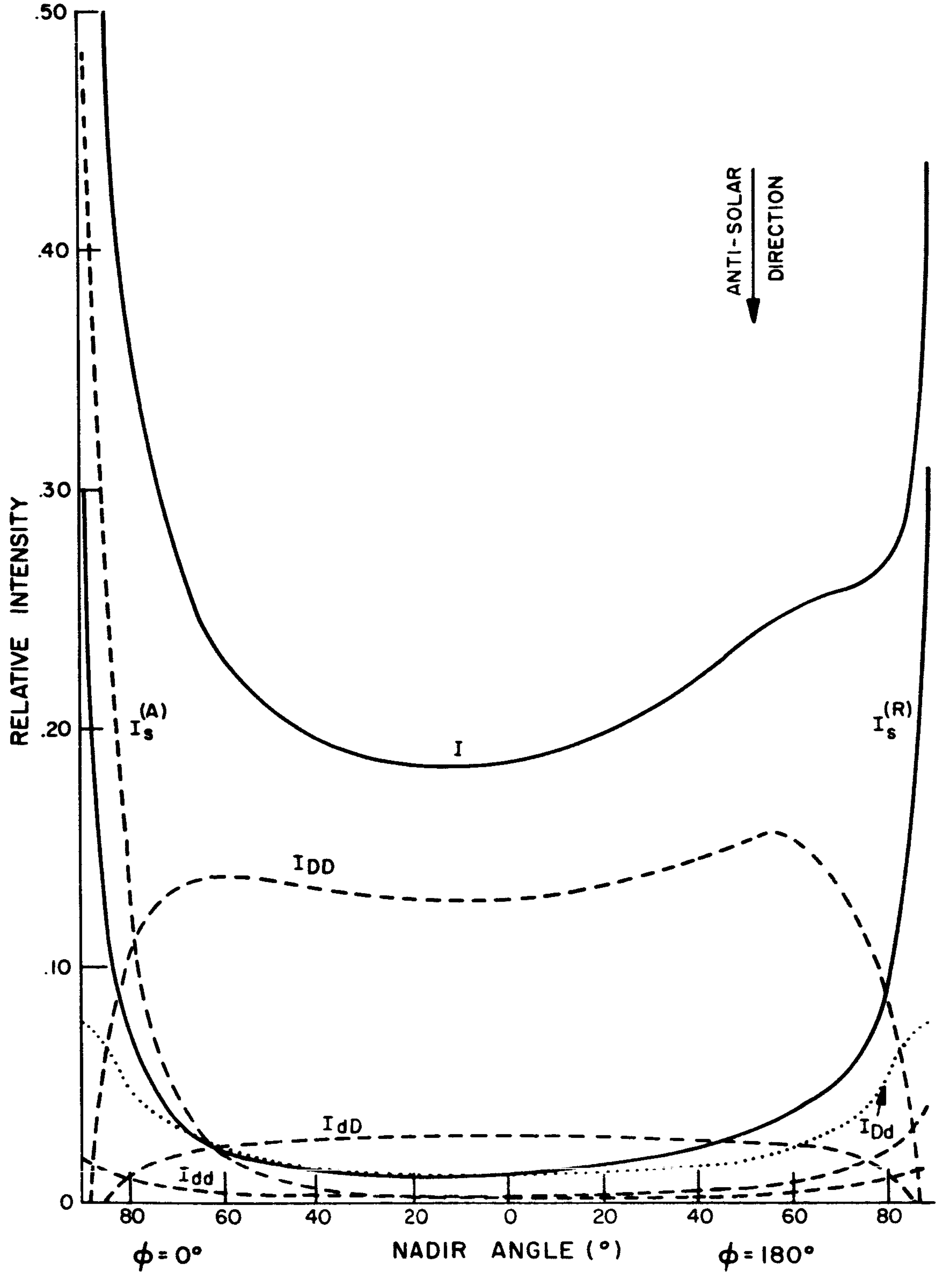

Fig. 72 Total intensity and intensity of individual components of radiation emerging from top of a slightly turbid atmosphere overlying a surface of desert sand ($\lambda = 6430\text{Å}$, $\theta_o = 53°$, principal plane)

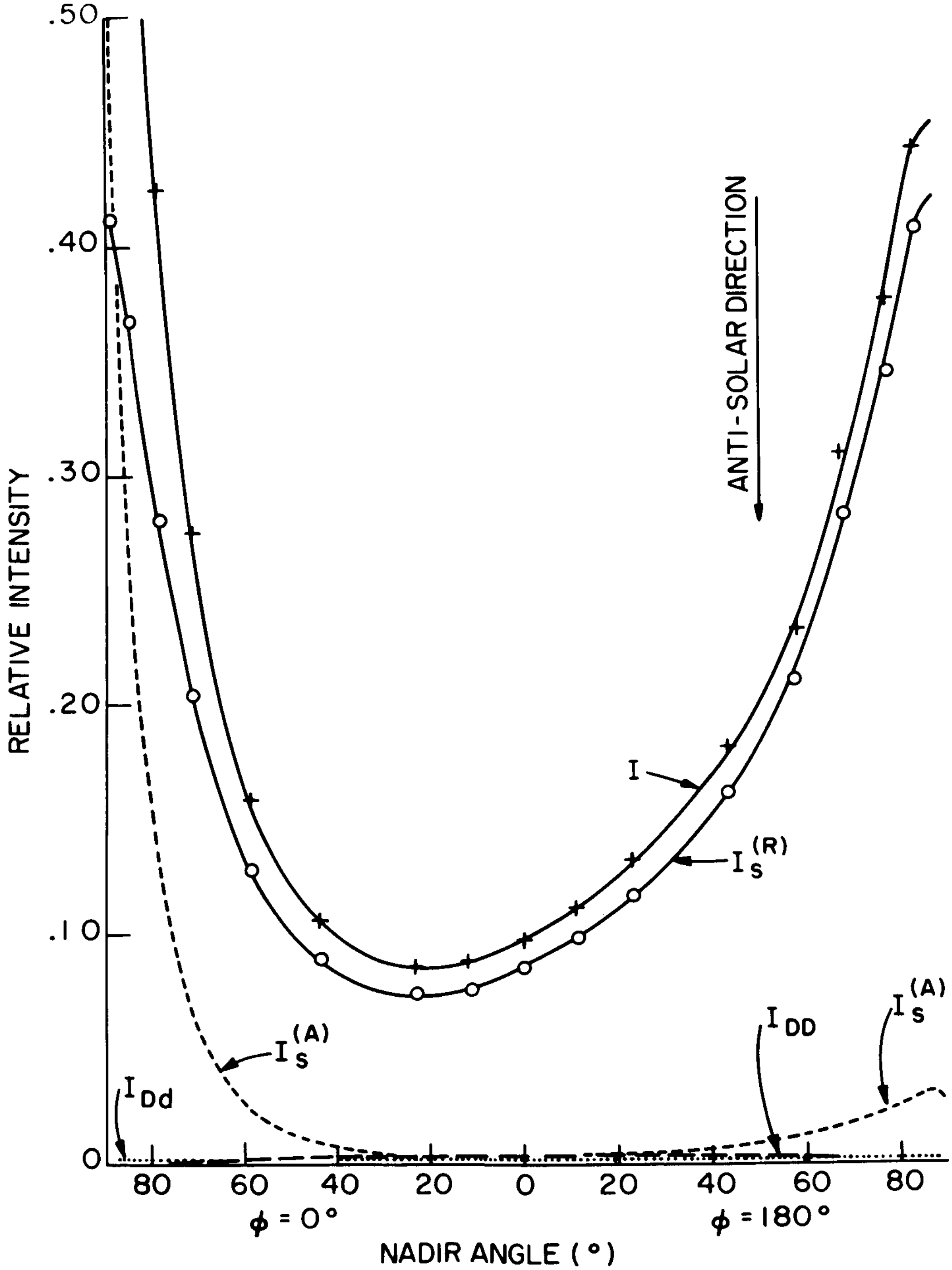

Fig. 73 Total intensity and intensity of individual components of radiation emerging from top of slightly turbid atmosphere overlying a surface of clipped green grass. The compoents I_{dD} and I_{dd} are everywhere less than 0.002 and are not plotted. (λ = 4050 A, $\theta_0 = 53^\circ$, principal plane)

2. Polarization

In the previous section, the relative intensities of the various components, and of their sum were shown for the surfaces: red clay, white quartz sand, desert sand, and green grass. Here we show the degree of linear polarization of the total radiation emerging from the top of the atmosphere for the same surfaces.

Since the calculations for red clay and quartz sand were made assuming a a Rayleigh atmosphere, it is interesting to compare the results with the corresponding results for a Lambert surface reflecting with the same albedo. In fact the Lambert surface value is just $P_{LAM}(0;\mu,\varphi) =$

$$\frac{Q_s + 1/2\, I_g \left\{ \gamma_r(\mu) - \gamma_l(\mu) \right\}}{I_s + 1/2\, I_g \left\{ \gamma_r(\mu) + \gamma_l(\mu) \right\}} \tag{68}$$

where Q_s and I_s are the "standard" case solutions. The quantity I_g is given by:

$$\frac{\bar{R}\mu_o}{2(1 - \bar{R}\,\bar{s})} \left\{ \gamma_e(\mu_o) + \gamma_r(\mu_o) \right\} \tag{69}$$

A summary of these parameters is given:

Sample	μ_o	λ	τ_1	$\bar{R} = \int_0^1 \int_0^{2\pi} \rho(\mu,\varphi)\, \mu d\mu d\varphi$	I_g
Red clay	.60	4920Å	.15	.200	.109
Red clay	.60	6430Å	.05	.447	.263
Quartz Sand	.60	4920Å	.15	.519	.295
Quartz Sand	.60	6430Å	.05	.606	.359
Quartz Sand	1.00	6430Å	.05	.493	.492

a. Results for Red Clay Surface

Fig. 74 shows the degree of polarization of the emergent radiation in the principal plane, as a function of nadir angle, for a red clay surface. The wavelength is 4920Å, and the zenith angle of the sun is 53.1°. The curve is compared with the solution obtained assuming a Lambert surface reflecting with an equivalent albedo. The generally higher values of the degree of polarization for the sample, atmosphere combination reflect the polarization characteristics of the sample, although the situation is by no means that simple. In fact, the degree of polarization of the emergent radiation, $P^{(1)}$, may be written:

$$P^{(1)} = \frac{I_s P_s + I_{DD} P_{DD} + I_{Dd} P_{Dd} + I_{dD} P_{dD} + I_{dd} P_{dd}}{I_s + I_{DD} + I_{Dd} + I_{dD} + I_{dd}} \tag{70}$$

In our approximation scheme, P_{dD}, $P_{dd} \equiv 0$, and the product $I_{Dd} P_{Dd}$ is, in general, quite small. Hence $P^{(1)}$, is approximately:

$$P^{(1)} = \frac{I_s P_s + I_{DD} P_{DD}}{I\ (\text{Total})} \tag{71}$$

However $P_{DD} = P$ (surface), and thus equation (71) shows the explicit dependence of $P^{(1)}$ on the surface polarization. However, the intensity component I_{DD} also plays a significant role, and a comparison of $P^{(1)}$ with the polarization of the emergent radiation in the presence of a Lambert surface can only be made by comparing (71) with (68). A very good approximation to (68) is:

$$P_{LAM}(0;\mu,\varphi) = \frac{P_s I_s}{I_s + 1/2\, I_g\{\gamma(\mu) + \gamma_1(\mu)\}} \tag{72}$$

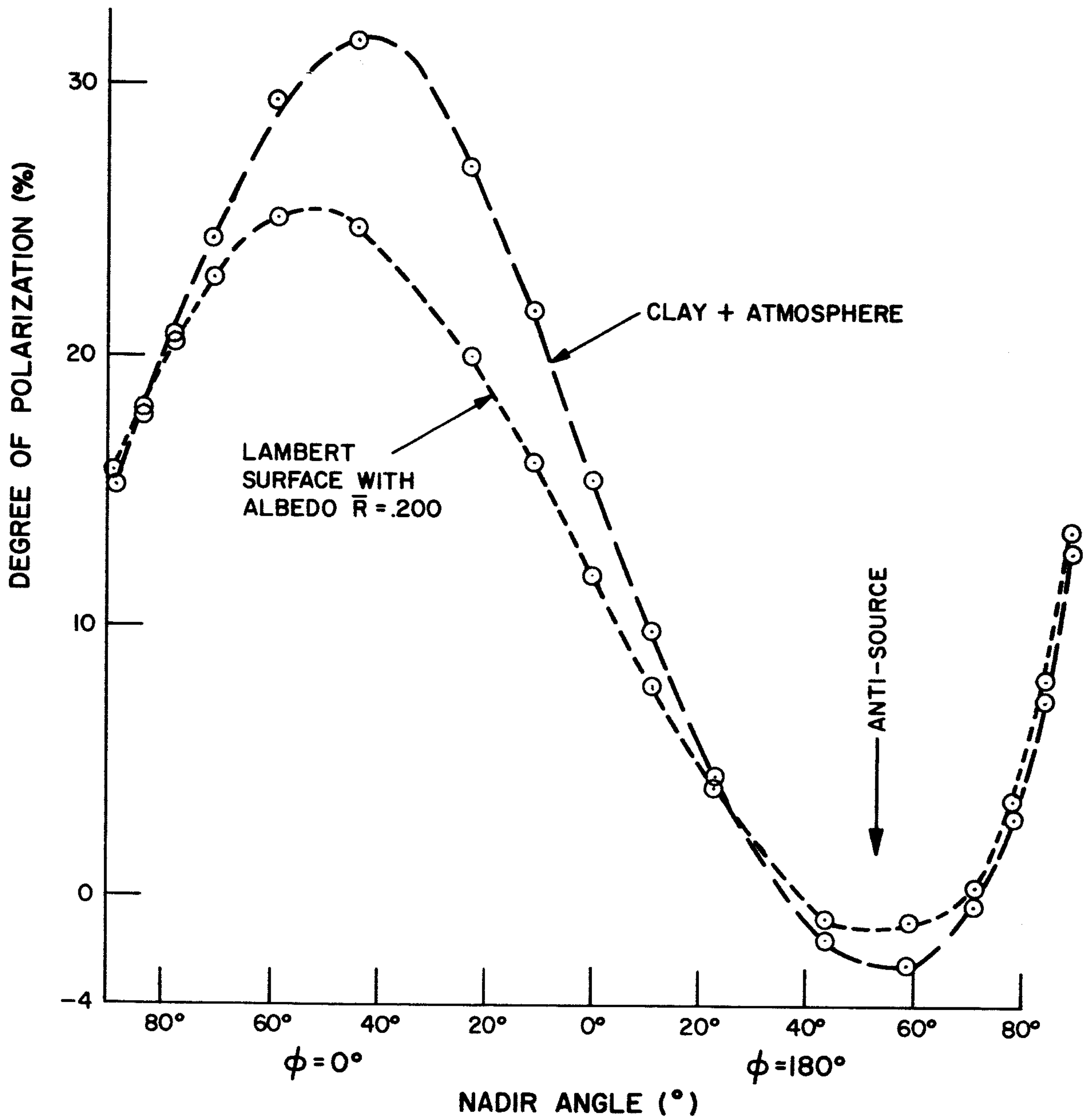

Fig. 74 A comparison of the degree of polarization of the emergent radiation of a clay surface and a Lambert surface having an albedo the same as the clay surface (Principal plane, $\lambda = 4920\text{Å}$, $\theta_0 = 53°$)

Fig. 75 shows the resulting polarization curves for the same red clay surface, same sun zenith angle, but for a wavelength of 6430 Å. The hump in the clay plus atmosphere curve is explained by the interaction of the various components as described by equation (71). For a wavelength $\lambda = 6430$Å, the I_s solution falls off more quickly as one moves from the horizon toward the nadir direction than for the case $\lambda = 4920$ Å. Also component I_{DD} should in general be more significant at this wavelength because:

(1) surface reflectivities are generally higher.

(2) the optical thickness is smaller, thus permitting less attenuation.

Since surface polarization is generally lower for the longer wavelength, the net effect would seem to be that the degree of polarization of the emergent radiation would usually be less at the longer wavelength, but the surface reflection characteristics play a more important role in determining the polarization profile.

b. Results for White Quartz Sand

Fig. 76 shows the polarization curves of the emergent radiation for the sand plus atmosphere and the Lambert surface with an equivalent albedo. The curves are for a wavelength $\lambda = 4920$ Å, and a sun zenith angle of 53°. The importance of surface polarization is again seen in the next figure. Fig. 77 shows the degree of polarization of the emergent radiation for a wavelength $\lambda = 6430$ Å. The profile is seen to be quite different for the corresponding case with the red clay surface. It is interesting to compare Fig. 76 and Fig. 77 with the corresponding surface polarization curves, shown

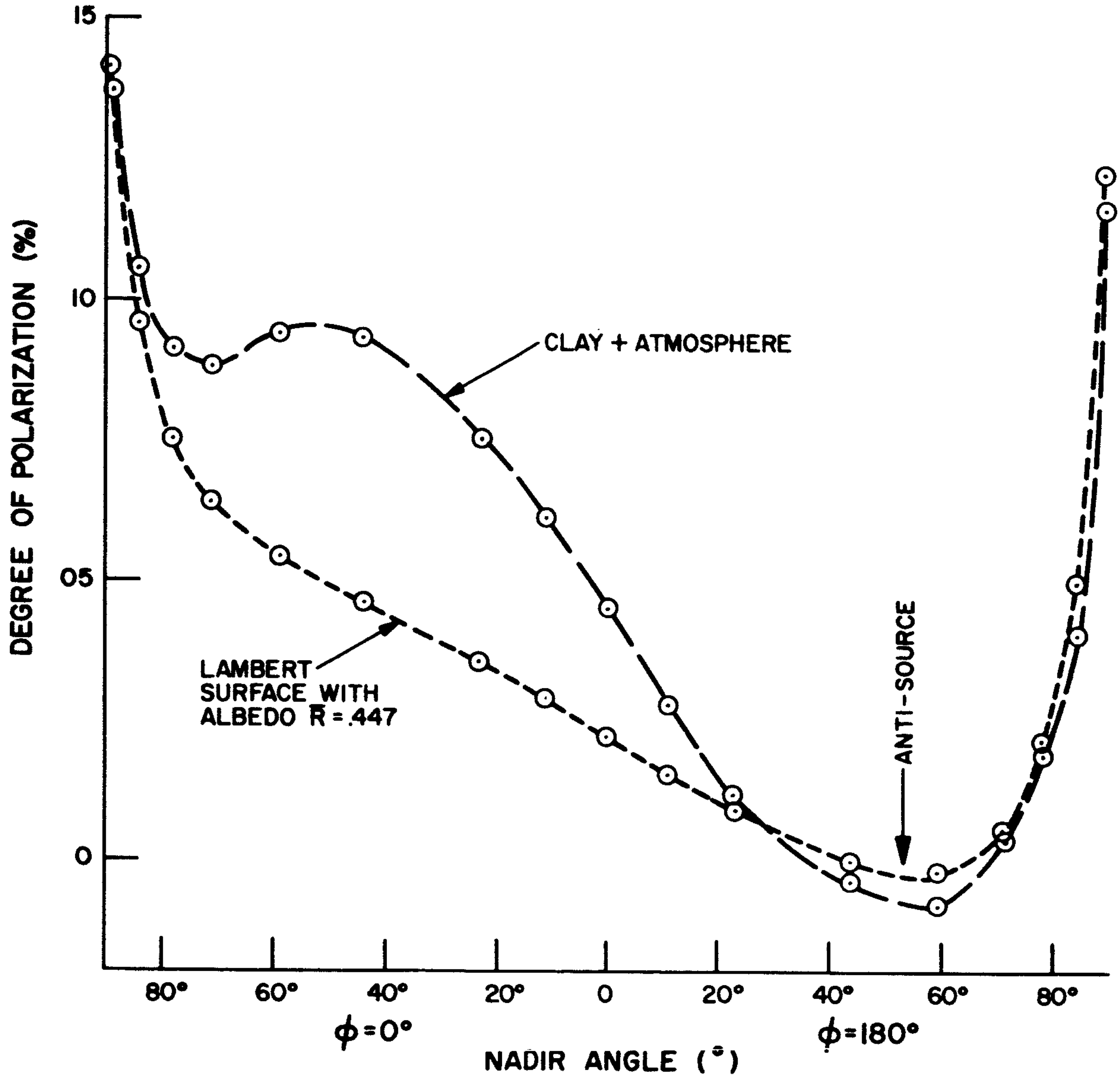

Fig. 75 A comparison of the degree of polarization of the emergent radiation of a clay surface and a Lambert surface having an albedo the same as the clay surface (Principal plane, $\lambda = 6430\text{Å}$, $\theta_o = 53^o$)

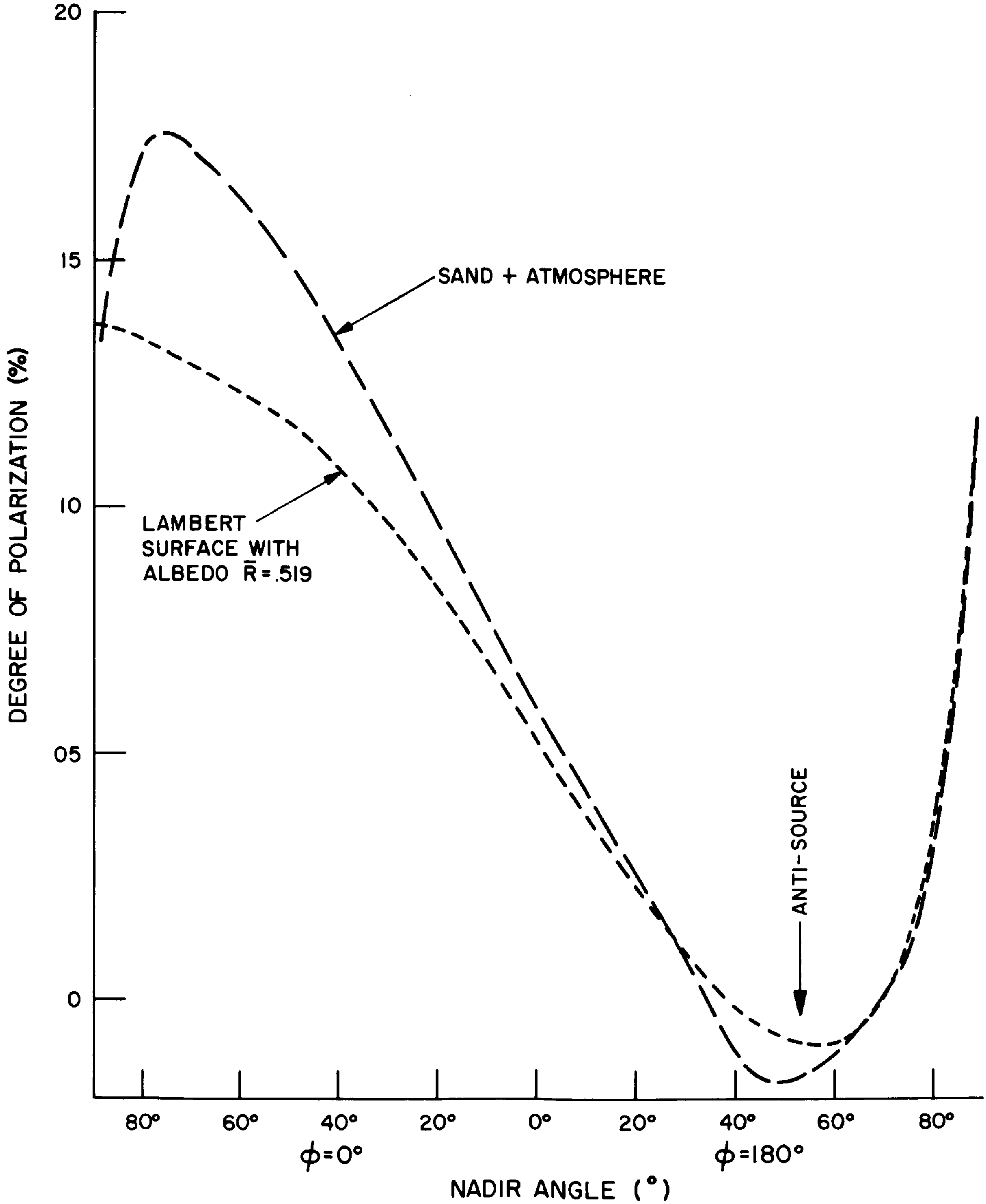

Fig. 76 A comparison of the degree of polarization of the emergent radiation of a white quartz sand surface and a Lambert surface having an albedo the same as the sand surface (Principal plane, $\lambda = 4920Å$, $\theta_0 = 53^{\circ}$)

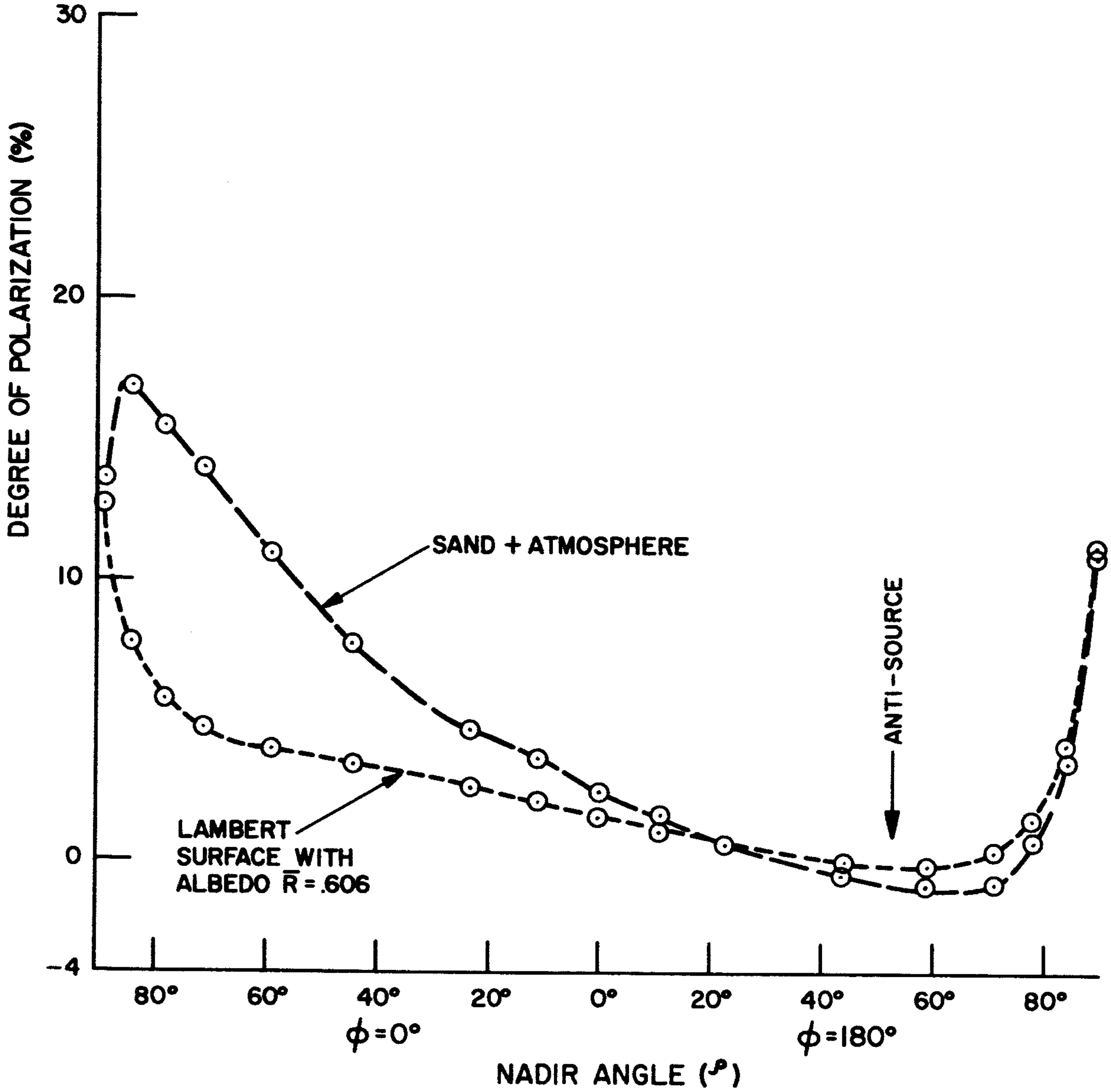

Fig. 77 A comparison of the degree of polarization of the emergent radiation of a white quartz sand surface and a Lambert surface having an albedo the same as the sand surface (Principal plane, $\lambda = 6430\mathring{A}$, $\theta_o = 53^o$)

as Figures 78 and 79 .

Figure 80 is interesting. It shows little difference between the sand plus atmosphere and the Lambert surface solution. The reasons for this are: (1) The surface polarization of white quartz sand with the source at the zenith show the polarization to be less than 2% for $0^{\circ} \leq \theta \leq 80^{\circ}$.
(2) The variation of directional reflectance for $0^{\circ} \leq \theta \leq 75^{\circ}$ was also less than .02. Hence, for the source at the zenith, white quartz sand is a fairly good approximation to a Lambert surface.

c. Results for Desert Sand Surface

Fig. 81 shows the degree of polarization of the emergent radiation in the principal plane, as a function of nadir angle, for a desert sand surface. The wavelength is 4920 Å, and the zenith angle of the sun is 78.5°. The low sun angle and increased optical thickness due to the presence of aerosols combine to minimize the effects of surface reflection on the polarization profile. The main effect of the ground is to act as a depolarizer of the polarization due to the combined standard case solutions for the aerosol and Rayleigh scattering. The existence of the neutral point (Arago) at $\varphi = 0$, $\theta = 80^{\circ}$ is a combination of: (1) This is predicted for Rayleigh scattering alone for sun zenith angles $> 70^{\circ}$. (2) The scattering angle at these parameters is not too far from the forward direction. The aerosol model also has negative polarization for small scattering angles.

Fig. 82 shows the same sample, but for a wavelength of 6430 Å and a sun zenith angle of 53°. The increased wavelength and decreased zenith angle combine to increase the importance of surface reflection characteristics

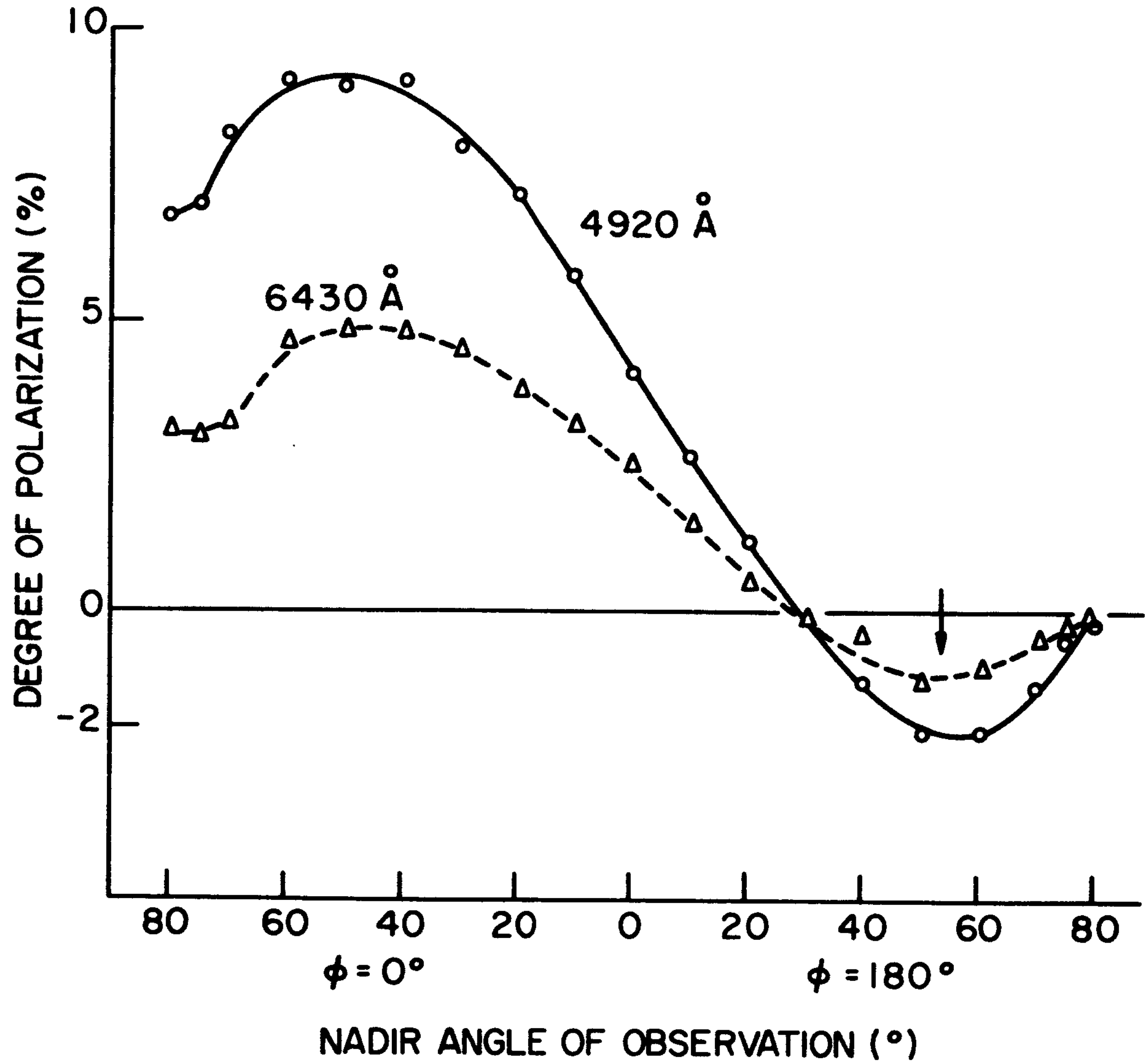

Fig. 78 Degree of polarization of light reflected from red clay, as a function of angle of observation, for two different wavelengths. $\theta_o = 53^o$, (Principal Plane)

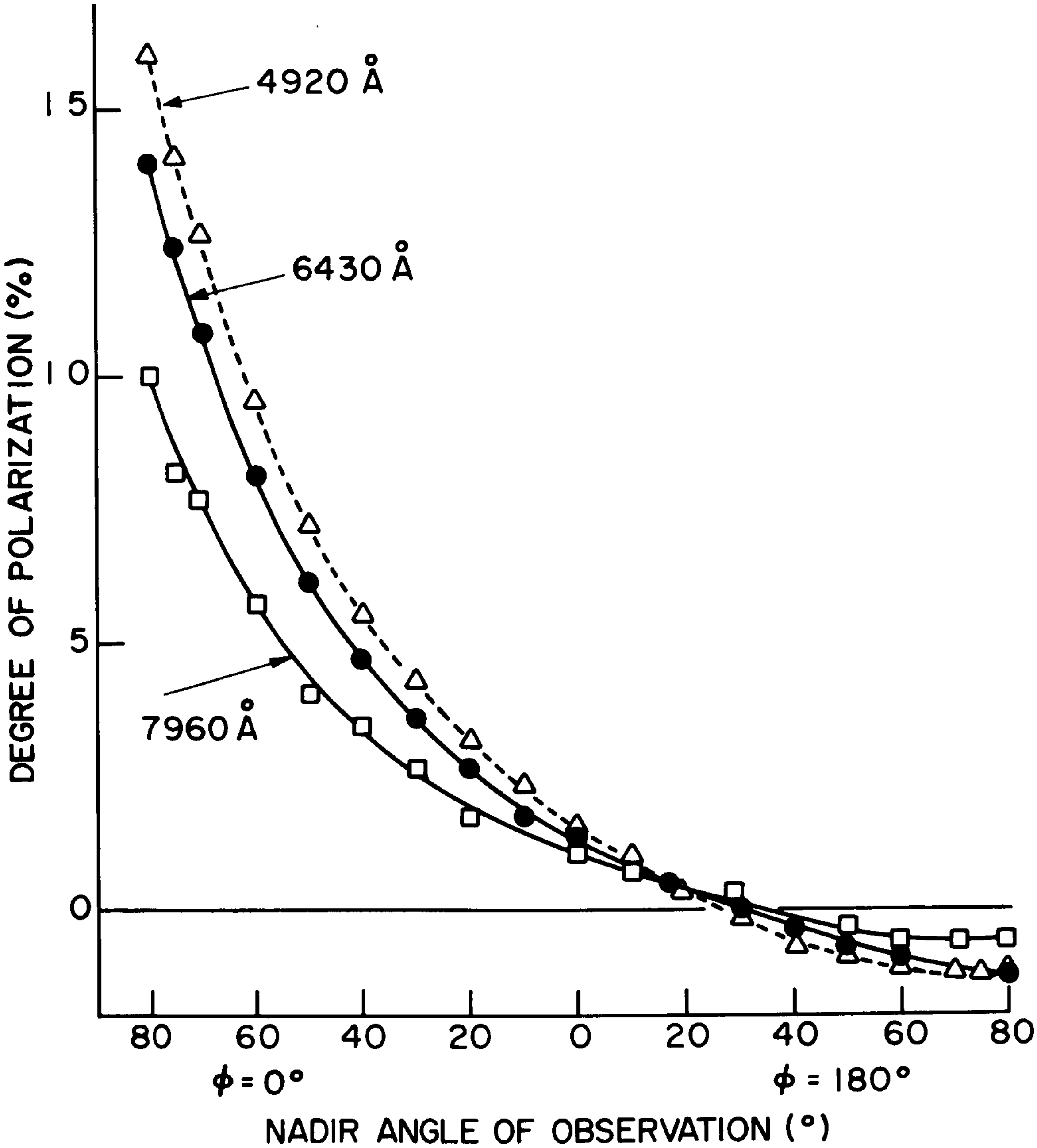

Fig. 79 Degree of polarization of light reflected from white quartz sand, as a function of angle of observations, for three different wavelengths. $\theta_o = 53°$, (Principal plane)

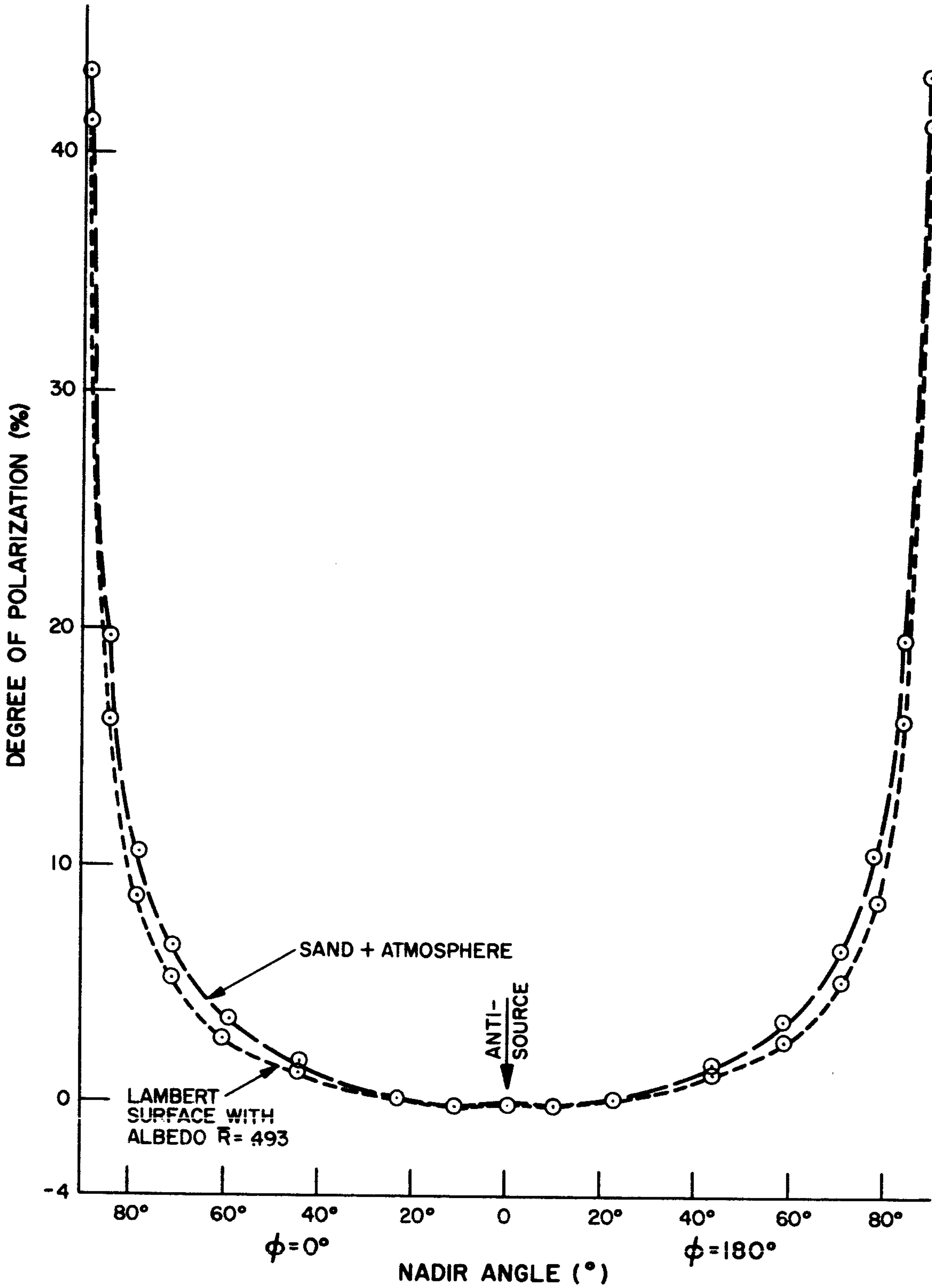

Fig. 80 A comparison of the degree of polarization of the emergent radiation of a white quartz sand surface and a Lambert surface having an albedo the same as the sand surface (Principal plane, $\lambda = 6430Å$, $\theta_0 = 0°$)

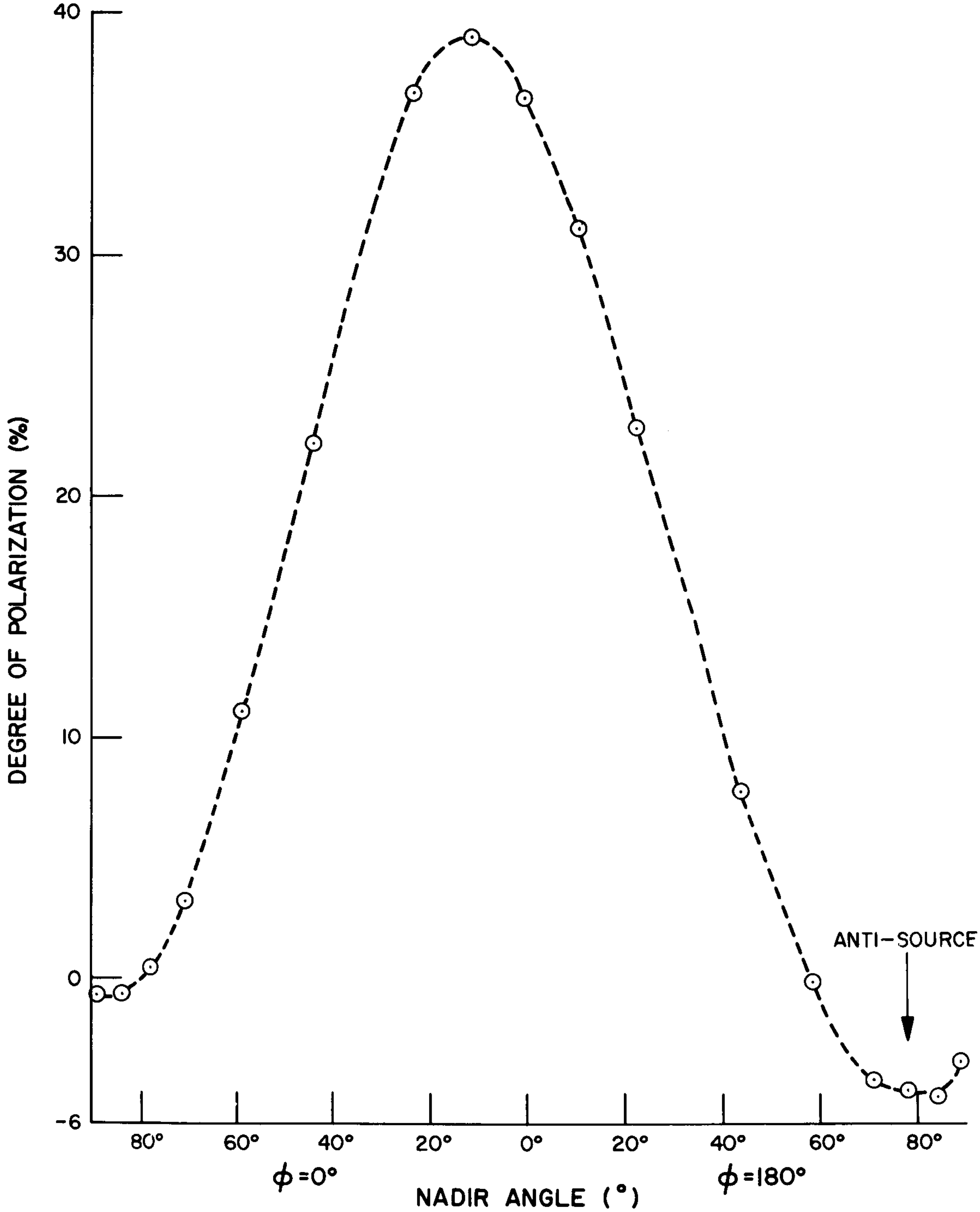

Fig. 81 Degree of polarization of the emergent radiation for a desert sand surface (Principal plane, $\lambda = 4920Å$, $\theta_o = 78.5^o$)

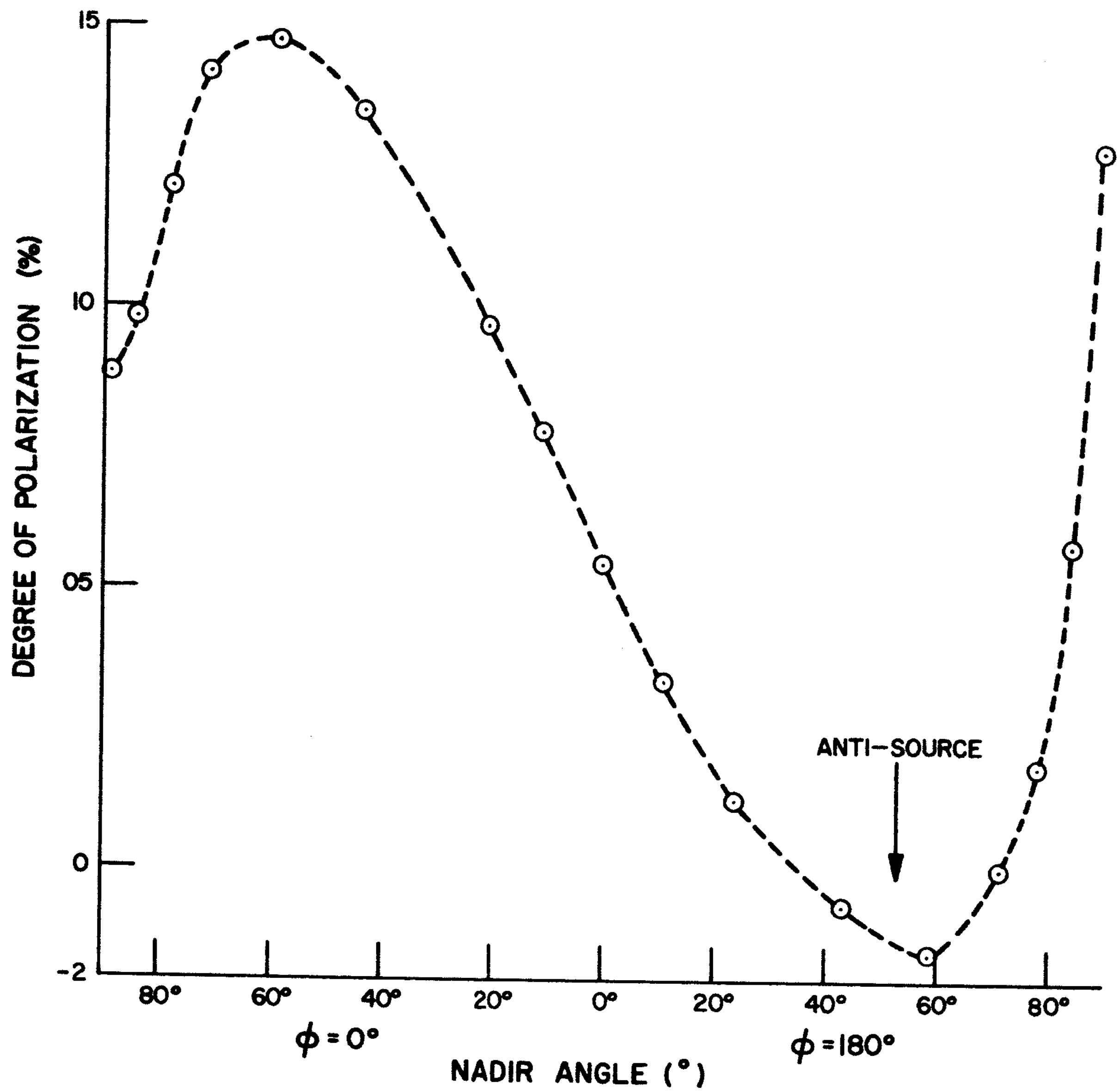

Fig. 82 Degree of polarization of the emergent radiation for a desert sand surface (Principal plane, $\lambda = 6430\text{Å}$, $\theta_0 = 53°$)

in determining the polarization profile.

d. Results for Green Grass Surface

Fig. 83 shows the degree of polarization of the emergent radiation for a sample of clipped green grass for a sun zenith angle of 53°. The combination of short wavelength (4050 Å), $\tau_1 \sim .50$, and low surface reflectivity ($\bar{R} = .026$) imply that ground reflection effects will have virtually no contribution in altering the polarization profile. In fact, Rayleigh scattering is seen to be the dominant factor, with the aerosol acting as a depolarizer.

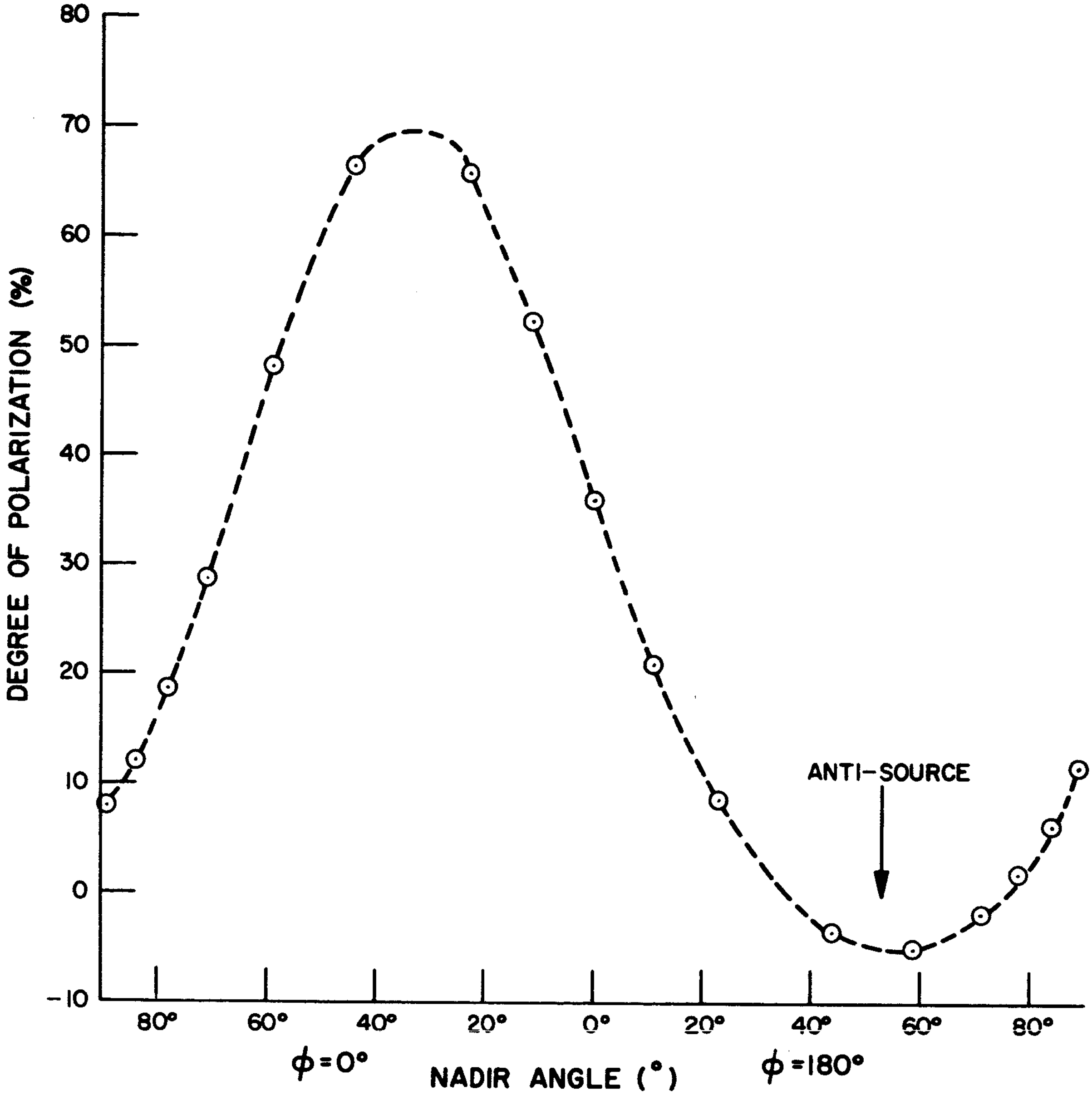

Fig. 83 Degree of polarization of the emergent radiation for for a green grass surface (Principal plane, $\lambda = 4050\AA$, $\theta_0 = 53^\circ$)

References

Chandrasekhar, S. (1950) - Radiative Transfer, Oxford, Clarendon Press, 385 pp.

Coulson, K. L., G. M. B. Bouricius, and E. L. Gray (1964), "Effect of Surface Properties on Planet-Reflected Sunlight," T.I.S. Rept. R64SD74, General Electric Co., Philadelphia, Pa.

____________ (1965) " A Study of the Reflection and Polarization Characteristics of Selected Natural and Artificial Surfaces," T.I.S. Rept. R65SD4, General Electric Co., Philadelphia, Pa.

Coulson, K. L., J. V. Dave, and Z. Sekera (1960), Tables Related to Radiation Emerging from a Planetary Atmosphere, University of California Press.

Deirmendjian, D., (1955) Annales de Geophysique, Vol. 13, p. 286.

Dollfus, A. (1957) "Étude des planètes par la polarixation de leur lumière," Supplement No. 4, Ann. d'Astrophys.

Dollfus, A. (1961) "Polarization Studies of the Planets," Chap. 9 in Planets and Satellites, edited by G. P. Kuiper and B. M. Middlehurst, University of Chicago Press

Fraser, R. S., (1959), "Scattering Properties of Atmospheric Aerosols," University of California, Department of Meteorology, Los Angeles, Scientific Report No. 2.

Gates, D. M., H. G. Keegan, J. C. Schleter, and V. R. Weidner (1965), "Spectral Properties of Plants" Applied Optics, Vol. 4, No. 1, pp 11-20.

Hovis, W. A. (1965) Private Communication.

Kondratiev, K. Y., Z. F. Mironova, and A. N. Otto (1965) "Spectral Albedo of Natural Surfaces," Pure and Applied Geophysics, 59, 207-216

Krinov, E. L. (1947) "Spektral'naia otraznatel'naia sposobnost' priorodnykh obrazovanii," Laboratoriia Aerometodov, Akad. Nauk, SSSR, Moscow, 271 pp (Spectral reflectance properties of natural surfaces," Technical Translation TT-439, Nat. Res. Council of Canada, Ottawa, 1953).

Lyot, B. (1929) Recherches sur la polarisation de la lumière des planètes et de quelques substances terrestres," Ann. de l'Obs. de Paris, Sect. de Meudon, 8 (1)

References

Penndorf, R. (1954), "The Vertical Distribution of Mie Particles in the Troposphere," J. of Meteorology, 11: 3, 245-247.

Sekera, Z. and E. Ashburn (1953), "Tables Relating to Rayleigh Scattering of Light in the Atmosphere," Navord Rpt. 2061, China Lake, California.

Sekera, Z., and G. Blanch (1952), "Tables Relating to Rayleigh Scattering of Light in the Atmosphere," Contract No. AF 19(122) - 239, University of California, Department of Meteorology, Los Angeles.

APPENDIX A

Effect of Surface Reflection on the Propagation of Optical Contrasts - K. L. Coulson and E. L. Gray

Revised June 18, 1965

Effect of Surface Reflection on the Propagation of Optical Contrasts - K. L. Coulson and E. L. Gray

I Introduction

The problem of contrast attenuation by the atmosphere has been the subject of renewed interest since the advent of satellites and very high altitude reconnaissance aircraft. The Cornell Aeronautical Laboratory [1961] performed a relatively extensive study of the photographic reconnaissance problem, one of their main conclusions being that contrast reduction is strongly related to the reflectances of both the object and its surrounding background. In a more recent and comprehensive analysis of the problem from a theoretical standpoint, Fraser [1964b] also emphasized the role played by background reflection on contrast transfer in the earth's atmosphere.

Of particular interest in Fraser's investigation is the possibility of contrast enhancement by the use of a polarizing optical system in the camera. He showed that for certain atmospheric conditions and geometries of solar and viewed angles, the whole-atmosphere contrast transmission coefficient for one of the orthogonal intensity components is as much as 20% greater than that for the total intensity at a wavelength of $\lambda = 4360$ Å. For $\lambda = 8090$ Å it is possible to get a contrast transmission coefficient of 99% by use of an analyzer inthe system.

The contrast transmission is shown by Fraser to be relatively sensitive to surface reflectance, corroborating the results obtained at the Cornell Aeronautical Laboratory [1961]. Fraser considered the surface reflectance to be that of a Lambert surface (intensity independent of direction and zero polarization of the reflected radiation) with a total reflectance of 0, 0.25, or 0.80. It is known, however, that most natural surfaces do not exhibit Lambert type reflection.

In an effort to determine quantitatively the effects introduced into the atmospheric radiation regime by reflection from non-Lambert surfaces, we are in the process of making measurements of the reflection properties of a number of natural surfaces and introducing those data into the radiative transfer theory for selected models of the earth's atmosphere. So far we have measurements for vegetation, different types of sands, various kinds of soils, and a number of other materials. The present discussion of the effects of reflection from a natural surface on contrast transmission is based on the data for two types of surfaces, namely, green grass, such as that in a closely clipped lawn, and a sample of desert-type sand obtained from the region near Mojave, California. The details of both the method and the results obtained are outlined in the following sections.

II Method

The method follows closely that used by Fraser [1964b], but certain modifications have been necessary in order to introduce our reflectance measurements. We assume a target of some known reflectance $\pi \rho_t (\mu, \varphi; \mu_o, \varphi_o)$ to be positioned on a horizontal surface of background material with reflectance $\pi \rho_b (\mu, \varphi; \mu_o, \varphi_o)$. Both reflectances are in general dependent on the solar zenith angle $\theta_o = \arccos \mu_o$ and azimuth φ_o with respect to an arbitrary azimuth, and on the nadir angle $\theta = \arccos \mu$

and azimuth φ at which the surface is viewed.

The intrinsic contrast between target and background is taken as the basic contrast which exists at the level of the surface and includes no contrast degradation effects by the atmosphere. It is defined as

$$C\ (\tau = \tau_1; \mu, \varphi) \equiv \frac{\rho_t(\mu, \varphi; \mu_0, \varphi_0) - \rho_b(\mu, \varphi; \mu_0, \varphi_0)}{\rho_b(\mu, \varphi; \mu_0, \varphi_0)} = \frac{I_t(\mu, \varphi; \mu_0, \varphi_0) - I_b(\mu, \varphi; \mu_0, \varphi_0)}{I_b(\mu, \varphi; \mu_0, \varphi_0)} \tag{1}$$

The equation holds for intensities as well as for reflectances, since the incident radiation is assumed the same for both surfaces. The normal optical thickness τ of the atmosphere is the same at the surface as the whole-atmosphere value τ_1. If the target-background combination is viewed from some altitude above the surface at which $\tau = \tau_2$, atmospheric effects enter the problem and produce an apparent contrast which is in general different from the intrinsic contrast. In particular, at the top of the atmosphere where $\tau = 0$, the apparent contrast is

$$C\ (0; \mu, \varphi) = \frac{I_t\ (0; \mu, \varphi) - I_b(0; \mu, \varphi)}{I_b(0; \mu, \varphi)} \tag{2}$$

The problem of contrast transmission for the whole atmosphere thus consists essentially of determining $I_t\ (\mu, \varphi)$ and $I_b\ (\mu, \varphi)$ at the top and bottom of the atmosphere.

It should be realized that the intensities in Eq. (2) may be the total specific intensity as a scalar quantity, the total vector intensity, or any of the well-known Stokes parameters $I_e(\mu, \varphi)$, $I_r(\mu, \varphi)$, $U\ (\mu, \varphi)$, where e and r denote the orthogonal directions parallel and normal, respectively, to the vertical plane through the observed direction. For the case in which all of the Stokes parameters can be determined, the state of linear polarization $P(0;\mu, \varphi)$ of the emergent radiation can be computed, as is done below for these selected cases. Such information may be valuable in designing instrumentation for high altitude reconnaissance or in other problems in which contrast enhancement is desired.

In order to obtain values for the intensities of Eq. (1) and Eq. (2), we assume a model system consisting of a uniform horizontal surface underlying a plane parallel atmosphere of total normal optical thickness $\tau_1(\lambda)$ at wavelength λ. The atmosphere may be composed entirely of molecular size particles, in which case $\tau_1(\lambda) = \tau_1^{(R)}(\lambda)$ where $\tau_1^{(R)}$ is the Rayleigh optical thickness, or it may have some dust or haze particles of known distribution and scattering properties. For this latter case, $\tau_1(\lambda) = \tau_1^{(R)}(\lambda) + \tau_1^{(A)}(\lambda)$, $\tau_1^{(A)}(\lambda)$ being the optical thickness of the aerosols only.

The radiation which is directed upward from the top of such a model consists of the five components shown schematically in Fig. 1, each component having undergone its own history of transmission or scattering in the atmosphere. While a complete discussion of the various components is outside the scope of this paper, they are discussed elsewhere [Coulson, Gray, and Bouricius, 1965], and the final expressions are given below.

If unpolarized incident solar flux of $\pi\mu_0 \underset{\sim}{F}(-\mu_0, \varphi_0)$ is incident on a unit horizontal surface at the top of the atmosphere, the individual components

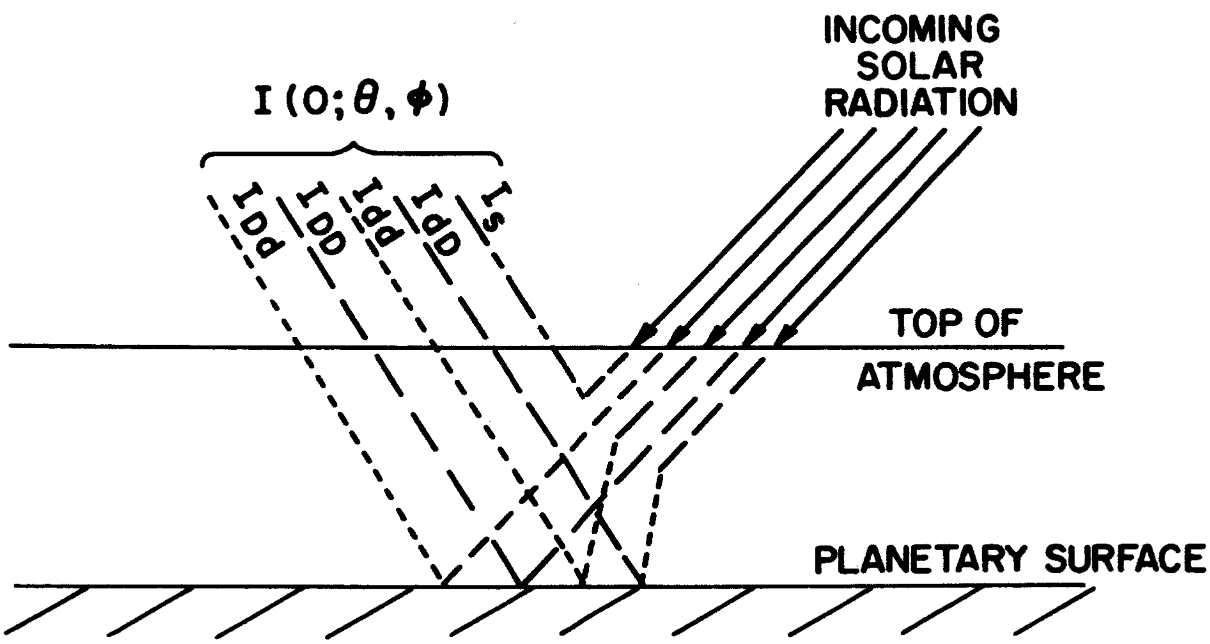

Fig. 1. Schematic diagram illustrating the various components of solar radiation emerging from the top of the atmosphere.

– – – – – direct transmission
-------- diffuse transmission

of the emergent radiation are the following:

Component No. 1 - Radiation which is transmitted directly through the atmosphere, reflected from the surface, and transmitted directly back out through the atmosphere. It is given by the vector expression

$$\underset{\sim}{I}_{DD}\ (0;\mu,\varphi) = 1/2\ \pi F \mu_o\ \rho_b(\mu,\varphi;\mu_o,\varphi_o)\, e^{-\tau_1\left(\frac{\mu+\mu_o}{\mu\mu_o}\right)}\ \underset{\sim}{N}(\mu,\varphi) \tag{3}$$

The symbols used are defined in Table I below.

Component No. 2 - Radiation which is transmitted directly through the atmosphere, reflected from the surface, and transmitted diffusely back out through the atmosphere. It also is a vector and is given by the expression

$$\underset{\sim}{I}_{Dd}(0;\mu,\varphi) = \frac{1}{8\mu}\,\mu_o F e^{-\tau/\mu_o} \int_0^1\int_0^{2\pi} \rho_b(\mu_o,\varphi_o;\mu',\varphi')\ \underset{\sim}{T}(\mu,\varphi;\mu',\varphi')\ \underset{\sim}{N}\ (\mu',\varphi')\, d\mu'\, d\varphi' \tag{4}$$

Component No. 3 - Radiation which is transmitted diffusely through the atmosphere, reflected from the surface, and transmitted directly back out through the atmosphere. In order to simplify the computation of components 3 and 4, an assumption has been made that the diffuse skylight is reflected from the surface by Lambert's law of reflection, the total reflectance being obtained by integrating the measured directional reflectance $\rho_b(\mu,\varphi;\mu_o,\varphi_o)$ over the hemispheric solid angle. The approximation is reasonably good for three reasons. First, the diffuse character of the skylight minimizes the directional effects and the resultant polarization of the resultant flux at the surface. Secondly, the quasi-diffuse nature of reflectance from the natural materials used in these measurements further decreases directional effects in the surface-reflected radiation. Finally, the skylight contributes a relatively small portion of the total energy incident at the surface, particularly for cases of small optical thicknesses and small solar zenith angles. Unfortunately these last criteria do not apply to all three of the cases discussed here, however.

With the Lambert approximation for the skylight, component number 3 is expressed as

$$I_{dD} \ (0; \mu, \tau_1, \bar{R}) = \pi F \mu_0 \frac{\bar{R}}{\pi} \left\{ \frac{\gamma_\ell(\mu_0) + \gamma_r(\mu_0)}{2(1-\bar{R}\bar{s})} - e^{-\tau_1/\mu_0} \right\} e^{-\tau_1/\mu} \tag{5}$$

This includes the part of the surface-reflected radiation which is scattered back down to the surface by the overlying atmosphere.

Component No. 4 - Radiation which is transmitted diffusely through the atmosphere, reflected from the surface, and transmitted diffusely back out through the atmosphere. We again invoke the Lambert surface approximation and express this component as

$$I_{dd}(0, \mu, \tau_1, \bar{R}) = \pi F \mu_0 \frac{\bar{R}}{\pi} \left\{ \frac{\gamma_\ell(\mu_0) + \gamma_r(\mu_0)}{2(1-\bar{R}\bar{s})} - e^{-\tau_1/\mu_0} \right\} \left\{ \frac{\gamma_\ell(\mu) + \gamma_r(\mu)}{2} - e^{-\tau_1/\mu} \right\} \tag{6}$$

Downward scattering of the surface reflected radiation is accounted for here also.

Component No. 5 - Radiation which is backscattered by the atmosphere without ever having reached the surface. This component is given in its complete vector form by

$$\underset{\sim}{I}_s \ (0; \mu, \varphi) = \frac{1}{4\pi\mu} \ \underset{\sim}{S}(\mu, \varphi; \mu_0, \varphi_0) \ \pi \ \underset{\sim}{F} \tag{7}$$

This corresponds to the "standard" case of Chandrasekhar [1950].

regardless of the position of either the carriage or the instrument carrier arm. The two degrees of freedom then provide the possibility of the instrument viewing the surface at any (θ, φ) direction within the ranges $0^{\circ} \leq \theta \leq 80^{\circ}$, $0 \leq \varphi \leq 360$. The carriage can be positioned on the track in a position such that the single instrument carrier arm will never shade the viewed area from a single source or from direct sunlight, although it will, of course, cut off a small amount of the skylight. In order to minimize the interruption of skylight by the instrument mount, the whole structure has been kept very low. Fig. 3 is a photograph of the assembly showing additional details.

C. Optical System and Color Filter Curves

The reflectometer sensor head itself is shown schematically in Fig. 4. The light, L, enters the collimator tube, C, is chopped by a chopper rotated by motor, M, and passes successively through a rotating analyzer, A, an optical filter F, a divergent lens, G, and finally activates the cathode surface of photomultiplier tube, P.

The response of the photomultiplier is amplified and recorded on a standard strip-chart recorder. The acceptance field for the instrument is limited to a 2.5° half-angle cone by the diaphragms within the collimator tube. In order to minimize possible polarization sources within the instrument, the optical components have been restricted to the bare essentials; no mirrors are used and the only lens is behind the analyzer in the optical train. The analyzer, a Glan-Thompson prism, is rotated, by a synchronous motor, at approximately 7.6 revolutions per minute. The photomultiplier tube is an end-on type, RCA #7236. Measurements taken of a natural light source

Fraser [1964b], the apparent contrast $C(0;\mu,\varphi)$ between target and background as seen at the top of the atmosphere can be expressed in terms of the inherent contrast $C(\tau_1;\mu,\varphi)$ which exists at the bottom of the atmosphere and an atmospheric contrast transmission coefficient $Y(\tau_1;\mu,\varphi)$ such that

$$C(0;\mu,\varphi) = Y(\tau_1;\mu,\varphi)\, C(\tau_1;\mu,\varphi) \tag{8}$$

The utility of this formulation can be seen from the following consideration. The relationship between the intensities of the emergent and surface-reflected radiations is expressed by the formal solution to the transfer equation, which is (cf. Chandrasekhar [1950], page 12)

$$I(0;\mu,\varphi) = I(\tau_1;\mu,\varphi)\, e^{-\tau_1/\mu} + \int_0^{\tau_1} J(t,\mu,\varphi)\, e^{-t/\mu}\, \frac{dt}{\mu} \tag{9}$$

The quantity J is the so-called source function. By substituting Eq. (9) in Eq. (2), we obtain

$$C(0;\mu,\varphi) = \frac{\{I_t(\tau_1;\mu,\varphi) - I_b(\tau_1;\mu,\varphi)\}\, e^{-\tau_1/\mu}}{I_b(\tau_1;\mu,\varphi)\, e^{-\tau_1/\mu} + \int_0^{\tau_1} J(t;\mu,\varphi)\, e^{-t/\mu}\, \frac{dt}{\mu}}$$

From Eq. (8) it is seen that

$$Y(\tau_1;\mu,\varphi) = \frac{C(0;\mu,\varphi)}{C(\tau_1;\mu,\varphi)} = \frac{I_b(\tau_1;\mu,\varphi)\, e^{-\tau_1/\mu}}{I_b(\tau_1;\mu,\varphi)\, e^{-\tau_1/\mu} + \int_0^{\tau_1} J(t;\mu,\varphi)\, e^{-t/\mu}\, \frac{dt}{\mu}} \tag{10}$$

As pointed out by Fraser [1964], this is a very convenient situation, for the transmission coefficient depends only on the radiation field due to the atmosphere and background, and not at all on the characteristics of the target as long as the target fulfills the criterion of being small relative to the background. This means that we can compute $Y(\tau_1;\mu,\varphi)$ for a selected surface such as, for instance, desert sand, and then easily determine by means of Eq. (8) the apparent contrast for any target we desire as long as the reflection characteristics of the target are known.

The coefficient $Y(\tau_1;\mu,\varphi)$ can be expressed in terms of the five components of intensity of the emergent radiation discussed above (cf. Equations (3) to (7)) as

$$Y(\tau_1;\mu,\varphi) = \frac{I_{DD} + I_{dD}}{I_{DD} + I_{Dd} + I_{dD} + I_{dd} + I_s} \tag{11}$$

Curves of $Y(\tau_1;\mu,\varphi)$ and of the individual components are given in the next section.

III Results

Three cases have been selected to show the effect of surface reflection on the contrast transmission coefficient and the resulting contrast that would be seen at the top of the atmosphere. Desert sand, at two wavelengths and two solar zenith angles ($\lambda = 4920$ Å, $\theta_o = 78.5°$; $\lambda = 6430$ Å, $\theta_o = 53.1°$), has been selected as a surface with moderately high reflectance, and a sample of closely clipped green grass has been chosen as a surface with low reflectance associated with a relatively large optical thickness ($\lambda = 4050$ Å, $\tau_1 = 0.50$, $\theta_o = 53.1°$). A slightly turbid atmosphere has been assumed for all cases, the size distribution of the aerosol particles being that of a continental type aerosol (Model C, Fraser [1964a]). An exponential decrease of aerosol concentration with altitude has been assumed, with a scale height of 0.98 km. (Penndorf [1954])

The directional reflectance of the two surfaces as measured in the laboratory is shown by the plot of the quantity $\pi \rho (\mu, \varphi; \mu_0, \varphi_0)$ as a function of nadir angle at which the surface is viewed in Fig. 2. The factor π is a normalization constant. The curves are for the principal plane (vertical plane through direction of incident radiation), the direction of the anti-source ($\theta = \theta_0$, $\varphi = 180^\circ$) being indicated by the arrows. The curves in the vicinity of the arrows have been faired in by eye, since an interference between instrument and source prohibit measurements just at $\theta = \theta_0$. The total reflectance $\bar{R}$, obtained by a hemispheric integration of the directional reflectance $\rho(\mu, \varphi; \mu_0, \varphi_0)$, for the three cases is the following:

Desert Sand, $\lambda = 4920$ Å, $\theta_0 = 78.5^\circ$: $\bar{R} = 0.310$
Desert Sand, $\lambda = 6430$ Å, $\theta_0 = 53.1^\circ$: $\bar{R} = 0.360$
Green Grass, $\lambda = 4050$ Å, $\theta_0 = 53.1^\circ$: $\bar{R} = 0.026$

The polarizing characteristics of the surfaces are shown by the data from laboratory measurements in Fig. 3, in which the degree of polarization of the reflected radiation is plotted as a function of nadir angle in the principal plane at which the surface was viewed. The incident radiation was unpolarized for all of the measurements. Measurements at other azimuths permitted hemispheric maps of $P(\mu, \varphi)$ to be constructed, from which a value of P for any direction in the hemisphere could be obtained.

By use of the measured values of $\rho(\mu, \varphi; \mu_0, \varphi_0)$ and $P(\mu, \varphi)$ for the selected surfaces, the individual components of the emergent radiation were computed by Equations (3) to (7). The relative intensity of the various components for desert sand at $\lambda = 4920$ Å are shown, as a function of nadir angle in the principal plane, by Fig. 4. The top curve represents the total intensity I of the emergent radiation and is simply the sum of the individual components.

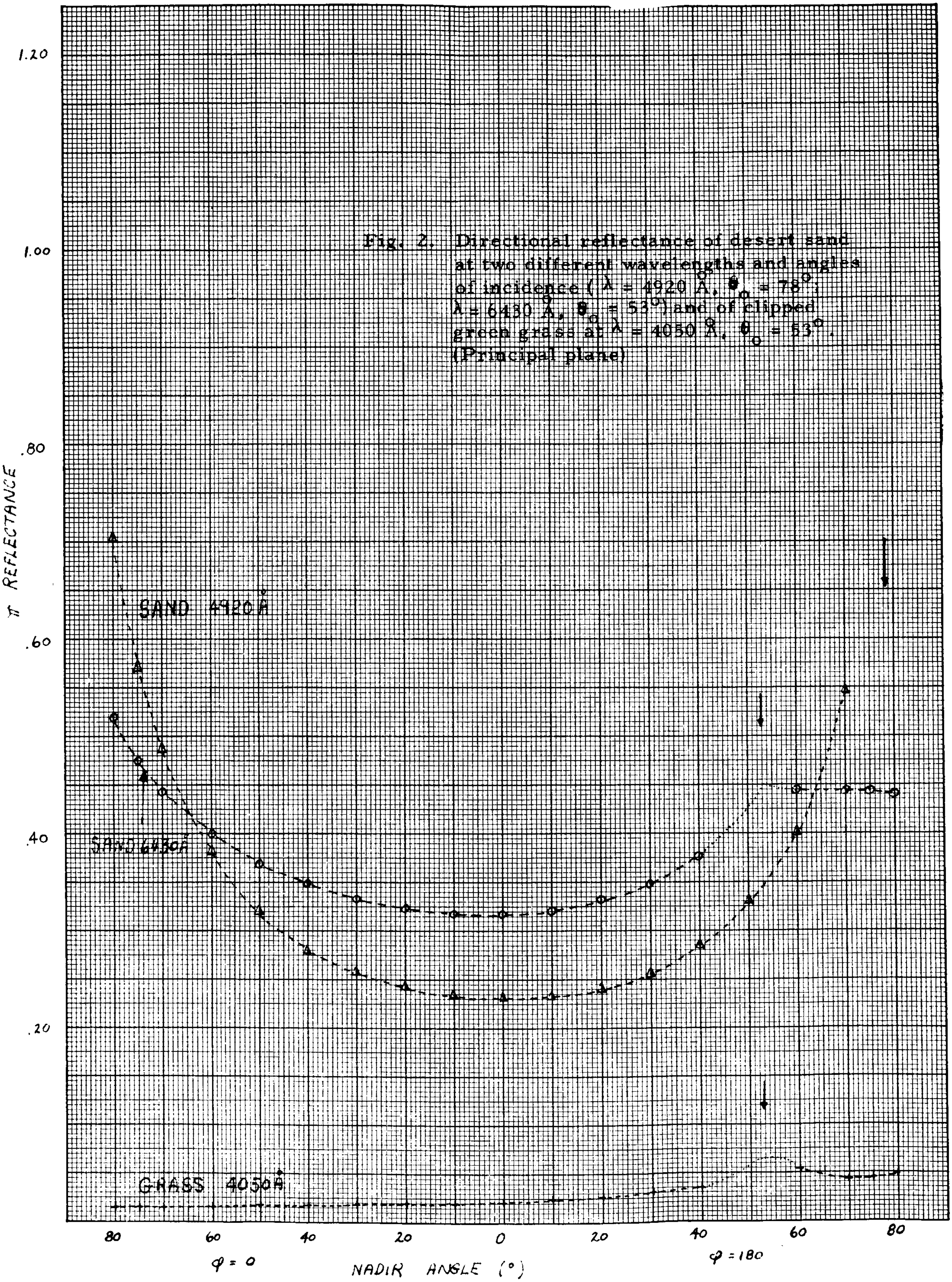

Fig. 2. Directional reflectance of desert sand at two different wavelengths and angles of incidence (λ = 4920 Å, θ_o = 78°; λ = 6430 Å, θ_o = 53°) and of clipped green grass at λ = 4050 Å, θ_o = 53°. (Principal plane)

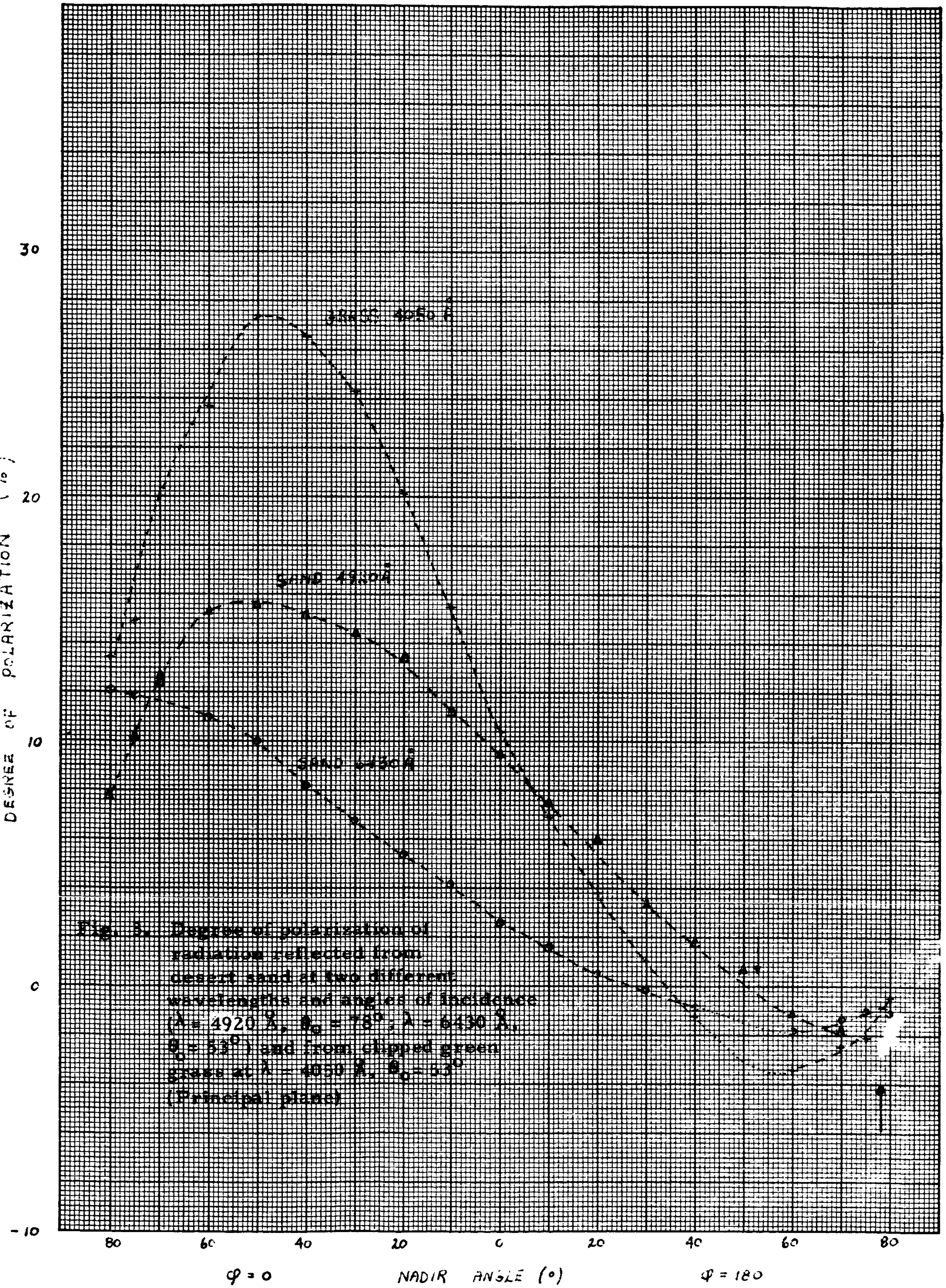

Fig. 3. Degree of polarization of radiation reflected from desert sand at two different wavelengths and angles of incidence (λ = 4920 Å, θ_o = 78°; λ = 6430 Å, θ_o = 53°) and from clipped green grass at λ = 4050 Å, θ_o = 53° (Principal plane)

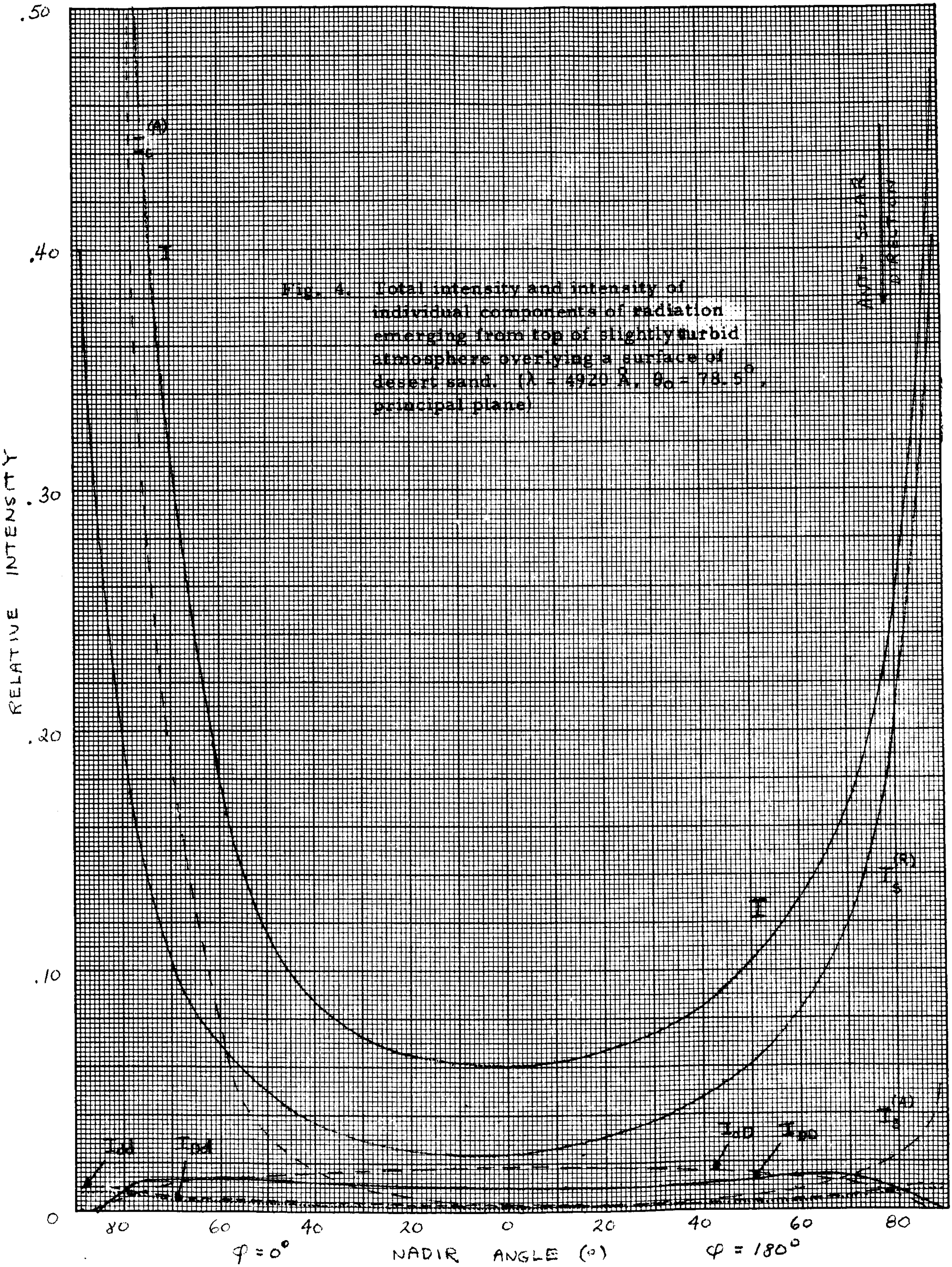

Fig. 4. Total intensity and intensity of individual components of radiation emerging from top of slightly turbid atmosphere overlying a surface of desert sand. (λ = 4920 Å, θ_0 = 78.5°, principal plane)

While a complete discussion of Fig. 4 is outside the scope of this paper, two features should be mentioned. First, the strong limb brightening, due largely to the Rayleigh part $I_s^{(R)}$ of I_s, is exaggerated somewhat by the assumption of a plane parallel atmosphere, but the effect is not important at $\theta < 80^{\circ}$. Secondly, the strongly asymmetric character of the curve for the aerosol part $I_s^{(A)}$ of I_s is a result of the well-known asymmetric scattering pattern of aerosol particles.

The contrast transmission coefficient $Y(\tau_1; \mu, \varphi)$ for this case, obtained by the introduction of the intensities of Fig. 4 into Eq. (8), is shown by the middle curve of Fig. 5. In the nadir direction the apparent contrast as seen from the top of the atmosphere would be about half of the inherent contrast which exists at the surface, while the longer atmospheric pathlengths in other directions cause a greater degradation of the contrast during its atmospheric traverse.

In the discussion of the five individual intensities which emerge from the top of the atmosphere, it was seen that curves similar to those of Fig. 4 can be computed for the two orthogonal components I_e and I_r. From those results, the contrast transmission coefficients Y_i and Y_j can likewise be computed by Eq. (8). This procedure has yielded the Y_i and Y_j curves of Fig. 5.* Since the inherent contrast in one orthogonal component is transmitted considerably better than that in either the total intensity or the other orthogonal component, it would be of considerable practical advantage, other things

* The indices j and i represent the directions in and normal, respectively, to the plane of polarization, while the indices e and r refer to the directions in and normal, respectively, to the vertical plane through the observed direction. In the principal plane directions i and e coincide, as do directions j and r, but this is not generally true otherwise.

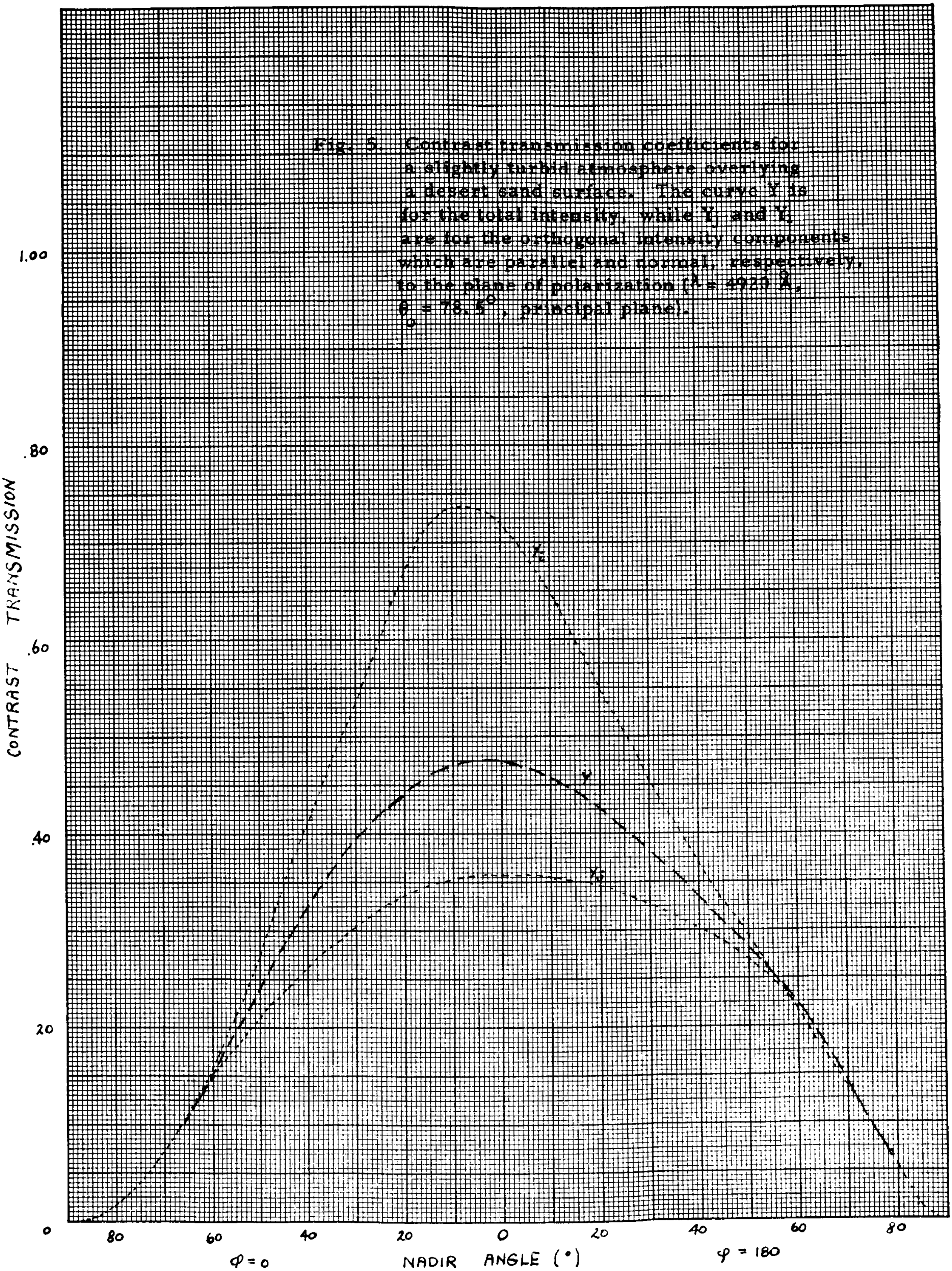

Fig. 5. Contrast transmission coefficients for a slightly turbid atmosphere overlying a desert sand surface. The curve Y is for the total intensity, while Y_l and Y_r are for the orthogonal intensity components which are parallel and normal, respectively, to the plane of polarization ($\lambda = 4920$ Å, $\theta_0 = 78.5°$, principal plane).

E. Operation and Calibration Procedure

Calibration of the instrument response versus relative radiant intensity was performed once each day during the measurements program by introducing neutral density filters of known transmission characteristics serially in the optical path at a constant incident intensity, and measuring the recorder deflection produced. The calibration curve determined by these data points was fitted by the least squares method with a third degree polynomial. Every reflectance measurement was then corrected by the application of the polynomial during the data reduction process.

In order to eliminate the necessity for absolute energy measurements, the ratio of the intensity of radiation reflected from the sample surface to that reflected from an assumed perfectly reflecting standard surface was used to compute directional reflectance $\rho(\theta, \varphi)$. In the regular operational procedure followed in the measurements, the sample reflectance in the normal direction was measured immediately after that of the standard surface, the illumination being considered constant over the minute or so necessary to complete the two measurements. Thus the sample measurement in the normal direction became a secondary standard of known reflectance. Repeated returns to the normal direction during the measurements sequence permitted corrections to be made for amplifier drifts and changes of light output of the source.

The normal sequence of measurements, for one wavelength and one position of the source, was as follows:

(1) Standard surface at $\theta = 0^{\circ}$

(2) Sample at $\theta = 0^{\circ}$ (this used as secondary standard)

Fig. 6 Distribution of the contrast transmission coefficient Y_t over the downward hemisphere for the case of desert sand, $\lambda = 4920$ Å, and $\theta_o = 78.5^\circ$. The pattern is symmetrical with respect to the principal plane.

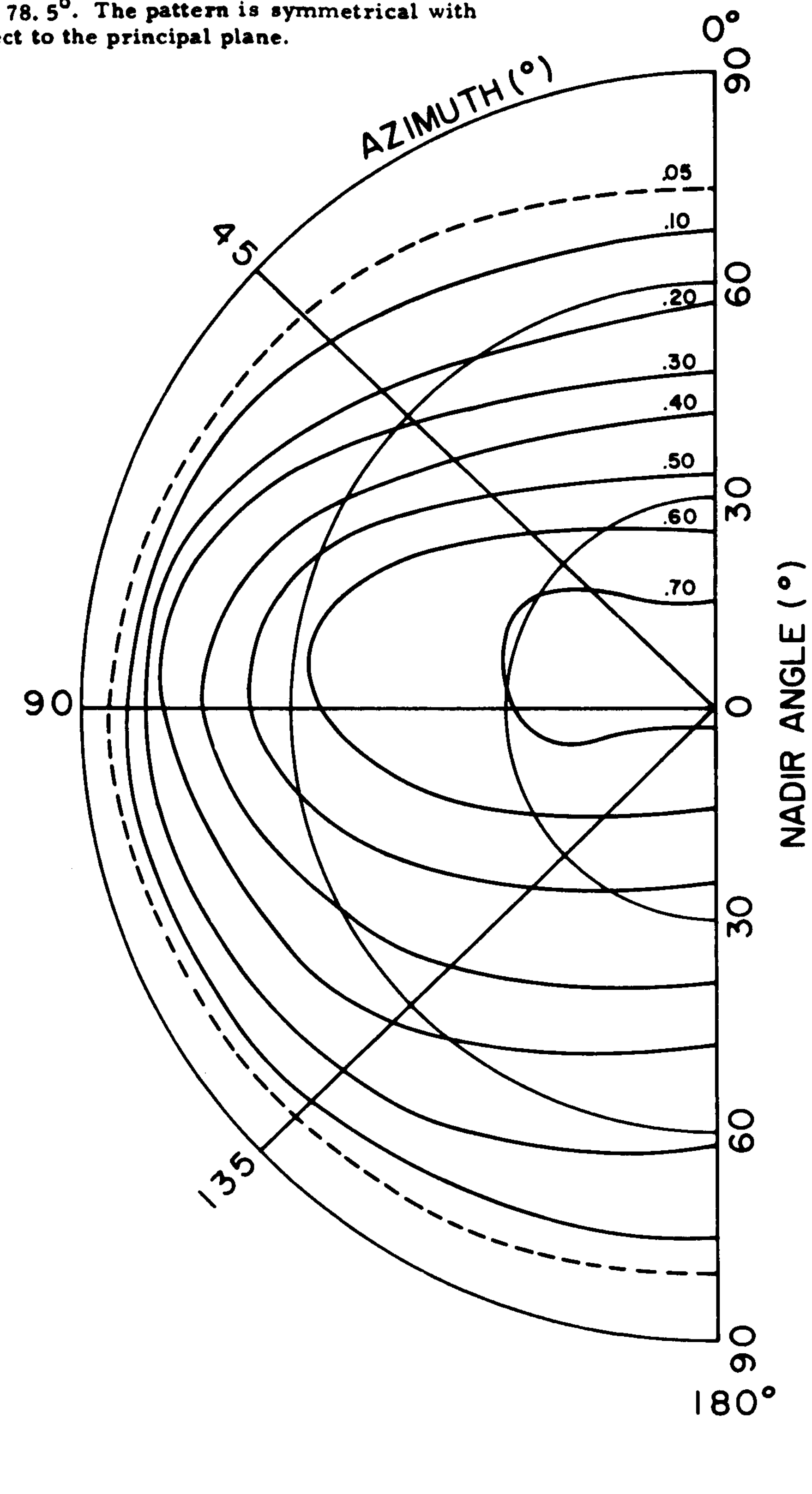

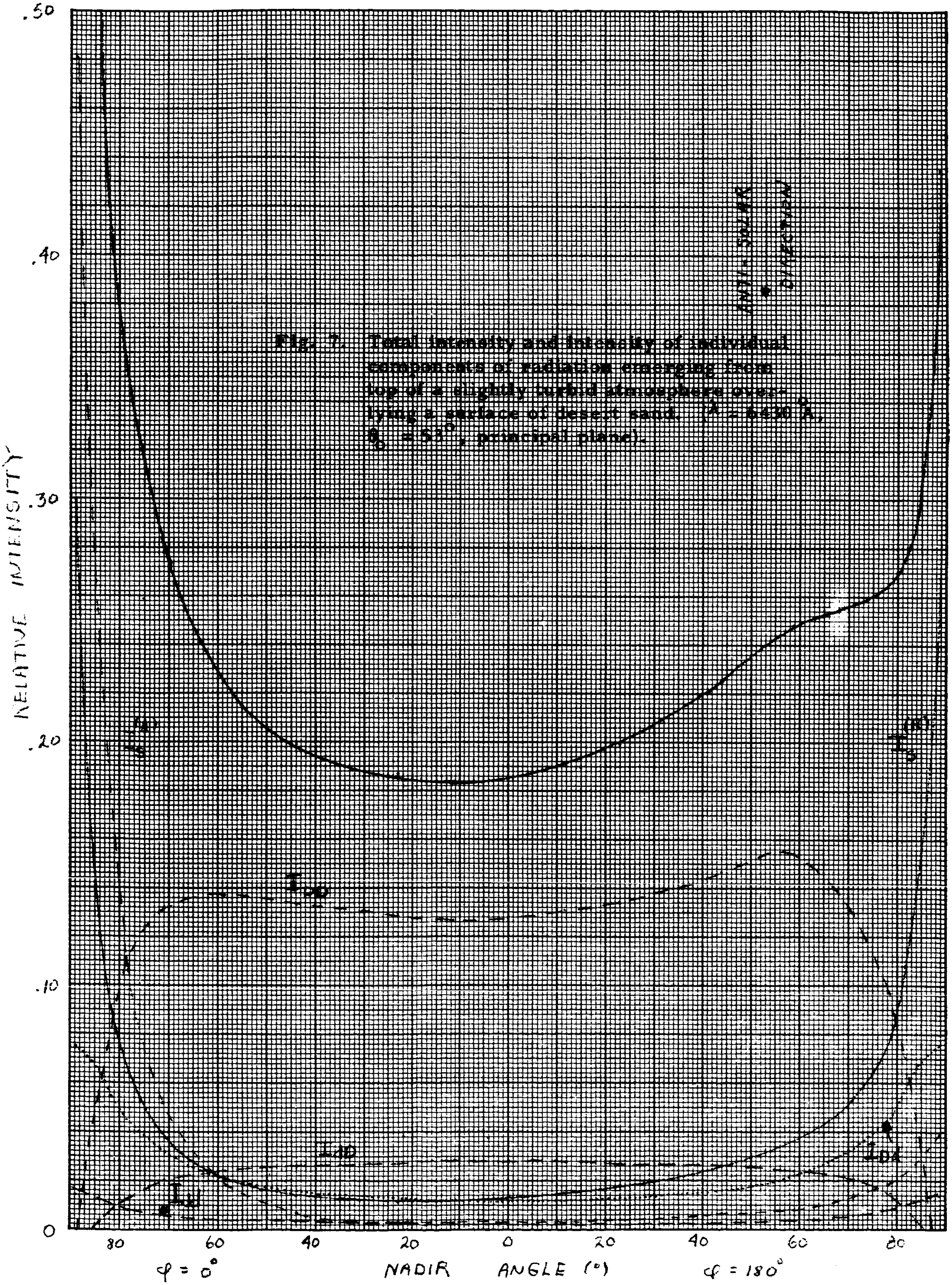

Fig. 7. Total intensity and intensity of individual components of radiation emerging from top of a slightly turbid atmosphere overlying a surface of desert sand. (λ = 6430 Å, θ_0 = 53°, principal plane).

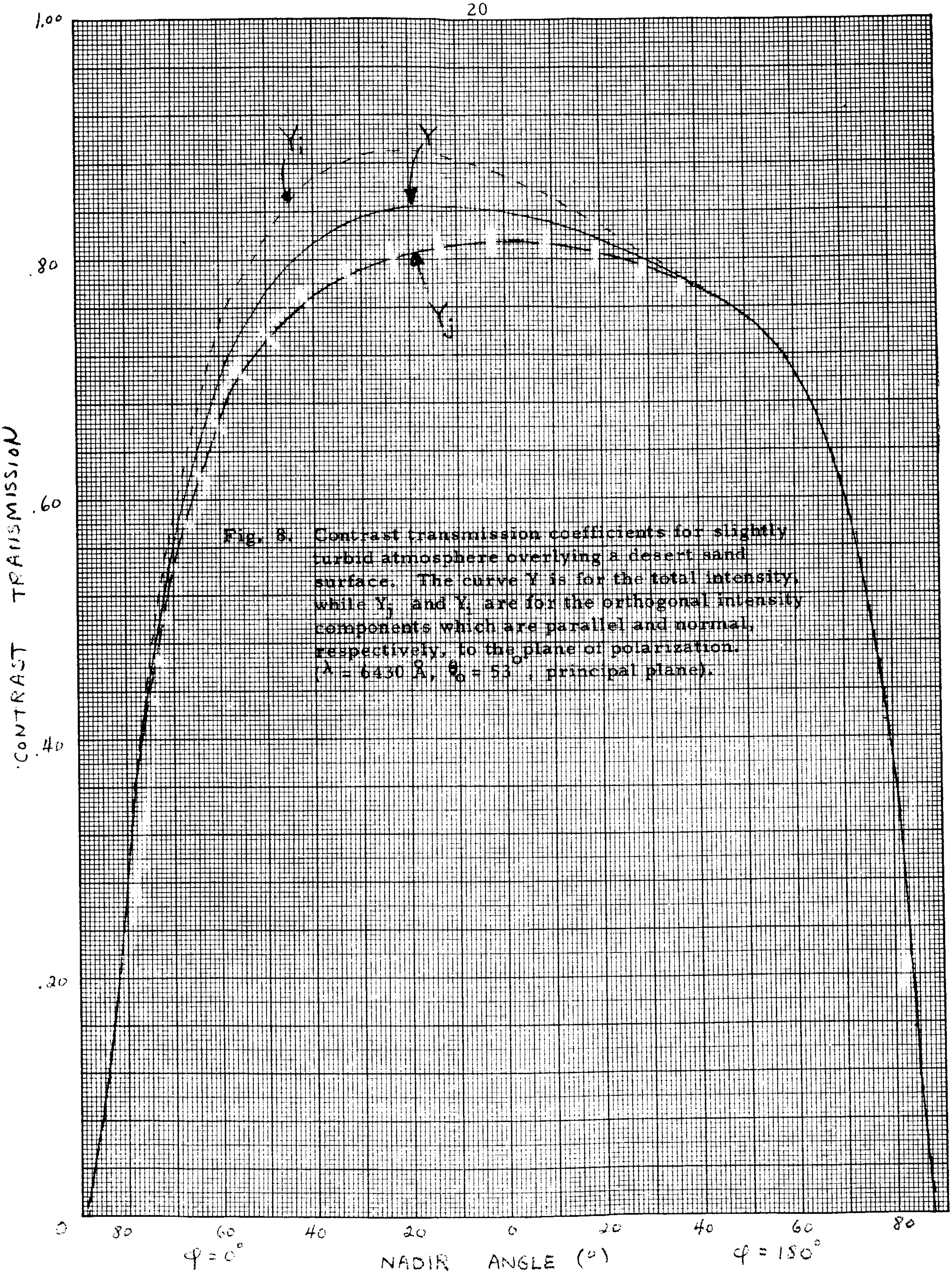

Fig. 8. Contrast transmission coefficients for slightly turbid atmosphere overlying a desert sand surface. The curve Y is for the total intensity, while $Y_\parallel$ and $Y_\perp$ are for the orthogonal intensity components which are parallel and normal, respectively, to the plane of polarization. (λ = 6430 Å, θ_o = 53°, principal plane).

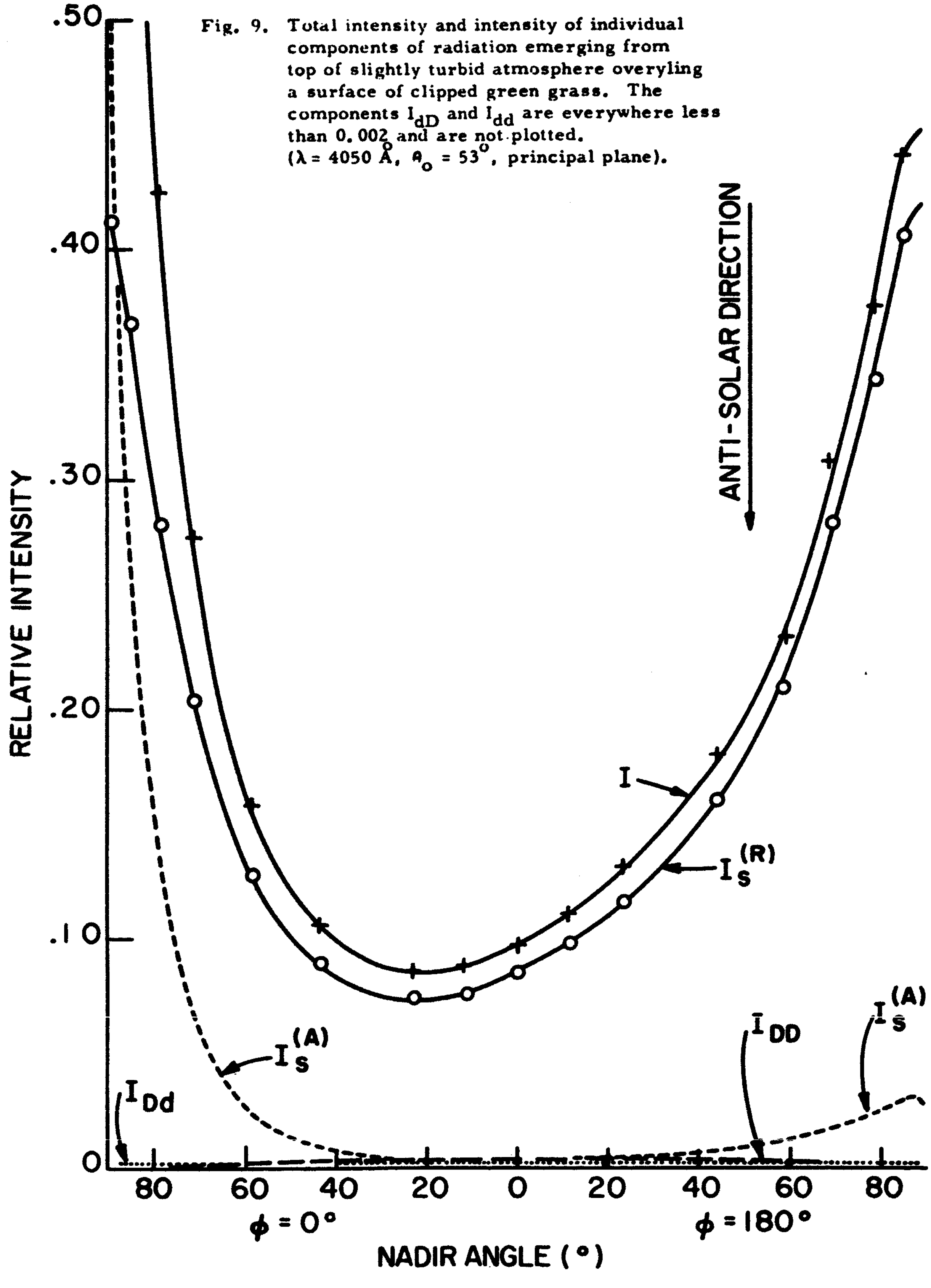

Fig. 9. Total intensity and intensity of individual components of radiation emerging from top of slightly turbid atmosphere overyling a surface of clipped green grass. The components I_{dD} and I_{dd} are everywhere less than 0.002 and are not plotted. (λ = 4050 Å, θ_o = 53°, principal plane).

$I_s^{(R)}$ and $I_s^{(A)}$ due to atmospheric scattering, however, dominate the picture throughout the whole hemisphere. As a consequence, the numerator of Eq. (8) is very small compared to the denominator, and the very low contrast transmissions shown by Fig. 10 are the result. Since most of the intensity is supplied by the relatively highly polarized atmospheric scattered components, there is a large difference between Y_i and Y_j near the angle of maximum polarization for Rayleigh scattering.

IV Discussion

It is instructive to compare the intensity* of the background radiation with the intensity of the radiation which a typical target would exhibit, both being observed at the top of the atmosphere. For this purpose we assume that a target is located in the nadir direction at ground level and that the target reflects isotropically 80% of the radiation which falls on it. The inherent and apparent contrasts between the target and background, as well as the contrast transmission coefficient and the intensities of radiation from the background and target at the top of the atmosphere, are listed for the three cases in Table II.

* Although intensities are given in relative units in this paper, they are easily converted to absolute units. In the computations the magnitude of F has been taken as unity, thereby making the incident flux across a unit surface oriented normal to the direction of propagation at the outside of the atmosphere equal to π. In order to change to the case in which the incident flux has Φ units of energy per unit time and unit frequency interval, it is only necessary to multiply these results by Φ / π.

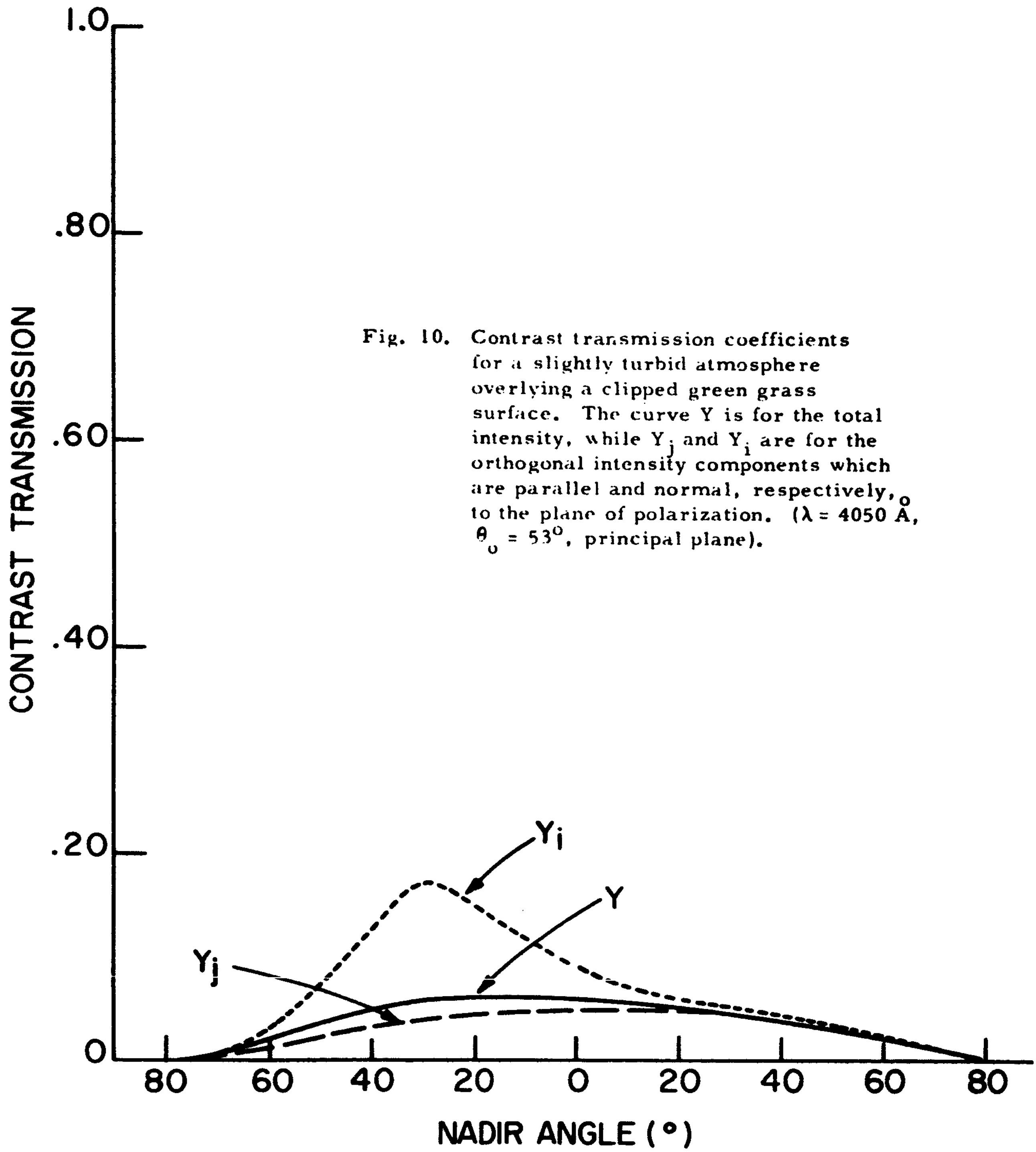

Fig. 10. Contrast transmission coefficients for a slightly turbid atmosphere overlying a clipped green grass surface. The curve Y is for the total intensity, while Y_j and Y_i are for the orthogonal intensity components which are parallel and normal, respectively, to the plane of polarization. (λ = 4050 Å, $\theta_0 = 53^\circ$, principal plane).

Table II - Contrast between target of $\bar{R} = 0.80$ and background as seen from ground ($C(\tau = \tau_1)$) and as seen from top of atmosphere ($C(\tau = 0)$), together with contrast transmission coefficient (Y) and intensities of background (I_b) and target (I_t) at top of atmosphere. The data all apply to the nadir direction.

Surface	$\lambda(\mathring{A})$	$\theta_o(^\circ)$	$C(\tau=\tau_1)$	Y	$C(\tau=0)$	$I_b(\tau=0)$	$I_t(\tau=0)$
Desert Sand	4920	78.5	2.43	.472	1.15	.060	.129
Desert Sand	6430	53.1	1.52	.839	1.27	.186	.422
Green Grass	4050	53.1	35.4	0.062	2.19	0.097	0.309

It is seen that although inherent contrast and contrast transmission are both reasonably large for the desert sand at 4920 Å, their product gives less apparent contrast than that of either of the other cases. For desert sand at 6430 Å, the low inherent contrast is compensated by a high value of Y, and the very high inherent contrast between target and grass at 4050 Å is transmitted sufficiently well to give the highest apparent contrast of the three cases.

The relative intensities of the background radiation (I) and of the radiation in the direction of the target (I_t) are compared graphically in Fig. 11. The three curves in the diagram are the total relative intensities of the background radiation, and the superimposed bars represent those in the direction of the target.

Acknowledgment

This investigation is sponsored by the National Aeronautics and Space Administration under Contract No. NAS 5-3925.

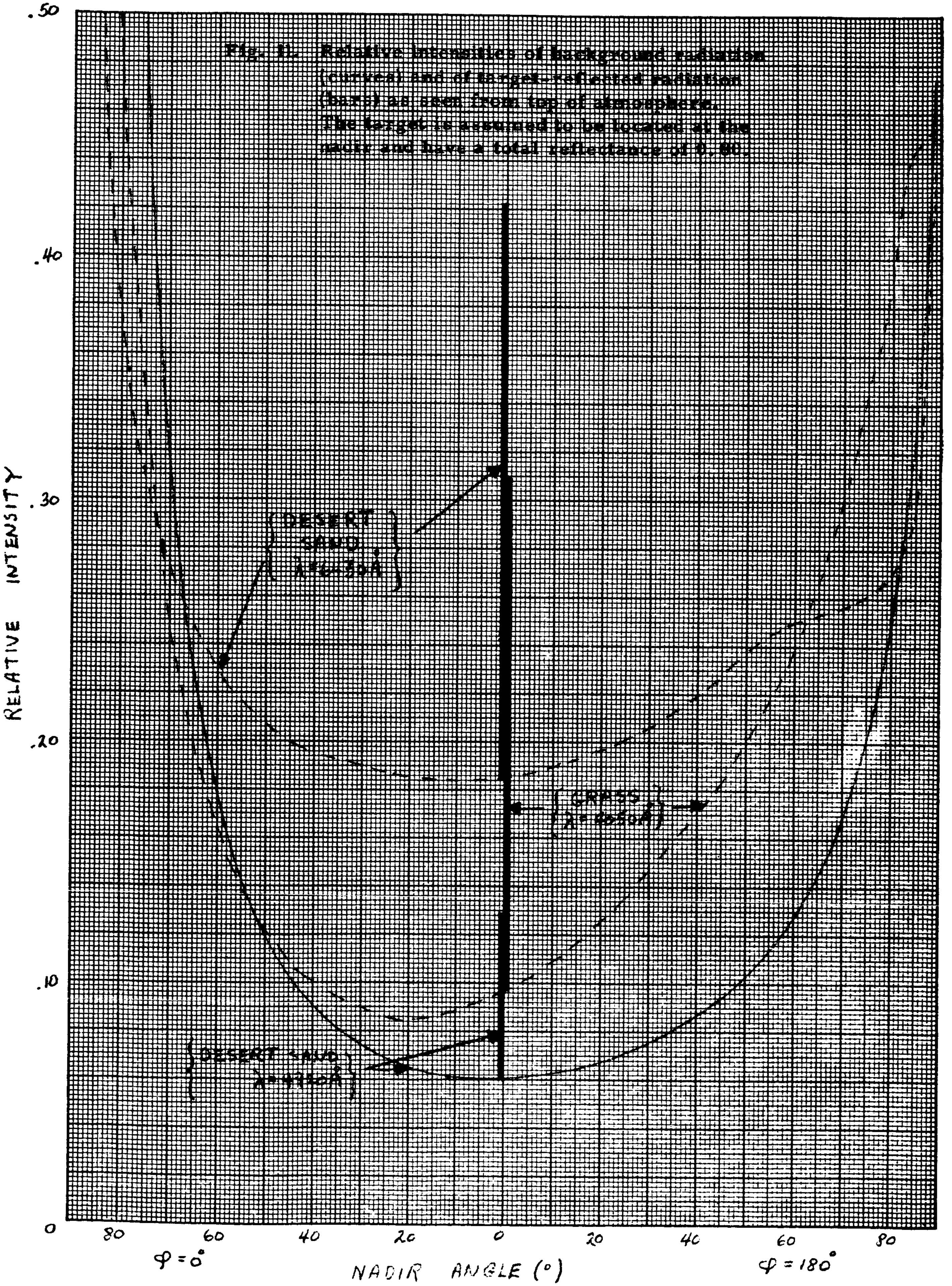

Fig. 11. Relative intensities of background radiation (curves) and of target-reflected radiation (bars) as seen from top of atmosphere. The target is assumed to be located at the nadir and have a total reflectance of 0.80.

References

Chandrasekhar, S. (1950) - Radiative Transfer, Oxford Clarendon Press

Cornell Aeronautical Laboratory (1961) - "A Scientific Investigation into Photographic Reconnaissance from Space Vehicles," Final Report, Contract AF33(616)-5870, ASTIA No. AD 260694.

Coulson, K. L., E. L. Gray, and G. M. B. Bouricius (1965) "Effect of Surface Reflection on Planetary Albedo," Icarus (in press)

Fraser, R. S. (1964a) - "Computed Intensity and Polarization of Light Scattered Outwards from the Earth and an Overlying Aerosol," J. Opt. Soc. Am., 54 (2), 157-168.

Fraser, R. S. (1964b) - "Apparent Contrast of Objects on the Earth's Surface as Seen from above the Earth's Atmosphere," J. Opt. Soc. Am., 54 (3), 289-300.

Penndorf, R. (1954) - "The Vertical Distribution of Mie Particles in the Stratosphere," J. of Meteorology, 11 (3), 245-247

Sekera, Z. and G. Blanch (1952) - "Tables Relating to Rayleigh Scattering of Light in the Atmosphere," Contract No. AF 19(122)-239, University of California, Los Angeles

Sekera, Z. and E. V. Ashburn (1953)- "Tables Relating to Rayleigh Scattering of Light in the Atmosphere," NAVORD Rept. 2061, U. S. Naval Ordnance Test Station, Inyokern, California